9-Anthracenemethoxycarbonyl Protected Dipeptide-Based Soft Materials for Biomedical Applications

Ph.D. Thesis

by

PRAMOD KUMAR GAVEL

DISCIPLINE OF CHEMISTRY

INDIAN INSTITUTE OF TECHNOLOGY INDORE

AUGUST 2020

9-Anthracenemethoxycarbonyl Protected Dipeptide-Based Soft Materials for Biomedical Applications

A THESIS

Submitted in partial fulfillment of the requirements for the award of the degree of

DOCTOR OF PHILOSOPHY

by

PRAMOD KUMAR GAVEL

DISCIPLINE OF CHEMISTRY

INDIAN INSTITUTE OF TECHNOLOGY INDORE

AUGUST 2020

INDIAN INSTITUTE OF TECHNOLOGY INDORE

CANDIDATE'S DECLARATION

I hereby certify that the work which is being presented in the thesis entitled **9-Anthracenemethoxycarbonyl Protected Dipeptide-Based Soft Materials for Biomedical Applications** in the partial fulfillment of the requirements for the award of the degree of **DOCTOR OF PHILOSOPHY** and submitted in the **DEPARTMENT OF CHEMISTRY, Indian Institute of Technology Indore**, is an authentic record of my own work carried out during the time period from July 2015 to August 2020 under the supervision of **Dr. APURBA K. DAS**, Associate Professor, Department of Chemistry, Indian Institute of Technology Indore

The matter presented in this thesis has not been submitted by me for the award of any other degree of this or any other institute.

31/08/2020

PRAMOD KUMAR GAVEL

This is to certify that the above statement made by the candidate is correct to the best of my/our knowledge.

Dr. APURBA K. DAS

PRAMOD KUMAR GAVEL has successfully given his/her Ph.D. Oral Examination held on 08.01.2021

(Dr. Debasis Nayak)	(Prof. Bhubaneswar Mandal)	
Signature of Chairperson (OEB)	Signature of External Examiner	Signature(s) of Thesis Supervisor(s)
Date: 08.01.2021	Date: 08.01.2021	Date: 08.01.2021
(Dr. Anjan Chakraborty)	(Dr. Santosh K. Sahu)	
Signature of PSPC Member #1	Signature of PSPC Member #2	Signature of Convener, DPGC
Date: 08.01.2021	Date: 08.01.2021	Date: 08.01.2021

Signature of Head of Discipline
Date: 08.01.2021

ACKNOWLEDGEMENTS

I am very grateful to LORD SHIVA for giving me good health, strength and ability to perform the research work.

I would like to express my deep and special gratitude to my thesis supervisor Dr. Apurba K. Das for his constant trust and support during the research work. I am very grateful to him for his sincerity, vision and foresightedness towards my thesis work. I am highly indebted to him for his generous guidance, expert advice and excellent supervision which lead to the completion of thesis work.

I would also like to extend my deepest acknowledgment to Dr. Anjan Chakraborty and Dr. Santosh K. Sahu for their invaluable time, insightful comments and suggestions during my entire research work which helped me to improve my thesis work.

I am ineffably thankful to my external collaborator Dr. Hamendra S. Parmar (Assistant Professor, Devi Ahilya University Indore) for providing biological research facilities. It was a great privilege and honor to work under the guidance of him.

I am extending my heartfelt thanks to Dr. Anand Nighojkar (Principal) and Dr. Sheetal Bhasin, Maharaja Ranjit Singh College Indore for providing microbiological research facilities.

I am very thankful to Prof. Suman Mukhopadhyay, Prof. Rajneesh Misra, Dr. Sampak Samanta, Dr. Tushar Kanti Mukherjee (DPGC, Chemistry), Dr. Biswarup Pathak (HoD, Chemistry), Dr. Shaikh M. Mobin,Dr. Tridib Kumar Sarma, Dr. Satya S. Bulusu, Dr. Sanjay Kumar Singh, Dr. Chelvam Venkatesh, Dr. Amrendra Kumar Singh, Dr. Abhinav Raghuvanshi, Dr. Dipak Kumar Roy, Dr. Selvakumar Sermadurai, Dr. Umesh A. Kshirsagar for their precious time and guidance during my research work.

I am thankful to Dr. Hem Chandra Jha and Dr. Mirza S. Baig for allowing me to access the cell culture facilities at BSBE IIT Indore.

I would also like to thank Dr. Radhe Shyam Ji, Mr. Ghanashyam A. Bhavsar, Mr. Kinny Pandey, Dr. Ravinder, Mr. Manish Kushwaha, Mr. Parthiban P K, Mrs. Vinita Kothari, Mr. Rameshwar Dauhare for their various scientific and technical support.

From the bottom of my heart, I offer my gratitude to my friends Dr. Kuber S. Rawat, Dr. Novina Malviya, Dr. Priyanka Garg, Mrs. Shikha Khandelwal, Dr. Arun K. Verma, Dr. Eshan Khan, Ms. Chanchal Sonkar,

Mr. Uma Shankar, Mr. Rameshwar Lal Kumawat for their unconditional help and mental support during the research work.

I am pleased to acknowledge my all seniors, juniors and current group members Dr. Narendra Kumar, Dr. Dnyaneshwar B. Rasale, Mr. Maruthi Konda, Dr. Manoj K. Manna, Dr. Bharati Agrawal, Dr. Dharm Dev, Dr. Sagar Biswas, Dr. Aditi Roy Chowdhury, Soumitra Bhowmik, Rohit Jadhav, Ankan Biswas, Sayan Maiti, Ritu Chahal, Jonu Yadav, Antara Reja, Devraj Singh, Tapas Ghosh, Vishakha Singh, Deepak Kori, Mithu Roy, Meenu Sharma, Likhi, Sourav Bhowmik, Nikita Sharma, Sachin Kumar for their cooperation, help and support for various experimental work.

I am very thankful to Dr. Ramesh Margani, Dr. T. Sheshashena Reddy, Dr. R. V. Ramana Reddy, Dr. Arpan Bhattacharya, Ms. Jamuna K. Vaishnav, Ramesh Reddy B, Soumya Kanti De, Dr. Ambikesh Dwivedi for their help.

I would also like to thank Mr. Tanim A. Singh and Mrs. Sanjula Verma for their precious help and suggestions during microbiological experiments.

I am very glad to acknowledge my dearest friends Dr. Pankaj Patidar (Scientific Officer, Sagar), Dr. Sunil Patidar (Assistant Professor, Khandwa), Dr. Ravi Vishwakarma (Assistant Professor, Jhabua), Pankaj Bhariya (Assistant Professor, Jhabua), Dr. Ravikant Mahant (General Surgeon, NSCB Jabalpur) for their help and suggestions.

I also wish to thank Dr. KVS Ranganath (Associate Professor, BHU Varanasi) for giving me motivation and encouragement towards the research work.

I am extremely grateful to my mother Mrs. Sawita D. Gavel and my father Mr. Dewanand Gavel for their love, care, prayers and sacrifice for my dream, and passion. I am very thankful to my younger brother Mr. Pradeep K. Gavel for his support and encouragement during my ups and downs. I am also thankful to my sister Mrs. Lipika Gavel for her care and affection. I am glad to thanks my brother-in-law Mr. Puspendra Gavel and my niece Ms. Ridhima Gavel for their love and care.

It is my pleasure to thank my family members Late Shri Harvansh K. Gavel, Late Shri Chandra Vijay Gavel, Mr. Rajendra P. Gavel, Mr. Jivendra K. Gavel and Narendra K. Gavel for their love and affection.

I am thankful to all my family members, relatives, teachers, friends, colleagues, seniors and juniors who supported and helped me a lot either directly or indirectly in any part of my life which made the journey beautiful.

Pramod Kumar Gavel

Dedicated to My Beloved

Parents (Maa & Babu Ji)

Abstract

Peptide self-assembly has been extensively investigated for the preparation of functional biomaterials that can be used for the various interdisciplinary areas of research which include antibacterial therapy, wound healing, drug delivery and tissue engineering. The low-molecular-weight peptide-based hydrogels have attracted significant attentions in the area of biomedical research because of their biocompatibility, non-immunogenicity, biodegradability, and chemical simplicity. In the thesis work, the Amoc (9-anthracenemethoxycarbonyl)-capped dipeptides have been designed and synthesized which self-assemble into the water and form hydrogels owing to the participation of noncovalent interactions. The synthesized hydrogels have been employed for various in vitro and in vivo biological applications.

The main objectives of the present study are:

1. To design and synthesize the Amoc-capped dipeptide-based biocompatible and injectable hydrogels for the differential biological effect on bacterial and human blood cells.
2. To design and synthesize an Amoc-capped dipeptide-based hydrogel which show anti-inflammatory activity on rat air pouch model of acute inflammation.
3. To design and synthesize an Amoc-capped dipeptide-based coassembled nanofibrous and thixotropic hydrogel for dermal wound healing.
4. To design and synthesize an Amoc-capped dipeptide-based coassembled hydrogel for in vivo wound dressing application.

1. Investigations of peptide-based biocompatible injectable shape-memory hydrogels: differential biological effects on bacterial and human blood cells

Chapter 2 describes the self-assembly of Amoc-capped dipeptides, which self-assembled to form injectable and self-healable hydrogels with inherent antibacterial properties. Self-supporting hydrogels **1** and **2** were obtained through molecular self-assembly of Amoc-capped dipeptides **1** and **2** (peptide **1**: Amoc-FL-OH; peptide **2**: Amoc-FY-OH; F = L-phenylalanine, L = L-leucine, and Y = L-tyrosine) at physiological conditions (pH 7.4, 37 °C). The noncovalent interactions such as hydrogen bonding and π-π stacking interactions are the driving force for the self-assembly of Amoc-capped dipeptides. TEM and SEM revealed 3D dense nanofibrillar networks of the hydrogels. The rheological experiments revealed that the hydrogels are robust and self-healing up to several cycles with nonsignificant loss of their strength. The self-assembly process was analyzed by fluorescence spectroscopy, and the presence of a secondary structure in peptide hydrogels was confirmed by PXRD, FTIR, and CD spectroscopy experiments. The inherent antibacterial properties of hydrogels were evaluated using two Gram-positive *Staphylococcus aureus*, *Bacillus subtilis* and three Gram-negative *Escherichia coli*, *Pseudomonas aeruginosa*, and *Salmonella typhi* bacteria. These hydrogels exhibited potent antibacterial efficacy against Gram-positive and Gram-negative bacteria. The biocompatibility and cytotoxicity of the hydrogels were evaluated using 3-(4,5-dimethythiazol-2-yl)-2,5-diphenyl tetrazolium bromide (MTT),

hemolysis, and lipid peroxidation (LPO) assay on human blood cells. The hydrogels were hemocompatible and they decreased LPO values on human red blood cells probably via increased cellular stability against oxidative stress. Furthermore, MTT data showed that the hydrogels were biocompatible and promoted cell viability and proliferation on cultured human white blood cells.

2. Investigations of anti-inflammatory activity of a peptide-based hydrogel using rat air pouch model

Chapter 3 describes the design and development of peptide-based biocompatible materials with inherent therapeutic potentials. An Amoc-capped dipeptide **3** (Amoc-LF-OH: L = L-leucine, F = L-phenylalanine) was designed and synthesized for acute inflammation, which encapsulated large amount of water and formed biocompatible, injectable, thixotropic, and self-healable hydrogel **3** at physiological condition (pH 7.4, 37 °C). The SEM and TEM images revealed the dense and cross-linked nanofibrillar networks, which were responsible for the formation of thixotropic hydrogel. The self-assembly process was investigated by UV-vis, fluorescence and time-correlated single photon counting spectroscopy, which suggest strong noncovalent interactions between hydrogelators. The secondary structure was analyzed by FTIR and CD spectroscopic techniques which showed antiparallel arrangement of peptides in the self-assembled state. The rheological experiment showed viscoelastic nature of the hydrogel. In vitro cytotoxicity of the hydrogel was investigated with the human embryonic kidney cell (HEK293) line which suggested that the synthesized peptide was noncytotoxic. The hydrogel showed an antibacterial efficacy against Gram-positive and Gram-negative bacteria. In vivo anti-inflammatory activity of the hydrogel was investigated using the rat air pouch model of acute inflammation. The major parameters considered for the anti-inflammatory study were exudate volume, total and differential white blood cell count, tissue histology, and lipid peroxidation assay. These experimental data suggest biocompatibility and potential therapeutic applications of peptide hydrogel in inflammation.

3. Evaluation of a peptide-based coassembled nanofibrous and thixotropic hydrogel for dermal wound healing

Chapter 4 presents a paradigm of coassembled hydrogel with a suitable mechanical strength that exhibited in vitro and in vivo biological applications. The designed and synthesized Amoc-capped dipeptide **4** (Amoc-FF-OH: F = L-phenylalanine) self-assembled into the tough and robust hydrogel **4** owing to participation of various noncovalent interactions. The coassembled hydrogels **5-8** were prepared by physical integration of various equivalents (0.25, 0.5, 1 and 2) of β-cyclodextrin (β-CD), respectively. The mechanical strength of the hydrogel was tuned by incorporation of equimolar β-CD with self-assembling peptides (peptide:β-CD = 1:1) which led to the formation of a coassembled hydrogel **7**. The coassembled hydrogel **7** demonstrated simple syringe injectability and thixotropy. The nanostructural morphology of the coassembled hydrogel revealed highly

crosslinked and entangled nanofibrillar network. Insight into the coassembly process, ^{1}H NMR, FTIR, PXRD and circular dichroism spectroscopic data elucidated the presence of noncovalent interactions between *β*-CD and peptide, which could be the driving force for the formation of ordered nanostructures. The coassembled hydrogel **7** showed potent antibacterial activity against Gram-positive bacteria. In vitro biocompatibility of the coassembled hydrogel was investigated with the human embryonic kidney (HEK293) and MCF-7 cell lines. Additionally, confocal laser scanning microscopic images showed cell penetration of the hydrogel **7** with blue fluorescence. Moreover, the in vivo wound healing activity of coassembled hydrogel **7** was investigated by histopathology study. The biochemical parameters such as nitric oxide, collagen contents were evaluated by Griess and hydroxy proline assay. All the results corroborate wound healing efficacy of nanofibrillar antibacterial coassembled hydrogel **7**.

4. Investigations of a Coassembled Hydrogel as a Wound Dressing System

Chapter 5 illustrates an Amoc-capped dipeptide **5** (Amoc-YY-OH: Y = L-tyrosine) based coassembled hydrogel, which exhibited in vivo wound dressing applications. The Amoc-capped dipeptide (20 mmol L^{-1}) **5** self-assembled and formed hydrogel **9**. Additionally, the Amoc-capped dipeptide coassembled with β-cyclodextrin (*β*-CD) at physiological conditions (pH 7.4, 37 °C), which resulted into the stable and self-supporting hydrogel **10**. The electron microscopic images of hydrogel **10** revealed the presence of entangled nanofibrillar networks owing to the coassembly of peptide and *β*-CD. The rheological investigations illustrated the viscoelastic nature of the hydrogel **10**. Additionally, the coassembled hydrogel **10** showed shear thinning because of dynamic making and breaking of cross-linked entangled networks through the noncovalent interactions. The coassembled hydrogel **10** exhibited inherent antibacterial activity against Gram positive *Bacillus subtilis* and *Staphylococcus aureus* bacteria. The biocompatibility of hydrogel was investigated using HEK293 and MCF-7 cell lines, which suggested noncytotoxic nature of the hydrogel. Moreover, the progress of wound dressing activity of hydrogel **10** was monitored by optical photographs and histopathological analysis of wound tissue. Furthermore, the hydrogel **10** significantly reduced the nitrite level and worked as an anti-inflammatory agent during the healing process. All the experimental data showed the coassembly of peptide and *β*-CD into a self-supporting hydrogel **10**, which exhibited as in vivo wound dressing system.

List of Publications:

1. **Gavel, P. K**., Dev, D., Parmar, H. S., Bhasin, S., Das, A. K. (2018), Investigations of Peptide-Based Biocompatible Injectable Shape-Memory Hydrogels: Differential Biological Effects on Bacterial and Human Blood Cells, *ACS Appl. Mater. Interfaces*, 10, 10729–10740 (DOI: 10.1021/acsami.8b00501). (Impact Factor = 8.758)

2. **Gavel, P. K**., Parmar, H. S., Tripathi, V., Kumar, N., Biswas, A., Das, A. K. (2019), Investigations of Anti-Inflammatory Activity of a Peptide-Based Hydrogel Using Rat Air Pouch Model, *ACS Appl. Mater. Interfaces*, 11, 2849–2859 (DOI: 10.1021/acsami.8b19228). (Impact Factor = 8.758)

3. **Gavel, P. K**., Kumar, N., Parmar, H. S., Das, A. K. (2020), In vivo Investigations of Wound Healing Efficacy of a Peptide-Based Nanofibrous Coassembled Hydrogel, *ACS Appl. Bio Mater*., 3, 3326−3336 (DOI: 10.1021/acsabm.0c00252). (Impact Factor = Pending)

4. Das, A. K., **Gavel, P. K**. (2020), Low molecular weight self-assembling peptide-based materials for cell culture, antimicrobial, anti-inflammatory, wound healing, anticancer, drug delivery, bioimaging and 3D bioprinting applications. *Soft Matter* (DOI: 10.1039/D0SM01136C). (Impact Factor = 3.14)

5. Biswas, A., Ghosh, T., **Gavel P. K**., Das, A. K. (2020), PEG Functionalized Stimuli Responsive Self-Healable Injectable Dynamic Imino-Boronate G-Quadruplex Hydrogel for the Delivery of Doxorubicin, *ACS Appl. Bio Mater.*, 3, 1052−1060 (DOI: 10.1021/acsabm.9b01034). (Impact Factor = Pending)

6. Ghosh, T., Biswas, A., **Gavel P. K**., Das, A. K. (2020), Engineered Dynamic Boronate Ester-Mediated Self-Healable Biocompatible G-Quadruplex Hydrogels for Sustained Release of Vitamins, *Langmuir*, 36, 1574−1584 (DOI: 10.1021/acs.langmuir.9b03837). (Impact Factor = 3.557)

Conferences Presentation:

1. **Gavel, P. K**., Das, A. K. Investigations of Anti-Inflammatory and Anti-Bacterial Activity of Peptide-Based Hydrogels, First in-house Chemistry Symposium "CHEM 2019" February 28, 2019 at Discipline of Chemistry, Indian Institute of Technology Indore (Oral Presentation).

2. **Gavel, P. K**., Das, A. K. Investigations of Anti-Inflammatory Activity of a Peptide-Based Hydrogel Using Rat Air Pouch Model, International conference on "Emerging Trends in Chemistry" during July 12-15, 2019 at Discipline of Chemistry, Indian Institute of Technology Indore (Poster Presentation).

TABLE OF CONTENTS

LIST OF FIGURES

LIST OF SCHEMES

LIST OF TABLES

ACRONYMS

The abbreviations used for amino acids, peptides and their derivatives, substituents, reagents, etc. are largely in accordance with the recommendations of the IUPAC-IUB commission on Biochemical Nomenclature, 1974, Pure and Applied Chemistry, 40, 315-331. All amino acids are L-configuration. Standard single and three letter coding is used to denote the amino acids throughout the thesis.

abbreviations used in this thesis are listed below:

Amoc:	9-Anthracenemethyloxycarbonyl
Fmoc:	9-Fluorenylmethyloxycarbonyl
Nmoc:	Naphthalene-2-methoxycarbonyl
Boc:	tert-butyloxycarbonyl
$NaHCO_3$:	Sodium Bicarbonate
$NaCO_3$:	Sodium Carbonate
HCl:	Hydrochloric Acid
NaOH:	Sodium Hydroxide
PBS:	Phosphate Buffer Saline
TFA:	Trifluoroacetic Acid
DMF:	Dimethyl Formamide
DMSO:	Dimethyl sulfoxide
DCM:	Dichloromethane
EtOAc:	Ethyl Acetate
MeOH:	Methanol
ACN:	Acetonitrile
TCA:	Trichloroacetic Acid
TBA:	Thiobarbituric Acid
TBARs:	Thiobarbituric Acid Reactive Substances
MDA:	Malondialdehyde
UV/Vis:	UV-Visible Spectroscopy
DCC:	Dicyclohexylcarbodiimide

DIPC:	Diisopropylcarbodiimide
HOBt:	1-Hydroxybenzotriazole
DCU:	Dicyclohexyl Urea
F/Phe:	L-Phenylalanine
Y/Tyr:	L-Tyrosine
L/Leu:	L-Leucine
TLC:	Thin Layer Chromatography
LMWHs:	Low-Molecular Weight Hydrogels
CAC:	Critical Aggregation Concentration
ACQ:	Aggregation-Caused Quenching
CD:	Circular Dichroism
β-CD:	β-Cyclodextrin
ESI-MS:	Electrospray Ionization Mass Spectrometry
HRMS:	High-Resolution Mass Spectrometry
FTIR:	Fourier Transform Infrared Spectroscopy
NMR:	Nuclear Magnetic Resonance
TCSPC:	Time-Correlated Single Photon Counting
PXRD:	Powder X-ray Diffraction
WAXD:	Wide Angle X-ray Diffraction
SEM:	Scanning Electron Microscope
TEM:	Transmission Electron Microscope
HRTEM:	High-Resolution Transmission Electron Microscopy
HPLC:	High-Performance Liquid Chromatography
CLSM:	Confocal Laser Scanning Microscopy
LVE:	Linear Viscoelastic
LVR:	Linear Viscoelastic Region
NO:	Nitric Oxide
cfu:	Colony-Forming Units
HEK293:	Human Embryonic Kidney

LPO:	Lipid Peroxidation
MTT:	3-(4,5-Dimethythiazol-2-yl)-2,5-Diphenyl Tetrazolium Bromide
DMEM:	Dulbecco's Modified Eagle's Medium
FBS:	Fetal Bovine Serum
PCV:	Packed Cell Volume
LPO:	Lipid Peroxidation
RBCs:	Red Blood Cells
WBCs:	White Blood Cell
OD:	Optical Density
NA:	Nutrient Agar
NB:	Nutrient Broth
IC:	Inhibitory Concentration
MIC:	Minimum Inhibitory Concentration
S. aureus:	*Staphylococcus aureus*
B. subtilis:	*Bacillus subtilis*
E. coli:	*Escherichia coli*
P. aeruginosa:	*Pseudomonas aeruginosa*
S. typhi:	*Salmonella typhi*
H&E:	Hematoxylin and Eosin
BSA:	Bovine Serum Albumin

NOMENCLATURE

θ	Angle
λ	Wavelength
Å	Angstrom
α	Alfa
β	Beta
γ	Gamma
s	Singlet
d	Doublet
t	Triplet
q	Quartet
m	Multiplet
br	Broad
dd	Doublet of Doublet
nm	Nanometer
ω	Angular Frequency
τ	Life Time
δ	Chemical Shift
MHz	Mega Hertz
N	Normal
M	Molar
mM	Millimolar
μM	Micromolar
nM	Nanomolar
mL	Milliliter
μL	Microliter
G'	Storage Modulus
G"	Loss Modulus

Chapter 1

General Introduction

1.1 Introduction of Self-Assembling Peptides

In the era of biomaterial science, self-assembling systems have emerged for the development of various well-defined and self-organized structures.[1-9]In supramolecular chemistry, the monomeric units are spontaneously assembled into the thermodynamically favoured highly regular nanostructures.[10-12] Many interacting self-assembling components connect and form organized complex architectures with the aim to design and implement the chemical functional systems.[13] The noncovalent interactions such as hydrogen bonding, π- π stacking and van der Waals forces are considered as the foundation in self-assembling systems.[14] Molecular self-assembly of natural biomolecules such as peptides, proteins, nucleic acids, lipids, polysaccharides and other cellular components are widely used to study their functions related with their self-assembling structures.[15-18] Recently, peptides are widely used for the development of stimuli responsive and self-adaptive biomaterials, which could be used for different biomedical applications (Figure 1.1).[19-21]

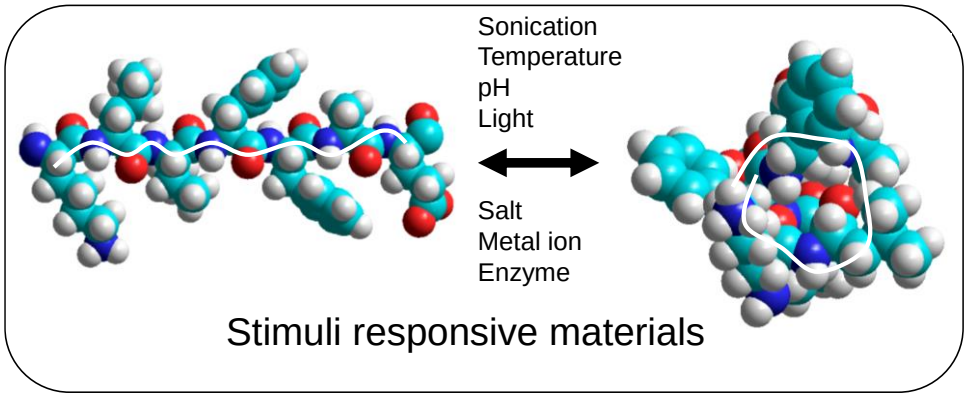

Figure 1.1 Self-assembly of stimuli responsive peptide-based materials.

The self-organization of molecules at cellular and subcellular levels plays an imperative role in the construction of energetically favoured micro to nanostructures.[22] The self-assembling biomaterials are the results of noncovalent interactions, which is reversible in nature, hence, the major advantages include easy processability, recyclability, self-healing, stimuli responsive and controlled injectability.[23,24] In this context, the complex micro to nanostructures, which exhibit a wide variety of functions, have been obtained through the supramolecular interactions among the constitutive components.[25,26] One of the major objectives in supramolecular chemistry is to design and synthesize low molecular weight based building blocks, which can form ordered supramolecular structures through reversible noncovalent interactions.[27,28] There is great interest in the development of self-assembling peptide-based functional materials owing to the several key properties including chemical versatility and easy to functionalization with controllable self-assembling behavior.[29-31] The various combinations of amino acids help to design and synthesize enormous number of self-assembling peptides

with different biological functions under suitable conditions.[32,33] Twenty naturally occurring amino acids are used as building blocks for the development of self-assembling peptide and protein-based functional biomaterials.[34] However, several non-natural amino acids are also available for the design of self-assembling peptides.[35] The naturally occurring amino acids are divided into various categories such as polar, nonpolar, aliphatic, aromatic, acidic and basic according to their side chain functional groups (Figure 1.2).

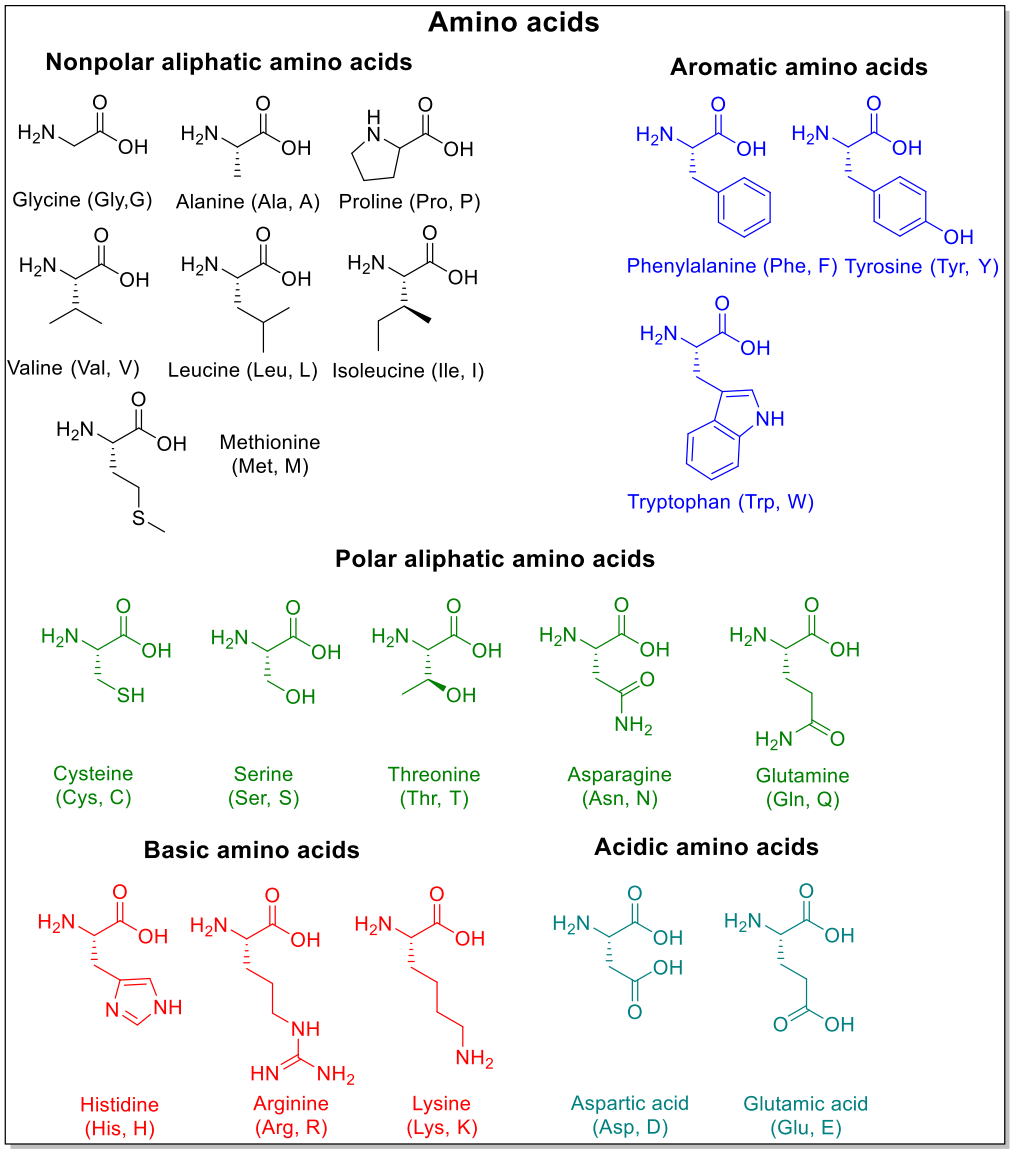

Figure 1.2 Structure and classification of twenty amino acids, which are the building blocks of peptides.

The ionized amino acids are hydrophilic and behave as acidic (E: glutamic acid, D: aspartic acid) and basic (H: histidine, R: arginine, K: lysine) in nature. The

nonionized amino acids at neutral pH are considered as hydrophobic amino acids, which include aromatic (F: phenylalanine, Y: tyrosine, W: tryptophan) and aliphatic (alanine: A, isoleucine: I, leucine: L, valine: V, methionine: M) side chains. All naturally occurring amino acids contain chiral center except glycine (G) and have similar kind of structure with different side chain functional groups. The various combinations of side chain functional groups in self-assembling peptides exhibit the properties and biological applications.[36-39] Peptides with hydrophilic or hydrophobic amino acid sequences, that self-assemble in different solvents, form functional materials. The choice of amino acid sequences in peptide backbone is the key parameter for the design and development of self-assembling peptides.[40] A significant number of peptides such as di, tri, tetra, penta and oligopeptides are synthesized which self-assembled into water to give various structural architectures and functional biomaterials.[41,42] Suitable hydrophobic/hydrophilic balance of an ideal self-assembling peptide is essential where molecular self-assembly dominates against the precipitation of the peptides.[43] The noncovalent interactions including hydrogen bonding, π-π stacking and hydrophobic interactions are the driving force for the self-assembly of peptides, which can be tuned by different stimuli including pH, temperature, sonication, light, salt, enzymes and metal ions.[44] The structural complementarity and different noncovalent interactions lead to the formation of various energetically favoured structures such as α-helix, β-sheets and turns.

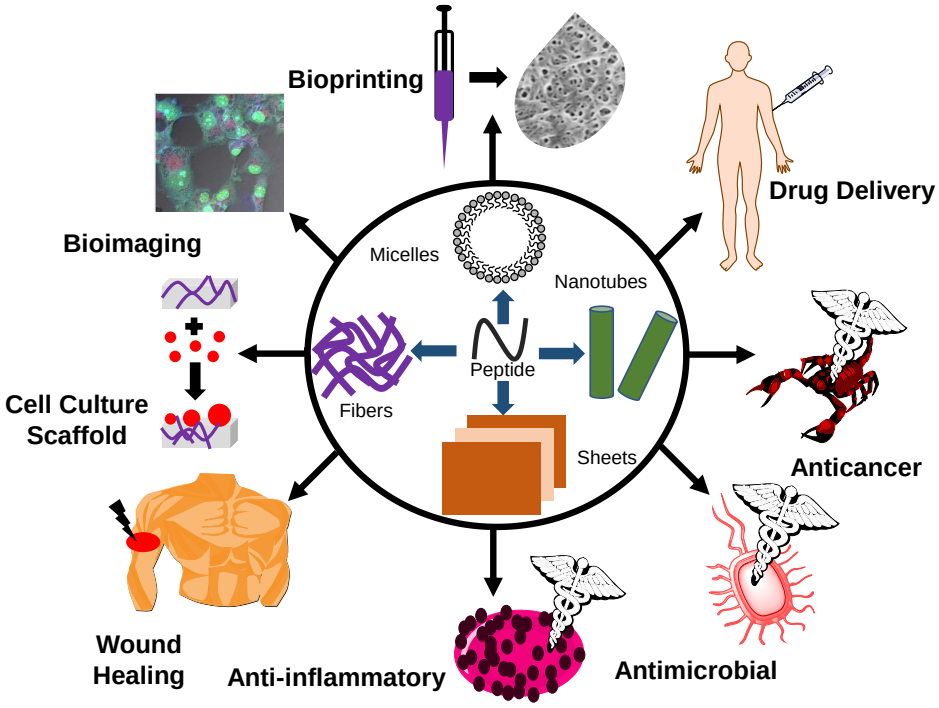

Figure 1.3 The self-assembly of peptides owing to involvement of noncovalent interactions lead to formation of various nanostructures which are used for different biomedical applications.

The self-assembled peptides exhibit remarkable physicochemical properties with broad-spectrum applications in various interdisciplinary areas of research including antimicrobial, anti-inflammatory, anticancer, wound healing, drug delivery, bioimaging and bioprinting (Figure 1.3).[45-50] The aromatic amino acids such as F, Y and W have been used extensively to design functional self-assembled peptides.[51] However, the additional hydrophobicity and aromatic interactions can be enhanced by incorporation of N-terminal aromatic protection which shows synergetic effect in peptide self-assembly.[52,53] The low-molecular-weight peptides protected with N-terminal aromatic groups have been used to tune the properties of self-assembling peptides.[54]

1.2 Design of Self-Assembling Peptides

Molecular self-assembly is one of the most studied approaches for the construction of ordered structures for specific outcome with minimal human and machine intervention.[55] The self-assembled peptides can compete with the biologically active proteins and offer useful biological functions and structural diversity as soft biomaterials.[56,57] Among various molecules, peptide amphiphiles, which are ornamented with hydrophilic and hydrophobic groups, are suitable building blocks for molecular self-assembly.[58,59] The self-assembling peptide-based aromatic amphiphiles contain three major components in their chemical structure: N-terminal aromatic protecting group, methoxycarbonyl group, the peptide building blocks (Figure 1.4).

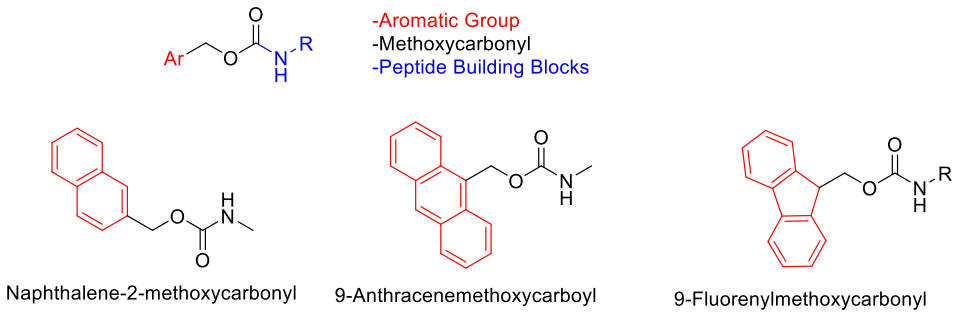

Figure 1.4 General structure of self-assembling peptide and various examples of N-terminal protecting groups used for the fabrication of self-assembling peptides.

The peptide amphiphiles aggregate to form various supramolecular architectures in aqueous conditions in presence of different stimuli.[60] In general, the self-assembling short peptides are decorated with synthetic hydrophobic group in order to facilitate the ordered pattern.[61] Additionally, the self-assembling peptides can also be designed by using a hydrophobic skeleton covalently interlinked with

hydrophilic groups on both ends.[62,63] The peptides with two polar head groups attached with hydrophobic core are called bola-type which have proven to be better nanostructure forming peptides.[64-68] Peptide-based bolaamphiphiles with appropriate functional groups exhibit supramolecular nanoarchitectures with broad-spectrum applicability.[69-72] The therapeutic self-assembling peptides with inherent biological activity are used for the treatment of various diseases.[73] In general, the self-assembling nature of peptides into the thermodynamically stable structures is common phenomenon of several bioactive peptides. This hypothesis is well supported by previously reported articles exhibiting that peptides never exist as a single molecule in solutions because of the involvement of noncovalent interactions.[37] It is important to understand the relationship between thermodynamic dissolution parameters including enthalpy and entropy of the peptides and their self-assembling ability for the design of a gelator molecule.[74]

1.3 Self-Assembling Carbamate Protected Peptides

The objective of N-terminal protection is to facilitate the unidirectional peptide synthesis to achieve the desired product in excellent yields with the formation of minimum side products.[75] Thus, a promising protecting group is required to control the coupling reaction and regioselective amide bond formation. An ideal protecting group must be stable at various reaction conditions (temperature, pH), and can be easily attached/removed from amino acids and peptides.[75] The N-terminal protection of peptide and amino acids by aromatic groups refers to a variety of interactions such as hydrogen bonding, hydrophobic, π-π stacking and other ionic interactions. Self-assembling peptides featuring with Fmoc (9-fluorenylmethoxycarbonyl) group have been extensively studied owing to their inherent biocompatibility and hydrophobicity.[76-78] The Fmoc group assists the self-assembly process and enhance the intermolecular aromatic-aromatic interactions.[79] Similarly, the N-terminal of peptides and amino acids are protected by other aromatic groups such as phenyl, naphthalene, anthracene and pyrene to enhance the self-assembling tendency.[80-82] The Nmoc (naphthalene-2-methoxycabonyl), Amoc (9-anthracenemethoxycarbonyl) and Fmoc group attached with peptides facilitate the self-assembling behaviour of peptides.[83] The hydrogelation is affected by the choice of peptide backbones and aromatic groups, which allow the hydrogen bonding and π-π stacking interactions among molecules. Peptide-based hydrogelators have been designed by various other protecting groups that can respond to external stimuli such as temperature, light, pH, enzymes and mechanical stress.[84] Anthracene protected photo-responsive peptide gelators are used for various applications including drug delivery, biosensor, microfluidics and supramolecular electronics.[84,85] Anthracene protected peptides exhibit photodimerization reaction when irradiated under UV light at a particular wavelength. The [4+4] cycloaddition reaction is well known for anthracene-based molecules when irradiated with UV light (>300 nm).[84] The inherent hydrophobicity and planarity of anthracene molecules offer optimum

hydrophobicity for the formation of nanostructures through noncovalent interactions.[86]

1.3.1 Self-Assembling Naphthalene-2-methoxycabonyl (Nmoc) Protected Peptides

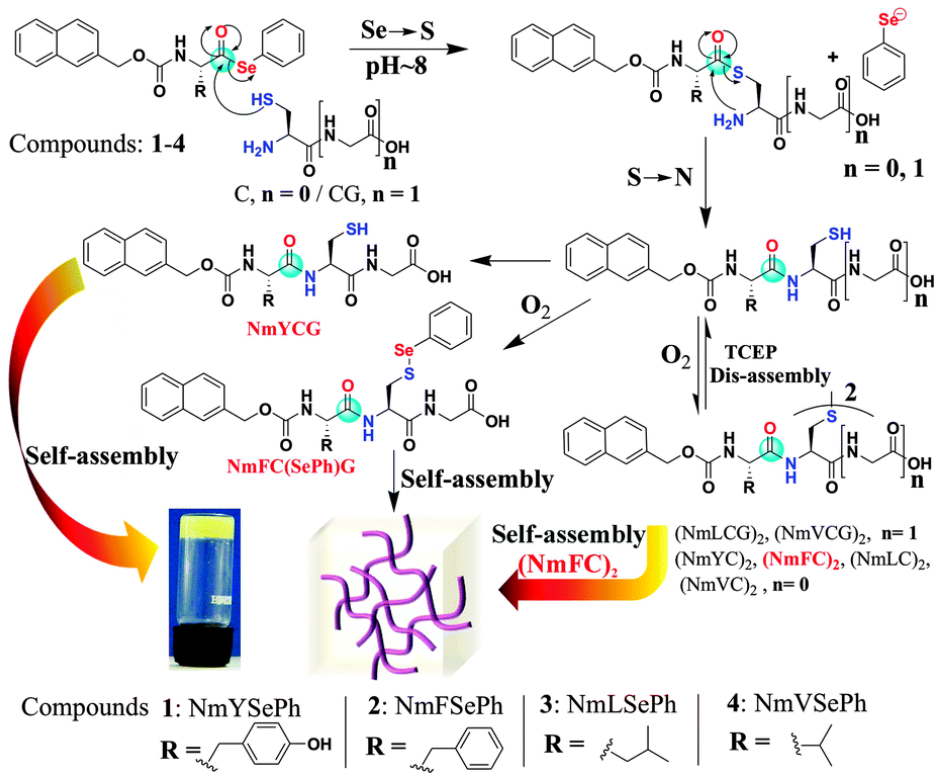

Figure 1.5 The schematic representation of selenoester mediated native chemical ligation (NCL) reaction for the generation of Nmoc-capped self-assembled peptides. Reproduced from ref. 93.

During the development of self-assembling peptide based materials, various N-terminal aromatic-protecting groups have been used which can participate in aromatic-aromatic interactions with suitable hydrophobicity required for the hydrogelation.[87] Therefore, the amino acids and peptides are protected with naphthalene group which is more biocompatible aromatic motif for the fabrication of soft biomaterials.[88,89] Das et al. designed N-terminal aromatic protecting group naphthalene-2-methoxycarbonyl (Nmoc) for the synthesis of peptide-based self-assembling materials.[90,91] Nmoc-protected tripeptides were reported for the evolution of enzyme-catalysed thermodynamically stable Nmoc-protected peptides, which were driven by π-π stacking interactions.[90] An enzyme lipase was used for the inclusion of gastrodigenin with a number of Nmoc-protected dipeptides, which evolved blue light emitting peptide nanofibers.[92] The same group reported oxo-ester and seleno-ester directed native chemical ligation (NCL)

of Nmoc protected peptides, which led to the generation of self-assembled materials at room temperature (Figure 1.5).[93,94] Further, native chemical ligation followed by desulfurization techniques were used to control peptide self-assembly (Figure 1.6). The thiol groups of cysteine and penicillamine of the ligated peptides converted into Ala and Val moieties using desulfurization reactions.[94]

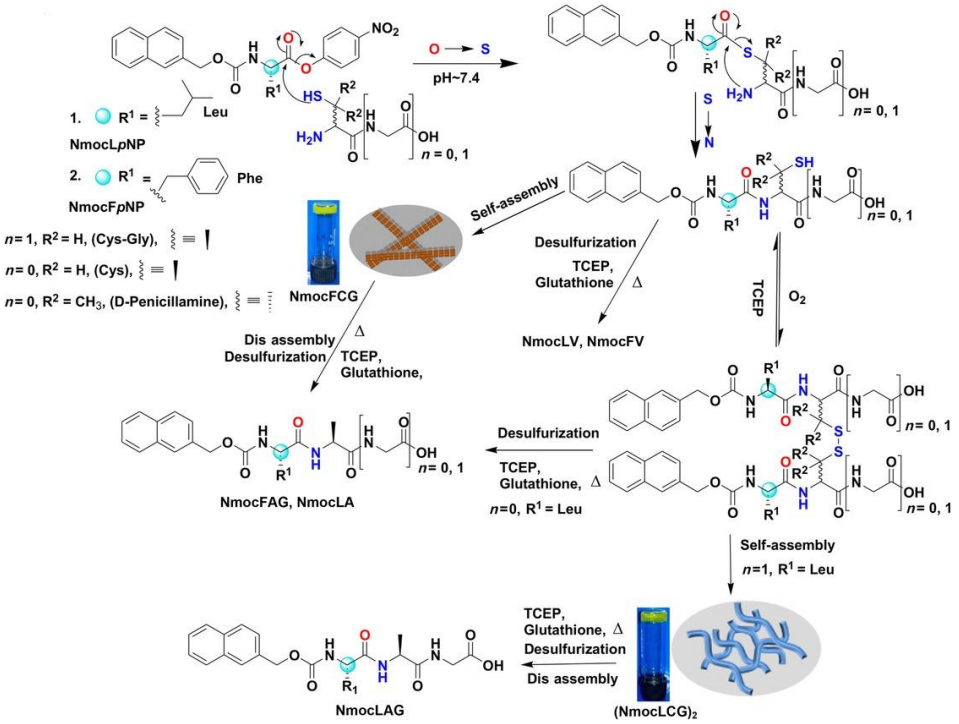

Figure 1.6 Native chemical ligation followed by desulfurization control peptide self-assembly and evolution of functionalized peptides. TCEP=Tris(2-carboxyethyl)phosphine. Reproduced from ref. 94.

1.3.2 Self-Assembling 9-Anthracenemethoxycarbonyl (Amoc) Protected Peptides

The N-terminal of peptides and amino acids can be functionalized with more robust, planner and aromatic anthracene ring to obtain self-supporting, thixotropic and injectable soft biomaterials for various biological applications.[95,96] 9-Anthracenemethoxycarbonyl (Amoc) protected peptides enhance the hydrophobicity of the peptides and facilitate the better hydrogelation because of low concentration aggregation of the peptides with well-defined structures.[96,97] Additionally, Amoc aromatic peptides showed synergetic effect in π-π stacking interactions which self-assembled into highly entangled fibrillar structures.[98] A robust N-terminal protecting group 9-anthracenemethoxycarbonyl (Amoc) was used for the preparation of various Amoc-capped dipeptide-based hydrogelators (Figure 1.7). [96] The same group reported the hydrogelation of Amoc-capped dipeptides at room temperature, which showed excellent rheological properties for biomedical applications. The hydrogels formed various 3D shapes and showed

syringe injectability and self-recovery. The aggregation tendency of hydrogelators was used for antibacterial applications. In another report, the same research group exhibited anti-inflammatory activity of an Amoc-capped peptide which self-assembled in water and formed thixotropic, injectable, antibacterial and noncytotoxic hydrogel.[97]

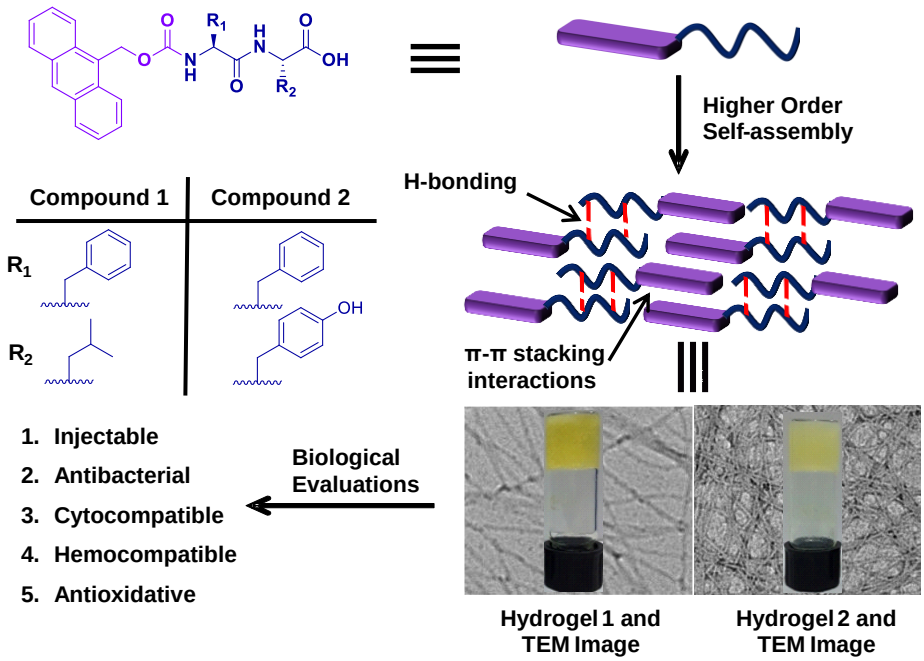

Figure 1.7 Schematic representation of self-assembly leading to the formation of nanofibrillar hydrogels and biological evaluations with the self-supporting hydrogels. Reprinted with permission from ref. 96.

Recently, a coassembled thixotropic hydrogel was reported which was prepared by incorporation of *β*-cyclodextrin (CD) with self-assembling hydrogelator Amoc-FF-OH (Figure 1.8). [98]

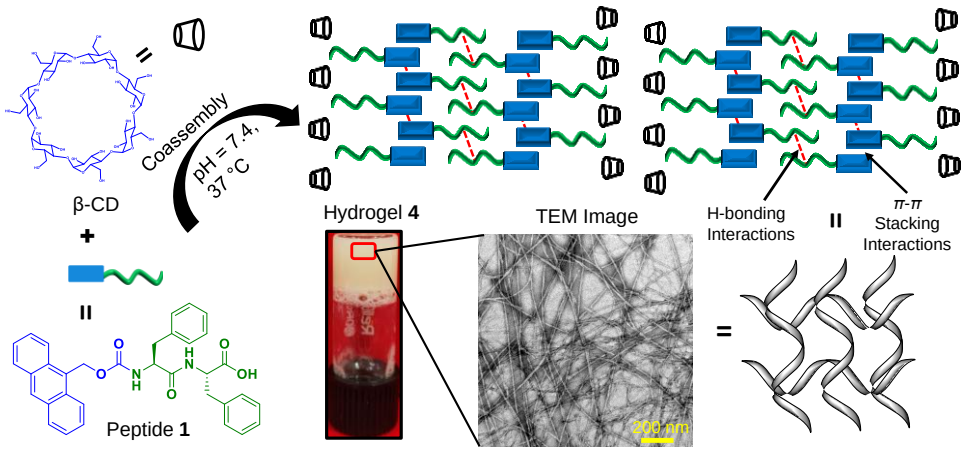

Figure 1.8 Graphical Representation of Coassembly between Peptide 1 and *β*-CD Leading to the Formation of Ordered Structures which Results into Hydrogel 4 (Peptide 1:*β*-CD = 1:1). Reproduced from ref. 98.

The toughness of the hydrogels was tuned by the physical integration of *β*-CD with dipeptide (Amoc-FF-OH) owing to optimum noncovalent interactions between *β*-CD and peptides, which exhibited better thixotropy and syringe injectability.

1.3.3 Self-Assembling 9-Fluorenylmethyloxycarbonyl (Fmoc) Protected Peptides

The Fmoc-protected peptides have been used for the fabrication of supramolecular soft biomaterials.[99] The amphiphilicity of peptides is acquired by N-terminal protection using aromatic functionalities.[100,101] The Fmoc-group is one of the versatile N-terminal protecting groups, which is commonly used for the solid phase peptide synthesis. Nowadays, the Fmoc protected peptides are used for the preparation of self-supporting hydrogels.[102] The Fmoc protected aliphatic amino acids-based dipeptide hydrogels (Fmoc-LD, Fmoc-AD, Fmoc-ID) were reported by Vegners and coworkers. The thermoreversible peptide hydrogels were soluble at 100 °C, which formed viscoelastic hydrogel at lower temperature (60 °C). Further, the drug was loaded into the hydrogel, which was injected into the rabbits to evaluate the extent of antigenicity caused by drug loaded hydrogel.[103] Later Xu et al. reported proteolytically stable Fmoc-AA-OH (A = D-alanine)-based short oligopeptidic hydrogelator.[104] This dipeptide formed hydrogel and showed ligand-receptor interactions, which was evident from gel-sol transition upon peptide-vancomycin interactions. The vancomycin disrupted the hydrophobic and intermolecular hydrogen bonding interactions between peptide hydrogelators and induced a sol-gel transition. In another report, a simple and robust approach was described for the preparation of peptide-based biomimetic hydrogel that specifically responded to the potassium (K^+) ion concentration.[105] A controllable pH change method was used for the preparation of homogenous and reproducible peptide hydrogels using glucono-δ-lactone (GdL) as an acidifying agent.[106] In another approach, the addition of dilute acid caused rapid pH change and produced inhomogeneous and opaque region suspended in a clearer region. The authors explained the kinetics of in situ gluconic acid generation, which is slower because of sustained GdL hydrolysis. Hence, the pH of the system reduced slowly that resulted into the formation of homogeneous hydrogel. Rheological properties of the hydrogels were significantly affected when the hydrogels were prepared by NaOH / HCl method. An aromatic dipeptide was modified, which self-assembled to form rigid and tough hydrogel.[107] The rigidity and 3D shape of the hydrogel was the outcome of the aromatic interactions between the building blocks. Interestingly, the hydrogel contains less than 1% of Fmoc-FF dipeptide that converted into amyloid-like fibrillar structures in the self-assembled state. The dipeptide Fmoc-FF is the smallest building block, which mimics the amyloid-like

fibrillar morphology. The rheological data revealed the concentrations-dependent mechanical strength and 10 mg/mL of peptide concentrations formed rigid and robust hydrogel. A series of Fmoc protected self-assembling dipeptides by combinations of four different amino acids (G, A, L and F) have been reported.[108] Self-supporting hydrogels of dipeptides were prepared by pH switch method. The hydrogelation pH of the designed peptides varied according to their pKa values and was found to acidic pH (pH < 4) for Fmoc-GG, Fmoc-AG, Fmoc-AA, Fmoc-LG, Fmoc-FG and neutral pH (pH < 8) for Fmoc-FF peptides. The importance of chemical functionality such as NH_2, COOH or OH in Fmoc hydrogels has been investigated, which can influence the cellular viability.[109] The circular dichroism (CD) spectra of hydrogels revealed peak at 304-308 nm, which is associated with π-π* transition in the fluorenyl groups. The self-assembly of Fmoc-based dipeptides was explained by spectroscopic analysis suggesting the antiparallel β-sheet formation with anti-parallel π-π stacking interactions between fluorenyl groups, which are responsible for the formation of an ordered structure.[110,111] The secondary structures of the peptides were corroborated by FTIR spectroscopy that exhibited peaks at 1635-1646 and 1685-1691 cm^{-1} indicating the presence of β-sheet structure with an antiparallel arrangement.[110,111] Banerjee et al. reported Fmoc protected hydrogelator (Fmoc-VD-OH) that self-assembled and formed stable hydrogel with minimum gelation concentration of 0.2% w/v.

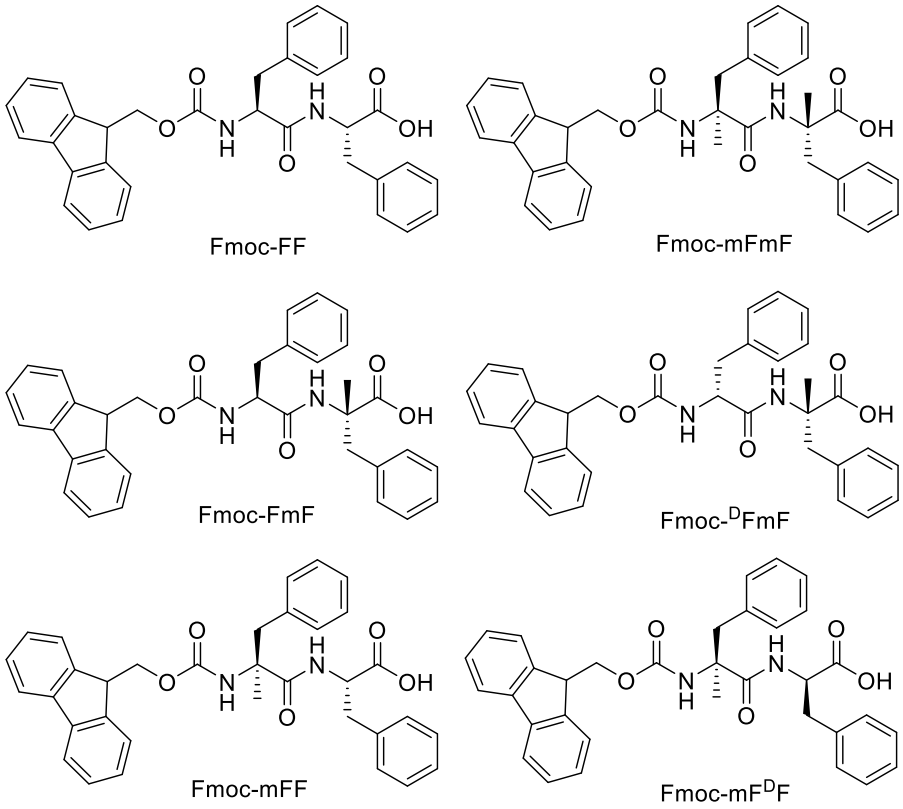

Figure 1.9 Chemical structure of different Fmoc protected dipeptides.

They have utilized the hydrogels for the preparation and stabilization of fluorescent silver nanocluster within the 3D networks.[112] The same group also reported proteolytic stable hydrogel that was composed of β-amino acid residue in self-assembling peptides.[113] The peptides (Fmoc-βA-V and Fmoc-βA-F) with β-amino acid residue formed viscoelastic hydrogels and exhibited better tolerance to external force. The minimum gelation concentration of the peptide was 0.1% (w/v) in PBS (50 mM) at physiological conditions (pH 7.46, 37 °C). Recently, Fmoc-K(Fmoc)-D peptide was investigated and designated as "hypergelator" that self-assembled at lowest gelation concentration (0.002% w/v, 28.3×10^{-6} M).[114] The peptide Fmoc-K(Fmoc)-D was designed by the incorporation of additional Fmoc group protection to K side chain that provides additional rigidity from the carbamate group, H-bonding from the amide group and aromatic interactions from fluorenyl ring. Recently, Ikeda et al. reported a series of Fmoc-capped α-methyl-L-phenylalanine-based self-assembling dipeptides (Figure 1.9).[115] They showed that the position and number of methyl group attached to the dipeptides had a significant impact on the self-assembled nanostructures and hydrogelation ability. The amide modifications of a dipeptide Fmoc-FF with a new ureidopeptide Fmoc-FuF (Fmoc-F-CONHCO-F) endowed different properties and applications compared to parent peptide.[116] The designed ureidopeptide gelator Fmoc-FuF increased the hydrogen bonding interactions, which exhibited improved mechanical strength with shear thinning and self-healing properties as compared to Fmoc-FF hydrogel. The ureidopeptide hydrogelator Fmoc-FuF showed antifouling properties and sustained release of encapsulated urea molecules, which ensures the biomedical application of Fmoc-FuF hydrogel.

1.4 Different Aromatic N-terminal Protected Self-Assembling Peptides

The self-assembling peptides can be fabricated using naphthalene, pyrene, naphthaleneimide and naphthalenediimide groups for the N-terminal protection (Figure 1.10).[117] Naphthalene (Nap)-protected self-assembling peptides have been used for the preparation of supramolecular nanofibers.[118] The Nap-capped peptides showed good biocompatibility, biostability and non-immunogenicity.[119] Pyrene-capped peptides offer excellent luminescent behavior mainly due to the transitions of different excimers of self-assembled pyrene-capped peptide.[120] Naphthalimide (NI) moieties are very versatile N-terminal aromatic protecting group and known as electron acceptor core ring.[121] The 1,8-naphthalimide protected peptides self-assemble into the water and various organic solvents due to aromatic interactions and form organized structure with excellent photophysical and mechanical properties.[122]

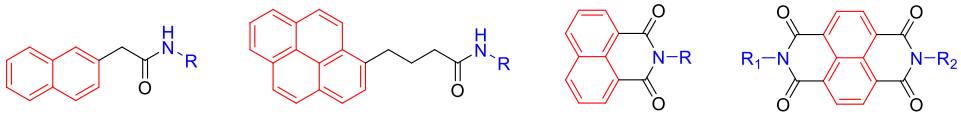

Figure 1.10 Various N-terminal protecting groups in self-assembling peptides.

Supramolecular hydrogelation of NI-GFF and NI-FFG was demonstrated at neutral pH and highlighted the importance of peptide sequence for the formation of ordered nanostructures.[123] Similarly, naphthalenediimides (NDIs) possess planner structure, high electron density, thermal stability and functionalization tendency that has attracted researchers to design and develop N-terminal protected self-assembling peptide amphiphiles.[124] DNA intercalation, antitumor and antimicrobial activity of NDIs offer wide-range of applications in the area of biomaterials science.

1.4.1 Self-Assembling Naphthalene Protected Peptides

During the development of various N-terminal protecting group researchers found various aromatic compounds which can participate in aromatic interactions with suitable hydrophobicity required for the hydrogelation.[125] Therefore, the amino acids and peptides are protected with naphthalene (Nap) group which is more biocompatible aromatic motif for the fabrication of soft biomaterials.[126,127] Additionally, the Nap moiety is used in many commercial drug molecules such as propranolol, naproxen, butenafine and naftopidil.[51] Zhao and coworkers reported Nap conjugated self-assembling peptide Nap-FF-NO for myocardial infarction.[128] The authors showed that the Nap-FF-NO peptide release nitric oxide (NO) molecules in response to β-galactosidase which improve the cardiac function by promoting the angiogenesis. The self-assembly behavior of various aromatic protecting groups including Fmoc, naphthalene (Nap) and benzyloxy-carbonyl (Cbz) attached with the N-terminal of peptides was studied.[129] The Nap protected various dipeptides such as Nap-FF, Nap-FY, Nap-FL, Nap-FS were synthesized (Figure 1.11).[129]

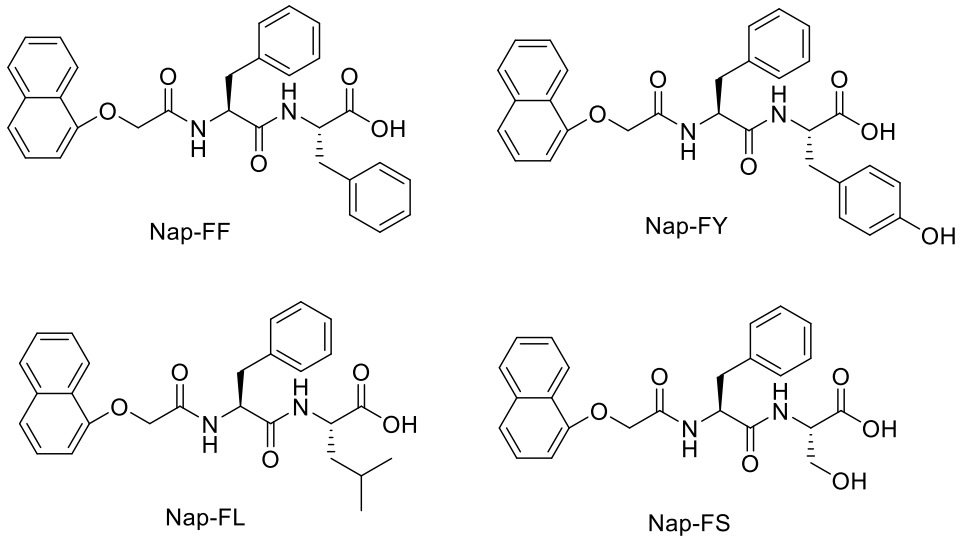

Figure 1.11 Chemical structure of naphthalene (Nap) protected self-assembling peptides.

The author investigated the role of N-terminal aromatic protection and C-terminal hydrophobic amino acids in the self-assembly of different peptides. The authors demonstrated the inverse relation between hydrophobicity (clog P) and minimum gelation concentrations (MGC) of peptides. The MGC value for Nap-FY and Nap-FS increased compare to more nonpolar residue bearing peptides Nap-FF and Nap-FL. Naphthalene protected tetrapeptide (Nap-GFFpY-OMe) was developed as super gelator that self-assemble after enzymatic reaction and form hydrogel at lowest concentrations (0.01% w/v) of peptide.[130] Other synthesized peptides formed hydrogel with slightly higher MGC values 0.08 and 0.4% (w/v) for Nap-GFFpY-OH and Nap-FFpY-OMe, respectively. Additionally, the N-terminal protecting group and G amino acid played a crucial role for the formation of super hydrogelator. Different N-terminal aromatic protecting group with similar peptide sequence (Fmoc-GFFpY-OMe) showed higher MGC value (0.1% w/v) compared to the Nap-GFFpY-OMe peptide. A naphthalene containing self-assembling peptide (Nap-GFFY) based hydrogel was synthesized for ophthalmic drug delivery.[131] The Nap-GFFY peptide (0.5% w/v) formed self-assembled hydrogel by heating and cooling method in PBS (pH = 7.4). The Nap-GFFY and diclofenac sodium self-assemble together into the hydrogel and showed excellent in vivo ocular biocompatibility without showing any corneal irritation, opacity and redness which suggest the Nap-capped peptides are suitable biomaterial for the biomedical applications.

1.4.2 Self-Assembling Pyrene Protected Peptides

Pyrene is another N-terminal aromatic protecting group, which reinforce the aromatic stacking interactions of the peptides.[132] The aromatic pyrene group protected peptides and amino acids show monomer and excimer emission with different wavelength under different conditions.[133] The inherent photophysical stability and photoluminescence properties of pyrene group attracted the researchers for the development of fluorophoric self-assembled aggregates with defined functional structures. Furthermore, the pyrene group has greater fluorescence quantum yield compare to anthracene group, thereby the pyrene protected peptides form easily detectable excimers. The molecular self-assembly of pyrene containing molecules exhibits different photophysical properties from their constitutive building blocks. The emission property of pyrene containing self-assembled materials is changed, which can be detected optically. In particular, pyrene protected peptides show excited state electron transfer from fluorophore to the different biological analytes and molecules.[134] Pyrene containing fluorescent hydrogels with ordered structural arrangements are used for the fabrication of biosensor systems and devices. The ordered structural arrangement of pyrene containing peptides endows a suitable microenvironments for the inclusion of bioanalytes and molecules via several noncovalent interactions.[134] Bhattacharya

et al. reported pyrene-appended peptide which self-assembles to form thixotropic hydrogel in presence of octafluoronaphthalene via complementary quadrupole-quadrupole interaction owing to the arene-perfluoroarene complexation.[135] Lee et al. developed N-terminal pyrene protected peptide amphiphiles which were used for intracellular Ag^+ ion detection in HeLa cells.[136] Xu et al. synthesized a pair of pyrene conjugated pentapeptides Py-A (Py-RMLRF-OH) and Py-B (Py-IQEVN-OH) (Figure 1.12).[81] The mixture of pyrene conjugate peptides Py-A and Py-B results into the self-supporting hydrogel. However, the individual peptide remained in solution prior to the mixing at 5 mM that showed synergetic effect of peptides in hydrogelation process. Additionally, the author synthesized C-terminal protected pyrene-based similar pentapeptides A-Py and B-Py which demonstrated α-helix to β-sheet transformation at gel-state owing to aromatic-aromatic interactions.

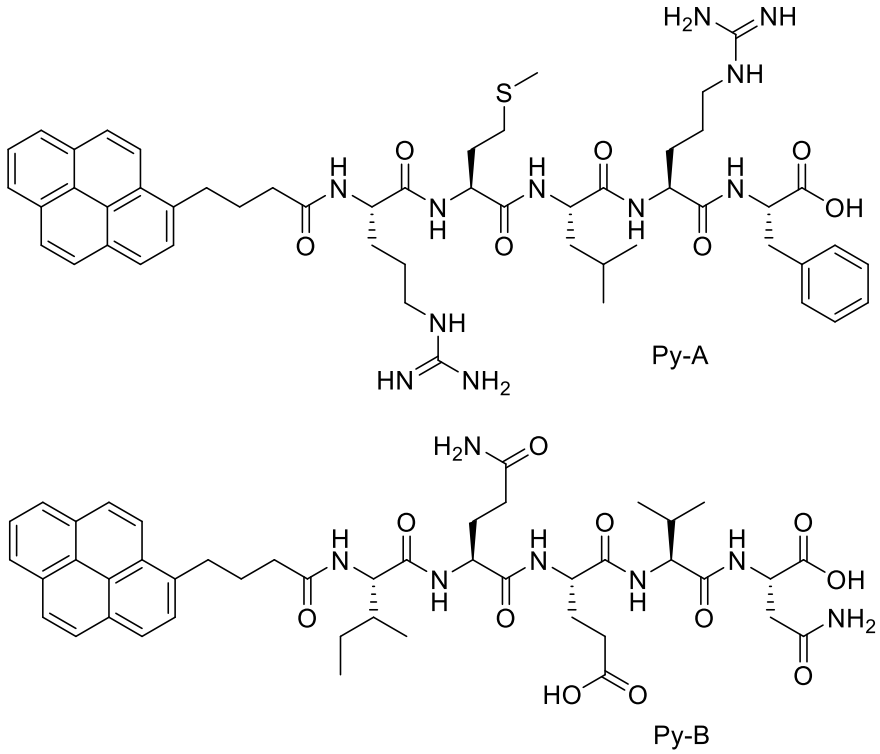

Figure 1.12 Chemical structure of N-terminal protected pentapeptide Py-A (Py-RMLRF-OH) and Py-B (Py-IQEVN-OH) hydrogelators.

1.4.3 Self-Assembling Peptides Protected with Naphthalene Imides and Naphthalene Diimides

Supramolecular soft biomaterials were designed by using naphthalene imide (NI) and naphthalene diimide (NDI) groups as an N-terminal aromatic protecting group.[123,137] Among the various protecting groups, the NI and NDI have paid great attention because of cell penetrating ability, DNA intercalating activity, redox

active and electron-deficient aromatic ring that can be easily functionalized with peptides for different applications.[138-140] Naphthaleneimide protected phenylalanine (NI-F) based supramolecular hydrogelator self-assembled in water at pH 7.4 and formed self-supporting hydrogel.[141] The aggregation-induced emission of NI-F suggested the intermolecular π- π stacking and hydrogen bonding interactions. The fluorescence intensity increased upon the increase of water fraction in the water/DMSO mixture because of strong aggregation between gelators. The fluorescent fibers of NI-F were employed for live/dead cell imaging of human mesenchymal stem cells (hMSCs). NDI-appended peptide-based self-supporting hydrogel was used for the intracellular imaging (Figure 1.13).[142] The peptide showed pH dependent aggregation. Upon increasing the pH of the medium, the NDI-appended peptide determined the pH of alkaline mitochondrial matrix by fluorescence colocalization techniques. Other NDI-conjugated hydrogels have been prepared using different chain length and influence of amino acids on self-assembling propensity was investigated for various applications.[143-145]

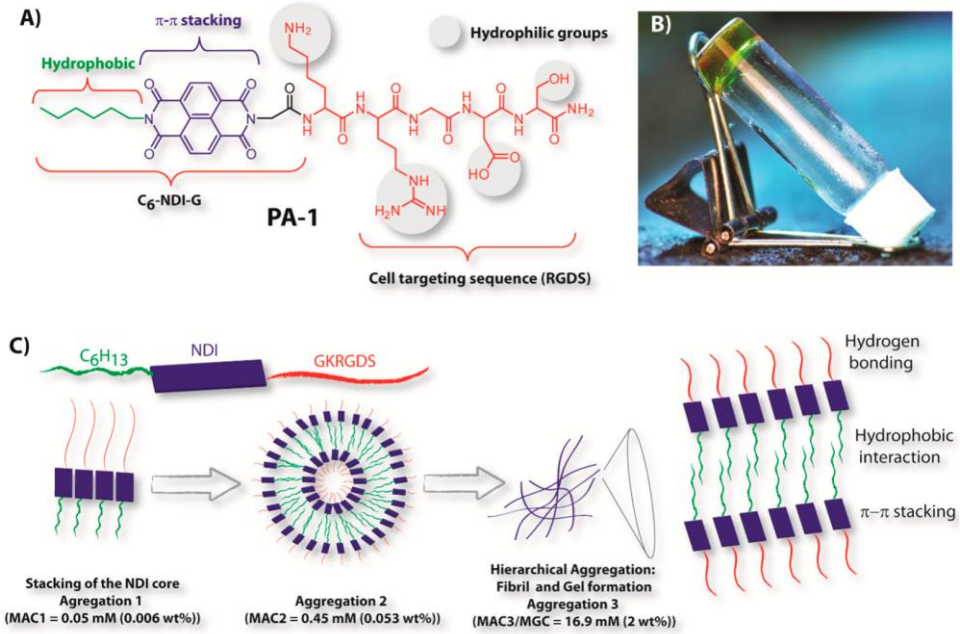

Figure 1.13 (A) Chemical Structure of PA-1 Showing Different Interactions and Functional Sites in the Molecule, (B) Photograph of a 2 wt % (16.9 mM) Hydrogel of PA-1 in Water under UV light, and (C) Pictorial Presentation of the Stepwise Hierarchical Aggregation of PA-1 to Form a Hydrogel. Reprinted with permission from ref. 142.

1.5 Self-Assembling Peptide Amphiphiles

The peptide-based hydrogelators are designed by incorporation of long chain alkyl groups at the N-terminal end of peptides that enforce the molecules for aggregation in water via hydrophobic interactions.[146-148] However, the hydrophilicity of the

peptide amphiphiles is maintained by combination of suitable amino acids which participate in hydrogen bonding and π-π stacking interactions.[149,150] Long alkyl chain functionalized peptides showed excellent aggregation properties and formed functional soft biomaterials with integrated biomedical applications such as antibacterial and drug delivery vehicles.[151,152] The nanostructural morphology and aggregation concentrations of the peptides can be tuned by simple change on alkyl chain length.[151] Although the different amino acid sequences in a peptide demonstrate a variety of self-assembling features.[153] Very recently, Hamley et al. studied the self-assembly and biological activity of amphiphilic lipopeptide PAEPKI-C_{16} using several microscopic, spectroscopic and small angle X-ray scattering techniques.[154] The cytotoxicity of the peptides against human dermal fibroblast (HDFa) and MCF-7 cells were significantly affected by the sequences of peptide amphiphiles. The peptide with free proline residue showed greater cytotoxicity probably due to different self-assembly modes. The same group reported carnosine-derived lapidated peptide (C_{16}KTTβAH) which self-assembled into water and formed β-sheet type nanotape structure.[155] The hydrogel (1% w/v C_{16}KTTβAH in PBS) showed slow uptake and sustained release of fluorescent Congo red dye. The authors investigated the anticancer activity of the hydrogel against the MCF-7 cell line. Banerjee et al. employed histidine amino acid for the preparation of thermal and mechanical stable charged hydrogel. The imidazole ring of histidine participates in the formation of extended supramolecular structures via noncovalent interactions between the oppositely charged self-assembling entities.[156]

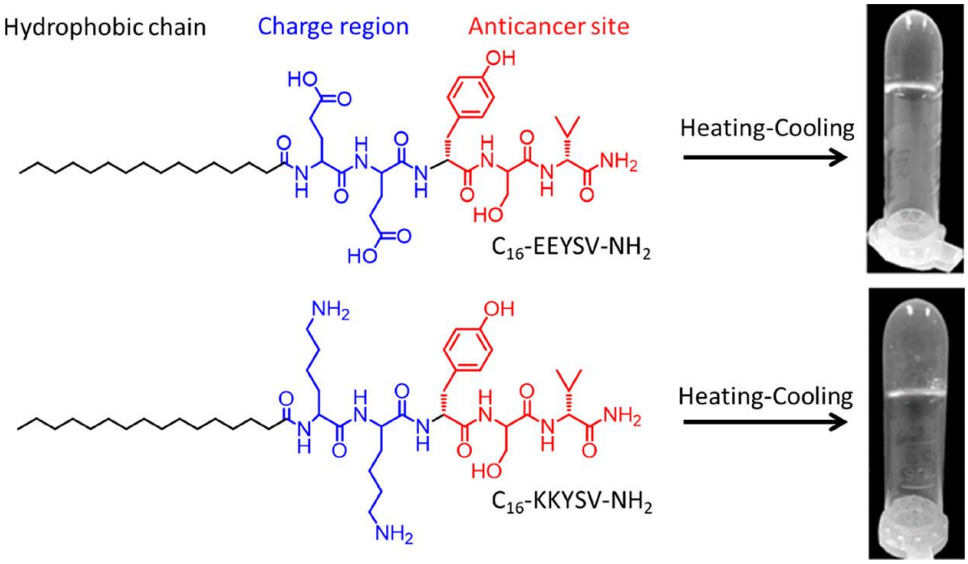

Figure 1.14 Chemical structures of lipidated peptides and photos of C_{16}-EEYSV-NH_2 and C_{16}–KKYSV-NH_2 hydrogels formed by the heating-cooling process. Reprinted with permission from ref. 160.

Stupp et al. designed and developed several peptide amphiphile-based soft biomaterials for various biological applications including tissue and organ regenerations.[157-159] The hydrogel with suitable mechanical strength is important for the growth of three-dimensional neuronal cells and neuronal regeneration. The nanofibers have direct influence on cell adhesion, growth and proliferation, thus the peptide-amphiphile-based hydrogels showed the burn wound healing.[157] An anticancer peptide tyoservaltide (YSV) was lipidated into C_{16}-EEYSV-NH_2 (anionic) and C_{16}-KKYSV-NH_2 (cationic) which self-assembled in PBS (pH 7.4) at 1 mM concentrations and formed translucent hydrogels (Figure 1.14).[160] Interestingly, the unlipidated and charged peptides Ac-YSV-NH_2, Ac-EEYSV-NH_2 and Ac-KKYSV-NH_2 didn't self-assemble to form hydrogel even at higher concentrations (10 mM) suggesting the significant role of alkyl chains in the hydrophobic interactions that is essential for the peptide self-assembly. Banerjee at al. reported a series of long alkyl chain containing peptide-based hydrogelators [H_2N-$(CH_2)_n$-CONH-F-CONHC_{12} (n = 1-5, C_{12} = dodecylamine)] with a free amine group at the N-terminus end (Figure 1.15).[161] The self-supporting hydrogels of all synthesized peptide amphiphiles were prepared at pH 6.6 and 25 °C. The rheological data showed the stiffness of the hydrogels, which increased with increase in alkyl chain length probably due to the increase in hydrophobic interactions between the peptide amphiphiles. The FTIR and PXRD data showed hydrogen-bonded β-sheet like structure with the π-π stacking arrangement between peptide amphiphile in the self-assembled state.

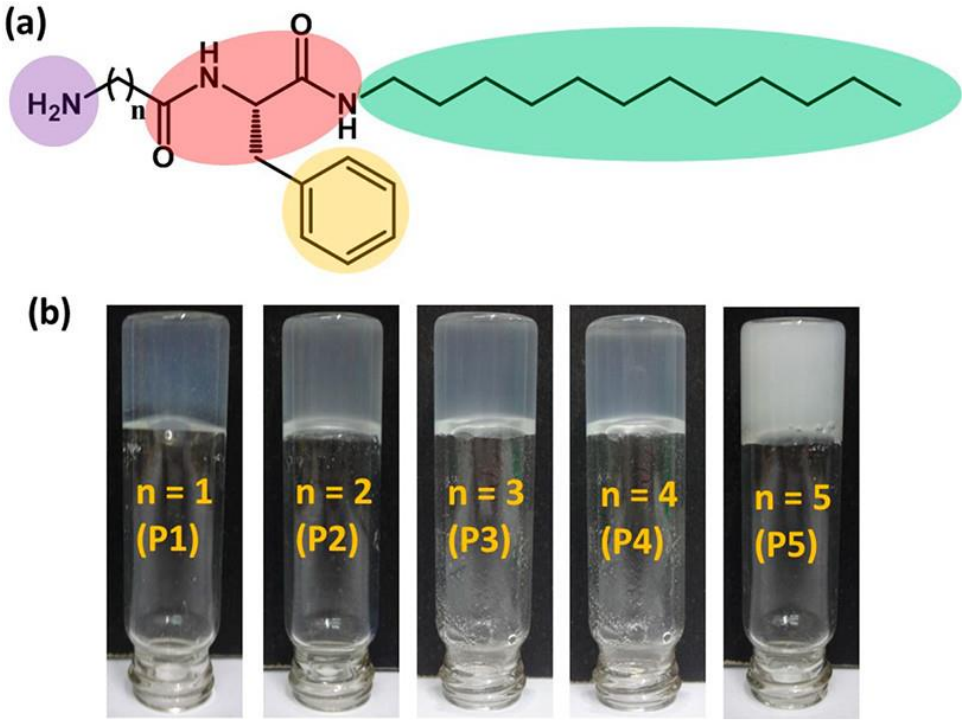

Figure 1.15 (a) General molecular structure of the gelator peptides. (b) Pictures of vials containing hydrogels of P1−P5 at 3.65 mM concentration. Reprinted with permission from ref. 161.

1.6 Self-Assembling Peptide Bolaamphiphiles

The majority of self-assembling peptides are designed by N-terminal aromatic protection or covalently linked with long aliphatic chains to the constitutive peptides.[162] However, an interesting class of self-assembling peptides are designed by incorporation of relative hydrophilic groups at both ends of long alkyl chains or hydrophobic core groups, which are called as peptide bolaamphiphils.[163,164] Generally, the peptide bolaamphiphiles contain double sided relative hydrophilic residues compared to the central hydrophobic groups which ensure better water solubility and multidirectional hydrogen bonding interactions of the self-assembling peptides.[165,166] However, the peptide bolaamphiphiles can be symmetrical and asymmetrical, which depend upon the application of the molecules.[167-169] A pseudopeptide bolaamphiphile HO-D-Oxd-L-Phe-CO$(CH_2)_7$CO-L-Phe-D-Oxd-OH formed hydrogel, which was used in 3D cell culture. A peptide-based noncytotoxic bolaamphiphile HO-WF-Suc-LW-OH (Suc: succinic acid) showed morphological conversion from nanovesicles to nanofibers. The electron microscopy images of self-assembled bolaamphiphile showed the formation of nanovesicles. However, the serial transformation in the self-assembled structure from nanovesicles (day 1) to nanocapsule (day 2) was observed and further incubation led to the formation of nanofibrillar structure after 4 days.

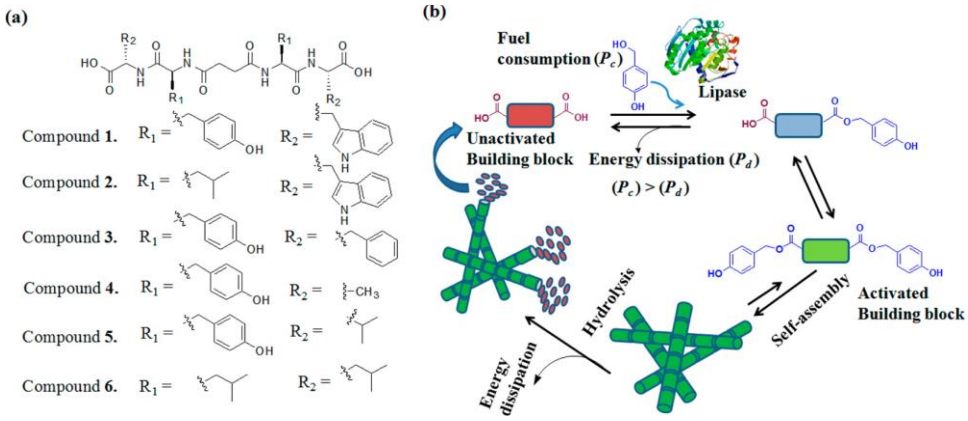

Figure 1.16 (a) Structures of peptide bolaamphiphiles (b) Dissipative reaction cycle of the system. Unactivated peptide bolaamphiphile 1 incorporates energy in the form of p-hydroxy benzylalcohol to give monoester and then diester. The diester self-assembles into nanofibers and forms hydrogel. The subsequent hydrolysis leads to dissipate the energy of diester which results in collapse the hydrogel. The rate of enzymatic energy dissipation (Pd) (ester hydrolysis) is lower

than the consumption of the energy (Pc) (esterification) to allow the formation of self-assembled architecture. Reprinted with permission from ref. 170.

Another report demonstrated dissipative self-assembly of peptide bolaamphiphile (HO-WY-Suc-YW-OH) through lipase-catalyzed ester bond formation between *p*-hydroxybenzyl alcohol and bolaamphiphile (Figure 1.16).[170] The lipase enzyme generates dynamic combinatorial libraries (DCL) of monoester and diester but the activated diester led to the formation of self-supporting and thixotropic hydrogel. Several peptide bolaamphiphiles (HO-WY-Suc-YW-OH, HO-WL-Suc-LW-OH, HO-FY-Suc-YF-OH, HO-AY-Suc-YA-OH, HO-VY-Suc-YV-OH, HO-LL-Suc-LL-OH) were synthesized for the development of dynamic combinatorial library (DCL). Interestingly, the DCL reaction was observed only when the peptide bolaamphiphile is decorated with W residue at the terminal end of the peptide. However, the self-assembled hydrogel was observed in the case of peptide bolaamphiphile HO-WY-Suc-YW-OH, which was used for human umbilical cord stem cell proliferation.

1.7 Biomedical Applications of Peptide-Based Self-Assembling Materials

1.7.1 Self-Assembling Peptides as Cell Culture Scaffold

Cell adhesion and proliferation on self-assembled nanofibrillar peptide surface are very complex process, which is mediated through specific cellular interactions between peptides and animal cells.[171,172] The design and synthesis of extracellular matrix (ECM) mimetic peptide-based hydrogels are promising candidate for cell culture and tissue engineering applications.[173,174] The peptide-based tissue engineering scaffold can be designed by combination of two different bioactive self-assembling peptides such as Fmoc-FF (fluorenylmethoxycarbonyl-diphenylalanine) and Fmoc-RGD (arginine-glycine-aspartate) (Figure 1.17).[175,176] In such binary peptide-based hydrogel system, one component provides structural rigidity, stability and nanofibrous environment and second component works as bioactive ligand on the surface of nanofibrillar networks. The RGD peptide is a bioactive ligand, which was located inside the hydrophilic loop of fibronectin and collagen I protein and worked as a cell attachment site via binding with integrin (cell-surface receptor).[177] The ECM mimetic materials are extensively used for cell adhesion, cell migration and differentiations in the area of tissue engineering.[178] Biomaterial for bone tissue engineering was developed by a bicomponent (Fmoc-FF and Fmoc-R) hydrogel. The arginine rich hydrogel showed high affinity to hydroxyapatite ($Ca_{10}(PO_4)_6(OH)_2$) that was responsible for bone mineralization and growth of human osteoblasts. The peptide-based 3D scaffolds showed suitable rigidity and mechanical strength for bone tissue regeneration through promoting the fibroblast cell (3T3 cells) adhesion and proliferation. Stimuli responsive and thixotropic γ-peptide hydrogels were used for 2D cell culture using normal (HEK293T) and cancer cell (LN229) lines.[179] Fmoc-capped amino acid and peptide-based hydrogel was used for 2D and 3D cell culture of chondrocytes.[108] In 3D cell culture experiments, chondrocytes were carefully

mixed with the Fmoc-dipeptide hydrogels. Fluorescence microscopy was used to analyze the imbedded cells, which were stained by a fluorescent 2-(4-amidinophenyl)-6-indolecarbamidine dihydrochloride (DAPI) dye. Another self-assembling dipeptide hydrogel was reported as a scaffold for in situ 3D cell culture.[180] The resulting concentrations of peptide were 0.5 and 1.0% (w/v) in self-supporting hydrogel for 3D cell culture. The higher concentrations of peptide increased the toughness of the hydrogel. The formation of tough hydrogel was ensured by test tube vial inversion method. The reported method is very simple and economical, which eliminates the chemical complexity associated with polymeric hydrogels. An octapeptide FEFEFKFK based hydrogel was used for 3D cell cultures of chondrocytes.

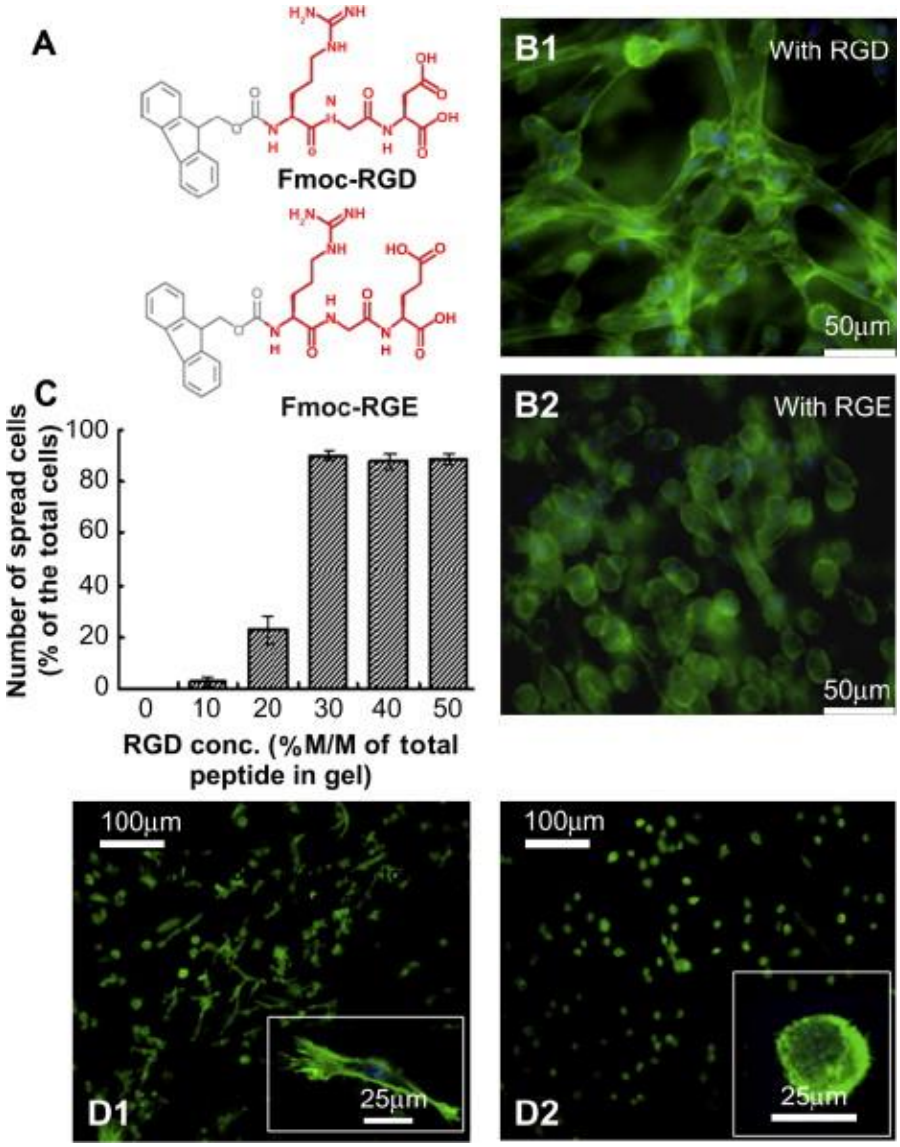

Figure 1.17 (A) The structures of the two chemical analogs: Fmoc-RGD and Fmoc-RGE. (B) Cell adhesion and morphology in the Fmoc-FF/RGD and Fmoc-

FF/RGE hydrogels: human adult dermal fibroblasts (HDFa) are well-spread in the Fmoc-FF/RGD hydrogels, and form a three-dimensional cell network 48 h post culture (B1); HDFa in the Fmoc-FF/RGE hydrogels maintain a round morphology after 48 h (B2). (C) The Fmoc-RGD concentration also influenced cell spreading: in the hydrogels with 30–50% Fmoc-RGD incorporated, adequate cell spreading occurs with over 90% spread cells. (D) Integrin blocking experiments proved direct interaction of the cells with RGD after 20 h: Cells with unblocked α5β1 integrins were able to spread and directly attach to the RGD sites on the nanofibers (D1); Cells with blocked α5β1 integrins were unable to attach to the RGD sites and remained rounded (D2). Reprinted with permission from ref. 175. Copyright (2009) Elsevier Ltd.

Recently, self-assembling pentapeptides were described as injectable delivery (RAPID) hydrogels for oligodendrocyte progenitor cells (OPCs).[181] The RAPID hydrogel shielded OPCs from mechanical and physical membrane injury owing to the syringe injection and supported cell viability and proliferation. Hamley et al. reported arginine-capped peptide bolaamphiphile for the fibroblast cell viability and adhesion applications.[64] The coating of peptide RFL_4FR (0.1 and 0.3% w/v) showed good cell adhesion on solid surface with normal fibroblastic morphology. Recently, shortest collagen inspired peptide (Nap-FFGSO) was reported that self-assembled in the presence of laminin mimetic peptides.[182] The self-assembled structure of hydrogel provided 3D nanofibrous network that mimicked biological activity of the natural ECM. The 3D nanofibrous network of the hydrogels is essential for cellular communication through biochemical signals that promotes the cellular viability, growth and proliferation. Similarly, a peptide-based bioadhesive hydrogel was designed which mimicked the function of fibronectin protein present in ECM.[183] The self-assembled hydrogel was achieved by combination of two different unprotected peptides ^{D}FFL and ^{D}FFLDV. The peptide ^{D}FFL formed stable nanofibrillar structure at physiological conditions and the bioactive moiety (LDV) was attached with the second peptide ^{D}FFLDV. The fibroblast cells were viable in ^{D}FFL containing hydrogel but the cell proliferation and adhesion were occurred when the bioactive peptides ^{D}FFLDV was mixed with self-assembling peptide.

1.7.2 Self-Assembling Peptides as Antibacterial Agents

The microbial infections and contaminations are one of the serious global issues, which cause heavy economy burdens in both healthcare and industrial sector. This problem is reduced and battered by the use of antibiotics. Unfortunately, the boundless use of antibiotics significantly leads to the growth of antibiotic resistant bacteria that is mentioned in World Health Organization (WHO) as a threatens to the human life. The emergence of methicillin-resistant *Staphylococcus aureus* bacteria attracted extensive research attention for the development of regenerative medicines due to their significant concern to the public health.[184] The ideal antibiotic alternatives are required to display potent activity towards the growth of

drug resistance strain.[184] It is still a huge challenge to develop a synthetic compound that may effective against antibiotic resistant bacteria.[185] Notably, the clinical use of antimicrobial peptides (AMPs) has emerged as the alternative approach for the development of new class of therapeutic agents.[186] Such AMPs are specially designed and developed to combat the unwanted bacterial growth.[187] However, several AMPs are involved naturally those are originated from animals and plants, which provide broad-spectrum antimicrobial activity and serve as a key and important component of innate immune response. Moreover, low molecular weight-based AMPs are cheap, economical, easy to synthesize and functionalize by traditional chemical routes thus attractive candidate for the biomedical diagnostics and therapies.[56]

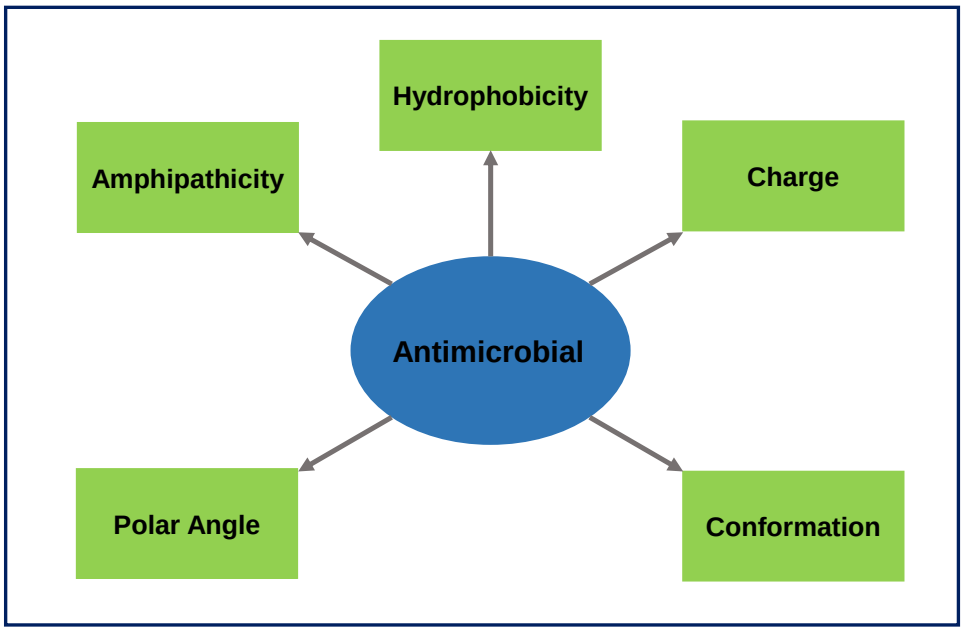

Figure 1.18 Various biochemical components of AMPs responsible for antimicrobial activity.

A novel class of AMPs are self-assembling peptides, which include hydrogels, nanofibers, nanovesicles, nanotubes, nanocoatings and other nanostructures.[188] Many of the self-assembling AMPs are amphipathic in nature and composed of hydrophobic and hydrophilic amino acids. Several AMPs contain net positive charge owing to the presence of lysine, arginine and histidine amino acids.[189] The antimicrobial peptides often contain the negative charge due to the presence of aspartic and glutamic acid. Other AMPs contain hydrophobic amino acids such as valine, leucine, isoleucine, alanine, phenylalanine, tryptophan and tyrosine, which have been reported with remarkable antibacterial activity.[190] The AMPs are divided in different class on the basis of their conformation and secondary structures like α-helical, β-sheet, partial loop and extended structures. The well-organized secondary structure shows better antimicrobial activity.[191] Most of the

AMPs belong to two groups *i.e.* α-helical and β-sheet peptides. Sometimes AMPs only become helical and sheet upon interactions with microbial phospholipid membranes.[191] The hydrophobicity and net charge on the AMPs are generally worked as a better antimicrobial agent (Figure 1.18).[192] The peptide hydrophobicity is an essential feature of AMPs, which works as the degree of penetration into the lipid membranes.[193] The higher hydrophobic-based AMPs show better and effective membrane permeabilization (Figure 1.18).[194] However, the greater hydrophobic peptides cause significant toxicity towards the red blood cells and shows hemolysis. Hence, the balance between hydrophobicity and hydrophilicity of AMPs is very essential for better selectivity of the peptides.[194] Additionally, the polar angle is considered as polar versus nonpolar faces of AMPs. For example, the one face of AMPs is composed with hydrophobic groups and the opposite face of AMPs is composed with charged residue, then the polar angle would be 180°. In such cases, the reduction in polar angle owing to the folding of the peptides shows better antimicrobial activity.[192,194] The rate of microbial membrane permeabilization, translocation and pore formation increases with the reduction with the polar angle. A wide variety of techniques are used to elucidate the mechanism of action of the antimicrobial peptides. Microscopic techniques are most common method to visualize the mode of action of antimicrobial peptides on microbial cell membranes.[195] The AMPs are mixed with phospholipid membrane or vesicle to assess the interaction and mechanism between peptide and model membrane.[195] In this technique, artificial model membrane is utilized to determine the type of cellular damage induced by antimicrobial peptides.[196] The thickness and integrity of lipid membranes can be investigated by spectroscopic and microscopic techniques such as SEM, TEM, NMR, FTIR, CD, Raman and fluorescence spectroscopy. The secondary structure of the AMPs plays a key role for the antimicrobial activity that can be analyzed be CD spectroscopy.[197] The orientation of AMPs bound to the lipid cell membranes is analyzed by CD and compared with the orientations of unbound peptides to understand the importance of secondary structure. The AMPs attracted to bacterial cell membranes owing to the electrostatic interactions between cationic AMPs and anionic groups such as phospholipid and phosphate groups of lipopolysaccharides present in Gram-negative bacteria and teichoic acid on the surface of Gram-positive bacteria.[198] The interactions between peptides and cell membrane leads to the depolarization of bacterial cell wall and cell membrane which results into the death of bacterial cells.[199]

1.7.3 Self-Assembling Peptides as Antifungal Agents

Fungal infections are emerged as major cause of morbidity and mortality and known as very devasting microbial infection.[200] Fungal infections can be divided into two major classes such as opportunistic and primary infection. Several fungi are opportunistic microorganism and show disease only in immunocompromised individuals. The individuals, who are weaker in their immune systems, are so called immunocompromised individuals. The opportunistic infections are mainly

developed in immunocompromised individuals such as human immunodeficiency virus (HIV), diabetes mellitus (DM), tuberculosis (TB), bronchiectasis and cancer patient. However, the primary infections are generally developed in immunocompetent individuals. Mainly the fungal infections are caused by three pathogens *Candida albicans* (*C. albicans*; 20-40%), *Aspergillus fumigatus* (*A. fumigatus*; 50-90%) and *Cryptococcus neoformans* (*C. neoformans*; 20-70%). The fungal pathogen *C. albicans* is commensal organism, which causes different types of candidiasis including mucosal and invasive candidemia. The invasive candidemia is a life-threatening invasive infection that enters into the blood-stream and affects the vital organs. The *C. albicans* are often associated with biological implant-mediated infections, associated with biofilm formation of urinary catheter, cardiovascular devices and prosthesis. In recent year, the excessive use of antimycotic agents is responsible for significant cause of the growth of resistant strains. Additionally, many of the synthetic antimycotic molecules suffer with several drawbacks such as poor solubility, cytotoxicity, immunogenicity, poor pharmacokinetics and efficacy. Despite the medical advancement and management, there are huge demand for the treatments of nonconventional microbial infections and contaminations. Thus, it is important to develop new biocompatible and antifungal molecules which can combat in broad spectrum with unusual mode of action.[201] In the search of regenerative medicines, peptides are highly promising noncytotoxic and highly selective biomolecules for the treatment of microbial infections.

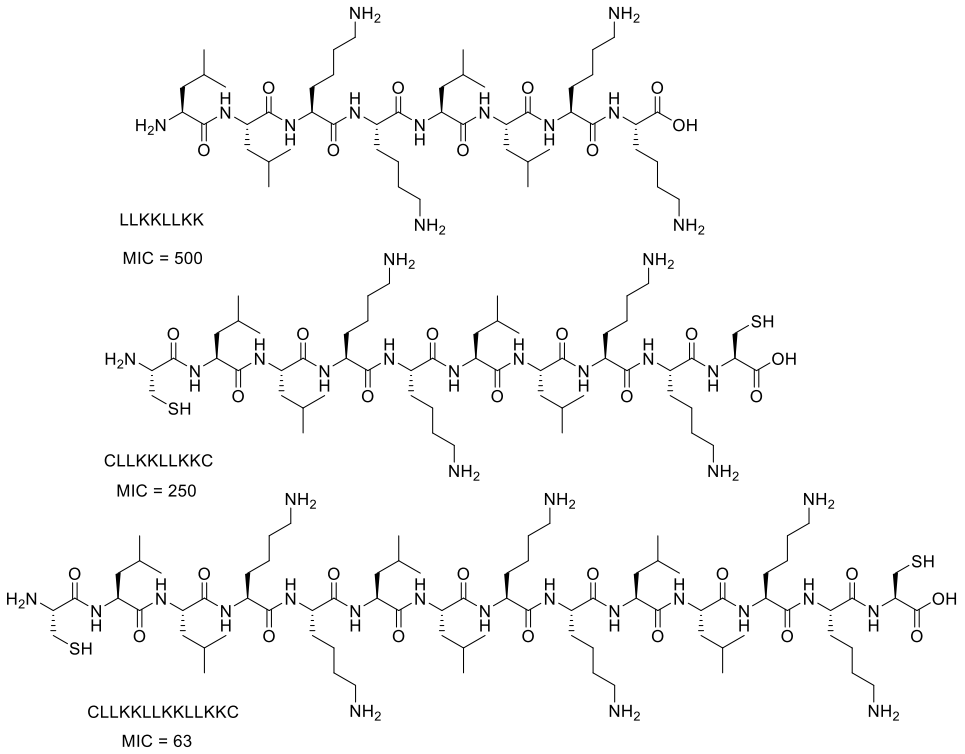

Figure 1.19 Chemical structure of antifungal peptides.

A novel class of antifungal tripeptide-based molecules were developed with high selectivity against the growth of *C. neoformans* (MIC = 1.25 μg/mL^{-1}).[202] These tripeptides consist of histidine, arginine and lysine amino acids in their sequences and cationic part plays crucial role for the antibacterial and antifungal applications. Various antifungal peptides were correlated with their antifungal activity with the hydrophobicity of side chain amino acids of the peptides.[203] In this report, helical structure forming peptides further influenced the selectivity and inhibited the growth of *C. albicans*. Similarly, cell penetrating conjugated peptide aldehydes Tat-A and Tat-B showed potent antifungal activity and eradicated biofilm of *C. albicans* at micromolar concentrations.[204] The ultra-short peptidomimetics exhibited excellent *in vitro* antifungal activity against *C. neoformans* and found the IC_{50} values in the range of 0.16-19 μg/mL.[205] Ying et al. reported α-helical forming self-assembling peptide for biofilm caused keratitis treatment (Figure 1.19).[206] The author reported antifungal activity of peptides $(LLKK)_2$, $C(LLKK)_2C$ and $C(LLKK)_3C$ showed higher antifungal activity over animal cells. The cysteine residue attached at terminal end of self-assembling peptides exhibited greater antifungal activity and MIC values were found 500, 250 and 63 mg L^{-1} for $(LLKK)_2$, $C(LLKK)_2C$ and $C(LLKK)_3C$ peptides, respectively. Authors illustrated that the antifungal activity of the peptides increased with the addition of cysteine residue at the terminal end of self-assembling peptides. The higher α-helical propensity of peptides showed greater antifungal activity owing to the greater affinity of anionic membrane. These α-helical peptides were water soluble and biocompatible eradicated the biofilm of *C. albicans* in the mice eyes.[206] Various tripeptides were designed which showed antifungal activity against 24 strains of pathogenic fungi. All synthesized antimicrobial peptides displayed potent antifungal activity with low micromolar MIC against pathogenic fungal strain. The antimicrobial peptides were used for the treatment of human skin and nail model of candidiasis (*C. albicans*) and onychomycosis (*Trichophyton rubrum*), respectively.[207]

1.7.4 Self-Assembling Peptides as Anti-inflammatory Agents

Inflammation is a first and natural host defense response and it is evoked by various stimuli including physical damage, microbial infection, allergic and autoimmune reactions. Inflammation can be easily identified by various biological phenomena such as swelling, heat, redness, pains and loss of functions. The inflammatory response is mediated through the secretion and activation of various proinflammatory mediators which include cytokines, chemokines, interleukins and growth factors.[208] In the recent advancement in biomaterial science, there are exciting opportunities to demonstrate the construction of various functional and biological active soft biomaterials. Inflammations are associated with different types of diseases including cancer, Alzheimer's, rheumatoid arthritis and cardiovascular disease.[209] However, the steroidal anti-inflammatory drugs (SAIDs) and non-steroidal anti-inflammatory drugs (NSAIDs) are used for the

treatment of the acute and chronic inflammations. The SAIDs show several side effects on vital organs and prolonged use of the drug causes osteoporosis, peptidic ulcer, organ and tissue failure. Additionally, NSAIDs are also associated with adverse gastrointestinal, renal and cardiovascular diseases.[210] Moreover, it is important to design and synthesize the anti-inflammatory molecules with a suitable biocompatibility. The amino acids in small peptides play a key role for the activity of anti-inflammatory compounds. The anti-inflammatory activity of peptides is achieved through the balancing of lipophilic and lipophobic parts of the small peptide-based compounds. Such peptides are known to work as an anti-inflammatory compound by inhibiting the cyclooxygenase (COX) isoenzymes activity (Figure 1.20).[211]

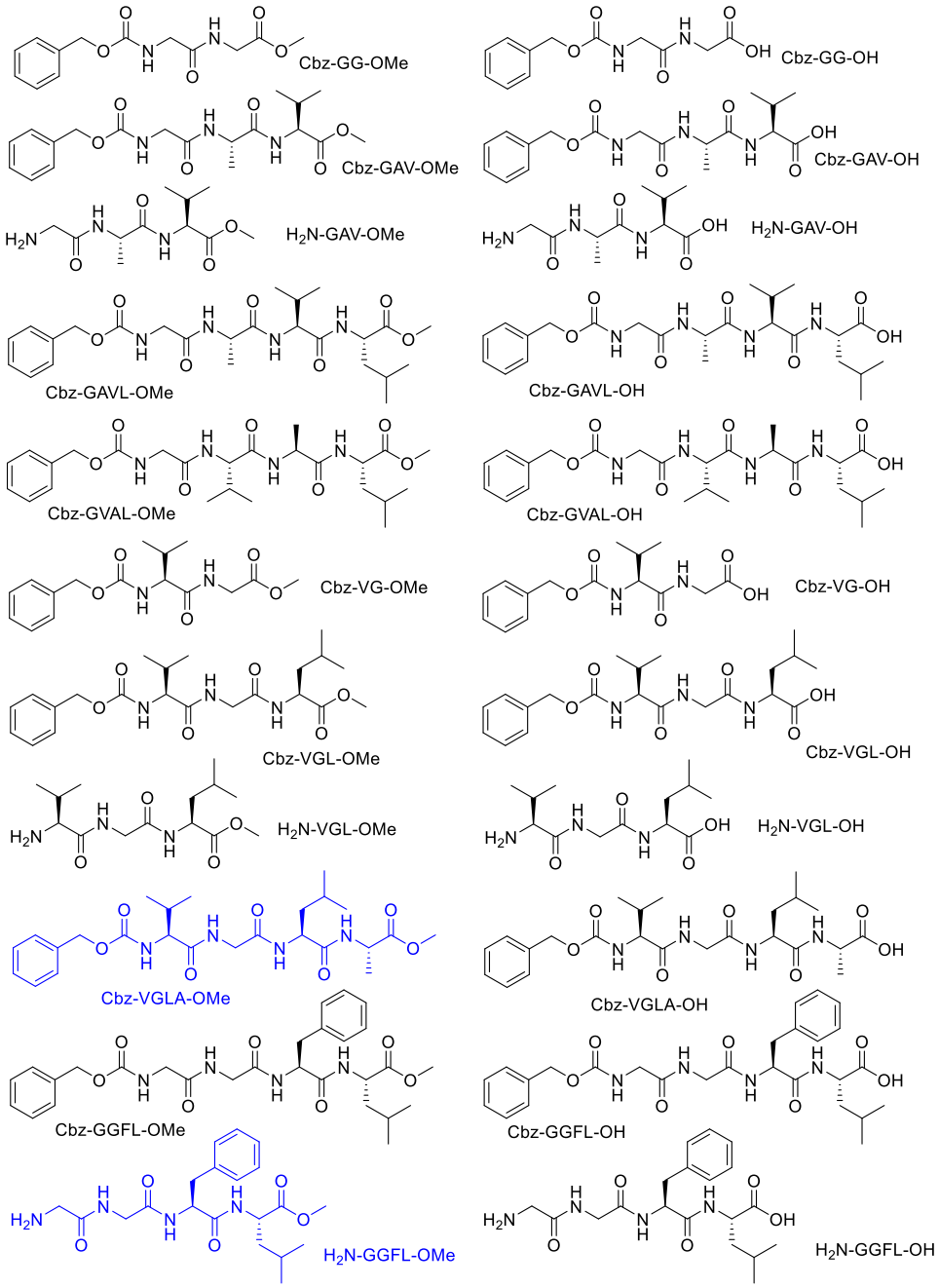

Figure 1.20 Chemical structure of anti-inflammatory peptides.

The synthesized peptides were subjected to COX-1 and COX-2 inhibition assay. The hydrophobic nature of the synthesized tetrapeptides interact with the COX. The author reported that the peptide Cbz-VGLA-OMe and H_2N-GGFL-OMe showed better anti-inflammatory activity compared to the other synthesized peptides with IC_{50} values of 80 and 60 nM, respectively. Further, the COX inhibition reduces the production of prostaglandins that is lipid based compound and responsible for several cellular processes such as apoptosis, angiogenesis, and

cell migration.[212] Proinflammatory properties of prostaglandin have been well studied which play important and crucial roles for the recruitment of the inflammatory cells. Prostaglandin biosynthesis dramatically increases during the pathogenesis of microorganism and allergic reactions.[212] The four major biological active prostaglandins are PGE_2, PGI_2, PGD_2, $PGF_{2\alpha}$ associated with the inflammation. Generally, prostaglandin production depends upon the activity of COXs enzyme, which exists as COX-1 and COX-2 isoforms. The COX-1 is expressed in most of the cells and mainly responsible for gastric epithelial cytoprotection and homeostasis. However, COX-2 is induced by inflammatory stimuli and mainly responsible for acute and chronic inflammation. Hence, the anti-inflammatory peptides and NSAIDs drug are specially designed to target the arachidonic acid pathway, thereby, the production of prostaglandin rapidly inhibited. These molecules are competitive active site inhibitor of COXs and irreversibly binding to the COXs site results the termination of biosynthesis pathway of prostaglandin. In a recent report, the indole appended-dipeptide showed the anti-inflammatory and anti-hyperalgesic activities.[213] The proline centered pentapeptide is isoconformational to the arachidonic acid and exhibited anti-inflammatory activity by binding with COX-2.[214]

1.7.5 Self-Assembling Peptides in Wound Healing

Skin is the largest and important organ of animal body and works as a protective barrier between the internal tissues and external environment such as chemical, thermal and bacterial infection.[215] Wound healing is a multistep process including hemostasis, immune response, inflammatory events, cell proliferation and matrix remodeling in which injured tissues are repaired or replaced by new functional tissues with native integrity.[216] In recent years, hydrogels have been extensively used for the wound healing applications. Hydrogels are three-dimensional polymeric material, which retain significant amount of water. Thus, hydrogels serve as a soft and extra cellular matrix (ECM). Additionally, hydrogels provide high surface area for cell migration, and allow the gaseous exchange and nutrition, which accelerate the healing process.[217,218] Hydrogels for wound healing applications work as a sealant material to stop excessive bleeding from damaged tissues and organs. However, common hydrogels have various limitations to be applied as good wound healing materials due to poor mechanical strength, unwanted inflammatory response and introduction of microbial infections owing to the excessive moist environment. Although, promising hydrogels for wound healing applications must absorb exudates from wound and must combat to the bacterial infections. Furthermore, the traditional wound dressing biomaterials are designed and fabricated by antibiotics to eliminate the microbial infection near the wound site.[219] An inherent antibacterial biomaterial for wound healing minimizes the growth of antibiotic-resistant bacteria. Importantly, the nanofibrous morphology of biomaterials are very crucial for wound healing applications due to the high surface area to volume, interconnected porosity and similarity to the ECM.

Peptide-functionalized hydrogels were used as hemostasis agent with antibacterial activity for wound healing.[220]

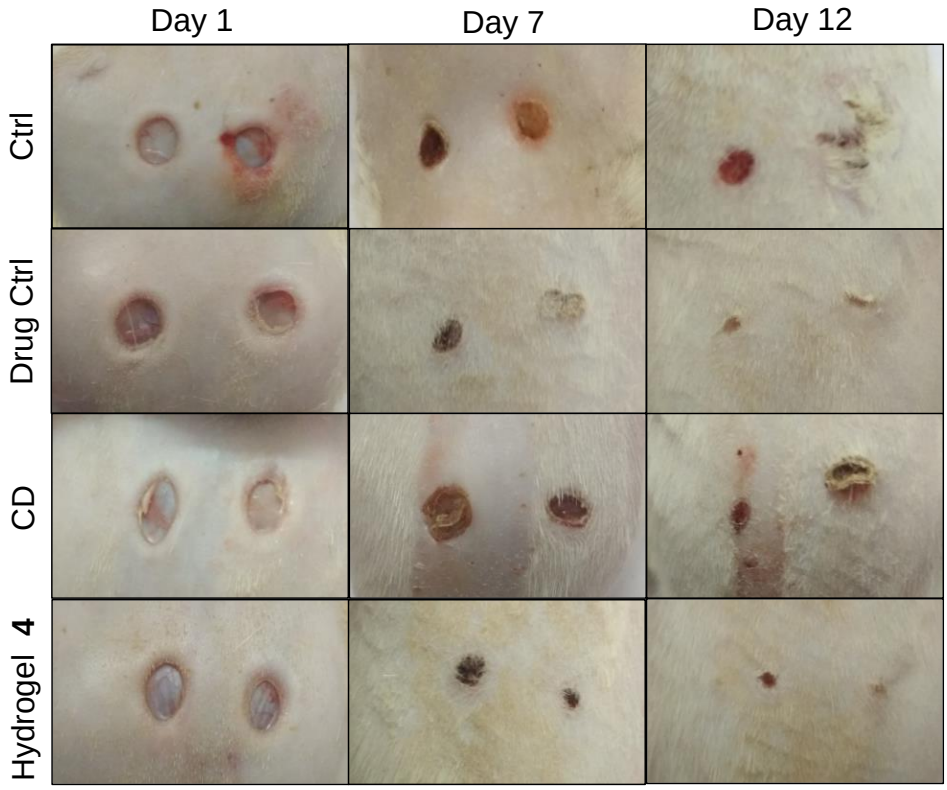

Figure 1.21 Optical photographs of in vivo wound healing activity of different groups showing the increase in healing activity using hydrogel **4**. Reprinted with permission from ref. 98. Copyright (2020) American Chemical Society.

Fmoc-FF based peptide-polymer hydrogel was explored for in vivo wound healing activity. The drug curcumin was loaded into the Fmoc-FF by coassembly approach, which showed anti-inflammatory and antibacterial activity.[221] Heparin mimetic peptide nanofibers were reported for the treatment of diabetic wounds by accelerating the production of the angiogenic growth factors and re-epithelization.[222] The self-assembling peptides showed positive impact on tissue regeneration and inflammatory response.[223-225] However, the wound healing peptides can be loaded into the hyaluronic acid based hydrogel for the excisional wound healing activity by promoting the migration of fibroblasts, keratinocytes and endothelial cells.[226] It is well accepted that free radical near the wound site causes oxidative stress that can damage the DNA and protein resulting into the delay in the healing process.[227] Hence, the improved wound healing activity can be achieved by biocompatible and antioxidant peptide-based supramolecular hydrogel (Figure 1.21).[98,227] The collagen derived tripeptides (CAG) exhibit enhanced in vitro wound healing activity by showing endothelial cell adhesion, growth and proliferation.[228] Since, the inflammation is important biochemical

process for the secretion of proinflammatory cytokines, chemokines and macrophages. Sometimes, prolonged inflammation causes delayed in wound healing activity. Therefore, the anti-inflammatory hydrogels reduce the scar formation and accelerate the wound healing activity by increasing the collagen deposition (Figure 1.21).[98,229]

1.7.6 Self-Assembling Peptides as Anticancer Agents

Cancer is the second leading cause of human deaths (16%) after cardiovascular disease worldwide.[230] Cancer cells have the innate ability to develop resistant against various chemotherapeutic drugs and become multi drug resistance (MDR), which is a major obstacle for the treatment of cancer. Advancement in the bioorganic chemistry and cancer biology offer new strategies for the treatment of cancer.[231] Nowadays, peptides as anticancer agents are emerged as new therapeutics and molecular tool to induce morphological change and cellular death.[232] Self-assembling peptides have been recognized as a new approach in the area of cancer and tumor biology.[233] However, unwanted and uncontrolled self-assembly of the peptides and proteins lead to the generation of structural aggregates that causes neurodegenerative diseases. Interestingly, the self-assembly of the peptides and proteins in a controlled manner could be the novel therapeutic approach for the inhibition of cancer cells.[234] Most of the peptides as anticancer agents are amphipathic in nature and their structural features are important for the activity and selectivity.[235] The peptides as anticancer agents self-assemble into the nanofibrous structure which inhibits the proliferation of cancer cells. The self-assembling NapFF nanostructures selectively inhibited the growth of glioblastoma cells by the disruption of the self-organization of the microtubules and tubulins protein.[236] The noncovalent interactions between self-assembling peptides and cell skeleton proteins actuate the caspase dependent signaling pathway leading to the cellular apoptosis. The design of mitochondria targeted and penetrated peptide is a promising approach to kill the tumorigenic cells.[237] Mitochondria are considered as the powerhouse of the cells. Triphenyl phosphonium (TPP) is small molecular motif, which can target the mitochondrial matrix. In cancerous cells, alkaline phosphatase is overexpressed and TPP containing peptides self-assemble on the surface of cancerous cells by enzyme-induced dephosphorylation process (Figure 1.22).[238] The anticancerous activity of mitochondria targeting peptides can be enhanced by coassembly of its enantiomeric pairs. Ryu et al. designed and synthesized diphenyl alanine-based mitochondria targeting peptides and named as Mito-FF (L-phenylalanine) and Mito-ff (D-phenylalanine), respectively.[239] These peptides coassembled owing to the presence of pyrene moiety and formed super-fibril morphology leading to the disruption of mitochondrial membrane.[239] In another approach, the self-assembling peptide amphiphile encapsulated the bioactive epitopes through the coassembly process on their nanofibrous structures. The advantage of coassembly between self-assembling pegylated and membrane lytic peptides showed better in vitro protease stability and antitumor activity.[240]

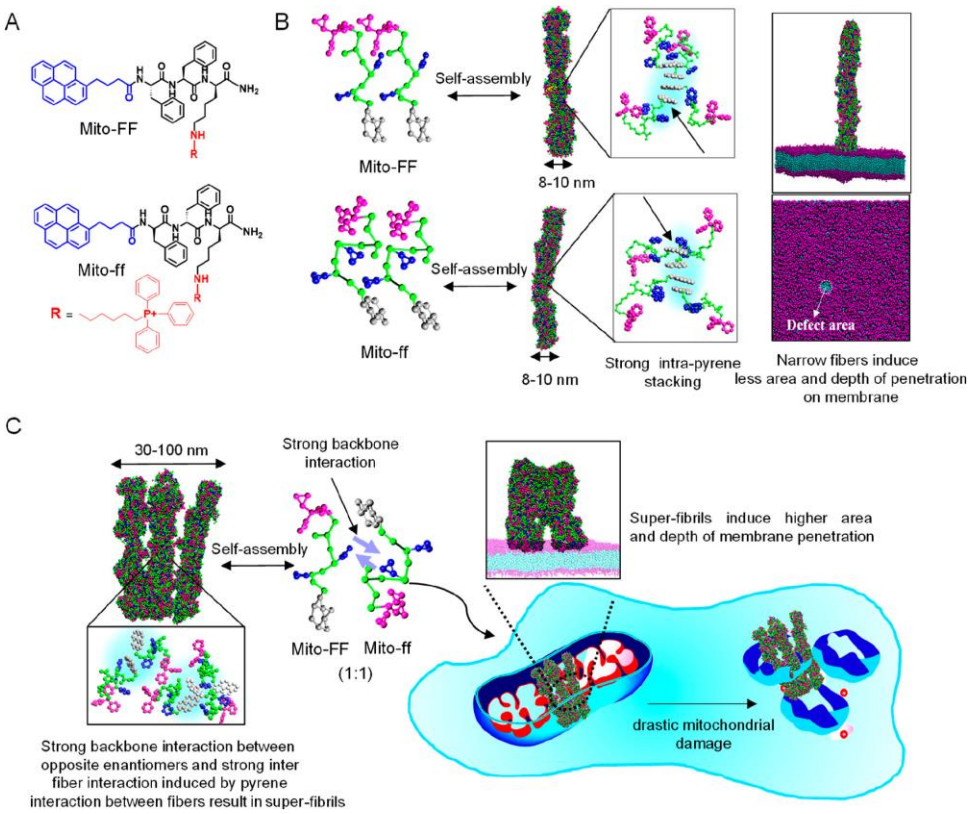

Figure 1.22 Schematic illustration. (A) Chemical structure of mitochondria penetrating peptides Mito-FF and Mito-ff. (B) In the case of the enantiomer, Mito-FF or Mito-ff self-assembles into narrow fibers of diameter 8–10 nm. In both fibers, intrapyrene interactions between enantiomers are strong, and pyrene packing is located inside the fiber. (C) The assembly of 1:1 racemic mixture of Mito-FF and Mito-ff forms a superfibril. In the 1:1 mixture, each diphenyl alanine between between Mito-FF and Mito-ff interacts strongly and consequently produces less pyrene stacking. The superfibrils are formed as a result of interfiber interaction induced by pyrene interactions between the fibers. A cellular incubation of 1:1 mixture targets mitochondria to form superfibrils inside mitochondria to more drastically destroy than that of homo enantiomeric fibers. The super fibrils induce a higher area and depth of membrane penetration. Molecular structure, interaction, and membrane penetration obtained from CGMD simulation. Reprinted with permission from ref. 238. Copyright (2019) American Chemical Society.

The self-assembling peptides and anticancer drug conjugates are effective therapeutics for the treatment of cancer.[241] In this approach, a chemotherapy drug chlorambucil (CRB) was covalently conjugated with self-assembling peptide (FFE), which was interlinked with tyroservatide (YSV) peptide. The design of hydrogelator was based on the following reasons: (1) diphenylalanine (FF) is inherent self-assembling entity; (2) CRB is nitrogen mustard chemotherapy drugs

that can be used to enhance the noncovalent interactions and (3) peptide YSV is anticancerous in nature. The in vivo experiments showed that the peptide CRB-FFE-YSV easily penetrated tumor cells and induced the cell apoptosis and necrosis (Figure 1.23).[241]

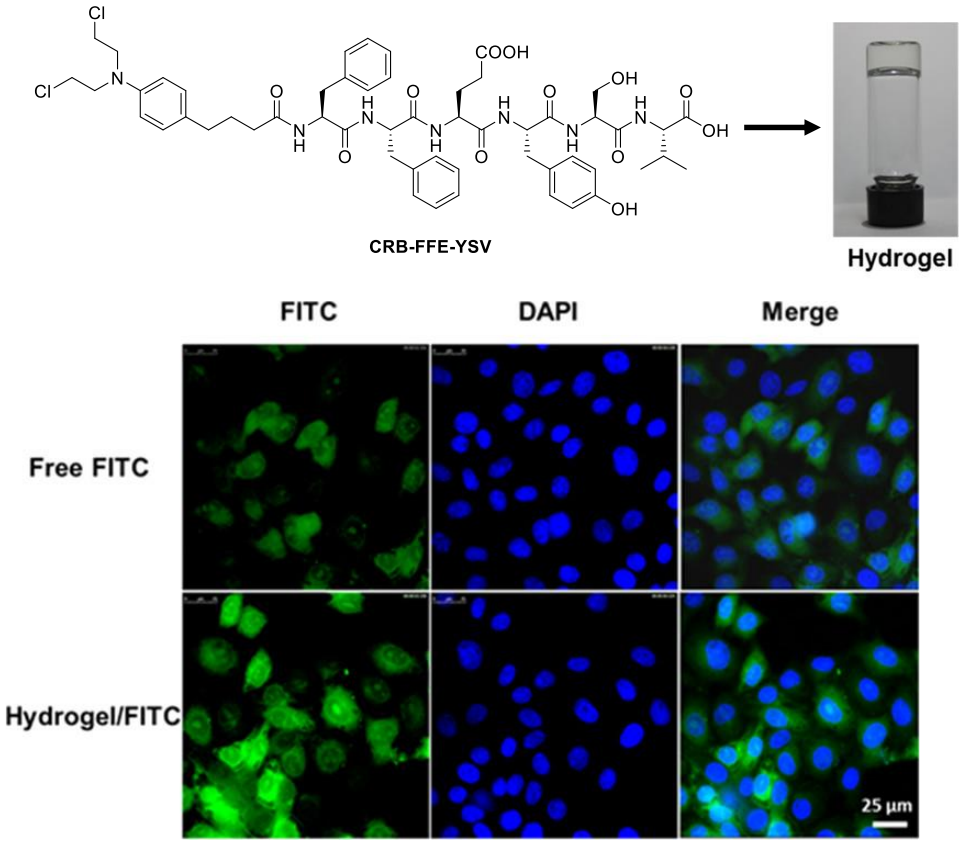

Figure 1.23 Chemical structure of CRB-FFE-YSV peptide showing anticancer activity against HepG2 cells. Adapted with permission from ref. 241. Copyright (2019) American Chemical Society.

Similarly, anticancer drug Taxol conjugated peptide tyroservatide (YSV) was synthesized to enhance the antitumor efficiency and in vivo biocompatibility.[242] The biostability of peptides can be increased by using D-amino acids, which can resist the in vivo peptidase hydrolysis. Yan et al. prepared injectable, shear-thinning and self-healable hydrogel using combination of positive charge poly-L-lysine (PLL) and Fmoc-FF peptide.[243] The Fmoc-FF/PLL-SH self-assembled into the helical nanostructures through disulfide bond and worked as a powerful tumor inhibitor. The hydrogel activated the auto immune response of animal body by providing T cell immunity through tumor antigen recognition. Yang et al. reported NSAID modified D-tetrapeptides ($G^DF^DF^DY^D$) for the antitumor activity.[244] The authors developed cancer vaccine adjuvants by using NSAID drugs for the N-terminal protection of peptides. The self-assembling peptides exhibited anticancer

activity by increasing the host immune response against the tumor cells. The peptides increased immunoglobin (IgG2a) production and stimulate the IFN-γ and IL-6 cytokines secretion.

1.7.7 Self-Assembling Peptides as Cargo for Drug Delivery

Peptide-based supramolecular hydrogels are versatile biomaterials for *in vitro* and *in vivo* sustained release of encapsulated drug molecules.[245,246] The term 'smart hydrogel' is used according to their ability to receive, transmit and respond to the external stimuli for useful applications.[247] Peptide-based biomaterials are easier to design and their mechanical and nanostructural morphology can be tuned by changing the peptide sequences. The objective of the development of a drug delivery carrier and vehicle is to minimize the systemic adverse effect of the drugs by delivering to the targeted site.[248] Particularly, injectable biomaterials are emerging as next generation biocompatible and biodegradable vehicle for targeted drug delivery applications.[249] Self-assembling peptides encapsulate the drug molecules within the porous 3D matrix and show the stimuli responsive changes in their structural network. The porous 3D matrix and drug loading capacity can be tuned by controlling the density of assembling entities in aqueous microenvironment.[250] The drug release kinetics depend upon the diffusion coefficient of the encapsulated molecules from the hydrogel matrix. Sometimes high-water content and hydrophobicity of the loaded drug molecules often result in rapid drug release from the hydrogel matrix. Hence, the drug delivery rate of the hydrogels are different for different drug molecules and can be tuned by maintaining the hydrophilic-hydrophobic ratios.[251] Banerjee et al. developed a tripeptide-based hydrogel for the entrapment and sustained release of vancomycin and vitamin B_{12}.[252] The supramolecular cage-like fibrous network of the hydrogel acts as a drug delivery template at physiological conditions. The self-assembling tetrapeptide-based hydrogels have been used for the encapsulation and release of anticancer drug doxorubicin. These peptide-based hydrogels encapsulate 8.62 and 13.79 mM of drug solutions at their minimum gelation concentrations. The quantitative analysis of doxorubicin diffusion was calculated by nonsteady state diffusion model equation:

$$(M_t/M_\alpha) = 4(Dt/\pi\lambda^2)^{1/2}$$

where M_α is the initial amount of drug used for the experiment, M_t is the final amount of drug released, λ represents hydrogel thickness, D represents diffusion constant of the drug, t represents time of the experiment.[252] MMP-9 responsive self-assembling peptide amphiphile was capable for sustained release of hydrophobic drug doxorubicin from fiber matrix (Figure 1.24).[253] A hexapeptide-based hydrogel was reported for delivery of fluorescein sodium and ciprofloxacin hydrochloride, which showed two stage zero-order kinetics with cumulative 80% release profile.[254] A redox responsive dipeptide self-assembled into the vesicles through the noncovalent interactions of tryptophan residues. These vesicles entrap DOX (16% w/w) and showed redox-triggered drug delivery inside the MDA-MB-231and HeLa cells due to the high cytosolic GSH concentrations.[255] A peptide

amphiphile-based drug carrier was reported for in vitro and in vivo anticancer applications. The in vitro studies showed the DOX loaded hydrogel is more cytotoxic compared to only DOX after 48 h incubation, probably due to sustained release of entrapped drug.[256]

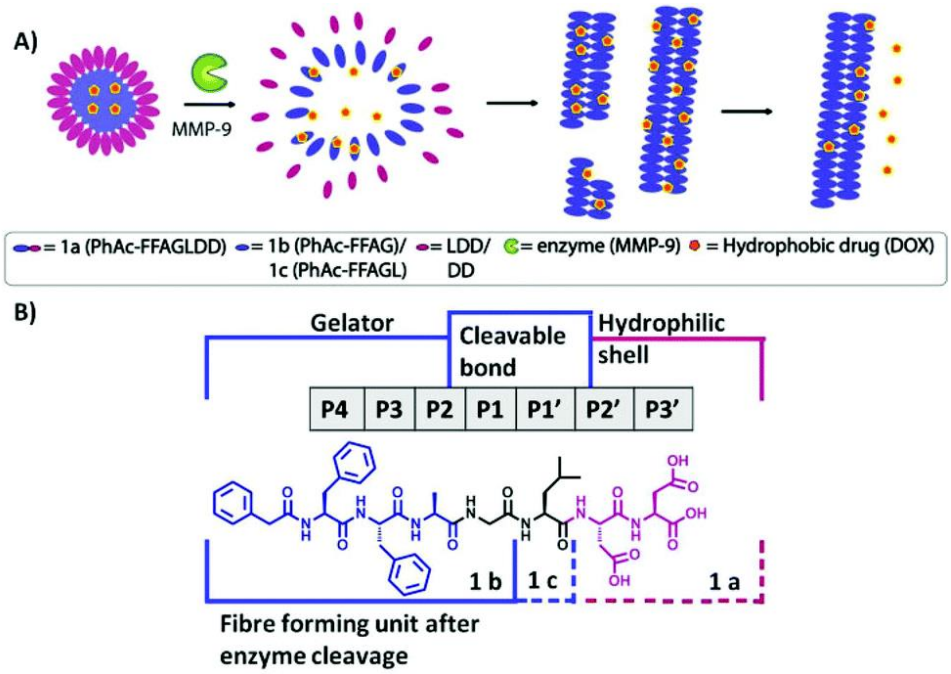

Figure 1.24 (A) Schematic representation of micelle to fiber transition induced by MMP-9 cleavage showing disassembly of micelles and the re-assembly into fibers after the removal of the hydrophilic group enabling prolonged drug release. (B) Chemical structure of the biocatalytic gelation system and its components. Reproduced from ref. 253 with permission from The Royal Society of Chemistry.

The in vivo DOX loaded hydrogel and only DOX injection to the tumor site showed lowest tumor growth rate in DOX loaded hydrogel compare to DOX injection, which ensures the better anticancer activity of DOX entrapped hydrogel. The thixotropic property of a hydrogel is useful for targeted delivery of anticancer drugs with reduced organ cytotoxicity.[257] Ribonucleotide reductase (RR) is an enzyme that plays an important role in de novo DNA synthesis by catalyzing the reduction of ribonucleotides to 2-deoxyribonucleotides. A Fmoc-capped tripeptide was designed and synthesized, which selectively binds to the mouse RR enzyme and works as an antiviral and anticancer therapeutics.[258] In the area of drug delivery, self-assembling peptide amphiphiles are used to encapsulate the drug molecules thereby the solubility and bioavailability of drug increases. Amphiphilic peptide nanofibers were utilized to encapsulate camptothecin, which is naturally occurring hydrophobic chemotherapeutic drug. The camptothecin drug was encapsulated by simple solvent evaporation technique in the hydrophobic pocket of the self-assembling peptide in its biologically active form. A dipeptide hydrogel

was reported as a photosensitive drug (chlorin e6) delivery cargo for enhanced photodynamic (PDT) therapy.[259] Peptide-based self-assembled systems provide an approach to improve the activity and functions of the system via sustained release of the drug in a stimuli responsive manner.

1.7.8 Self-Assembling Peptides as Bioimaging Agents

In the advancement of biomedical research, fluorescent peptide-based nanostructures are highly attractive due to their bioactivity and biocompatibility.[260,261] Certainly, the remarkable fluorescent properties are achieved by using various nanoparticles, quantum dots, dyes and inorganic ligands.[262] Unfortunately, the cytotoxicity at nanomolar and photobleaching of such materials are widely accepted and documented which further restricts the biomedical applications.[263] Tyrosine based peptide is cell permeable and shows green fluorescent with excellent photostability (Figure 1.25).[264]

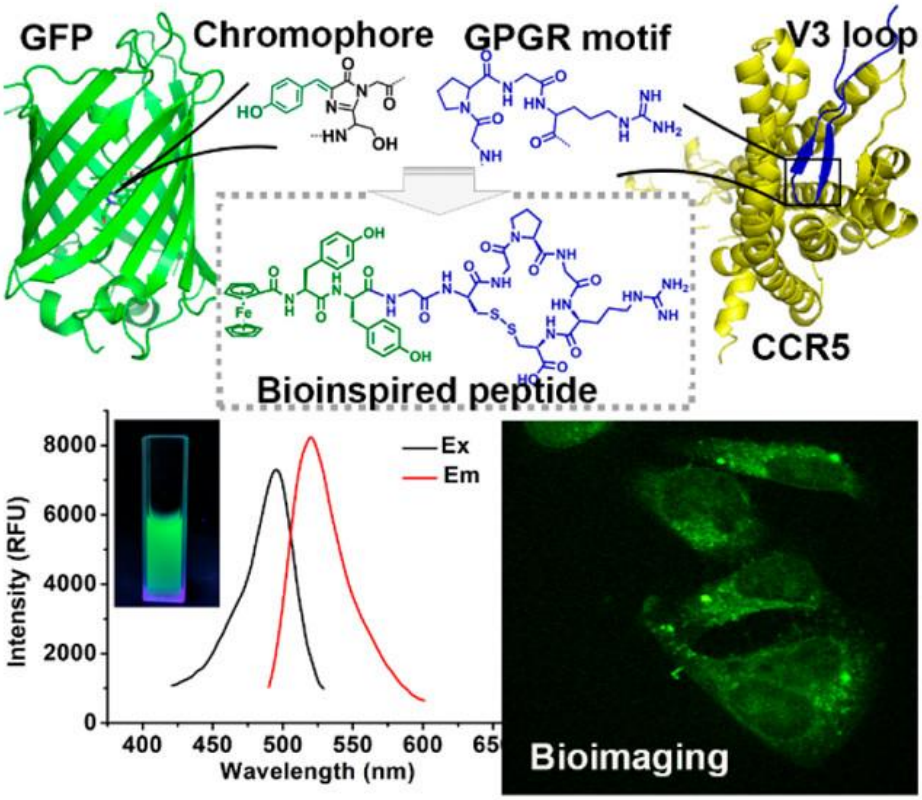

Figure 1.25 (a) GFP (green colored β-barrel, Protein Database (PDB) entry 1emb) and the chemical structure of its chromophore. Inspired by the chromophore of GFPs, bioinspired Tyr-Tyr (YY) dipeptides as the basic unit (green colored chemical structure) was designed. In addition, HIV V3 loop peptide (blue β-sheet, PDB ID: 5VN8) was docked with the C−C chemokine receptor type five (CCR5) receptor (yellow helix, PDB ID: 4MBS) and the GPGR motif in V3 tip was buried in the pocket of CCR5. Chemical structure of the GPGR motif was shown in blue

color. Chemical structure of Fc-YYGCGPGRC peptide. Fluorescence excitation (ex) and emission (em) spectra of cyclized Fc-YYGCGPGRC assemblies. Fluorescence intensity of HeLa cells when treated with tyrosine-based peptides (0.1 mg/mL) for 6 h. Reprinted with permission from ref. 264. Copyright (2020) American Chemical Society.

However, peptide-based fluorescent materials offer cell-penetrating ability and broad-spectrum biocompatibility and biodegradability.[263] Among the various amino acids, phenylalanine (F), tyrosine (Y) and tryptophan (W) are intrinsic fluorescent and their organized assembly can lead their fluorescence signal from ultraviolet to visible region with good quantum yield.[260] A simple dipeptide diphenylalanine (FF) self-assembled into various ordered structures and generated intense photoluminescence with emission maxima at λ_{em} = 450 nm.[264] Tryptophan-based aromatic cyclo-dipeptides were designed, which were subcutaneously injected in nude mice and showed distinct visible and NIR fluorescent signal.[265] Diphenylalanine (FF)-based green fluorescent probe was originated from the coassembly of amphiphilic Fc-FF-based peptides through the noncovalent interactions.[266] The enzyme-triggered intracellular self-assembly of aromatic hydrogelators exhibited strong photoluminescence signal inside the live cells.[267] Hydrogen peroxide (H_2O_2) is an oxidative stress marker and the presence of hydrogen peroxide is related to cancer disease that is determined by peptide-based fluorescence probe.[268] The tetrapeptide-based fluorescent probe for cancer cell imaging has been developed.[269] TPE-capped self-assembling tripeptides showed nanomolar response to toxic metal Hg^{2+} both in solution and living cells.[270] The cysteine containing peptide detected the Hg^{2+} ion through AIE phenomenon with strong blue fluorescence at 470 nm. The cell imaging experiment was performed using Hg^{2+}-preloaded HeLa cells and treated with peptides for 20 min. The peptide exhibited fast membrane permeability with good fluorescent signal due to binding with Hg^{2+} ion inside the cells. Additionally, the peptide showed in vivo Hg^{2+} sensing in the brain and periphery of eyes of zebrafish, which suggested that the peptide has the ability to penetrate the blood brain barrier.

1.7.9 Self-Assembling Peptides for 3D-Bioprinting

The printable biomaterials with appropriate mechanical strength and stiffness have revolutionized the design and development of various biological constructs.[271,272] Three-dimensional bioprinting of tissues and organs can replace the *in vivo* study for various consumer products and tissue specific drug trial for biocompatibility, toxicity and efficacy.[273] The bioprinting technique is rapidly growing for the preparation of 3D biological constructs for cell studies, drug testing and regenerative medicines. Particularly, hydrogels-based inks are suitable due to tunable mechanical strength and their similar cellular microenvironment for different biomedical applications.[274,275] Peptide-based hydrogels fulfill all the eligibility criteria for a bio-printable materials because of the resemblance to the

native cellular microenvironment.[276] Lysine-containing hexapeptides self-assembled to form strong and rigid nanofibrous hydrogels with stiffness up to 40 kPa. The biocompatible hexapeptide (Ac-ILVAGK-NH_2, Ac-LIVAGK-NH_2, Ac-AIVAGK-NH_2: Ac = acetyl; A = alanine; I = isoleucine; L = leucine; V = valine; G = glycine; K = lysine)-based hydrogel scaffolds supported the growth and proliferation of human stem cells. These hydrogels showed differentiation of primary cells into organotypic structures such as gastrointestinal and skin.[277]

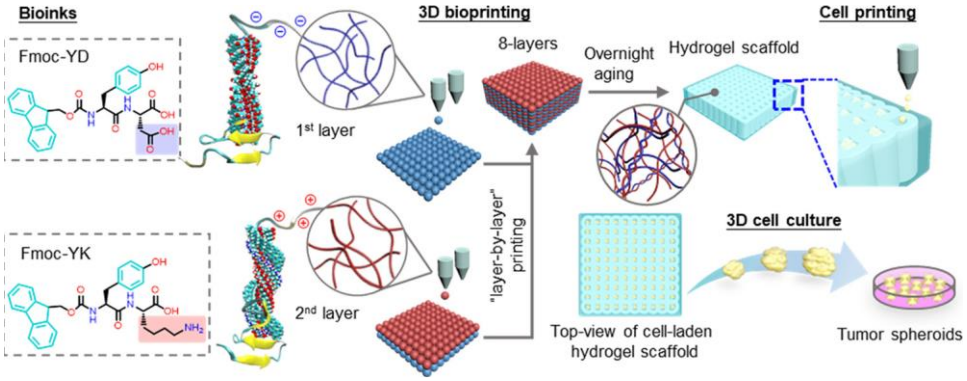

Figure 1.26 Schematic representations of a Fmoc-dipeptide-based bioink design, 3D bioprinting, and cell culture process for in vitro construction of tumor spheroid models. Reprinted with permission from ref. 278. Copyright (2019) American Chemical Society.

Recently, short self-assembled peptide hydrogels were exploited to mimic the ECM for 3D bioprinting applications (Figure 1.26).[278] In this report, oppositely charged binary peptides were bioprinted using layer-by-layer approach for biological construct. In another report, micelle mediated disulfide crosslinking of cysteine containing peptide (Fmoc-FFC) resulted into the printable hydrogel.[279] The peptide was solubilized in water by changing the pH 11 using 0.5 M NaOH solution. This peptide solution formed work-like micelle owing to the noncovalent interactions. The hydrogel was attributed from viscous peptide solution, which could be the reason of cross-linking between sulfhydryl group in alkaline aqueous solutions.

1.8 Organization of Thesis

This thesis work describes the basic understanding of supramolecular chemistry which is used as a tool for the programming of the chemical systems for the development well organized nanostructures. The thesis work presents Amoc group as N-terminus protecting group and their role in self-assembly. The N-terminal Amoc-capped dipeptides were used for the construction and fabrication of self-assembled soft biomaterials which were used for the antibacterial, anti-inflammatory and wound healing applications.

Chapter 2: This chapter includes the self-assembly of Amoc-capped dipeptides owing to the participation of noncovalent interactions which results into the biocompatible hydrogels for antibacterial applications.

Chapter 3: This chapter describe the anti-inflammatory applications of Amoc-capped dipeptide-based self-assembled thixotropic and biocompatible hydrogel in rat air pouch model of acute inflammation.

Chapter 4: This chapter present the coassembly of cyclodextrin and Amoc-capped dipeptides leads to formation of soft material which is used for the in vivo dermal wound healing applications.

Chapter 5: This chapter demonstrate the in vivo applications of Amoc-capped dipeptide-based coassembled hydrogel as wound dressing system.

Chapter 6: This chapter describe the general conclusion of the thesis work and scope for future work.

1.9 References

(1) Irwansyah I., Li Y. Q., Shi W., Qi D., Leow W. R., Tang M. B. Y., Li S., X. Chen X. (2015), Gram-positive antimicrobial activity of amino acid-based hydrogels, Adv. Mater., 27, 648–654 (DOI: 10.1002/adma.201403339).

(2) Qi Y., Min H., Mujeeb A., Zhang Y., Han X., Zhao X., Anderson G. J., Zhao Y., Nie, G. (2018), Injectable hexapeptide hydrogel for localized chemotherapy prevents breast cancer recurrence**,** ACS Appl. Mater. Interfaces, 10, 6972–6981 (DOI: 10.1021/acsami.7b19258).

(3) Clarke D. E., Parmenter C. D. J., Scherman O. A. (2018), tunable pentapeptide self-assembled β-sheet hydrogels, Angew. Chem., Int. Ed., 57, 7709–7713 (DOI: 10.1002/anie.201801001).

(4) Ren P., Li J., Zhao L., Wang A., Wang M., Li J., Jian H., Li X., Yan X., Bai S. (2020), Dipeptide self-assembled hydrogels with shear-thinning and instantaneous self-healing properties determined by peptide sequences**,** ACS Appl. Mater. Interfaces, 12, 21433–21440 (DOI: 10.1021/acsami.0c03038).

(5) Tang J. D., Roloson E. B., Amelung C. D., Lampe K. J. (2019), Rapidly Assembling Pentapeptides for Injectable Delivery (RAPID) Hydrogels as Cytoprotective Cell Carriers, ACS Biomater. Sci. Eng., 5, 2117–2121 (DOI: 10.1021/acsbiomaterials.9b00389).

(6) Chen C., Wang J., Hao R., Wang Z., Hou Z., Zhao Y., Zong C., Xu H., (2018), Transglutaminase-triggered gelation and functionalization of designed self-assembling peptides for guiding cell migration, ACS Appl. Bio Mater., 1, 2110–2119 (DOI: 10.1021/acsabm.8b00557).

(7) Zhao Y., Wang Z., Mei C., Jiang Z., Feng Y., Gao R., Wang Q., Huang J. (2018), Protein enables conformation transition of a hydrogel based on pentapeptide and boosts immune response in vivo, Bioconjugate Chem., 29, 1519–1524 (DOI: 10.1021/acs.bioconjchem.8b00044).

(8) Veloso S. R. S., Almeida B. G., Coutinho P. J. G., Castanheira E. M. S., Martins J. A., Jervis P. J., Ferreira P. M. T., Hilliou L., Amorim C. O., Amaral V. S., Jervis P. J., Moreira R., Pereira D. M., (2020), Dehydropeptide-based plasmonic

magnetogels: a supramolecular composite nanosystem for multimodal cancer therapy, J. Mater. Chem. B, 2019, 8, 45–64 (DOI: 10.1039/C9TB01900F).
(9) Das S., Kumar R., Jha N. N., Maji S. K. (2017), Controlled exposure of bioactive growth factor in 3D amyloid hydrogel for stem cells differentiation, Adv. Healthcare Mater., 6, 1700368 (DOI: 10.1002/adhm.201700368).
(10) Li Q., Jia Y., Dai L., Yang Y., Li J. (2015), Controlled rod nanostructured assembly of diphenylalanine and their optical waveguide properties, ACS Nano, 9, 2689–2695 (DOI: 10.1021/acsnano.5b00623).
(11) Chen J., Qin S., Wu X., Chu, P. K. (2016), Morphology and pattern control of diphenylalanine self-assembly *via* evaporative dewetting, ACS Nano, 10, 832–838 (DOI: 10.1021/acsnano.5b05936).
(12) Gong Z., Liu X., Dong J., Zhang W., Jiang Y., Zhang J., Feng W., Chen K., Bai J. (2019), Transition from vesicles to nanofibres in the enzymatic self-assemblies of an amphiphilic peptide as an antitumour drug carrier, Nanoscale, 11, 15479–15486 (10.1039/C9NR02874A).
(13) Lehn J. M. (2017), Supramolecular chemistry: where from? where to?, Chem. Soc. Rev., 46, 2378–2379 (DOI: 10.1039/c7cs00115k).
(14) Grimme S. (2008), Do special noncovalent π-π stacking interactions really exist?, Angew. Chem., Int. Ed., 47, 3430–3434 (DOI: 10.1002/anie.200705157).
(15) Uhlenheuer D. A., Petkau K., Brunsveld L. (2010), Combining supramolecular chemistry with biology, Chem. Soc. Rev., 39, 2817–2826 (DOI: 10.1039/b820283b).
(16) Mattia E., Otto S. (2015), Supramolecular systems chemistry, Nat. Nanotechnol., 10, 111–119 (DOI: 10.1038/nnano.2014.337).
(17) Tu Y., Peng F., Adawy A., Men Y., Abdelmohsen L. K. E. A., Wilson D. A., (2016), Mimicking the cell: bio-inspired functions of supramolecular assemblies**,** Chem. Rev., 116, 2023–2078 (DOI: 10.1021/acs.chemrev.5b00344).
(18) He Q., Huang D., Yang J., Huang Y., Wang S. (2019), Dual cross-link networks to preserve physical interactions induced by soaking methods: developing a strong and biocompatible protein-based hydrogel, ACS Appl. Bio Mater., 2, 3352–3361 (DOI: 10.1021/acsabm.9b00357).
(19) Li M., Ning Y., Chen J., Duan X., Song N., Ding D., Su X., Yu Z. (2019), Proline isomerization-regulated tumor microenvironment-adaptable self-assembly of peptides for enhanced therapeutic efficacy**,** Nano Lett., 19, 7965–7976 (DOI: 10.1021/acs.nanolett.9b03136).
(20) Wang Y., Matson J. B. (2019), Supramolecular nanostructures with tunable donor loading for controlled h_2s release, ACS Appl. Bio Mater., 2, 5093–5098 (DOI: 10.1021/acsabm.9b00768).
(21) Zheng D., Gao Z., Xu T., Liang C., Shi Y., Wang L., Yang Z. (2018), Responsive peptide-based supramolecular hydrogels constructed by self-immolative chemistry, Nanoscale, 10, 21459–21465 (DOI: 10.1039/C8NR07534D).
(22) Mello L. R., Aguiar R. B., Yamada R. Y., Moraes J. Z., Hamley I. W., Alves W. A., Reza M., Ruokolainen J., Silva E. R. (2020), Amphipathic design dictates

self-assembly, cytotoxicity and cell uptake of arginine-rich surfactant-like peptides, J. Mater. Chem. B, 8, 2495–2507 (DOI: 10.1039/C9TB02219H).
(23) Krieg E., Bastings M. M. C., Besenius P., Rybtchinski B. (2016), Supramolecular polymers in aqueous media, Chem. Rev., 116, 2414–2477 (DOI: 10.1021/acs.chemrev.5b00369).
(24) Gao J., Tang C., Elsawy M. A., Smith A. M., Miller A. F., Saiani A. (2017), Controlling self-assembling peptide hydrogel properties through network topology, Biomacromolecules, 18, 826–834 (DOI: 10.1021/acs.biomac.6b01693).
(25) Xing Q., Zhang J., Xie Y., Wang Y., Qi W., Rao H., Su R., He Z. (2018), Aromatic motifs dictate nanohelix handedness of tripeptides, ACS Nano, 12, 12305–12314 (DOI: 10.1021/acsnano.8b06173).
(26) Lian M., Chen X., Lu Y., Yang W. (2016), Self-assembled peptide hydrogel as a smart biointerface for enzyme-based electrochemical biosensing and cell monitoring, ACS Appl. Mater. Interfaces, 8, 25036–25042 (DOI: 10.1021/acsami.6b05409).
(27) Xiong Q., Jiang Y., Cai X., Yang F., Li Z., Han W. (2019), Conformation dependence of diphenylalanine self-assembly structures and dynamics: insights from hybrid-resolution simulations, ACS Nano, 13, 4455–4468 (DOI: 10.1021/acsnano.8b09741).
(28) Mason M. L., Lalisse R. F., Finnegan T. J., Hadad C. M., Modarelli D. A., Parquette J. R. (2019), pH-Controlled chiral packing and self-assembly of a coumarin tetrapeptide, Langmuir, 2019, 35, 12460–12468 (DOI: 10.1021/acs.langmuir.9b01939).
(29) Martin A. D., Wojciechowski J. P., Bhadbhade M. M., Thordarson P. (2016), A capped dipeptide which simultaneously exhibits gelation and crystallization behavior, Langmuir, 32, 2245–2250 (DOI: 10.1021/acs.langmuir.5b03963).
(30) Tan J., Zhang M., Hai Z., Wu C., Lin J., Kuang W., Tang H., Huang Y., Chen X., Liang G. (2019), Sustained release of two bioactive factors from supramolecular hydrogel promotes periodontal bone regeneration, ACS Nano, 13, 5616–5622 (DOI: 10.1021/acsnano.9b00788).
(31) Lian M., Xu L., Zhu X., Chen X., Yang W., Wang T. (2017), Seamless Signal Transduction from Three-Dimensional Cultured Cells to a Superoxide Anions Biosensor via In Situ Self-Assembly of Dipeptide Hydrogel, Anal. Chem., 89, 12843–12849 (DOI: 10.1021/acs.analchem.7b03371).
(32) Marchesan S., Styan K. E., Easton C. D., Waddington L., Vargiu A. V. (2015), Higher and lower supramolecular orders for the design of self-assembled heterochiral tripeptide hydrogel biomaterials, J. Mater. Chem. B, 3, 8123–8132 (DOI: 10.1039/C5TB00858A).
(33) Das S., Jacob R. S., Patel K., Singh N., Maji S. K. (2018), Amyloid fibrils: versatile biomaterials for cell adhesion and tissue engineering applications**,** Biomacromolecules, 19, 1826–1839 (DOI: 10.1021/acs.biomac.8b00279).
(34) Qian Y., Altamimi A., Yates S. A., Sarkar S., Cochran M., Zhou M., Levi-Polyachenko N., Matson J. B. (2020), H_2S-releasing amphiphilic dipeptide

hydrogels are potent *S. aureus* biofilm disruptors, Biomater. Sci., 8, 2564–2576 (DOI: 10.1039/D0BM00241K).
(35) Reja R. M., Patel R., Kumar V., Jha A., Gopi H. N. (2019), Divergent supramolecular gelation of backbone modified short hybrid δ-peptides, Biomacromolecules, 20, 1254–1262 (DOI: 10.1021/acs.biomac.8b01684).
(36) Zhao X., Pan F., Xu H., Yaseen M., Shan H., Hauser C. A. E., Zhang S., Lu J. R. (2010), Molecular self-assembly and applications of designer peptideamphiphiles, Chem. Soc. Rev., 39, 3480–3498 (DOI: 10.1039/B915923C).
(37) Jain R., Roy S. (2020), Controlling neuronal cell growth through composite laminin supramolecular hydrogels, ACS Biomater. Sci. Eng., 6, 2832–2846 (DOI: 10.1021/acsbiomaterials.9b01998).
(38) Aldilla V. R., Martin A. D., Nizalapur S., Marjo C. E., Rich A. M., Ho K. K. K., Ittner L. M., Black D. S. C., Thordarson P. Kumar N. (2018), Glyoxylamide-based self-assembly hydrogels for sustained ciprofloxacin delivery**,** J. Mater. Chem. B, 6, 6089–6098 (DOI: 10.1039/C8TB01290C).
(39) Bai J., Chen C., Wang J., Zhang Y., Cox H., Zhang J., Wang Y., Penny J., Waigh T., Lu J. R., Xu H. (2016), Enzymatic regulation of self-assembling peptide A_9K_2 nanostructures and hydrogelation with highly selective antibacterial activities, ACS Appl. Mater. Interfaces, 8, 15093–15102 (DOI: 10.1021/acsami.6b03770).
(40) Zhou P., Wang J., Wang M., Hou J., Lu J. R., Xu H. (2019), Amino acid conformations control the morphological and chiral features of the self-assembled peptide nanostructures: Young investigators perspective, J. Colloid Interface Sci., 548, 244–254 (DOI: 10.1016/j.jcis.2019.04.019).
(41) Restu W. K., Yamamoto S., Nishida Y., Ienaga H., Aoi T., Maruyama T. (2020), Hydrogel formation by short D-peptide for cell-culture scaffolds**,** Mater. Sci. Eng.: C., 111, 110746 (DOI: 10.1016/j.msec.2020.110746).
(42) Sahoo J. K., Nazareth C., Vandenberg M. A., Webber M. J. (2017), Self-assembly of amphiphilic tripeptides with sequence-dependent nanostructure**,** Biomater. Sci., 5, 1526–1530 (DOI: 10.1039/C7BM00304H).
(43) Karavasili C., Komnenou A., Katsamenis O. L., Charalampidou G., Kofidou E., Andreadis D., Koutsopoulos S., Fatouros D. G. (2017), Self-assembling peptide nanofiber hydrogels for controlled ocular delivery of timolol maleate, ACS Biomater. Sci. Eng., 3, 3386–3394 (DOI: 10.1021/acsbiomaterials.7b00706).
(44) Hu X., Liao M., Gong H., Zhang L., Cox H., Waigh T. A., Lu J. R. (2020), Recent advances in short peptide self-assembly: from rational design to novel applications, Curr. Opin. Colloid Interface Sci., 45, 1–13 (DOI: 10.1016/j.cocis.2019.08.003).
(45) Gao Y., Zhang C., Chang J., Yang C., Liu J., Fan S., Ren C. (2019), Enzyme-instructed self-assembly of a novel histone deacetylase inhibitor with enhanced selectivity and anticancer efficiency, Biomater. Sci., 7, 1477–1485 (DOI: 10.1039/C8BM01422A).
(46) Sun Y., Li W., Wu X., Zhang N., Zhang Y., Ouyang S., Song X., Fang X., Seeram R., Xue W., He L., Wu W. (2016), Functional self-assembling peptide

nanofiber hydrogels designed for nerve degeneration, ACS Appl. Mater. Interfaces, 8, 2348–2359 (DOI: 10.1021/acsami.5b11473).
(47) Saha P. C., Das R. S., Chatterjee T., Bhattacharyya M., Guha S. (2020), Supramolecular β-sheet forming peptide conjugated with near-infrared chromophore for selective targeting, imaging, and dysfunction of mitochondria**,** Bioconjugate Chem., 31, 1301−1306 (DOI: 10.1021/acs.bioconjchem.0c00153).
(48) Luo S., Feng J., Xiao L., Guo L., Deng L., Du Z., Xue Y., Song X., Sun X., Zhang Z., Fu Y., Gong T. (2020), Targeting self-assembly peptide for inhibiting breast tumor progression and metastasis, Biomaterials, 249, 120055 (DOI: 10.1016/j.biomaterials.2020.120055).
(49) Gong Z., Lao J., Gao F., Lin W., Yu T., Zhou B., Dong J., Liu H., Bai J. (2020), pH-Triggered geometrical shape switching of a cationic peptide nanoparticle for cellular uptake and drug delivery, Colloids Surf. B, 188, 110811 (DOI: 10.1016/j.colsurfb.2020.110811).
(50) Wang Q., Li X., Wang P., Yao Y., Xu Y., Chen Y., Sun Y., Jiang Q., Fan Y., Zhang X. (2020), Bionic composite hydrogel with a hybrid covalent/noncovalent network promoting phenotypic maintenance of hyaline cartilage, J. Mater. Chem. B, 8, 4402-4411 (DOI: 10.1039/D0TB00253D).
(51) Vilaça H., Hortelão A. C. L., Castanheira E. M. S., Queiroz M. J. R. P., Hilliou L., Hamley I. W., Martins J. A., Ferreira P. M. T. (2015), Dehydrodipeptide hydrogelators containing naproxen *n*-capped tryptophan: self-assembly, hydrogel characterization, and evaluation as potential drug nanocarriers, Biomacromolecules, 16, 3562–3573 (DOI: 10.1021/acs.biomac.5b01006).
(52) Cai Y., Shi Y., Wang H., Wang J., Ding D., Wang L., Yang Z. (2014), Environment-sensitive fluorescent supramolecular nanofibers for imaging applications, Anal. Chem., 86, 2193–2199 (DOI: 10.1021/ac4038653).
(53) Xu T., Liang C., Ji S., Ding D., Kong D., Wang L., Yang Z. (2016), Surface-induced hydrogelation for fluorescence and naked-eye detections of enzyme activity in blood, Anal. Chem., 88, 7318–7323 (DOI: 10.1021/acs.analchem.6b01660).
(54) Vilaça H., Castro T., Costa F. M. G., Melle-Franco M., Hilliou L., Hamley I. W., Castanheira E. M. S., Martins J. A., Ferreira P. M. T. (2017), Self-assembled RGD dehydropeptide hydrogels for drug delivery applications, J. Mater. Chem. B, 5, 8607–8617 (DOI: 10.1039/C7TB01883E).
(55) Mikhalevich V., Craciun I., Kyropoulou M., Palivan C. G., Meier W. (2017), Amphiphilic peptide self-assembly: expansion to hybrid materials, Biomacromolecules, 18, 3471–3480 (DOI: 10.1021/acs.biomac.7b00764).
(56) Li J., Xing R., Bai S., Yan X. (2019), Recent advances of self-assembling peptide-based hydrogels for biomedical applications, Soft Matter, 15, 1704–1715 (DOI: 10.1039/C8SM02573H).
(57) Hendricks M. P., Sato K., Palmer L. C., Stupp S. I. (2017), Supramolecular assembly of peptide amphiphiles, Acc. Chem. Res., 50, 2440–2448 (DOI: 10.1021/acs.accounts.7b00297).

(58) Diaferia C., Balasco N., Altamura D., Sibillano T., Gallo E., Roviello V., Giannini C., Morelli G., Vitagliano L., Accardo A. (2018), Assembly modes of hexaphenylalanine variants as function of the charge states of their terminal ends, Soft Matter, 14, 8219–8230 (DOI: 10.1039/C8SM01441H).
(59) Sahoo J. K., Nazareth C., VandenBerg M. A., Webber M. J. (2018), Aromatic identity, electronic substitution, and sequence in amphiphilic tripeptide self-assembly, Soft Matter, 14, 9168–9174 (DOI: 10.1039/C8SM01994K).
(60) Wang C., Wang Z., Zhang X. (2012), Amphiphilic building blocks for self-assembly: from amphiphiles to supra-amphiphiles, Acc. Chem. Res., 45, 608–618 (DOI: 10.1021/ar200226d).
(61) Martin A. D., Thordarson P. (2020), Beyond Fmoc: a review of aromatic peptide capping groups, J. Mater. Chem. B, 8, 863–877 (DOI: 10.1039/C9TB02539A).
(62) Meng Y., Jiang J., Liu M. (2017), Self-assembled nanohelix from a bolaamphiphilic diacetylene *via* hydrogelation and selective responsiveness towards amino acids and nucleobases, Nanoscale, 9, 7199–7206 (DOI: 10.1039/C7NR02126G).
(63) Lee C., Kim M. C., Lee S. Y. (2016), Hemoglobin-mimetic oxygen adsorbent prepared via self-assembly of cysteinyl bolaamphiphiles, Colloids Surfaces B Biointerfaces, 142, 360–366 (DOI: 10.1016/j.colsurfb.2016.03.012).
(64) Da Silva E. R., Walter M. N. M., Reza M., Castelletto V., Ruokolainen J., Connon C. J., Alves W. A., Hamley I. W. (2015), Self-assembled arginine-capped peptide bolaamphiphile nanosheets for cell culture and controlled wettability surfaces, Biomacromolecules, 16, 3180–3190 (DOI: 10.1021/acs.biomac.5b00820).
(65) Edwards-Gayle C. J. C., Castelletto V., Hamley I. W., Barrett G., Greco F., Hermida-Merino D., Rambo R. P., Seitsonen J., Ruokolainen J. (2019), self-assembly, antimicrobial activity, and membrane interactions of arginine-capped peptide bola-amphiphiles, ACS Appl. Bio Mater., 2, 2208–2218 (DOI: 10.1021/acsabm.9b00172).
(66) Nieto-Ortega B., Nebot V. J., Miravet J. F., Escuder B., Navarrete J. T. L., Casado J., Ramírez F. J., (2012), Vibrational circular dichroism shows reversible helical handedness switching in peptidomimetic l-valine fibrils, J. Phys. Chem. Lett., 3, 2120–2124 (DOI: 10.1021/jz300725d).
(67) Biswas S., Das A. K. (2019), Tuning the handedness: role of chiral component in peptide-appended bolaamphiphile-based coassembled hydrogels, Langmuir, 35, 2383-2391 (DOI: 10.1021/acs.langmuir.8b03651).
(68) Fleming S., Ulijn R. V. (2014), Design of nanostructures based on aromatic peptide amphiphiles, Chem. Soc. Rev., 43, 8150–8177 (DOI: 10.1039/C4CS00247D).
(69) Kwak J., Park S. I., Lee S. Y. (2013), Use of the self-assembly of tyrosine-containing bolaamphiphile molecules as a reactive template for metal deposition, Colloids Surf. B, 102, 70–75 (DOI: 10.1016/j.colsurfb.2012.07.038).

(70) Zheng C., Lin S., Chen Y., Li Y., Li B., Yang Y. (2019), *bola*-type Ala–Ala dipeptides: odd–even effect in molecular packing structures, Langmuir, 35, 11406–11413 (DOI: 10.1021/acs.langmuir.9b01241).
(71) Claussen R. C., Rabatic B. M., Stupp S. I. (2003), Aqueous self-assembly of unsymmetric peptide bolaamphiphiles into nanofibers with hydrophilic cores and surfaces, J. Am. Chem. Soc., 125, 12680–12681 (DOI: 10.1021/ja035882r).
(72) Maity I., Rasale D. B., Das A. K. (2012), Sonication induced peptide-appended bolaamphiphile hydrogels for *in situ* generation and catalytic activity of Pt nanoparticles, Soft Matter, 8, 5301–5308 (DOI: 10.1039/C2SM25126D).
(73) Chen L., Patrone N., Liang J. F. (2012), Peptide self-assembly on cell membranes to induce cell lysis, Biomacromolecules, 13, 3327–3333 (DOI: 10.1021/bm301106p).
(74) Muro-Small M. L., Chen J., McNeil A. J. (2011), Dissolution parameters reveal role of structure and solvent in molecular gelation, Langmuir, 27, 13248–13253 (DOI: 10.1021/la202702r).
(75) Isidro-Llobet A., Álvarez M., Albericio F. (2009), Amino acid-protecting groups, Chem. Rev., 109, 2455–2504 (DOI: 10.1021/cr800323s).
(76) Ryan D. M., Nilsson B. L. (2012), Self-assembled amino acids and dipeptides as noncovalent hydrogels for tissue engineering, Polym. Chem., 3, 18–33 (DOI: 10.1039/C1PY00335F).
(77) Dudukovic N. A., Zukoski C. F. (2014), Mechanical properties of self-assembled fmoc-diphenylalanine molecular gels, Langmuir, 30, 4493–4500 (DOI: 10.1021/la500589f).
(78) Xie Y., Wang X., Huang R., Qi W., Wang Y., Su R., He Z. (2015), Electrostatic and aromatic interaction-directed supramolecular self-assembly of a designed fmoc-tripeptide into helical nanoribbons, Langmuir, 31, 2885-2894 (DOI: 10.1021/la504757c).
(79) Rasale D. B., Das A. K. (2015), Chemical Reactions Directed Peptide Self-Assembly, Int. J. Mol. Sci., 16, 10797–10820 (DOI: 10.3390/ijms160510797).
(80) Das A. K., Bose P. P., Drew M. G. B., Banerjee A. (2007), The role of protecting groups in the formation of organogels through a nano-fibrillar network formed by self-assembling terminally protected tripeptides, Tetrahedron, 63, 7432-7442 (DOI: 10.1016/j.tet.2007.05.045).
(81) Li J., Du X., Hashim S., Shy A., Xu B. (2017), Aromatic–Aromatic Interactions Enable α-Helix to β-Sheet Transition of Peptides to Form Supramolecular Hydrogels, J. Am. Chem. Soc., 139, 71–74 (DOI: 10.1021/jacs.6b11512).
(82) Clemente M. J., Tejedor R. M., Romero P., Fitremann J., Oriol L. (2015), Photoresponsive supramolecular gels based on amphiphiles with azobenzene and maltose or polyethyleneglycol polar head, New J. Chem., 39, 4009–4019 (DOI: 10.1039/C4NJ02012J).
(83) Fleming S., Debnath S., Frederix P. W., Tuttle T., Ulijn R. V. (2013), Aromatic peptide amphiphiles: significance of the Fmoc moiety, Chem. Commun., 49, 10587-10589 (DOI: 10.1039/C3CC45822A).

(84) Draper E. R., Adams D. J. (2016), Photoresponsive gelators, Chem. Commun., 52, 8196–8206 (DOI: 10.1039/C6CC03485C).
(85) Chen L., Yang D., Feng J., Zhang M., Qian Q., Zhou Y. (2019), Switchable modulation of bacterial growth and biofilm formation based on supramolecular tripeptide amphiphiles, J. Mater. Chem. B, 7, 6420–6427 (DOI: 10.1039/C9TB00973F).
(86) Prakash G., Boopathy M., Selvam R., Johnsanthosh Kumar S., Subramanian K. (2018), The effect of anthracene-based chalcone derivatives in the resazurin dye reduction assay mechanisms for the investigation of Gram-positive and Gram-negative bacterial and fungal infection, New J. Chem., 42, 1037–1045 (DOI: 10.1039/C7NJ04125J).
(87) Yang Z., Liang G., Ma M., Gao Y., Xu B. (2007), Conjugates of naphthalene and dipeptides produce molecular hydrogelators with high efficiency of hydrogelation and superhelical nanofibers, J. Mater. Chem., 17, 850–854 (DOI: 10.1039/B611255B).
(88) Li M., Liu M., Shang Y., Ren C., Liu J., Jin H., Wang Z. (2020), The substitution of a single amino acid with its enantiomer for control over the adjuvant activity of self-assembling peptides, RSC Adv., 10, 13900–13906 (DOI: 10.1039/C9RA10325B).
(89) Cheng C., Tang M. C., Wu C. S., Simon T., Ko F. H. (2015), New Synthesis Route of Hydrogel through A Bioinspired Supramolecular Approach: Gelation, Binding Interaction, and in Vitro Dressing, ACS Appl. Mater. Interfaces, 7, 19306–19315 (DOI: 10.1021/acsami.5b05360).
(90) Rasale D. B., Maity I., Das A. K. (2012), Emerging π-stacked dynamic nanostructured library, RSC Adv., 2, 9791–9794 (DOI: 10.1039/C2RA21334F).
(91) Rasale D. B., Maity I., Konda M., Das A. K. (2013), Peptide self-assembly driven by oxo-ester mediated native chemical ligation, Chem. Commun., 49, 4815–4817 (DOI: 10.1039/C3CC41475B).
(92) Rasale D. B., Maity I., Das A. K. (2014), Lipase catalyzed inclusion of gastrodigenin for the evolution of blue light emitting peptide nanofibers, Chem. Commun., 50, 8685-8688 (DOI: 10.1039/C4CC02484B).
(93) Rasale D. B., Maity I., Das A. K. (2014), *In situ* generation of redox active peptides driven by selenoester mediated native chemical ligation, Chem. Commun., 50, 11397–11400 (DOI: 10.1039/C4CC03835E).
(94) Rasale D. B., Konda M., Biswas S., Das A. K. (2016), Controlling Peptide Self-Assembly through a Native Chemical Ligation/Desulfurization Strategy, Chem.-Asian J., 11, 926–935 (DOI: 10.1002/asia.201501458).
(95) Awhida S., Draper E. R., McDonald T. O., Adams D. J. (2015), Probing gelation ability for a library of dipeptide gelators, J. Colloid Interface Sci., 455, 24–31 (DOI: 10.1016/j.jcis.2015.05.032).
(96) Gavel P. K., Dev D., Parmar H. S., Bhasin S., Das A. K. (2018), Investigations of peptide-based biocompatible injectable shape-memory hydrogels: differential biological effects on bacterial and human blood cells, ACS Appl. Mater. Interfaces, 10, 10729-10740 (DOI: 10.1021/acsami.8b00501).

(97) Gavel P. K., Parmar H. S., Tripathi V., Kumar N., Biswas A., Das A. K. (2019), Investigations of anti-inflammatory activity of a peptide-based hydrogel using rat air pouch model, ACS Appl. Mater. Interfaces, 11, 2849-2859 (DOI: 10.1021/acsami.8b19228).
(98) P Gavel. K., Kumar N., Parmar H. S., Das A. K. (2020), Evaluation of a peptide-based coassembled nanofibrous and thixotropic hydrogel for dermal wound healing, ACS Appl. Bio Mater., 3, 3326–3336 (DOI: 10.1021/acsabm.0c00252).
(99) Sharma P., Kaur H., Roy S. (2019), Inducing differential self-assembling behavior in ultrashort peptide hydrogelators using simple metal salts, Biomacromolecules, 20, 2610–2624 (DOI: 10.1021/acs.biomac.9b00416).
(100) Debnath S., Roy S., Abul-Haija Y. M., Frederix P. W. J. M., Ramalhete S. M., Hirst A. R., Javid N., Hunt N. T., Kelly S. M., Angulo J., Khimyak Y. Z., Ulijn R. V. (2019), Tunable Supramolecular Gel Properties by Varying Thermal History, Chem. - Eur. J., 25, 7881–7887 (DOI: 10.1002/chem.201806281).
(101) Mayans E., Ballano G., Casanovas J., Díaz A., Pérez-Madrigal M. M., Estrany F., Puiggalí J., Cativiela C., Alemán C. (2015), Self-assembly of tetraphenylalanine peptides, Chem. - Eur. J., 21, 16895–16905 (DOI: 10.1002/chem.201501793).
(102) Criado-Gonzalez M., Wagner D., Rodon Fores J., Blanck C., Schmutz M., Chaumont A., Rabineau M., Schlenoff J. B., Fleith G., Combet J., Schaaf P., Jierry L., Boulmedais F. (2020), Supramolecular hydrogel induced by electrostatic interactions between polycation and phosphorylated-fmoc-tripeptide, Chem. Mater., 32, 1946–1956 (DOI: 10.1021/acs.chemmater.9b04823).
(103) Vegners R., Shestakova I., Kalvinsh I., Ezzell R. M., Janmey P. A. (1995), Use of a gel-forming dipeptide derivative as a carrier for antigen presentation, J. Pept. Sci., 1, 371–378 (DOI: 10.1002/psc.310010604).
(104) Zhang Y., Gu H., Yang Z., Xu B. (2003), Supramolecular hydrogels respond to ligand-receptor interaction, J. Am. Chem. Soc., 125, 13680–13681 (DOI: 10.1021/ja036817k).
(105) Vegners R., Shestakova I., Kalvinsh I., Ezzell R. M., Janmey P. A. (1995), Use of a gel-forming dipeptide derivative as a carrier for antigen presentation, J. Pept. Sci., 1, 371–378 (DOI: 10.1002/psc.310010604).
(106) Adams D. J., Butler M. F., Frith W. J., Kirkland M., Mullen L., Sanderson P. (2009), A new method for maintaining homogeneity during liquid–hydrogel transitions using low molecular weight hydrogelators, Soft Matter, 5, 1856–1862 (DOI: 10.1039/B901556F).
(107) Mahler A., Reches M., Rechter M., Cohen S., Gazit E. (2006), Rigid, self-assembled hydrogel composed of a modified aromatic dipeptide, Adv. Mater., 18, 1365–1370 (DOI: 10.1002/adma.200501765).
(108) Jayawarna V., Ali M., Jowitt T. A., Miller A. F., Saiani A., Gough J. E., Ulijn R. V. (2006), Nanostructured hydrogels for three-dimensional cell culture through self-assembly of fluorenylmethoxycarbonyl–dipeptides, Adv. Mater., 18, 611–614 (DOI: 10.1002/adma.200501522).

(109) Jayawarna V., Richardson S. M., Hirst A. R., Hodson N. W., Saiani A., Gough J. E., Ulijn R. V. (2009), Introducing chemical functionality in Fmoc-peptide gels for cell culture, Acta Biomater., 5, 934-943 (DOI: 10.1016/j.actbio.2009.01.006).
(110) Das A. K., Collins R., Ulijn R. V. (2008), Exploiting enzymatic (reversed) hydrolysis in directed self-assembly of peptide nanostructures, Small, 4, 279–287 (DOI: 10.1002/smll.200700889).
(111) Xu H., Das A. K., Horie M., Shaik M. S., Smith A. M., Luo Y., Lu X., Collins R., Liem S. Y., Song A., Popelier P. L. A., Turner M. L., Xiao P., Kinloch I. A., Ulijn R. V. (2010), An investigation of the conductivity of peptide nanotube networks prepared by enzyme-triggered self-assembly, Nanoscale, 2, 960–966 (DOI: 10.1039/B9NR00233B).
(112) Adhikari B., Banerjee A. (2010), Short-peptide-based hydrogel: a template for the in situ synthesis of fluorescent silver nanoclusters by using sunlight, Chem. - Eur. J., 16, 13698–13705 (DOI: 10.1002/chem.201001240).
(113) Nanda J., Banerjee A. (2012), β-Amino acid containing proteolitically stable dipeptide based hydrogels: encapsulation and sustained release of some important biomolecules at physiological pH and temperature, Soft Matter, 8, 3380–3386 (DOI: 10.1039/C2SM07168A).
(114) Chakraborty P., Tang Y., Yamamoto T., Yao Y., Guterman T., Zilberzwige-Tal S., Adadi N., Ji W., Dvir T., Ramamoorthy A., Wei G. (2020), Unusual two-step assembly of a minimalistic dipeptide-based functional hypergelator, Adv. Mater., 32, 1906043 (DOI: 10.1002/adma.201906043).
(115) Arakawa H., Takeda K., Higashi S. L., Shibata A., Kitamura Y., Ikeda M. (2020), Self-assembly and hydrogel formation ability of Fmoc-dipeptides comprising α-methyl-L-phenylalanine, Polym. J., 52, 923-930 (DOI: 10.1038/s41428-019-0301-5).
(116) Basavalingappa V., Guterman T., Tang Y., Nir S., Lei J., Chakraborty P., Schnaider L., Reches M., Wei G., Gazit E. (2019), Expanding the functional scope of the fmoc-diphenylalanine hydrogelator by introducing a rigidifying and chemically active urea backbone modification, Adv. Sci., 6, 1900218 (DOI: 10.1002/advs.201900218).
(117) Wang Y., Zhang Y., Li X., Li C., Yang Z., Wang L. (2018), A peptide-based supramolecular hydrogel for controlled delivery of amine drugs, Chem. - Asian J., 13, 3460–3463 (DOI: 10.1002/asia.201800708).
(118) Yang C., Chu L., Zhang Y., Shi Y., Liu J., Liu Q., Fan S., Yang Z., Ding D., Kong D., Liu J. (2015), Dynamic Biostability, Biodistribution, and Toxicity of l/d-Peptide-Based Supramolecular Nanofibers, ACS Appl. Mater. Interfaces, 7, 2735–2744 (DOI: 10.1021/am507800e).
(119) Xue Q., Ren H., Xu C., Wang G., Ren C., Hao J., Ding D. (2015), Nanospheres of doxorubicin as cross-linkers for a supramolecular hydrogelation, Sci. Rep., 5, 8764 (DOI: 10.1038/srep08764).
(120) Huang L., Wu C., Zhang L., Ma Z., Jia X. (2018), A mechanochromic and photochromic dual-responsive co-assembly with multicolored switch: a peptide-

based dendron strategy, ACS Appl. Mater. Interfaces, 10, 34475–34484 (DOI: 10.1021/acsami.8b10933).
(121) Gopikrishna P., Meher N., Iyer P. K. (2018), Functional 1,8-naphthalimide aie/aieegens: recent advances and prospects, ACS Appl. Mater. Interfaces, 10, 12081–12111 (DOI: 10.1021/acsami.7b14473).
(122) Felip-León C., Galindo F., Miravet J. F. (2018), Insights into the aggregation-induced emission of 1,8-naphthalimide-based supramolecular hydrogels, Nanoscale, 10, 17060–17069 (DOI: 10.1039/C8NR03755H).
(123) Yeh M. Y., Huang C. T., Lai T. S., Chen F. Y., Chu N. T., Tseng D. T. H., Hung S. C., Lin H. C. (2016), Effect of peptide sequences on supramolecular interactions of naphthaleneimide/tripeptide conjugates, Langmuir, 32, 7630–7638 (DOI: 10.1021/acs.langmuir.6b01809).
(124) Avinash M. B., Govindaraju T. (2012), Architectonics: design of molecular architecture for functional applications, Adv. Mater., 24, 3905–3922 (DOI: 10.1021/acs.accounts.7b00434).
(125) Li M., Liu M., Shang Y., Ren C., Liu J., Jin H., Wang Z. (2020),The substitution of a single amino acid with its enantiomer for control over the adjuvant activity of self-assembling peptides, RSC Adv. 13900–13906 (DOI: 10.1039/C9RA10325B).
(126) Ma M., Kuang Y., Gao Y., Zhang Y., Gao P., Xu B. (2010), Aromatic-aromatic interactions induce the self-assembly of pentapeptidic derivatives in water to form nanofibers and supramolecular hydrogels, J. Am. Chem. Soc., 132, 2719–2728 (DOI: 10.1021/ja9088764).
(127) Cheng C., Tang M. C., Wu C. S., Simon T., Ko F. H. (2015), New synthesis route of hydrogel through a bioinspired supramolecular approach: gelation, binding interaction, and in vitro dressing, ACS Appl. Mater. Interfaces, 7, 19306–19315 (DOI: 10.1021/acsami.5b05360).
(128) Yao X., Liu Y., Gao J., Yang L., Mao D., Stefanitsch C., Li Y., Zhang J., Ou L., Kong D., Zhao Q., Li Z. (2015), Nitric oxide releasing hydrogel enhances the therapeutic efficacy of mesenchymal stem cells for myocardial infarction, Biomaterials, 60, 130–140 (DOI: 10.1016/j.biomaterials.2015.04.046).
(129) Jain R., Khandelwal G., Roy S. (2019), Unraveling the design rules in ultrashort amyloid-based peptide assemblies toward shape-controlled synthesis of gold nanoparticles, Langmuir, 35, 5878–5889 (DOI: 10.1021/acs.langmuir.8b04020).
(130) Wang H., Yang C., Tan M., Wang L., Kong D., Yang Z. (2011), A structure–gelation ability study in a short peptide-based 'Super Hydrogelator' system, Soft Matter, 7, 3897–3905 (DOI: 10.1039/C0SM01405B).
(131) Liang R., Luo Z., Pu G., Wu W., Shi S., Yu J., Zhang Z., Chen H., Li X. (2016), Self-assembled peptide-based supramolecular hydrogel for ophthalmic drug delivery, RSC Adv., 6, 76093–76098 (DOI: 10.1039/C6RA11691D).
(132) Fleming S., Debnath S., Frederix P. W. J. M., Hunt N. T., Ulijn R. V. (2014), Insights into the coassembly of hydrogelators and surfactants based on aromatic

peptide amphiphiles, Biomacromolecules, 15, 1171–1184 (DOI: 10.1021/bm401720z).
(133) Reddy S. M. M., Dorishetty P., Augustine G., Deshpande A. P., Ayyadurai N., Shanmugam G. (2017), A low-molecular-weight gelator composed of pyrene and fluorene moieties for effective charge transfer in supramolecular ambidextrous gel, Langmuir, 33, 13504–13514 (DOI: 10.1021/acs.langmuir.7b03453).
(134) Madhu C., Roy B., Makam P., Govindaraju T. (2018), Bicomponent β-sheet assembly of dipeptide fluorophores of opposite polarity and sensitive detection of nitro-explosives, Chem. Commun., 54, 2280–2283 (DOI: 10.1039/C8CC00158H).
(135) Maiti B., Bhattacharjee S., Bhattacharya S. (2019), Perfluoroarene induces a pentapeptidic hydrotrope into a pH-tolerant hydrogel allowing naked eye sensing of Ca^{2+} ions, Nanoscale, 11, 2223–2230 (DOI: 10.1039/C8NR08126C).
(136) Kim I., Jeong H. H., Kim Y. J., Lee N. E., Huh K. M., Lee C. S., Kim G. H., Lee E. (2014), A “Light-up” 1D supramolecular nanoprobe for silver ions based on assembly of pyrene-labeled peptide amphiphiles: cell-imaging and antimicrobial activity, J. Mater. Chem. B, 2, 6478–6486 (DOI: 10.1039/C4TB00892H).
(137) Balachandra C., Govindaraju T. (2020), Cyclic dipeptide-guided aggregation-induced emission of naphthalimide and its application for the detection of phenolic drugs, J. Org. Chem., 85, 1525–1536 (DOI: 10.1021/acs.joc.9b02580).
(138) Rhoden Smith A., Iverson B. L. (2013), Threading polyintercalators with extremely slow dissociation rates and extended dna binding sites, J. Am. Chem. Soc., 135, 12783–12789 (DOI: 10.1021/ja4057344).
(139) Ikkanda B. A., Iverson B. L. (2016), Exploiting the interactions of aromatic units for folding and assembly in aqueous environments, Chem. Commun., 52, 7752–7759 (DOI: 10.1039/C6CC01861K).
(140) Chen Y., Li T., Li J., Cheng S., Wang J., Verma C., Zhao Y., Wu C. (2017), Stabilization of peptides against proteolysis through disulfide-bridged conjugation with synthetic aromatics, Org. Biomol. Chem., 15, 1921–1929 (DOI: 10.1039/C6OB02786E).
(141) Hsu S.M., Wu F.Y., Cheng H., Huang Y.T., Hsieh Y.R., Tseng D.T.H., Yeh M.Y., Hung S.C., Lin H.C. (2016), Functional supramolecular polymers: A fluorescent microfibrous network in a supramolecular hydrogel for high-contrast live cell-material imaging in 3D environments, Adv. Healthcare Mater., 5, 2406–2412 (DOI: 10.1002/adhm.201600342).
(142) Singha N., Gupta P., Pramanik B., Ahmed S., Dasgupta A., Ukil A., Das D. (2017), Hydrogelation of a naphthalene diimide appended peptide amphiphile and its application in cell imaging and intracellular pH sensing, Biomacromolecules, 18, 3630–36410 (DOI: 10.1021/acs.biomac.7b01048).
(143) Nelli S.R., Lin J.H., Nguyen T.N.A., Tseng D.T.H., Talloj S.K., Lin H.C. (2017), Influence of amino acid side chains on the formation of two component

self-assembling nanofibrous hydrogels, New J. Chem., 41, 1229–1234 (DOI: 10.1039/C6NJ02820A).
(144) Zhan F.K., Hsu S.M., Cheng H., Lin H.C. (2015), Remarkable influence of alkyl chain lengths on supramolecular hydrogelation of naphthalene diimide-capped dipeptides, RSC Adv., 5, 48961–48964 (DOI: 10.1039/C5RA05373K).
(145) Pandeeswar M., Khare H., Ramakumar S., Govindaraju T. (2014), Biomimetic molecular organization of naphthalene diimide in the solid state: tunable (chiro-) optical, viscoelastic and nanoscale properties, RSC Adv., 4, 20154–20163 (DOI: 10.1039/C3RA47257D).
(146) Fu Y., Li B., Huang Z., Li Y., Yang Y. (2013), Terminal is important for the helicity of the self-assemblies of dipeptides derived from alanine, Langmuir, 29, 6013–6017 (DOI: 10.1021/la400910g).
(147) Lin S., Qin J., Li Y., Li B., Yang Y. (2017), Chirality-driven parallel and antiparallel β-sheet secondary structures of Phe–Ala lipodipeptides, Langmuir, 33, 8246–8252 (DOI: 10.1021/acs.langmuir.7b01942).
(148) Matsumoto Y., Shundo A., Ohno M., Tsuruzoe N., Goto M., Tanaka K. (2017), Evolution of heterogeneity accompanying sol–gel transitions in a supramolecular hydrogel, Soft Matter, 13, 7433–7440 (DOI: 10.1039/C7SM01612C).
(149) Restu W.K., Nishida Y., Yamamoto S., Ishii J., Maruyama T. (2018), Short oligopeptides for biocompatible and biodegradable supramolecular hydrogels, Langmuir, 34, 8065–8074 (DOI: 10.1021/acs.langmuir.8b00362).
(150) Hutchinson J.A., Hamley I.W., Edwards-Gayle C.J., Castelletto V., Piras C., Cramer R., Kowalczyk R., Seitsonen J., Ruokolainen J., Rambo R.P. (2019), Melanin production by tyrosinase activity on a tyrosine-rich peptide fragment and pH-dependent self-assembly of its lipidated analogue, Org. Biomol. Chem., 17, 4543-4553 (DOI: 10.1039/C9OB00550A).
(151) Martí-Centelles R., Escuder B. (2018), Morphology diversity of L-phenylalanine-based short peptide supramolecular aggregates and hydrogels, Chem Nano Mat, 4, 796–800 (DOI: 10.1002/cnma.201800202).
(152) Adak A., Ghosh S., Gupta V., Ghosh S. (2019), Biocompatible lipopeptide-based antibacterial hydrogel, Biomacromolecules, 20, 1889–1898 (DOI: 10.1021/acs.biomac.8b01836).
(153) Hu T., Zhang Z., Hu H., Euston S.R., Pan S. (2020), A comprehensive study on self-assembly and gelation of C_{13}-dipeptides-from design strategies to functionalities, Biomacromolecules, 21, 670-679 (DOI: 10.1021/acs.biomac.9b01386).
(154) Pelin J.N.B.D., Edwards-Gayle C.J.C., Castelletto V., Aguilar A.M., Alves W.A., Seitsonen J., Ruokolainen J., Hamley I.W. (2020), Self-assembly, nematic phase formation, and organocatalytic behavior of a proline-functionalized lipopeptide, ACS Appl. Mater. Interfaces, 12, 13671–13679 (DOI: 10.1021/acsami.0c00686).
(155) Castelletto V., Edwards-gayle C.J.C., Greco F., Hamley I.W., Seitsonen J., Ruokolainen J. (2019), Self-assembly, tunable hydrogel properties, and selective

anticancer activity of a carnosine-derived lipidated peptide, ACS Appl. Mater. Interfaces, 11, 33573–33580 (DOI: 10.1021/acsami.9b09065).
(156) Bairagi D., Biswas P., Basu K., Hazra S., Hermida-Merino D., Sinha D.K., Hamley I.W., Banerjee A. (2019), Self-assembling peptide-based hydrogel: regulation of mechanical stiffness and thermal stability and 3D cell culture of fibroblasts, ACS Appl. Bio Mater., 2, 5235–5244 (DOI: 10.1021/acsabm.9b00424).
(157) Zhou S., Hokugo A., Mc Clendon M., Zhang Z., Bakshi R., Wang L., Segovia L.A., Rezzadeh K., Stupp S.I., Jarrahy R. (2019), Bioactive peptide amphiphile nanofiber gels enhance burn wound healing, Burns, 45, 1112–1121 (DOI: 10.1016/j.burns.2018.06.008).
(158) Godbe J.M., Freeman R., Burbulla L.F., Lewis J., Krainc D., Stupp S.I. (2020), Gelator length precisely tunes supramolecular hydrogel stiffness and neuronal phenotype in 3D culture, ACS Biomater. Sci. Eng., 6, 1196–1207 (DOI: 10.1021/acsbiomaterials.9b01585).
(159) Greenfield M.A., Hoffman J.R., De La Cruz M.O., Stupp S.I. (2010), Tunable mechanics of peptide nanofiber gels, Langmuir, 26, 3641–3647 (DOI: 10.1021/la9030969).
(160) Wang D., Zhang X., Li H., Luan Y., Wei G., Wang J. (2019), Anticancer properties of lipidated peptide drug supramolecular self-assemblies with enhanced stability, ACS Appl. Bio Mater., 2, 5995–6003 (DOI: 10.1021/acsabm.9b00913).
(161) Nandi N., Gayen K., Ghosh S., Bhunia D., Kirkham S., Sen S.K., Ghosh S., Hamley I.W., Banerjee A. (2017), Amphiphilic peptide-based supramolecular, noncytotoxic, stimuli-responsive hydrogels with antibacterial activity, Biomacromolecules, 18, 3621–3629 (DOI: 10.1021/acs.biomac.7b01006).
(162) Shimizu T., Ding W., Kameta N. (2020), Soft-matter nanotubes: A platform for diverse functions and applications, Chem. Rev., 120, 2347–2407 (DOI: 10.1021/acs.chemrev.9b00509).
(163) Konda M., Jadhav R.G., Maity S., Das A.K. (2018), Redox-active peptide-functionalized quinquethiophene-based electrochromic π-gel, Chem.-Asian J., 13, 204-209 (DOI: 10.1002/asia.201701460).
(164) Maity I., Mukherjee T.K., Das A.K. (2014), Photophysical study of a π-stacked β-sheet nanofibril forming peptide bolaamphiphile hydrogel, New J. Chem., 38, 376-385 (DOI: 10.1039/C3NJ00814B).
(165) Maity I., Rasale D.B., Das A.K. (2013), Exploiting a self-assembly driven dynamic nanostructured library, RSC Adv., 3, 6395-6400 (DOI: 10.1039/C3RA22401E).
(166) Bhattacharya A., Bhowmik S., Singh A.K., Kodgire P., Das A.K., Mukherjee T.K. (2017), Direct evidence of intrinsic blue fluorescence from oligomeric interfaces of human serum albumin, Langmuir, 33, 10606-10615 (DOI: 10.1021/acs.langmuir.7b02463).
(167) Mukai M., Minamikawa H., Aoyagi M., Asakawa M., Shimizu T., Kogiso M. (2013), A hydro/organo/hybrid gelator: A peptide lipid with turning aspartame

head groups, J. Colloid Interface Sci., 395, 154–160 (DOI: 10.1016/j.jcis.2012.12.060).
(168) Maity I., Manna M.K., Rasale D.B., Das A.K. (2014), Peptide-nanofiber-supported palladium nanoparticles as an efficient catalyst for the removal of N-terminus protecting groups, Chem Plus Chem, 79, 413-420 (DOI: 10.1002/cplu.201300348).
(169) Maity I., Rasale D.B., Das A.K. (2014), Peptide nanofibers decorated with Pd nanoparticles to enhance the catalytic activity for C–C coupling reactions in aerobic conditions, RSC Adv., 4, 2984-2988 (DOI: 10.1039/C3RA44787A).
(170) Das A.K., Maity I., Parmar H.S., McDonald T.O., Konda M. (2015), Lipase-catalyzed dissipative self-assembly of a thixotropic peptide bolaamphiphile hydrogel for human umbilical cord stem-cell proliferation, Biomacromolecules, 16, 1157–1168 (DOI: 10.1021/bm501835v).
(171) Dou X., Mehwish N., Zhao C., Liu J., Xing C., Feng C. (2020), Supramolecular hydrogels with tunable chirality for promising biomedical applications, Acc. Chem. Res., 53, 852-862 (DOI: 10.1021/acs.accounts.0c00012).
(172) Huang G., Li F., Zhao X., Ma Y., Li Y., Lin M., Jin G., Lu T.J., Genin G.M., Xu F. (2017), Functional and biomimetic materials for engineering of the three-dimensional cell microenvironment, Chem. Rev., 117, 12764–12850 (DOI: 10.1021/acs.chemrev.7b00094).
(173) Ghosh M., Halperin-Sternfeld M., Grigoriants I., Lee J., Nam K.T., Adler-Abramovich L. (2017), Arginine-presenting peptide hydrogels decorated with hydroxyapatite as biomimetic scaffolds for bone regeneration, Biomacromolecules, 18, 3541–3550 (DOI: 10.1021/acs.biomac.7b00876).
(174) Eckes K.M., Baek K., Suggs L.J. (2018), Design and evaluation of short self-assembling depsipeptides as bioactive and biodegradable hydrogels, ACS Omega, 3, 1635–1644 (DOI: 10.1021/acsomega.7b01641).
(175) Zhou M., Smith A.M., Das A.K., Hodson N.W., Collins R.F., Ulijn R.V., Gough J.E. (2009), Self-assembled peptide-based hydrogels as scaffolds for anchorage-dependent cells, Biomaterials, 30, 2523–2530 (DOI: 10.1016/j.biomaterials.2009.01.010).
(176) Scelsi A., Bochicchio B., Smith A., Workman V.L., Castillo Diaz L.A., Saiani A., Pepe A. (2019), Tuning of hydrogel stiffness using a two-component peptide system for mammalian cell culture, J. Biomed. Mater. Res., Part A, 107, 535–544 (DOI: 10.1002/jbm.a.36568).
(177) Sharma P., Kaur H., Roy S. (2019), Designing a tenascin-C-inspired short bioactive peptide scaffold to direct and control cellular behavior, ACS Biomater. Sci. Eng., 5, 6497–6510 (DOI: 10.1021/acsbiomaterials.9b01115).
(178) Wang H., Cui J., Zheng Z., Shi Q., Sun T., Liu X., Huang Q., Fukuda T. (2017), Assembly of RGD-modified hydrogel micromodules into permeable three-dimensional hollow micro tissues mimicking in vivo tissue structures, ACS Appl. Mater. Interfaces, 9, 41669–41679 (DOI: 10.1021/acsami.7b10960).

(179) Misra R., Sharma A., Shiras A., Gopi H.N. (2017), Backbone engineered γ-peptide amphitropic gels for immobilization of semiconductor quantum dots and 2D cell culture, Langmuir, 33, 7762–7768 (DOI: 10.1021/acs.langmuir.7b01283).
(180) Liebmann T., Rydholm S., Akpe V., Brismar H. (2007), Self-assembling Fmoc dipeptide hydrogel for *in situ* 3D cell culturing, BMC Biotechnol., 7, 88-92 (DOI: 10.1186/1472-6750-7-88).
(181) Tang J.D., Mura C., Lampe K.J. (2019), Stimuli-responsive, pentapeptide, nanofiber hydrogel for tissue engineering, J. Am. Chem. Soc., 141, 4886–4899 (DOI: 10.1021/jacs.8b13363).
(182) Jain R., Roy S. (2019), Designing a bioactive scaffold from coassembled collagen–laminin short peptide hydrogels for controlling cell behavior, RSC Adv., 9, 38745–38759 (DOI: 10.1039/c9ra07454f).
(183) Cringoli M.C., Romano C., Parisi E., Waddington L.J., Melchionna M., Semeraro S., De Zorzi R., Grönholm M., Marchesan S. (2020), Bioadhesive supramolecular hydrogel from unprotected, short D,L-peptides with Phe-Phe and Leu-Asp-Val motifs, Chem. Commun., 56, 3015–3018 (DOI: 10.1039/C9CC09947F).
(184) Liu Y., Song M., Ding S., Zhu K. (2019), Discovery of linear low-cationic peptides to target methicillin-resistant *staphylococcus aureus* in vivo, ACS Infect. Dis., 5, 123–130 (DOI: 10.1021/acsinfecdis.8b00230).
(185) Chen C., Hu J., Zeng P., Chen Y., Xu H., Lu J.R. (2014), High cell selectivity and low-level antibacterial resistance of designed amphiphilic peptide G(IIKK)$_3$I-NH_2, ACS Appl. Mater. Interfaces, 6, 16529–16536 (DOI: 10.1021/am504973d).
(186) Malhotra K., Shankar S., Rai R., Singh Y. (2018), Broad-spectrum antibacterial activity of proteolytically stable self-assembled αγ-hybrid peptide gels, Biomacromolecules, 19, 782–792 (DOI: 10.1021/acs.biomac.7b01582).
(187) Schnaider L., Brahmachari S., Schmidt N.W., Mensa B., Shaham-Niv S., Bychenko D., Adler-Abramovich L., Shimon L.J.W., Kolusheva S., Degrado W.F., Gazit E. (2017), Self-assembling dipeptide antibacterial nanostructures with membrane disrupting activity, Nat. Commun., 8, 1365 (DOI: 10.1038/s41467-017-01447-x).
(188) Baral A., Roy S., Ghosh S., Hermida-Merino D., Hamley I.W., Banerjee A. (2016), A peptide-based mechano-sensitive, proteolytically stable hydrogel with remarkable antibacterial properties, Langmuir, 32, 1836–1845 (DOI: 10.1021/acs.langmuir.5b03789).
(189) Debnath S., Shome A., Das D., Das P.K. (2010), Hydrogelation through self-assembly of Fmoc-peptide functionalized cationic amphiphiles: Potent antibacterial agent, J. Phys. Chem. B, 114, 4407–4415 (DOI: 10.1021/jp909520w).
(190) Brogden K.A. (2005), Antimicrobial peptides: Pore formers or metabolic inhibitors in bacteria? Nat. Rev. Microbiol., 3, 238–250 (DOI: 10.1038/nrmicro1098).
(191) Rodrigues De Almeida N., Han Y., Perez J., Kirkpatrick S., Wang Y., Sheridan M.C. (2019), Design, synthesis, and nanostructure-dependent

antibacterial activity of cationic peptide amphiphiles, ACS Appl. Mater. Interfaces, 11, 2790–2801 (DOI: 10.1021/acsami.8b17808).
(192) Gong H., Zhang J., Hu X., Li Z., Fa K., Liu H., Waigh T.A., McBain A., Lu J.R. (2019), Hydrophobic control of the bioactivity and cytotoxicity of de novo-designed antimicrobial peptides, ACS Appl. Mater. Interfaces, 11, 34609–34620 (DOI: 10.1021/acsami.9b10028).
(193) Argudo P.G., Contreras-Montoya R., Álvarez De Cienfuegos L., Martín-Romero M.T., Camacho L., Giner-Casares J.J. (2019), Optimization of amino acid sequence of Fmoc-dipeptides for interaction with lipid membranes, J. Phys. Chem. B, 123, 3721–3730 (DOI: 10.1021/acs.jpcb.9b01132).
(194) Chen C., Yang C., Chen Y., Wang F., Mu Q., Zhang J., Li Z., Pan F., Xu H., Lu J.R. (2016), Surface physical activity and hydrophobicity of designed helical peptide amphiphiles control their bioactivity and cell selectivity, ACS Appl. Mater. Interfaces, 8, 26501–26510 (DOI: 10.1021/acsami.6b08297).
(195) Qi R., Zhang N., Zhang P., Zhao H., Liu J., Cui J., Xiang J., Han Y., Wang S., Wang Y. (2020), Gemini peptide amphiphiles with broad-spectrum antimicrobial activity and potent antibiofilm capacity, ACS Appl. Mater. Interfaces, 12, 17220–17229 (DOI: 10.1021/acsami.0c01167).
(196) Edwards-Gayle C.J.C., Barrett G., Roy S., Castelletto V., Seitsonen J., Ruokolainen J., Hamley I.W. (2020), Selective antibacterial activity and lipid membrane interactions of arginine-rich amphiphilic peptides, ACS Appl. Bio Mater., 3, 1165–1175 (DOI: 10.1021/acsabm.9b00894).
(197) Liu K., Yang L., Peng X., Wang J., Lu J.R., Xu H. (2020), Modulation of antimicrobial peptide conformation and aggregation by terminal lipidation and surfactants, Langmuir, 36, 1737–1744 (DOI: 10.1021/acs.langmuir.9b03774).
(198) Porter S.L., Coulter S.M., Pentlavalli S., Thompson T.P., Laverty G. (2018), Self-assembling diphenylalanine peptide nanotubes selectively eradicate bacterial biofilm infection, Acta Biomater., 77, 96–105 (DOI: 10.1016/j.actbio.2018.07.033).
(199) Xu D., Chen W., Tobin-Miyaji Y.J., Sturge C.R., Yang S., Elmore B., Singh A., Pybus C., Greenberg D.E., Sellati T.J., Qiang W., Dong H. (2018), Fabrication and microscopic and spectroscopic characterization of cytocompatible self-assembling antimicrobial nanofibers, ACS Infect. Dis., 4, 1327–1335 (DOI: 10.1021/acsinfecdis.8b00069).
(200) Makovitzki A., Avrahami, D., Shai, Y. (2006), Ultrashort antibacterial and antifungal lipopeptides,Proc. Natl. Acad. Sci. U. S. A.,103, 15997–16002 (DOI: 10.1073/pnas.0606129103).
(201) Thota C. K., Berger A. A., Harms B., Seidel M., Böttcher C., Berlepsch H. von, Xie C., Süssmuth R., Roth C., Koksch B. (2020), Short self-assembling cationic antimicrobial peptide mimetics based on a 3,5-diaminobenzoic acid scaffold, Pept. Sci., 112, 1–9 (DOI: 10.1002/pep2.24130).
(202) Mittal S., Kaur S., Swami A., Maurya I. K., Jain R., Wangoo N., Sharma R. K. (2016), Alkylated histidine based short cationic antifungal peptides: synthesis,

biological evaluation and mechanistic investigations, RSC Adv., 6, 41951–41961 (DOI: 10.1039/C6RA05883C).
(204) Patel K. D., De Zoysa G. H., Kanamala M., Patel K., Pilkington L. I., Barker D., Reynisson J., Wu Z., Sarojini V. (2020), Novel cell-penetrating peptide conjugated proteasome inhibitors: anticancer and antifungal investigations, J. Med. Chem., 63, 334–348 (DOI: 10.1021/acs.jmedchem.9b01694).
(205) Mahindra A., Sharma K. K., Rathore D., Khan S. I., Jacob M. R., Jain R. (2014), Synthesis and antimicrobial activities of His(2-aryl)-Arg and Trp-His(2-aryl) classes of dipeptidomimetics, Med. Chem.Comm., 5, 671–676 (DOI: 10.1039/C4MD00041B).
(206) Wu H., Liu S., Wiradharma N., Ong Z. Y., Li Y., Yang Y. Y., Ying J. Y. (2017), Short synthetic α-helical-forming peptide amphiphiles for fungal keratitis treatment in vivo, Adv. Healthcare Mater., 6, 1600777 (DOI: 10.1002/adhm.201600777).
(207) Stensen W., Turner R., Brown M., Kondori N., Svendsen J. S., Svenson J. (2016), Short cationic antimicrobial peptides display superior antifungal activities toward candidiasis and onychomycosis in comparison with terbinafine and amorolfine, Mol. Pharmaceutics, 13, 3595–3600 (DOI: 10.1021/acs.molpharmaceut.6b00654).
(208) Dadar M., Shahali Y., Chakraborty S., Prasad M., Tahoori F., Tiwari R., Dhama K. (2019), Anti-inflammatory peptides: current knowledge and promising prospects, Inflamm. Res., 68, 125–145 (DOI: 10.1007/s00011-018-1208-x).
(209) Kalluri J. R., West J., Akkaraju G. R., Canham L. T., Coffer J. L. (2019), Plant-derived tandem drug/mesoporous silicon microcarrier structures for anti-inflammatory therapy, ACS Omega, 4, 8359–8364 (DOI: 10.1021/acsomega.9b00127).
(210) Li J., Kuang Y., Gao Y., Du X., Shi J., Xu B. (2013), D-Amino acids boost the selectivity and confer supramolecular hydrogels of a nonsteroidal anti-inflammatory drug (NSAID), J. Am. Chem. Soc., 135, 542–545 (DOI: 10.1021/ja310019x).
(211) Singh P., Kaur S., Kaur J., Singh G., Bhatti R. (2016), Rational design of small peptides for optimal inhibition of cyclooxygenase-2: development of a highly effective anti-inflammatory agent, J. Med. Chem., 59, 3920–3934 (DOI: 10.1021/acs.jmedchem.6b00134).
(212) Ricciotti E., Fitzgerald G. A. (2011), Prostaglandins and inflammation, Arter. Thromb. Vasc. Biol., 31, 986–1000 (DOI: 10.1161/atvbaha.110.207449).
(213) Singh P., Prasher P., Dhillon P., Bhatti R. (2015), Indole based peptidomimetics as anti-inflammatory and anti-hyperalgesic agents: Dual inhibition of 5-LOX and COX-2 enzymes, Eur. J. Med. Chem., 97, 104–123 (DOI: 10.1016/j.ejmech.2015.04.044).
(214) Kaur B., Kaur M., Kaur N., Garg S., Bhatti R., Singh P. (2019), Engineered substrate for cyclooxygenase-2: a pentapeptide isoconformational to arachidonic acid for managing inflammation, J. Med. Chem., 62, 6363–6376 (DOI: 10.1021/acs.jmedchem.9b00823).

(215) Memic A., Abudula T., Mohammed H. S., Joshi Navare K., Colombani T., Bencherif S. A. (2019), Latest progress in electrospun nanofibers for wound healing applications, ACS Appl. Bio Mater., 2, 952–969 (DOI: 10.1021/acsabm.8b00637).
(216) Sekhon U. D. S., Sen Gupta A. (2018), Platelets and platelet-inspired biomaterials technologies in wound healing applications, ACS Biomater. Sci. Eng., 4, 1176–1192 (DOI: 10.1021/acsbiomaterials.7b00013).
(217) Li Y., Han Y., Wang X., Peng J., Xu Y., Chang J. (2017), Multifunctional hydrogels prepared by dual ion cross-linking for chronic wound healing, ACS Appl. Mater. Interfaces, 9, 16054–16062 (DOI: 10.1021/acsami.7b04801).
(218) Xi Y., Ge J., Guo Y., Lei B., Ma P. X. (2018), Biomimetic elastomeric polypeptide-based nanofibrous matrix for overcoming multidrug-resistant bacteria and enhancing full-thickness wound healing/skin regeneration, ACS Nano, 12, 10772–10784 (DOI: 10.1021/acsnano.8b01152).
(219) Qu J., Zhao X., Liang Y., Zhang T., Ma P. X., Guo B. (2018), Antibacterial adhesive injectable hydrogels with rapid self-healing, extensibility and compressibility as wound dressing for joints skin wound healing, Biomaterials, 183, 185–199 (DOI: 10.1016/j.biomaterials.2018.08.044).
(220) Zhu J., Han H., Li F., Wang X., Yu J., Qin X., Wu D. (2019), Peptide-functionalized amino acid-derived pseudoprotein-based hydrogel with hemorrhage control and antibacterial activity for wound healing, Chem. Mater., 31, 4436–4450 (DOI: 10.1021/acs.chemmater.9b00850).
(221) Zhang F., Hu C., Kong Q., Luo R., Wang Y. (2019), Peptide-/drug-directed self-assembly of hybrid polyurethane hydrogels for wound healing, ACS Appl. Mater. Interfaces, 11, 37147–37155 (DOI: 10.1021/acsami.9b13708).
(222) Senturk B., Mercan S., Delibasi T., Guler M. O., Tekinay A. B. (2016), Angiogenic peptide nanofibers improve wound healing in stz-induced diabetic rats, ACS Biomater. Sci. Eng., 2, 1180–1189 (DOI: 10.1021/acsbiomaterials.6b00238).
(223) Gomes A., Teixeira C., Ferraz R., Prudencio C., Gomes P. (2017), Wound-healing peptides for treatment of chronic diabetic foot ulcers and other infected skin injuries, Molecules, 22, 1743 (DOI: 10.3390/molecules22101743).
(224) Stern D., Cui H. (2019), Crafting polymeric and peptidic hydrogels for improved wound healing, Adv. Healthcare Mater., 8, 1900104 (DOI: 10.1002/adhm.201900104).
(225) Meng H., Chen L., Ye Z., Wang S., Zhao X. (2009), The effect of a self-assembling peptide nanofiber scaffold (peptide) when used as a wound dressing for the treatment of deep second degree burns in rats, J. Biomed. Mater. Res. Part B Appl. Biomater., 89, 379–391 (DOI: 10.1002/jbm.b.31226).
(226) Wang S. Y., Kim H., Kwak G., Yoon H. Y., Jo S. D., Lee J. E., Cho D., Kwon I. C., Kim S. H. (2018), Development of biocompatible ha hydrogels embedded with a new synthetic peptide promoting cellular migration for advanced wound care management, Adv. Sci., 5, 1800852 (DOI: 10.1002/advs.201800852).

(227) Wei Q., Duan J., Ma G., Zhang W., Wang Q., Hu Z. (2019), Enzymatic crosslinking to fabricate antioxidant peptide-based supramolecular hydrogel for improving cutaneous wound healing, J. Mater. Chem. B, 7, 2220–2225 (DOI: 10.1039/c8tb03147a).
(228) Sharma S., Kulkarni C., Kulkarni M.M., Ali R., Porwal K., Chattopadhyay N., Tewari D., Verma S. (2020), Tripeptide-induced modulation of mesenchymal stem cell biomechanics stimulates proliferation and wound healing, Chem. Commun., 56, 3043-3046 (DOI: 10.1039/c9cc10043a).
(229) Zhao C.-C., Zhu L., Wu Z., Yang R., Xu N., Liang L. (2020), Resveratrol-loaded peptide-hydrogels inhibit scar formation in wound healing through suppressing inflammation, Regen. Biomater., 7, 99-107 (DOI: 10.1093/rb/rbz041).
(230) Siegel R. L., Miller K. D., Jemal A. (2019), Cancer statistics, 2019, Cancer J. Clin., 69, 7–34 (DOI: 10.3322/caac.21551).
(231) Zhou L., Qiu T., Lv F., Liu L., Ying J. Wang S. (2018), Self-assembled nanomedicines for anticancer and antibacterial applications, Adv. Healthcare Mater., 7, 1800670 (DOI: 10.1002/adhm.201800670).
(232) Wang H., Feng Z., Xu B. (2017), D-amino acid-containing supramolecular nanofibers for potential cancer therapeutics, Adv. Drug Deliv. Rev., 110–111, 102–111 (DOI: 10.1016/j.addr.2016.04.008).
(233) Gao Y., Long M. J. C., Shi J., Hedstrom L., Xu B. (2012), Using supramolecular hydrogels to discover the interactions between proteins and molecular nanofibers of small molecules, Chem. Commun., 48, 8404–8406 (DOI: 10.1039/c2cc33631f).
(234) Yang Z., Xu K., Guo Z. F., Guo Z. H., Xu B. (2007), Intracellular enzymatic formation of nanofibers results in hydrogelation and regulated cell death, Adv. Mater., 19, 3152–3156 (DOI: 10.1002/adma.200701971).
(235) Huang W., Seo J., Willingham S. B., Czyzewski A. M., Gonzalgo M. L., Weissman I. L., Barron A. E. (2014), Learning from host-defense peptides: cationic, amphipathic peptoids with potent anticancer activity, PLoS One, 9, e90397 (DOI: 10.1371/journal.pone.0090397).
(236) Kuang Y., Xu B. (2013), Disruption of the dynamics of microtubules and selective inhibition of glioblastoma cells by nanofibers of small hydrophobic molecules, Angew. Chem. Int. Ed., 52, 6944–6948 (DOI: 10.1002/ange.201302658).
(237) He H., Lin X., Guo J., Wang J., Xu B. (2020), Perimitochondrial enzymatic self-assembly for selective targeting the mitochondria of cancer cells, ACS Nano, 6, 6947–6955, (DOI:10.1021/acsnano.0c01388).
(238) Wang H., Feng Z., Wang Y., Zhou R., Yang Z., Xu B. (2016), Integrating enzymatic self-assembly and mitochondria targeting for selectively killing cancer cells without acquired drug resistance, J. Am. Chem. Soc., 138, 16046–16055 (DOI: 10.1021/jacs.6b09783).
(239) Jeena M. T., Jeong K., Go E. M., Cho Y., Lee S., Jin S., Hwang S. W., Jang J. H., Kang C. S., Bang W. Y., Lee E., Kwak S. K., Kim S., Ryu J. H. (2019),

Heterochiral assembly of amphiphilic peptides inside the mitochondria for supramolecular cancer therapeutics, ACS Nano, 13, 11022–11033 (DOI: 10.1021/acsnano.9b02522).
(240) Toft D. J., Moyer T. J., Standley S. M., Ruff Y., Ugolkov A., Stupp S. I., Cryns V. L. (2012), Coassembled cytotoxic and pegylated peptide amphiphiles form filamentous nanostructures with potent antitumor activity in models of breast cancer, ACS Nano, 6, 7956–7965 (DOI: 10.1021/nn302503s).
(241) Yang L., Zhang C., Ren C., Liu J., Zhang Y., Wang J., Huang F., Zhang L., Liu J. (2019), Supramolecular hydrogel based on chlorambucil and peptide drug for cancer combination therapy, ACS Appl. Mater. Interfaces, 11, 331–339 (DOI: 10.1021/acsami.8b18425).
(242) Ren C., Gao Y., Guan Y., Wang Z., Yang L., Gao J., Fan H. Liu J. (2019), Carrier-free supramolecular hydrogel composed of dual drugs for conquering drug resistance, ACS Appl. Mater. Interfaces, 11, 33706–33715 (DOI: 10.1021/acsami.9b12530).
(243) Xing R., Li S., Zhang N., Shen G., Möhwald H., Yan X. (2017), Self-assembled injectable peptide hydrogels capable of triggering antitumor immune response, Biomacromolecules, 18, 3514–3523 (DOI: 10.1021/acs.biomac.7b00787).
(244) Wang Z., Liang C., Shi F., He T., Gong C., Wang L., Yang Z. (2017), Cancer vaccines using supramolecular hydrogels of NSAID-modified peptides as adjuvants abolish tumorigenesis, Nanoscale, 9, 14058–14064 (DOI: 10.1039/c7nr04990k).
(245) Oyen E., Martin C., Caveliers V., Madder A., Van Mele B., Hoogenboom R., Hernot S., Ballet S. (2017), In vivo imaging of the stability and sustained cargo release of an injectable amphipathic peptide-based hydrogel, Biomacromolecules, 18, 994–1001 (DOI: 10.1021/acs.biomac.6b01840).
(246) Zarzhitsky S., Rapaport H. (2011), The interactions between doxorubicin and amphiphilic and acidic β-sheet peptides towards drug delivery hydrogels, J. Colloid Interface Sci., 360, 525–531 (DOI: 10.1016/j.jcis.2011.04.091).
(247) Gupta P., Vermani K., Garg S. (2002), Hydrogels: from controlled release to pH-responsive drug delivery, Drug Discov. Today, 7, 569–579 (DOI: 10.1016/s1359-6446(02)02255-9).
(248) Eskandari S., Guerin T., Toth I., Stephenson R. J. (2017), Recent advances in self-assembled peptides: Implications for targeted drug delivery and vaccine engineering, Adv. Drug Deliv. Rev., 110–111, 169–187 (DOI: 10.1016/j.addr.2016.06.013).
(249) Raymond D. M., Abraham B. L., Fujita T., Watrous M. J., Toriki E. S., Takano T., Nilsson B. L. (2019), Low-molecular-weight supramolecular hydrogels for sustained and localized in vivo drug delivery, ACS Appl. Bio Mater., 2, 2116–2124 (DOI: 10.1021/acsabm.9b00125).
(250) Hoare T. R., Kohane D. S. (2008), Hydrogels in drug delivery: Progress and challenges, Polymer, 49, 1993–2007 (DOI: 10.1016/j.polymer.2008.01.027).

(251) Baral A., Roy S., Dehsorkhi A., Hamley I. W., Mohapatra S., Ghosh S. Banerjee A. (2014), Assembly of an injectable noncytotoxic peptide-based hydrogelator for sustained release of drugs, Langmuir, 30, 929–936 (DOI: 10.1021/la4043638).
(252) Naskar J., Palui G., Banerjee A. (2009), Tetrapeptide-based hydrogels: for encapsulation and slow release of an anticancer drug at physiological pH, J. Phys. Chem. B, 113, 11787–11792 (DOI: 10.1021/jp904251j).
(253) Kalafatovic D., Nobis M., Javid N., Frederix P. W. J. M., Anderson K. I., Saunders B. R., Ulijn R. V. (2015), MMP-9 triggered micelle-to-fibre transitions for slow release of doxorubicin, Biomater. Sci., 3, 246–249 (DOI: 10.1039/C4BM00297K).
(254) Bibian M., Mangelschots J., Gardiner J., Waddington L., Diaz Acevedo M. M., De Geest B. G., Van Mele B., Madder A., Hoogenboom R., Ballet S. (2015), Rational design of a hexapeptide hydrogelator for controlled-release drug delivery, J. Mater. Chem. B, 3, 759–765 (DOI: 10.1039/C4TB01294A).
(255) S. Dhawan, S. Ghosh, R. Ravinder, S. S. Bais, S. Basak, Krishnan N. M. A., Agarwal M., Banerjee M., Haridas V. (2019), Redox sensitive self-assembling dipeptide for sustained intracellular drug delivery, Bioconjugate Chem., 30, 2458–2468 (DOI: 10.1021/acs.bioconjchem.9b00532).
(256) Cinar G., Ozdemir A., Hamsici S., Gunay G., Dana A., Tekinay A. B., Guler M. O. (2017), Local delivery of doxorubicin through supramolecular peptide amphiphile nanofiber gels, Biomater. Sci., 5, 67–76 (DOI: 10.1039/C6BM00656F).
(257) Ma Y., Shi L., Liu F., Zhang Y., Pang Y., Shen X. (2019), Self-assembled thixotropic silver cluster hydrogel for anticancer drug release, Chem. Eng. J., 362, 650–657 (DOI: 10.1016/j.cej.2019.01.096).
(258) Gao Y., Liehr S., Cooperman B. S. (2002), Affinity-driven selection of tripeptide inhibitors of ribonucleotide reductase, Bioorganic Med. Chem. Lett., 12, 513–515 (DOI: 10.1016/S0960-894X(01)00790-9).
(259) Liu K., Xing R., Zou Q., Ma G., Möhwald H., Yan X. (2016), Simple peptide-tuned self-assembly of photosensitizers towards anticancer photodynamic therapy, Angew. Chem. Int. Ed., 55, 3036–3039 (DOI: 10.1002/anie.201509810).
(260) Fan Z., Sun L., Huang Y., Wang Y., Zhang M. (2016), Bioinspired fluorescent dipeptide nanoparticles for targeted cancer cell imaging and real-time monitoring of drug release, Nat. Nanotechnol., 11, 388–394 (DOI: 10.1038/nnano.2015.312).
(261) Mehwish N., Dou X., Zhao Y., Feng C. L. (2019), Supramolecular fluorescent hydrogelators as bio-imaging probes, Mater. Horizons, 6, 14–44 (DOI: 10.1039/C8MH01130C).
(262) Kong J., Zhang J., Wang Y.,Qi W., Rao H., Hu L., Su R., He Z. (2020), Bioinspired pH-sensitive fluorescent peptidyl nanoparticles for cell imaging, ACS Appl. Mater. Interfaces, 12, 4212–4220 (DOI: 10.1021/acsami.9b17866).
(263) Liu Y. H., Hsu S. M., Wu F. Y., Cheng H.,Yeh M. Y., Lin H. C. (2014), Electroactive organic dye incorporating dipeptides in the formation of self-assembled nanofibrous hydrogels, Bioconjugate Chem., 25, 1794–1800 (DOI: 10.1021/bc500299c).

(264) Gan Z., Xu H. (2017), Photoluminescence of diphenylalanine peptide nano/microstructures: from mechanisms to applications, Macromol. Rapid Commun., 38, 1700370 (DOI: 10.1002/marc.201700370).

(265) Tao K., Fan Z., Sun L., Makam P., Tian Z., Ruegsegger M., Shaham-Niv S., Hansford D., Aizen R., Pan Z., Galster S., Ma J., Yuan F., Si M., Qu S., Zhang M., Gazit E. Li J. (2018), Quantum confined peptide assemblies with tunable visible to near-infrared spectral range, Nat. Commun., 9, 3217 (DOI: 10.1038/s41467-018-05568-9).

(266) Kong J., Wang Y., Qi W., Su R., He Z. (2019), Photo- and aromatic stacking-induced green emissive peptidyl nanoparticles for cell imaging and monitoring of nucleic acid delivery, ACS Appl. Mater. Interfaces, 11, 15401–15410 (DOI: 10.1021/acsami.9b03945).

(267) Gao Y., Shi J., Yuan D., B. Xu, Imaging enzyme-triggered self-assembly of small molecules inside live cells, Nat. Commun., 2012, 3, 1033 (DOI: 10.1038/ncomms2040).

(268) Zhao P., Wang K., Zhu X., Zhou Y., Wu J. (2018), A fluorescent probe for imaging hydrogen peroxide in ovarian cancer cells, Dye. Pigment., 155, 143–149 (DOI: 10.1016/j.dyepig.2018.03.038).

(269) Ding W. Q., Qin S. Y., Cheng Y. J., Ma Y. H., Zhang A. Q. (2018), Novel oligopeptide nanoprobe for targeted cancer cell imaging, RSC Adv.,8, 30887–30893 (DOI: 10.1039/C8RA06034G).

(270) Gui S.,Huang Y., Hu F., Jin Y., G. Zhang G., Zhang D., Zhao R. (2018), Bioinspired peptide for imaging hg^{2+} distribution in living cells and zebrafish based on coordination-mediated supramolecular assembling, Anal. Chem., 90, 9708–9715 (DOI: 10.1021/acs.analchem.8b00059).

(271) Murphy S. V., tala A. (2014), 3D bioprinting of tissues and organs, Nat. Biotechnol., 32, 773–785 (DOI: 10.1038/nbt.2958).

(272) Pospišil T., Ferhatović Hamzić L., Brkić Ahmed L., Lovrić M., Gajović S., Frkanec L. (2016), Synthesis, characterization and *in vitro* biocompatibility assessment of a novel tripeptide hydrogelator, as a promising scaffold for tissue engineering applications, Biomater. Sci., 4, 1412–1416 (DOI: 10.1039/C6BM00287K).

(273) Guvendiren M., Molde J., Soares R. M. D., Kohn J. (2016), Designing biomaterials for 3D printing, ACS Biomater. Sci. Eng., 2, 1679–1693 (DOI: 10.1021/acsbiomaterials.6b00121).

(274) Highley C. B., Rodell C. B., Burdick J. A. (2015), Direct 3D printing of shear-thinning hydrogels into self-healing hydrogels, Adv. Mater., 27, 5075–5079 (DOI: 10.1002/adma.201501234).

(275) Loo Y., Zhang S., Hauser C. A. E. (2012), From short peptides to nanofibers to macromolecular assemblies in biomedicine, Biotechnol. Adv., 30, 593–603 (DOI: 10.1016/j.biotechadv.2011.10.004).

(276) Almohammed S., Alruwaili M., Reynaud E. G., Redmond G.,Rice J. H., Rodriguez B. J. (2019), 3D-printed peptide-hydrogel nanoparticle composites for surface-enhanced raman spectroscopy sensing, ACS Appl. Nano Mater., 2, 5029–5034 (DOI: 10.1021/acsanm.9b00940).

(277) Loo Y., Lakshmanan A., Ni M., Toh L. L., Wang S. and Hauser C. A. E. (2015), Peptide bioink: self-assembling nanofibrous scaffolds for three-dimensional organotypic cultures, Nano Lett., 15, 6919–6925 (DOI: 10.1021/acs.nanolett.5b02859).
(278) Jian H., Wang M., Dong Q., Li J., Wang A., Li X., Ren P., Bai S. (2019), Dipeptide self-assembled hydrogels with tunable mechanical properties and degradability for 3D bioprinting, ACS Appl. Mater. Interfaces, 11, 46419–46426.
(279) Yang X., Wang Y., Qi W., Xing R., Yang X., Xing Q., Su R., He Z. (2019), Disulfide crosslinking and helical coiling of peptide micelles facilitate the formation of a printable hydrogel, J. Mater. Chem. B, 7, 2981–2988 (DOI: 10.1039/C8TB03121E).

Chapter 2

Investigations of Peptide-Based Biocompatible Injectable Shape-Memory Hydrogels: Differential Biological Effects on Bacterial and Human Blood Cells

2.1 Introduction

A great attention has been paid for the construction of highly biocompatible and biodegradable soft functional materials because of their significant use in the area of tissue engineering, wound dressing, drug delivery, and bacterial infection therapy.[1−10] In recent years, peptide-based low-molecular weight hydrogels (LMWHs) have attracted considerable attention in the area of bacterial infection therapy. Several polylysine,[11] cationic,[12−14] silver-containing,[15,16] antibioticbound,[17] and proteolytically stable[18] antibacterial hydrogels have been reported over past few decades. Antibacterial hydrogels are composed of hydrophobic and cationic residues, which disrupt the lipid bilayer in the cell membrane leading to the bacterial cell death.[19,20] Despite their bactericidal effectiveness, polycationic-based polymeric hydrogels require tedious purification process, which also causes cytotoxicity toward the animal cells.[21] As a result, overuse of antibiotic-integrated hydrogel materials potentially causes serious health issues and may result in the growth of antibiotic-resistance bacteria. In general, antibacterial hydrogels are designed by doping antibacterial agents to the hydrogels, which possess antibacterial activity for biomedical applications. In a doped system, the antibacterial agent is slowly released from the hydrogel surface and the hydrogels remain inactive over time.[22] In particular, inherent antibacterial hydrogels inhibit bacterial growth upon physical contact of bacteria on the hydrogel surface.[23,24] Additionally, the viscoelastic similarities of the hydrogel materials with soft tissues made them a promising candidate in the area of tissue engineering. Tissue engineering is involved in the development of regenerative alternatives to implant synthetic or natural tissues and organs that can restore and work as a normal function.[25-27] Different strategies were used for tissue or organ regeneration but the demanding approach utilizes the combination of desired cells with hydrogel materials.[28] In this regard, injectable hydrogels with good biocompatibility are used for tissue engineering because of their minimal invasive applications.[29,30] Several injectable hydrogels and biomimetic materials are reported to serve as a synthetic and artificial extracellular matrix, which provide a favorable microenvironment for cell growth and proliferation.[31−34] The key advantage of injectable hydrogel materials is that they have potential to adopt any desired size and shape of a cavity for tissue engineering applications. Peptide-based injectable hydrogels must fulfill a few basic requirements that have been considered in tissue engineering applications such as noncytotoxicity, hydrophilicity, biodegradability, and less immunogenicity or antigenicity of scaffold materials. Besides their biocompatibility, the injectable hydrogels must show quick gel-sol-gel transitions and the mechanical properties of the injectable hydrogels must retain quickly after injection to the target site.[35,36] Hydrogels are very prone to bacterial infection because of their moist environment.[37] Biomaterial-mediated infection retards cell and tissue regeneration, which results in significant numbers of implant-associated infections at the target site.[38] Hydrogels with inherent antibacterial activity that prevent secondary infections

and promote cell growth, differentiations, and/or proliferation are necessitating candidates for cell and tissue culture experiments.[39] Nevertheless, to improve biological effectiveness and to eliminate bacterial contamination during the tissue and cell culture experiments, hydrogels are sterilized by using UV irradiation or ethylene oxide treatment. Sterilization of hydrogel materials significantly changes their physical/chemical properties.[40] However, injectable and biocompatible LMWHs with inherent antibacterial properties for tissue and cell regeneration applications are very limited. Thus, the synthesis and preparation of an injectable and biocompatible hydrogel itself possess antibacterial property, which would hold great promise for localized bacterial infection, cell culture, and tissue regeneration applications. In the present work, our objectives include the development of: (a) peptide-based injectable and robust; (b) antibacterial; (c) noncytotoxic; (d) self-healing; (e) shape-memory; and (f) antioxidative hydrogels. In this consideration, we have synthesized a class of Amoc (9-anthracenemethoxycarbonyl)-capped dipeptide amphiphiles, which formed self-healing injectable hydrogels by the involvement of H-bonding and π-π stacking interactions of the gelator molecules. These self-supporting hydrogels show antibacterial property and promote cell viability and/or proliferations of human white blood cells (hWBCs). These hydrogels significantly decrease oxidative stress on human red blood cells (hRBCs) and provide cellular stability against oxidative stress.

2.2 Experimental Section

2.2.1 Materials and Methods

Anthracene-2-methanol and 4-nitro-phenyl chloroformate were purchased from Sigma-Aldrich, U.S.A. Amino acids, diisopropylcarbodiimide (DIPC), and 1-hydroxybenzotriazole (HOBt) were purchased from SRL chemicals, India, and used without further purification. All solvents were analytical grade, purchased from Merck chemicals and distilled prior to use. Thin-layer chromatography was performed on precoated silica gel plates (Kieselgel 60 F, Merck). Column chromatography was performed on silica gel (100−200 mesh size). Chemicals for biological experiments such as peptone, yeast extract, agar powder, sodium chloride, and 3-(4,5-dimethythiazol-2-yl)2,5-diphenyl tetrazolium bromide (MTT) assay kit were purchased from HiMedia Laboratories Pvt. Ltd., India. Trichloroacetic acid, Triton X-100, and thiobarbituric acids were purchased from Sigma-Aldrich, U.S.A. NMR spectroscopy was performed in $CDCl_3$ and DMSO-d_6 on a Bruker AV 400 MHz spectrometer. Chemical shifts (d) are reported in ppm, downfield of tetramethylsilane; peak multiplicities are reported as follows: singlet (s), doublet (d), doublet of doublets (dd), triplet (t), quartet (q), and multiplet (m). Fourier-transform infrared (FTIR) spectroscopy was performed on KBr pellets on a Bruker Tensor 27 FTIR spectrophotometer. Electrospray ionization mass spectrometry was acquired on a Bruker micrOTOF-Q II mass spectrometer.

2.2.2 Synthesis of 1 and 2

Scheme 2.1 Synthetic pathway of **1** and **2**

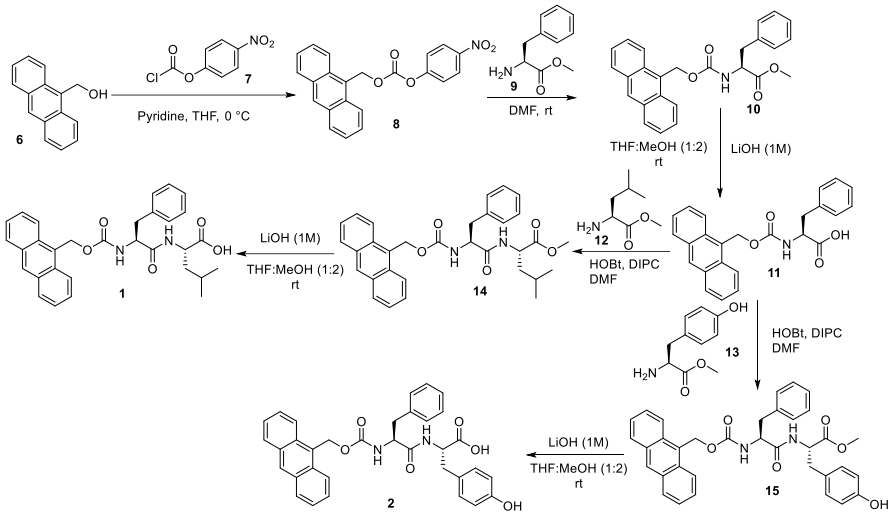

2.2.2.1 Synthesis of 8

7 (1.5 g, 7.44 mmol) was solubilized in dry THF under N_2 atmosphere. The solution was ice-cooled and pyridine (0.648 g, 8.18 mmol) was added into the cold solution. The white slurry was obtained after the addition of pyridine. **6** (1.29 g, 6.2 mmol) was solubilized in dry THF and the solution was added into the reaction mixture. The reaction mixture was allowed to stir (12 h) at room temperature. Product conversion was checked by TLC. THF was evaporated by a rotary evaporator. The reaction mixture was diluted with EtOAc (50 mL) and the mixture was washed with 1 M HCl (3 × 30 mL). The yellow-green product was obtained by evaporating the solvent under reduced pressure. The product was recrystallized by using benzene and yellow needle-shaped crystal of **8** was further used for the synthesis of **1** and **2**.

Yield: 1.7 g (73%). ^{1}H NMR (400 MHz, $CDCl_3$): δ = 8.58 (s, 1H, Amoc), 8.42-8.40 (d, *J* = 8.88 Hz, 2Hs, Ph), 8.26- 8.24 (d, *J*= 8.44 Hz, 2Hs, Amoc), 8.08-8.06 (d, *J* = 8.40 Hz, 2H, Amoc), 7.65-7.61 (t, *J* = 7 Hz, 2H, Amoc), 7.55-7.51 (t, *J* = 7.48 Hz, 2H, Amoc), 7.37-7.35 (d, *J* = 8.36 Hz, 2H, Ph), 6.39 (s, 2H, Amoc) ppm.

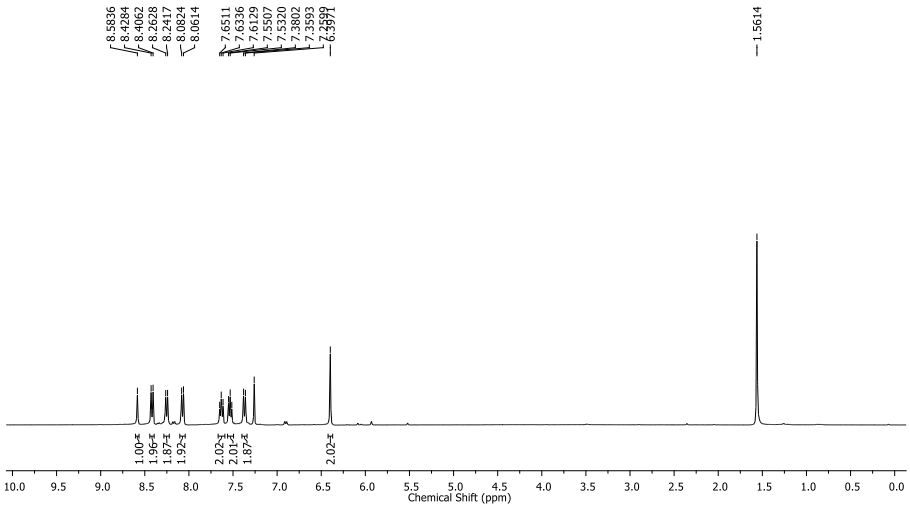

Figure 2.1 ^{1}H NMR spectrum (400 MHz) of **8** in $CDCl_3$.

2.2.2.2 Synthesis of 10

1.5 g (4.01 mmol) of **8** was dissolved in 3 mL DMF in a 100 mL round bottom flask and cooled it in an ice bath. A neutralized solution of **9** was extracted from its corresponding hydrochloride salt (1.44 g, 8.03 mmol) and concentrated to add to the reaction mixture. The reaction mixture was allowed to stir for 12 h. Product conversion was confirmed by TLC. The reaction mixture was diluted with ethyl acetate and washed with 1M HCl (3 × 30 mL), saturated Na_2CO_3 solution (3 × 30 mL) and then with brine. Solid yellow mass **10** was obtained after evaporating the solvent under reduced pressure.

Yield: 1.28 g (77%) ^{1}H NMR (400 MHz, DMSO-d_6): δ = 8.68 (s, 1H, Amoc), 8.34-8.32 (d, *J* = 8.68 Hz, 2H, Amoc), 8.14-8.12 (d, *J* = 8.20 Hz, 2H, Amoc), 7.71-7.69 (d, *J* = 8.00 Hz, 1H, NH), 7.62-7.51 (m, 4H, Amoc), 7.21-7.19 (m, 5H, Ph), 6.07-5.97 (q, 2H, Amoc), 4.31-4.25 (m, 1H, C^{α} H of Phe), 3.61 (s, 3H, OCH_3), 3.02-2.97 (dd, *J* = 5.08, 4.96 Hz, 1H, C^{β} H of Phe), 2.85-2.79 (dd, *J* = 10.24, 10.24 Hz, 1H, C^{β} H of Phe) ppm; MS (ESI): *m/z* calcd for $C_{26}H_{23}NO_4$: 436.1519 $[M+Na]^+$; found: 436.1654.

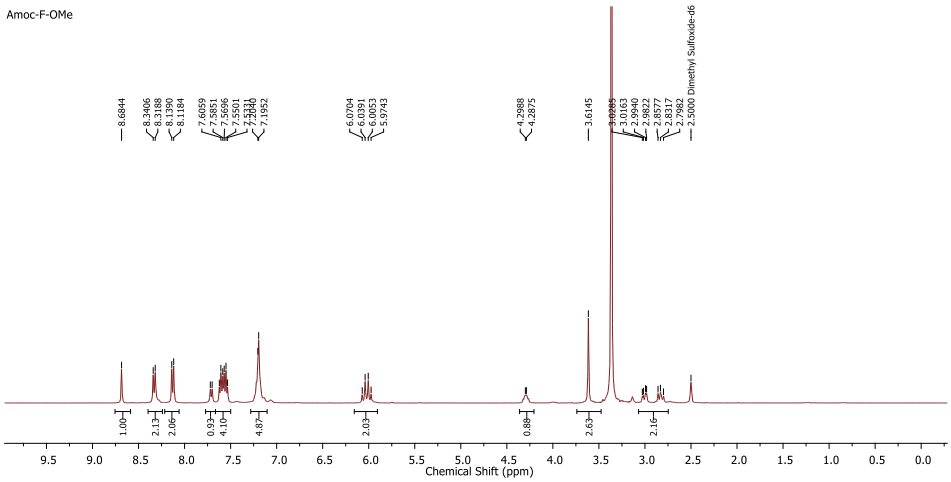

Figure 2.2 ^{1}H NMR spectrum (400 MHz) of **10** in DMSO-d_6.

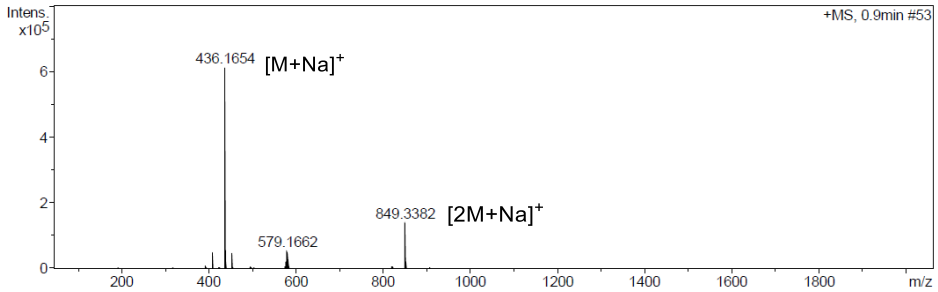

Figure 2.3 ESI-MS spectrum of **10**.

2.2.2.3 Synthesis of 11

1.0 g (2.41 mmol) of **10** was dissolved in 10 mL dry THF and 20 mL MeOH. In the reaction mixture 5 mL of 1M LiOH solution was added. The hydrolysis progress was monitored by TLC. The reaction mixture was stirred upto 4-6 h for complete hydrolysis. After the completion of the reaction, excess solvent was evaporated and diluted with 50 mL distilled water. The water mixture was taken

in a separating funnel and slowly washed with diethyl ether (20 mL). The aqueous layer was collected and cooled in an ice bath. Then, the solution was acidified with 1M HCl. The pH of aqueous layer was adjusted to 2 and the product was extracted with ethyl acetate (3 × 30 mL). The ethyl acetate layer was dried over anhydrous sodium sulphate and evaporated under reduced pressure to obtain solid **11**.

Yield: 0.794 g (82%) ^{1}H NMR (400 MHz, DMSO-d_6): δ = 8.67 (s, 1H, Amoc), 8.35–8.31 (d, *J* = 8.64 Hz, 2H, Amoc), 8.13–8.11 (d, *J* = 8.16 Hz, 2H, Amoc), 7.61–7.52 (m, 4H, Amoc), 7.50–7.48 (m, br, 1H, NH), 7.19 (s, 5H, Phe), 6.05–5.95 (q, 2H, Amoc), 4.20 (s, br, 1H, C^{α} H of Phe), 3.05–2.76 (m, 1H, C^{β} H of Phe), 2.82–2.76 (m, 1H, C^{β} H of Phe) ppm; MS (ESI): *m/z* calcd for $C_{25}H_{21}NO_4$: 422.1368 $[M+Na]^+$; found: 422.1330.

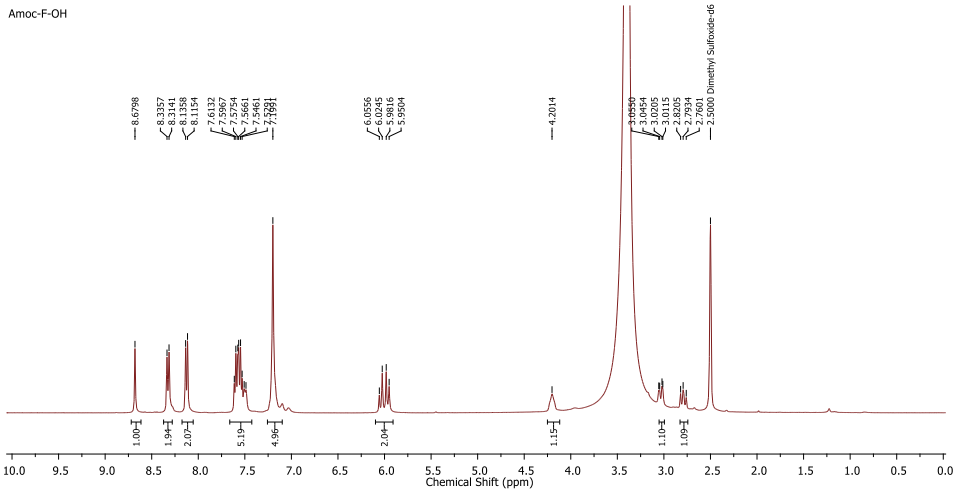

Figure 2.4 ^{1}H NMR spectrum (400 MHz) of **11** in DMSO-d_6.

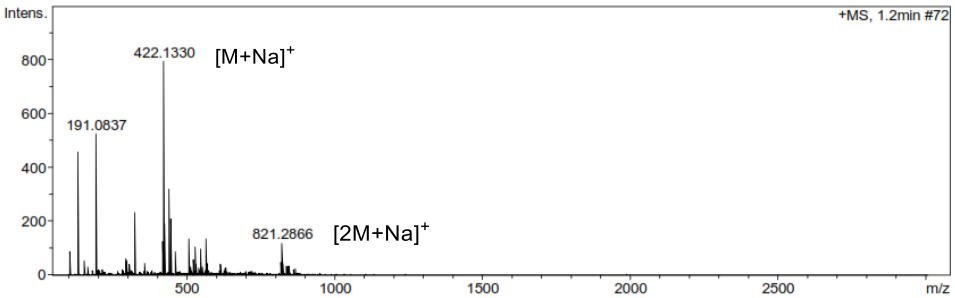

Figure 2.5 ESI-MS spectrum of **11**.

2.2.2.4 Synthesis of 14

A solution of **11** (0.980 g, 2.45 mmol) and HOBt (0.397 g, 2.94 mmol) was stirred in 3 mL of DMF. A neutralized solution of **12** (0.711 g, 4.90 mmol) was extracted from its corresponding hydrochloride salt. It was concentrated and added to the reaction mixture followed by coupling agent DIPC (0.371 g, 2.94 mmol) at 0° C and allowed to stir at room temperature for 12 h. After the reaction, the reaction mixture was diluted with ethyl acetate and organic layer was washed with 1M HCl (3 × 30 mL), saturated Na_2CO_3 (3 × 30 mL) and brine solution, ethyl acetate layer was dried over anhydrous Na_2SO_4 and evaporated under vacuum to found yellow-orange solid **14**.

Yield: 1.09 g (85%); ^{1}H NMR (400 MHz, DMSO-d_6): δ = 8.67 (s, 1H, Amoc), 8.35-8.33 (d, *J* = 7.72 Hz, 1H, NH), 8.31-8.29 (d, *J* = 8.44 Hz, 2H, Amoc), 8.13-8.11 (d, *J* = 7.72 Hz, 2H, Amoc), 7.59-7.52 (m, 4H, Amoc), 7.36-7.34 (d, *J* = 8.60 Hz, 1H, NH), 7.25-7.16 (m, 5H, Ph), 6.01-5.90 (q, 2H, Amoc), 4.36-4.27 (m, 2H, C^{α} H of Phe and Leu), 3.60 (s, 3H, OCH_3), 2.97-2.93 (dd, *J* = 3.68, 3.52 Hz, 1H, C^{β} H of Phe), 2.71-2.65 (dd, *J* = 10.84, 10.76 Hz, 1H, C^{β} H of Phe), 1.67-1.62 (m, 1H, C^{γ} H of Leu), 1.59-1.47 (m, 2H, C^{β} H of Leu), 0.91-0.90 (d, *J* = 6.44 Hz, 3H, C^{δ} H of Leu), 0.85-0.84 (d, *J* = 6.36 Hz, 3H, C^{δ} H of Leu) ppm; MS (ESI): *m/z* calcd for $C_{32}H_{34}N_2O_5$: 549.2365 $[M+Na]^+$; found: 549.2284.

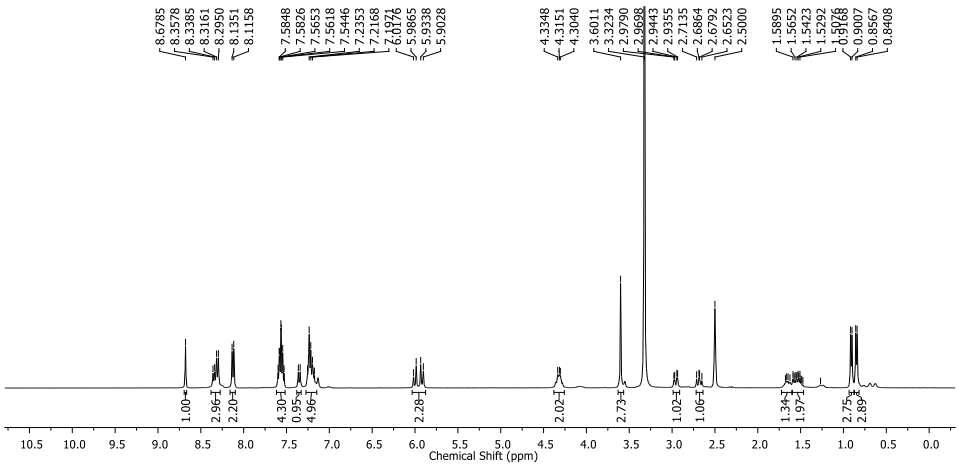

Figure 2.6 ^{1}H NMR spectrum (400 MHz) of **14** in DMSO-d_6.

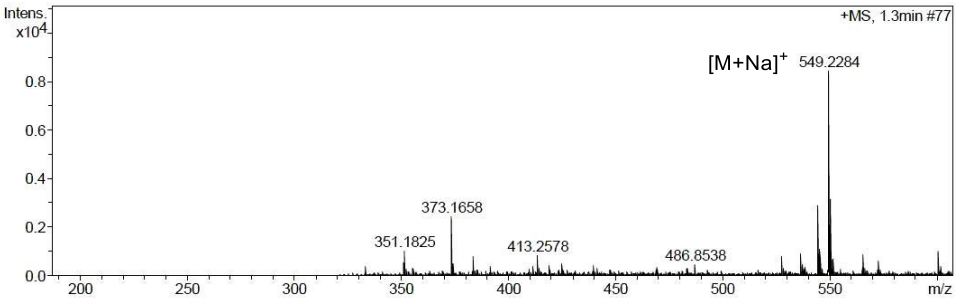

Figure 2.7 ESI-MS spectrum of **14**.

2.2.2.5 Synthesis of 1

1.1 g (2.08 mmol) of **14** was dissolved in 10 mL dry THF and 20 mL MeOH. In the reaction mixture 6 mL of 1M LiOH solution was added. The hydrolysis progress was monitored by TLC. The reaction mixture was stirred upto 4 h for complete hydrolysis. After the completion of the reaction, excess solvent was evaporated and diluted with 50 mL distilled water. The water mixture was taken in a separating funnel and slowly washed with diethyl ether (20 mL). The aqueous layer was collected and cooled in an ice bath. Then, the solution was acidified with 1M HCl. The pH of aqueous layer was adjusted to 2 and the product was extracted with ethyl acetate (3 × 30 mL). The ethyl acetate layer was dried over anhydrous

sodium sulphate and evaporated under reduced pressure to obtain orange-yellow solid **1**.

Yield: 0.93 g (87%); FT-IR (KBr): δ = 3298 (s, NH), 1707 (s, COOH), 1692 (s), 1654 (s), 1626 (br),1532 (s) cm^{-1}; ^{1}H NMR (400 MHz, DMSO-d_6): δ = 8.67 (s, 1H, Amoc), 8.31-8.29 (d, *J* = 8.40 Hz, 2H, Amoc), 8.21-8.19 (d, *J* = 7.84 Hz, 1H, NH), 8.13-8.11 (d, *J* = 8.04 Hz, 2H, Amoc), 7.59-7.52 (m, 4H, Amoc), 7.33-7.31 (d, *J* = 8.52 Hz, 1H, NH), 7.25-7.12 (m, 5H, Ph), 6.00-5.90 (q, 2H, Amoc), 4.35-4.22 (m, 2H, C^{α} H of Phe and Leu), 2.99-2.96 (d, *J* = 11.68 Hz, 1H, C^{β} H of Phe), 2.70-2.67 (d, *J* = 12.16, Hz, 1H, C^{β} H of Phe), 1.69-1.65 (m, 1H, C^{γ} H of Leu), 1.57-1.52 (m, 2H, C^{β} H of Leu), 0.92-0.90 (d, *J* = 6.40 Hz, 3H, C^{δ} H of Leu), 0.86-0.84 (d, *J* = 6.28 Hz, 3H, C^{δ} H of Leu) ppm; ^{13}C NMR (100 MHz, DMSO-d_6): δ = 174.02, 171.54, 156.03, 138.08, 134.55, 130.91, 130.46, 129.17, 128.89, 128.62, 127.67, 126.57, 126.19, 125.22, 124.16, 58.08, 56.00, 50.29, 24.27, 22.89, 21.34 ppm; HRMS (ESI): *m/z* calcd for $C_{31}H_{32}N_2O_5$: 535.2204 $[M+Na]^+$; found: 535.2200.

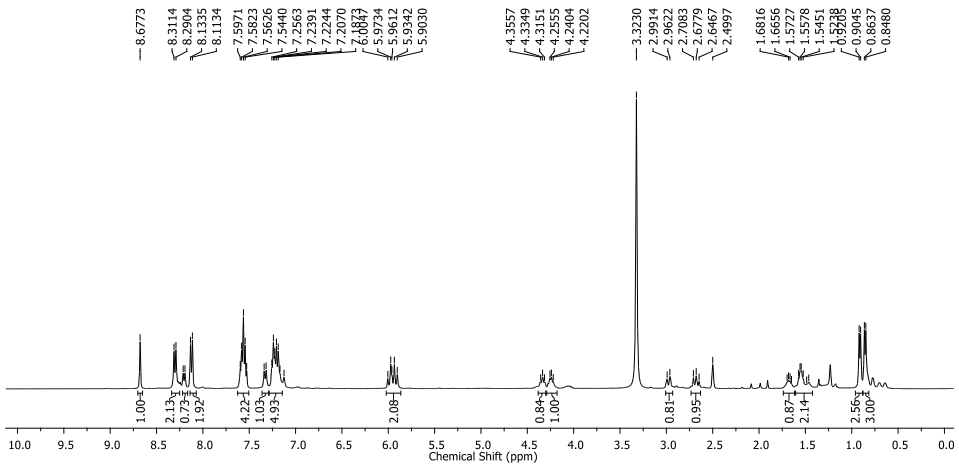

Figure 2.8 ^{1}H NMR spectrum (400 MHz) of **1** in DMSO-d_6.

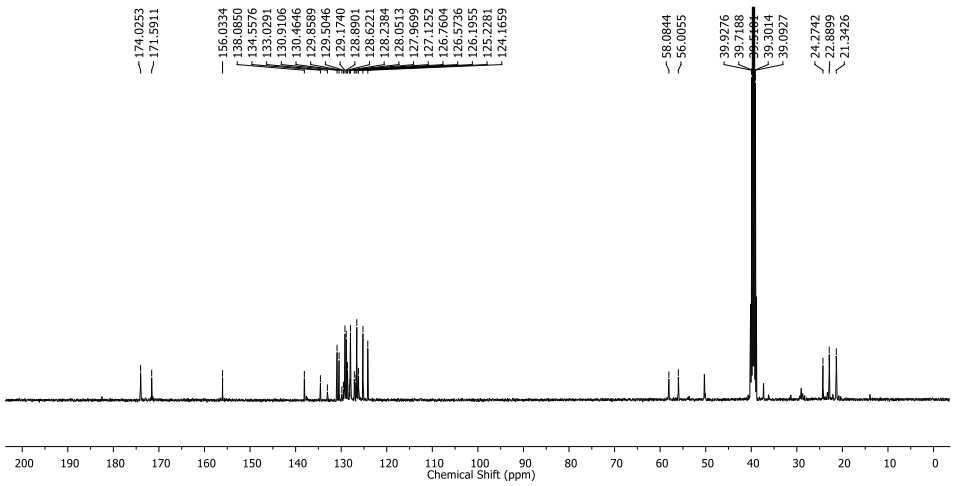

Figure 2.9 ^{13}C NMR spectrum (100 MHz) of **1** in DMSO-d_6.

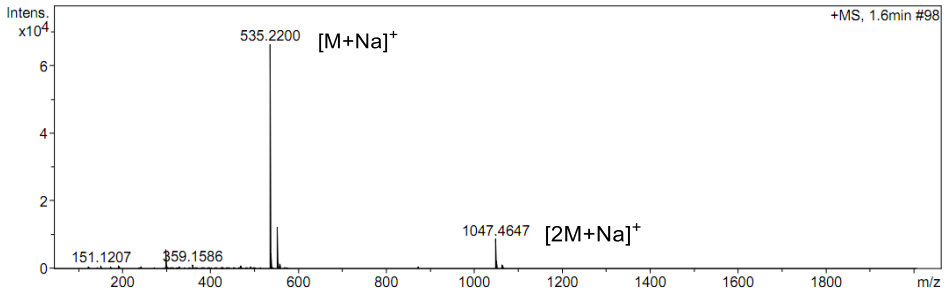

Figure 2.10 HRMS spectrum of **1**.

2.2.2.6 Synthesis of 15

11 (1.0 g, 2.50 mmol) and HOBt (0.405 g, 3.0 mmol) was dissolved in 3 mL of DMF. A neutralized solution of **13** (0.976 g, 5.0 mmol) was extracted from its corresponding hydrochloride salt and concentrated to add to the reaction mixture, followed by DIPC (0.379 g, 3.0 mmol) at 0° C and stirred at room temperature for 12 h. After completion of the reaction, the reaction mixture was diluted with ethyl acetate and washed with 1 M HCl (3 × 30 mL), saturated Na_2CO_3 (3 × 30 mL) and brine solution. Ethyl acetate layer was dried over anhydrous Na_2SO_4 and evaporated under vacuum to yield as yellow-orange solid **15**.

Yield: 1.28 g (88%); ^{1}H NMR (400 MHz, DMSO-d_6): δ = 9.25 (s, 1H, OH of Tyr), 8.67 (s, 1H, Amoc), 8.37-8.35 (d, *J* = 7.36 Hz, 1H, NH), 8.30-8.28 (d, *J* = 8.52 Hz, 2H, Amoc), 8.13-8.11 (d, *J* = 8.04 Hz, 2H, Amoc), 7.60-7.52 (m, 4H, Amoc), 7.33-7.31 (d, *J* = 8.64 Hz, 1H, NH), 7.22-7.15 (m, 5H, Ph), 7.03-7.01 (d, *J* = 8.16 Hz, 2H, Tyr), 6.69-6.67 (d, *J* = 8.12 Hz, 2H, Tyr), 5.95 (s, 2H, Amoc), 4.43-4.38 (m, 1H, C^{α} H of Tyr), 4.35-4.29 (m, 1H, C^{α} H of Phe), 3.55 (s, 3H, OCH_3), 2.92-2.84 (m, 3H, C^{β} Hs of Tyr and Phe), 2.67-2.61 (m, 1H, C^{β} H of Phe) ppm; MS (ESI): *m/z* calcd for $C_{35}H_{32}N_2O_6$: 599.2153 $[M+Na]^+$; found: 599.2097.

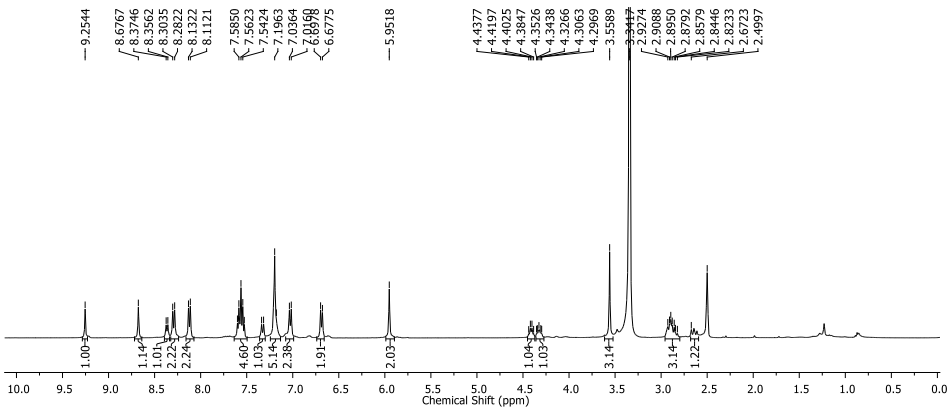

Figure 2.11 ^{1}H NMR spectrum (400 MHz) of **15** in DMSO-d_6.

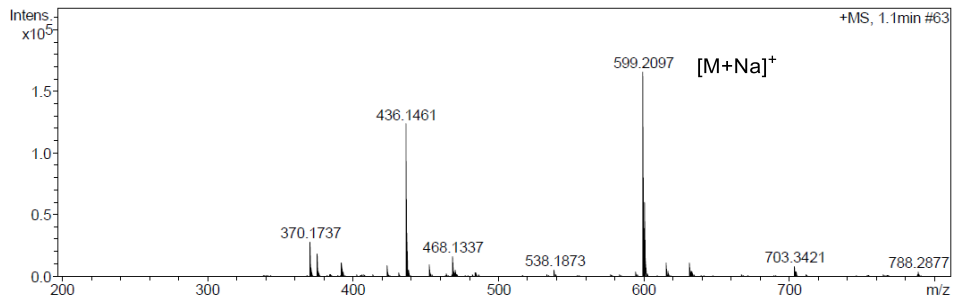

Figure 2.12 ESI-MS spectrum of **15**.

2.2.2.7 Synthesis of 2

1 g (1.73 mmol) of **15** was dissolved in 10 mL dry THF and 20 mL MeOH. A 6 mL 1 M LiOH was added to reaction mixture and the progress hydrolysis was monitored by TLC. The reaction mixture was stirred upto 4 h for complete hydrolysis. The excess solvent was evaporated and diluted with 50 mL distilled water. The mixture was taken in a separating funnel and slowly washed with diethyl ether (20 mL). The aqueous layer was collected and cooled in an ice bath. Then, the solution was acidified with 1 M HCl solution. The pH of aqueous layer was adjusted to 2 and the product was extracted with EtOAc (3 × 30 mL). The EtOAc layer was dried over anhydrous Na_2SO_4 and evaporated under reduced pressure to obtain solid **2**.

Yield: 0.8 g (82%); FT-IR (KBr): δ = 3305 (s, NH), 1708 (ms, H-bonded COOH), 1692 (s), 1654 (s), 1626 (ms), 1534 (s) cm^{-1}; ^1H NMR (400 MHz, DMSO-d_6): δ = 9.22 (s, br, 1H, OH of Tyr), 8.67 (s, 1H, Amoc), 8.29-8.27 (d, *J* = 8.48 Hz, 2H, Amoc), 8.16-8.15 (d, *J* = 7.72 Hz, 1H, NH), 8.13-8.11 (d, *J* = 7.80 Hz, 2H, Amoc), 7.59-7.52 (m, 4H, Amoc), 7.33-7.31 (d, *J* = 8.68 Hz, 1H, NH), 7.19-7.16 (m, 5H, Ph), 7.06-7.04 (d, *J* = 7.80 Hz, 2H, Tyr), 6.69-6.67 (d, *J* = 7.72 Hz, 2H, Tyr), 5.94 (s, 2H, Amoc), 4.38-4.29 (m, 2H, C^{α} H of Tyr and Phe), 2.98-2.92 (m, 2H, C^{β} Hs of Tyr), 2.86-2.80 (m, 1H, C^{β} H of Phe), 2.67-2.60 (m, 1H, C^{β} H of Phe) ppm; ^{13}C NMR (100 MHz, DMSO-d_6), δ = 173.36, 171.95, 156.46, 156.43, 138.49, 131.35, 130.92, 130.61, 129.59, 129.34, 129.08, 128.41, 127.82, 127.50, 127.09, 126.63, 125.70, 124.61, 115.48, 58.60, 56.52, 54.29, 37.80 ppm; HRMS (ESI): *m/z* calcd for $C_{34}H_{30}N_2O_6$: 561.2031 $[M-H]^-$; found: 561.2024.

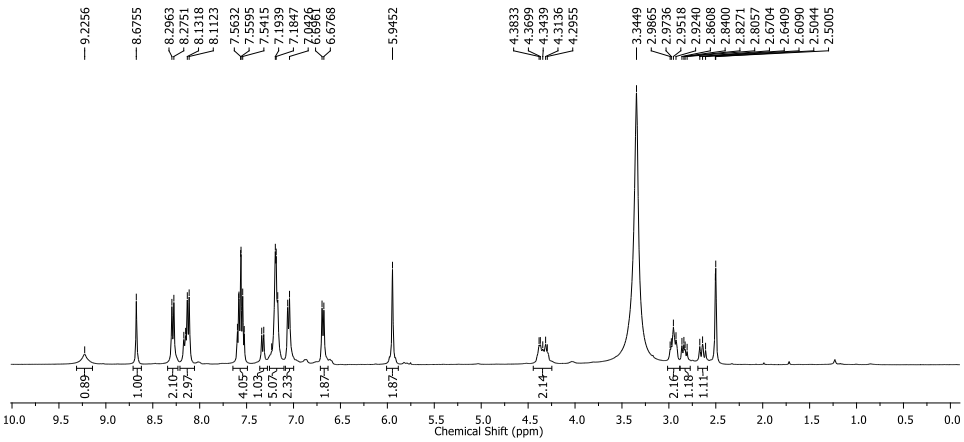

Figure 2.13 ^1H NMR spectrum (400 MHz) of **2** in DMSO-d_6.

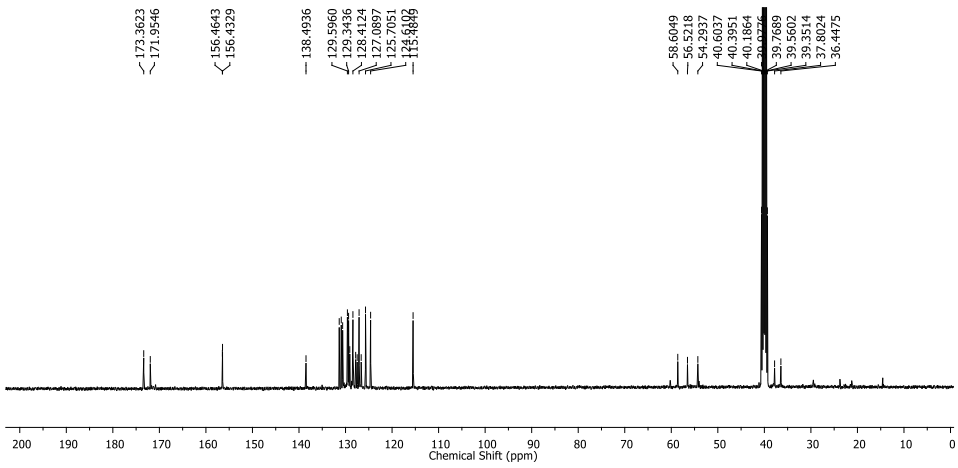

Figure 2.14 ^{13}C NMR spectrum (100 MHz) of **2** in DMSO-d_6.

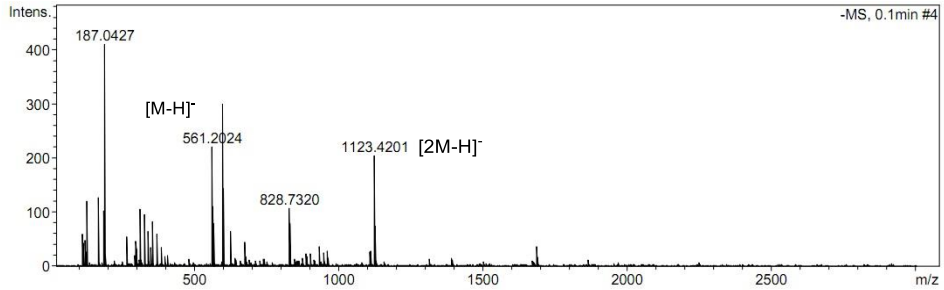

Figure 2.15 HRMS spectrum of **2**.

2.2.3 Preparation of Hydrogels

Peptides **1** and **2** (20 mM) were placed in 2 mL of Milli-Q water in a glass vial and partially solubilized by the slow addition of NaOH (0.5 M) solution. These solutions were vortexed and ultrasonicated to get complete dissolution of peptides, and the pH was raised up to 10. The pH of the solutions was decreased by the slow addition of HCl (0.1 M), and the final pH of the viscous solution was maintained at 7.4. Viscous solutions of peptides **1** and **2** were kept at rest at 37 °C for 30 min, which slowly formed hydrogels. The minimum gelation concentrations for peptides **1** and **2** are found as 10 and 15 mM, respectively.

2.2.4 Characterizations

UV/vis absorption spectra of peptides were recorded using a Varian Cary 100 Bio UV/Vis spectrophotometer at concentrations ranging from 20 to 200 μM. Fluorescence emission and excitation spectra of the hydrogels (20 mM) were recorded on a Horiba Scientific FluoroMax-4 spectrophotometer in a quartz cuvette (10 × 10 mm^2) at room temperature. The slit width for the emission and excitation spectra was set at 2 nm, and the data pitch was 1 nm. Emission spectra of hydrogels **1** and **2** were recorded at λ_{ex} 365 nm, and the data range was 240−449 nm. Excitation spectra of hydrogels **1** and **2** were recorded at λ_{em} 459 and 450 nm, respectively. A time-correlated single-photon counting (TCSPC) instrument was used to measure decay traces of the hydrogels. TCSPC studies were performed on

a Horiba Yovin (model: Fluorocube-01-NL) instrument. Samples were excited at λ_{ex} 375 nm using a picosecond diode laser. The signals were collected at magic angle (54.701) polarization using a photomultiplier tube (TBX-07C) as a detector, which had a dark count of less than 20 cps. The instrument response function (fwhm B 140 ps) was recorded using a very dilute scattering solution. Data analysis was performed using IBH DAS (version 6, HORIBA Scientific, Edison, NJ) decay analysis software. The excited-state average lifetimes of the hydrogels were measured by using equation

$$<\tau> = \sum_{i=1}^{n} \alpha_i \, \tau_i$$

where τ_i is the fluorescence lifetime of various fluorescent species and α_i is the normalized preexponential factor. Circular dichroism (CD) spectra were recorded at 25 °C using a JASCO J-815 spectropolarimeter at concentrations ranging from 20 to 600 μM. The spectra were recorded in a quartz cell (path length: 1 mm) within the range 500-190 nm with a data pitch of 0.1 nm. The bandwidth was set at 1 nm, the scanning speed was 20 nm min^{-1}, and the response time was 1 s. Experimental data were recorded in triplicate and the average data are shown. The molar ellipticity [θ] was calculated according to the equation $[\theta] = \theta/(c \times l)$, where θ is the measured ellipticity (mdeg), c is the sample concentrations in dmol/L, and l is the path length in cm. FTIR spectra of the hydrogels and peptides were recorded on a Bruker (Tensor 27) FTIR spectrophotometer by using KBr pallet technique. The FTIR measurements were recorded within the range of 500−4000 cm^{-1} over 64 scan at a resolution of 4 cm^{-1} and interval of 1 cm^{-1}.

2.2.5 Morphological Study of the Hydrogels

Field-emission scanning electron microscopy (FE-SEM) experiment was performed on a JEOL scanning electron microscope (model no. JSM-7600F). For FE-SEM study, small amounts of hydrogels were placed on a glass coverslip. The hydrogels were dried first in air and then in vacuum and coated with gold. Transmission electron microscopy (TEM) images were captured using a JEOL electron microscope (model: JEM-2100), operated at an accelerating voltage of 200 kV and a field-emission gun transmission electron microscope (model: Tecnai G2, F30), operated on a voltage of 300 kV. Hydrogel (50 μL) was dissolved in 450 μL of water, and the dilute solution of the hydrogels was dried on carbon coated copper grids (300 mesh) by slow evaporation in air and then lowed to dry separately under a reduced pressure at room temperature. The nanostructural morphology of hydrogels was analyzed by TEM experiments using 3% phosphotungstic acid as a negative stain.

2.2.6 Rheological Properties of the Hydrogels

Rheological experiments were performed at 25 °C on an Anton Paar Physica MCR 301 rheometer. The viscoelastic properties of hydrogels were measured by measuring the storage modulus (G') and loss modulus (G″). Hydrogel (1 mL) was transferred on a rheometer plate by using a microspatula and kept hydrated by using a solvent trap. A stainless steel parallel plate (diameter: 25 mm) was used to

sandwich the hydrogels with TruGap (0.5 mm). The dynamic strain sweep experiment was performed to determine the region of deformation of hydrogels in which linear viscoelasticity is valid. The exact strains for hydrogel materials were determined by linear viscoelastic regime at a constant frequency of 10 rad s^{-1}. The mechanical strengths of the hydrogels were determined by frequency sweep experiment. In the frequency sweep measurement, the graph was plotted as a function of frequency in the range of 0.05-100 rad s^{-1}. The thixotropic properties were investigated by step-strain experiments at the constant frequency of 10 rad s^{-1}, and applied strains were varied from 0.1 to 40%.

2.2.7 Antibacterial Experiment

2.2.7.1 Bacterial Culture

Staphylococcus aureus (MTCC 96), *Bacillus subtilis* (MTCC 619), *Escherichia coli* (MTCC 739), *Pseudomonas aeruginosa* (MTCC 741), and *Salmonella typhi* (MTCC 733) bacteria were obtained as a lyophilized powder from the Institute of Microbial Technology Chandigarh, India. Before the experiments, fresh inoculums of Gram-positive bacteria *S. aureus* and *B. subtilis* and Gram-negative bacteria *E. coli*, *P. aeruginosa*, and *S. typhi* were prepared. A single colony was harvested and subsequently inoculated in autoclaved nutrient broth medium for bacterial growth. The bacterial inoculums were kept in an incubator at 37 °C overnight. The turbidity of fresh overnight bacterial suspensions was diluted as 0.5 McFarland standards to give a working concentration in the range of 1-2 × 10^8 colony-forming units (cfu mL^{-1}). The optical density of all cultures was measured before and after incubation at 625 (OD_{625}) nm under aseptic conditions.

2.2.7.2 Culture Media

Nutrient broth medium was utilized as a liquid medium for bacterial cultivation, which was prepared by mixing peptone (10 g), yeast extracts (3 g), and sodium chloride (5 g, NaCl) in 1000 mL of sterile distilled water. Nutrient agar medium was prepared by adding additional agar-agar powder (15 g) in 1000 mL of nutrient broth medium. The pH of the nutrient broth and nutrient agar medium was adjusted to pH 7.0 using NaOH (0.1 M) solution. The nutrient broth and nutrient agar medium was sterilized in an Erlenmeyer flask (25 mL) at a pressure of 15 lbs and temperature of 121 °C for 30 min.

2.2.7.3 Antibacterial Properties of the Hydrogels

In vitro antibacterial efficacies of peptide hydrogels were investigated against both Gram positive (*S. aureus* and *B. subtilis*) and Gram-negative (*E. coli*, *P. aeruginosa*, and *S. typhi*) bacteria. The antibacterial activities of these hydrogels were investigated using optical density (OD_{625}) method. The sterilized nutrient broth (180 μL) medium was transferred into 96-well culture plates by using sterilized micropipette tips. After this, 10 μL of inoculums of various bacterial cultures was added in each well with an initial bacterial concentration of 1-2 × 10^8 cfu mL^{-1}. Ten microliter volume of peptide hydrogels with initial concentrations ranging from 20 to 0.031 mM was added to each well in triplicate (final concentrations were reported in the figures after dilutions). The bacterial solution devoid of hydrogels in nutrient broth was used as the control and only nutrient

broth was used as blank. Antibacterial test of higher concentrations of hydrogels were performed by using 5, 7.5, 10, 15, and 20 mM of hydrogels, and the total volume was maintained at 200 μL by adding nutrient broth for the required dilutions. These plates containing test organisms and hydrogels were kept in an incubator at 37 °C for 24 h. The absorbances of the test solution and control were recorded at 625 nm, and nutrient broth was utilized as a blank solution for the experiment. The antibacterial properties of peptide hydrogels were confirmed by using a microplate reader (Synergy H1 multimode microplate reader using 96-well microplates at 25 °C) by comparing the absorbance of the test solution with the control experiment.

2.2.8 Biocompatibility and Cytotoxicity of the Hydrogels

2.2.8.1 Selection of Doses

Minimum inhibitory concentration (MIC_{50}) from the antibacterial study was ranging from 10 to 200 μM. For the biocompatibility assays, we have chosen the hydrogel concentrations ranging from 200 to 0.312 μM. The objective was to evaluate the safety, toxicity, and efficacy parameters of the hydrogels at MIC_{50} to the human cells so that they can be used for antibacterial applications.

2.2.8.2 Isolation of Blood

Blood sample was collected in a vacuum tube in which sodium citrate solution (3.2 w/v %) was added as the anticoagulant. It is noteworthy that the blood sample was given by one of the researchers as a part of routine health checkup at a health center, in which blood plasma was separated and remaining blood cells were utilized for the experiments.

2.2.8.3 Isolation of Erythrocytes and WBCs

Erythrocytes were isolated from blood by using centrifugation at 1500 rpm for 5 min at room temperature. WBCs were collected from the buffy coat using a sterile syringe, and the rest of the cells was washed with 10 mM phosphate buffered saline (PBS) (0.9 w/v % NaCl, pH 7.4) thrice.

2.2.8.4 MTT Viability Assay

Cells (5×10^3) were seeded into 96-well plates in 198 μL of Dulbecco's modified Eagle medium (DMEM) containing 10% fetal bovine serum (FBS), and 2 μL of initial hydrogel concentrations (ranging from 20 to 0.031 mM) was added into wells (final concentrations were reported in the figures after dilutions). Only the medium containing FBS was used as a blank, whereas the control was containing cells in media along with 2 μL of buffer. Top five higher concentrations (5, 7.5, 10, 15, and 20 mM) of both the hydrogels were also used for the MTT test. hWBCs were grown and mixed with 50, 75, 100, 150, and 200 μL of hydrogels, and DMEM was used to make up the total volume to 200 μL. The cells were directly mixed in hydrogels (20 mM) and incubated for 24 h for the biosafety assessment of the hydrogels. For each group, eight wells were assigned and plates were kept for 24 h in a 5% CO_2 incubator. After completion of incubation, 5 μg of the final concentration of MTT (thiazolyl blue tetrazolium bromide, from Sigma-Aldrich, MO, USA) reagent (20 μL from 5 mg/mL stock) was used in each well. After 3 h incubation at 37 °C in the 5% CO_2 incubator, 100 μL of dimethyl sulfoxide

(DMSO) and ethanol (1:1) mixture was added into each well. Absorbance was taken by the microplate reader at 450 nm against blank.

2.2.8.5 Hemolytic Activity

To study hemolytic activity, 1% suspension of erythrocytes in PBS was used. Briefly, 990 μL of the cell suspension was incubated with 10 μL of initial hydrogel concentrations (ranging from 20 to 0.312 mM). In the hemolysis test, for higher hydrogel concentrations, top five higher concentrations (5, 7.5, 10, 15, and 20 mM) of both the hydrogels were used, and the total volume was maintained as 1 mL. The erythrocytes were directly mixed in hydrogels (20 mM) and incubated for 1 h for the hemolysis assessment of the hydrogels. Only PBS was used as a blank, whereas control samples were having erythrocytes in buffer and were devoid of hydrogels. The mixtures were then incubated at 37 °C for 1 h. After the completion of incubation, the mixtures were centrifuged at 1000 rpm for 10 min at 4 °C. The percentage hemolysis was analyzed using absorbance of the supernatant at 540 nm against blank. The percentage hemolysis was calculated, as compared to the respective control values (considered as 100%).

2.2.8.6 Lipid Peroxidation Assay in Erythrocytes

Isolated erythrocytes were washed thrice with PBS. Packed cell volume was adjusted to 5% with PBS, pH 7.4. In each tube, 990 μL of the cell suspension along with 10 μL of initial hydrogel concentrations (ranging from 20 to 0.312 mM) was used. In control tubes, 10 μL of buffer was added to the cell suspension, whereas only PBS without any cell was used as a blank. Each group was assigned six tubes (N = 6). Samples were then incubated for 1 h at 37 °C, followed by the addition of 2 mL of 28% trichloroacetic acid solution. Then, samples were centrifuged at 1000 rpm for 5 min and 2 mL of supernatant was collected from each tube. In each tube, 500 μL of 1% thiobarbituric acid was added and samples were placed on a boiling water bath for 1 h followed by cooling under running tap water. Samples were centrifuged again for 5 min at room temperature at 5000 rpm, and absorbance was taken at 532 nm against blank. Simultaneously, a standard curve was made for malondialdehyde (MDA), ranging from 0.1 to 10 nM/mL prepared in 10 mM PBS by following the same procedure as mentioned above. The standard curve was used to calculate the amount of thiobarbituric acid-reactive substances (TBARs) formed equivalent to MDA formed in nanomole/milliliter (nM/mL). Similarly, top five higher concentrations (5, 7.5, 10, 15, and 20 mM) of both the hydrogels were also evaluated for lipid peroxidation (LPO) study. The erythrocytes were directly mixed in hydrogels (20 mM) and incubated for 1 h for the LPO experiment.

2.2.9 Statistical Analyses

Statistical significance was ascribed at $P < 0.05$ or more. Data are expressed as mean ± SEM values and were analyzed by nonparametric analysis of variance followed by post hoc Dunnett's multiple comparison test, using a trial version of GraphPad Prism version 7.03 for Windows (GraphPad, San Diego, CA).

2.3 Results and Discussion

The designed low-molecular weight peptide-based amphiphiles generally entrap water and form self-supporting hydrogels, which would have great significance for biological applications. In our previous work, we have reported graphene quantum dot embedded Amoc-capped amino acid-based blue light-emitting hydrogels.[41] Amoc-capped amino acid-based material exhibits excellent gelation ability because of the involvement of aromatic π-π stacking and hydrophobic interactions. Here, we have designed and synthesized Amoc-capped dipeptide-based injectable hydrogels. The conventional solution-phase methodology was used for the synthesis of peptides **1** and **2** (peptide **1**: Amoc-FL-OH; peptide **2**: Amoc-FY-OH; F = L-phenylalanine, L = L-leucine, and Y = L-tyrosine). Peptides **1** and **2** form self-supporting hydrogels at pH 7.4. Self-supporting hydrogels **1** and **2** were used for antibacterial and cell culture applications (**Scheme 2.2**).

Scheme 2.2 Chemical Structures of Amoc-Capped Dipeptides[a]

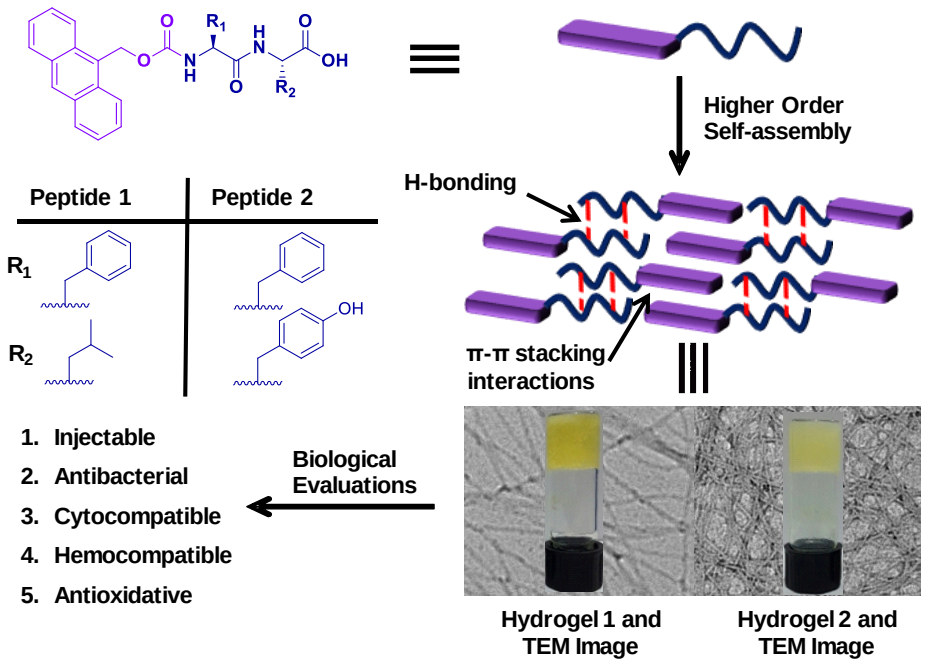

[a]Schematic representation of self-assembly leading to the formation of nanofibrillar hydrogels and biological evaluations with the self-supporting hydrogels.

Furthermore, Amoc-capped peptide amphiphiles and corresponding hydrogels **1** and **2** were characterized by various techniques. The nanostructural morphology of hydrogels was analyzed by electron microscopic (SEM and TEM) techniques. The SEM images of hydrogels reveal highly cross-linked nanofibrillar networks (Figure 2.16a,b). The presence of three dimensional (3D) nanofibrillar networks with several micrometers in length was revealed from the TEM analysis. The average diameters of nanofibrillar networks (Figure 2.16c,d) of hydrogels **1** and **2** are 20 and 25 nm, respectively. These microscopic studies evident that dense nanofibrillar networks are responsible for the formation of self-supporting hydrogels. Furthermore, concentration-dependent UV/vis spectra were recorded to

obtain insight into the intermolecular interactions the supramolecular aggregates.[42] Broad absorption bands from 355 to 399 nm are observed for hydrogels **1** and **2** at all studied concentrations (Figure 2.17a,b). The broad absorption peaks are most likely associated with the anthracene moiety present in the hydrogels **1** and **2**.[43,44] The broad absorption peaks are less prominent at lower hydrogel concentrations (20-80 μM).

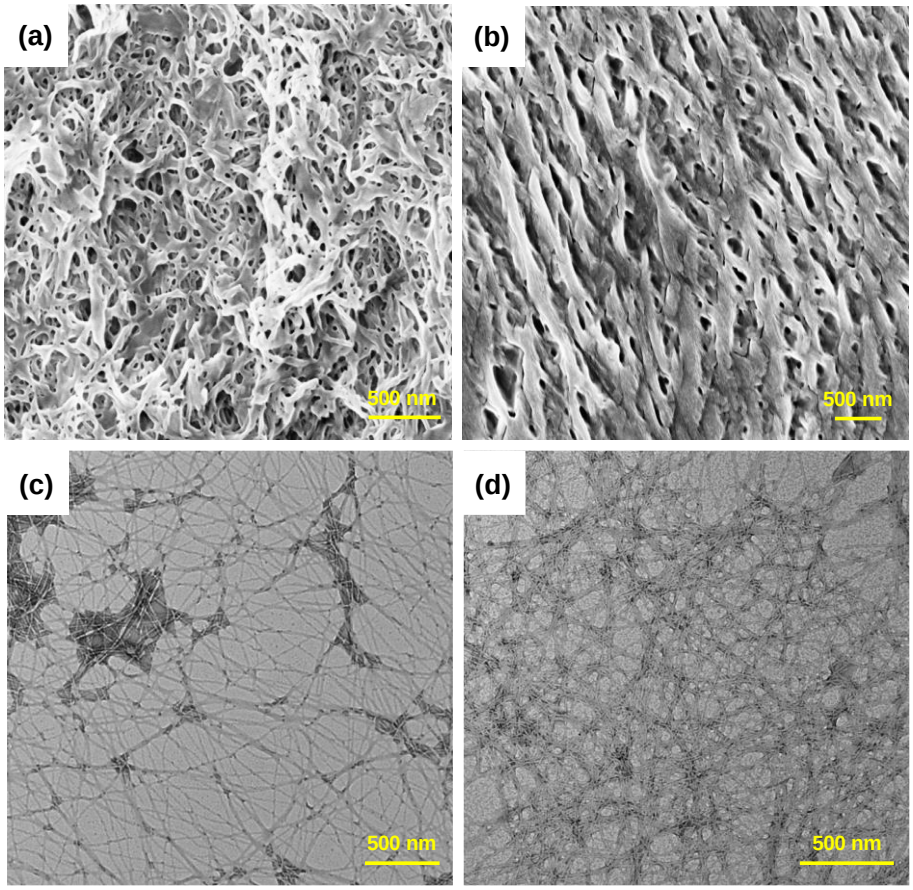

Figure 2.16 (a,b) FE-SEM images and (c,d) TEM images of hydrogels **1** and **2**, respectively.

The anthracene absorption peak intensity is gradually increased with the increase in hydrogel concentrations (>80 μM), and the peak positions remained constant. Absorption maxima at 254 nm (π-π* transition of phenylalanine amino acids) were observed for hydrogels **1** and **2**, whereas, a second absorption band at 269 nm (π-π* transition tyrosine amino acids) is observed for hydrogel **2**. The observed peak positions are constant, and the peak intensity is increased with the increase in hydrogel concentrations (20-200 μM). Concentration-dependent UV/vis spectra reveal that all peak positions are constant and aggregation still remained at the lower hydrogel concentrations (Figure 2.17a,b). The self-assembly process was confirmed by fluorescence spectroscopy experiments, which suggest that the driving force behind the self-assembly could be π-π stacking interactions between aromatic moieties.[45] The emission spectra of aqueous solutions of peptides **1** and

2 (Figure 2.17c) show three sharp emission maxima between 390 and 440 nm (λ = 365 nm), compared with the broad emission maximum at 459 and 450 nm (λ_{ex} = 365 nm) for their corresponding hydrogels, respectively (Figure 2.17d).

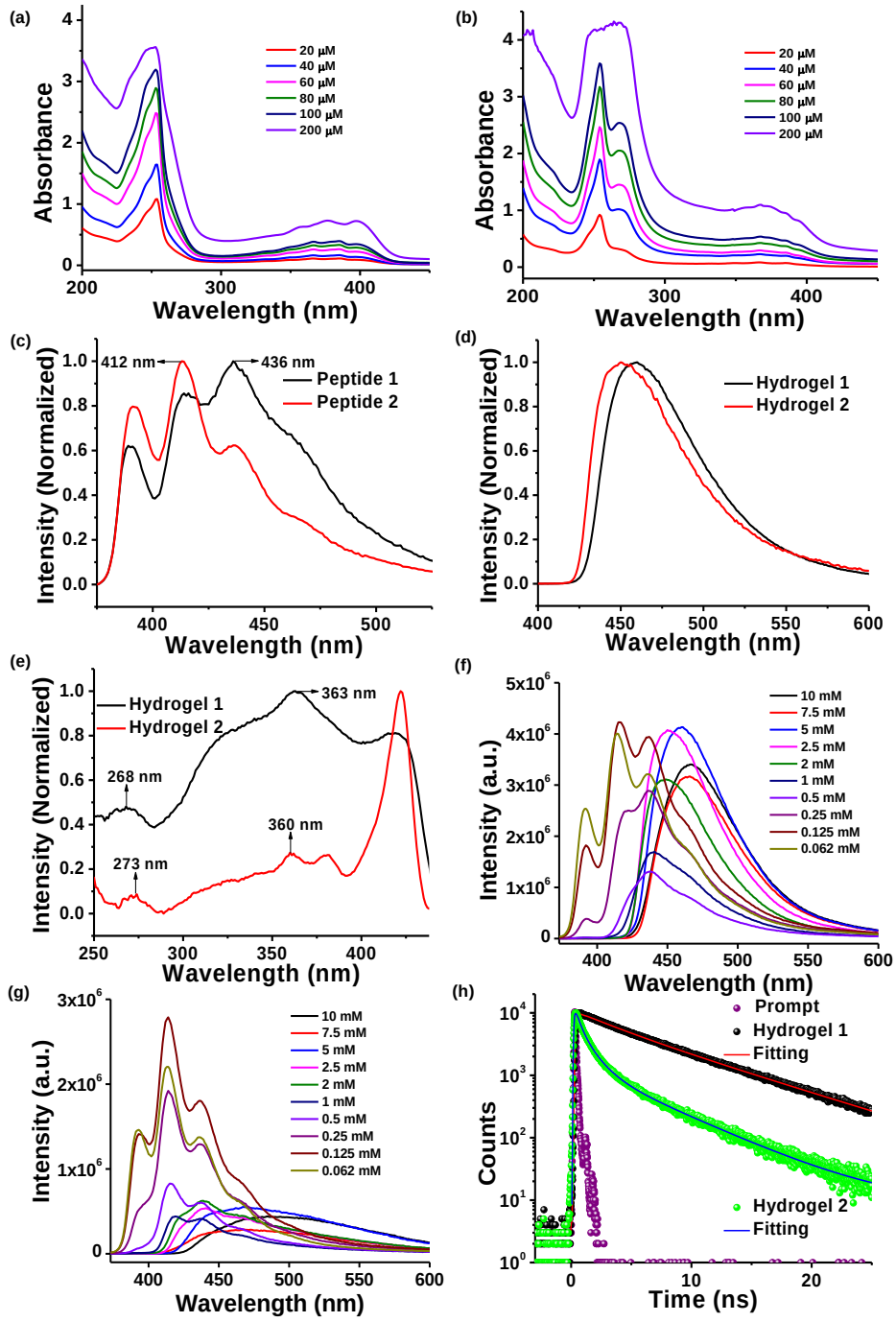

Figure 2.17 (a,b) are the concentration-dependent UV/vis spectra of aqueous solutions of hydrogels **1** and **2**, respectively. (c) Fluorescence spectra of peptides **1** and **2** at 10 μM concentration. (d) Fluorescence spectra (λ_{ex} = 365 nm) of hydrogels **1** and **2** at 20 mM concentration. (e) Excitation spectra of hydrogels **1** and **2**. (f,g) are concentration-dependent fluorescence spectra of peptides **1** and **2**. (h) Decay traces of hydrogels **1** and **2** at 20 mM concentration.

Both the hydrogels show red shift in emission maxima, which possibly indicates the formation of an extended π-stacked system with an antiparallel arrangement in their hydrogel state. These pronounced red-shifted emission spectra of the hydrogels suggest the aggregation of gelator molecules that are responsible for the formation of supramolecular nanofibers.[46] Overall, the prominent red-shifted emission spectra for hydrogels suggest that aromatic amino acids and anthracene rings play a key role during the self-assembly process.[47] Excitation spectra were also recorded at the emission wavelength of 459 and 450 nm for hydrogels **1** and **2**, respectively. The excitation spectra show peaks at 363 and 360 nm, respectively, for hydrogels **1** and **2** (Figure 2.17e). The critical aggregation concentration (CAC) is one of the important parameters for antimicrobial peptide amphiphiles, where aggregation of the peptides occurs upon interaction with bacterial cell membranes.[48] The CACs for peptides **1** and **2** were investigated with the help of concentration-dependent fluorescence experiments. The aggregation propensity of peptides 1 and 2 was consistent with antibacterial data. The CAC values for peptides 1 and 2 were found at around 0.5 mM and 2 mM concentrations, respectively (Figure 2.17f,g). Further, fluorescence excited-state lifetimes and the decay profiles of the excited species of hydrogels were measured by the TCSPC technique. The lifetimes and decay traces of hydrogels are anticipated by excitation-emission wavelengths at 375-459 and 375-450 nm for hydrogels **1** and **2**, respectively. The decay traces for hydrogel **1** was fitted with a biexponential function and hydrogel **2** was fitted with a triexponential function (Figure 2.17h). The average lifetime 6.12 ns with lifetime components of 3.288 ns (30%) and 7.335 ns (70%) is observed for hydrogel **1**, whereas the average lifetime 1.18 ns with lifetime components of 1.237 ns (35%), 5.180 ns (10%), and 0.425 ns (55%) is observed for hydrogel **2** (Table 2.1). The longer average lifetime for hydrogel **1** compared to hydrogel **2** suggests an excited-state stable complex by hydrogel **1** than hydrogel **2**.

Table 2.1. Decay parameters for hydrogels at 20 mM concentration

Name	α_1	α_2	α_3	τ_1 (ns)	τ_2(ns)	τ_3(ns)	τ_a(ns)	χ^2
Hydrogel **1**	0.30	0.70	-	3.288	7.335	-	6.12	1.34
Hydrogel **2**	0.35	0.10	0.55	1.237	5.180	0.425	1.18	1.20

τ_a = Average lifetime
α = Normalized amplitude of each component

Secondary structures of the peptides and their corresponding hydrogels were investigated by FTIR analysis. The presence of a prominent amide band I at 1652 cm^{-1} for peptide **1** and 1655 cm^{-1} for peptide **2** indicates that a major proportion of peptides in powder form is disordered in arrangements.[49] However, the additional peaks at 1690 and 1625 cm^{-1} for peptide 1 and 1689 and 1624 cm^{-1} for peptide **2**

suggest that the small proportion of peptides could be arranged in a β-sheet-like structure.[50] The peaks centered at 1690 and 1634 and 1692 and 1626 cm^{-1} suggest a more ordered antiparallel β-sheet-like arrangement for hydrogels **1** and **2**, respectively[51] (Figure 2.18a,b). Wide angle X-ray diffraction (WAXD) experiment was performed to investigate the molecular packing of peptides and their corresponding xerogels.

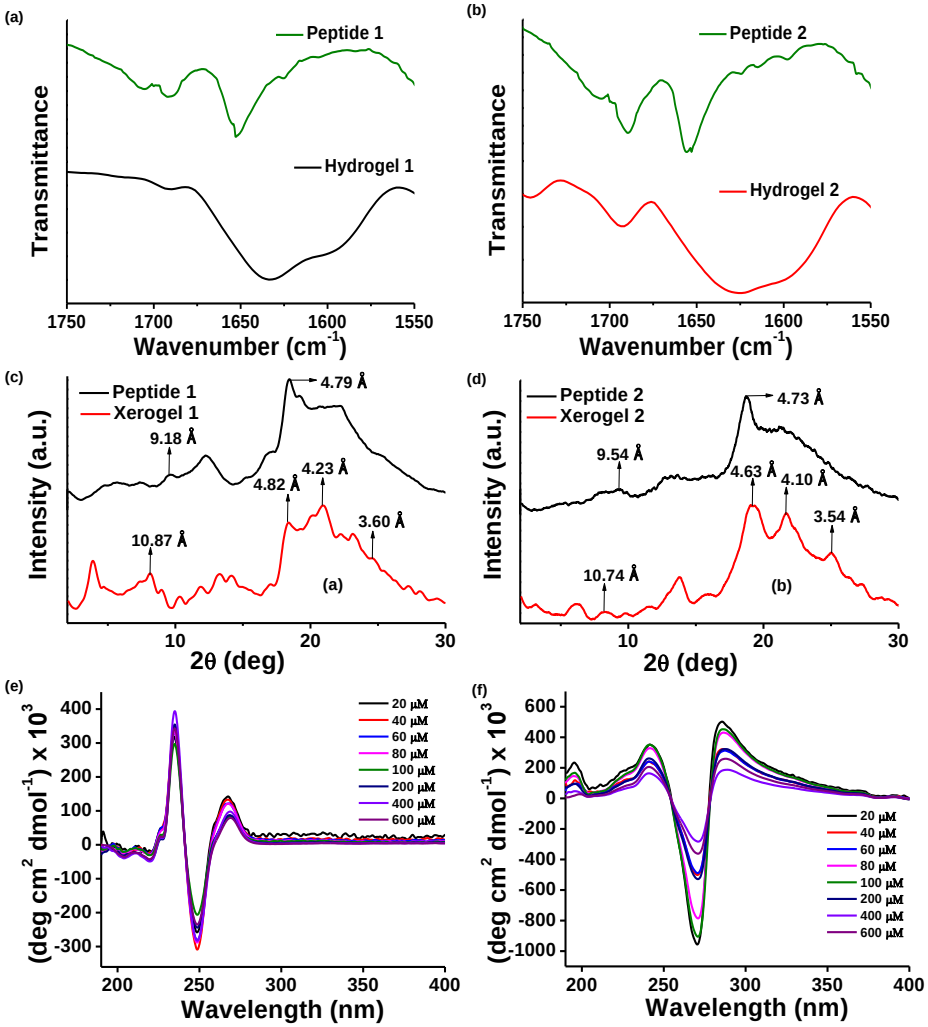

Figure 2.18 (a,b) FTIR spectra of peptides and hydrogels **1** and **2**, respectively. (c.d) are wide angle powder XRD spectra of peptide and xerogel, **1** and **2**, respectively. (e,f) are the concentration-dependent CD spectra of aqueous solutions of hydrogels **1** and **2**, respectively.

The powder X-ray diffraction (PXRD) experiment shows a sharp peak corresponding to d spacing at 4.82 Å accompanied by another peak at 10.87 Å for xerogel **1**. The peak at 4.82 Å represents the β-sheet-type hydrogen bonding with an antiparallel arrangement. Another peak at 10.87 Å represents the inter sheet stacking distances between β-sheet structures (Figure 2.18c).[52] The X-ray diffraction pattern of the xerogel **2** also shows a characteristic peak at 4.63 Å

accompanied by a second peak at 10.74 Å (Figure 2.18d). The X-ray diffraction patterns of these xerogels represent a similar type of antiparallel cross β-sheet arrangement. The peaks at 4.23 and 4.10 Å are observed because of the anthracene moieties present in xerogels **1** and **2**, respectively.[53,54] Moreover, the π-π stacking interactions between aromatic moieties are revealed from the characteristic diffraction peaks corresponding to d-spacing at 3.60 and 3.54 Å for xerogels **1** and **2**, respectively.[55,56] However, these peaks are not observed in their corresponding peptides **1** and **2**, indicating the crucial role of self-assembly process for the formation of well-defined nanostructures (Figure 2.18c,d). CD spectroscopy is a technique to elucidate the secondary structures of the peptide hydrogels. In our attempt to systematically analyze the growth of the self-assembly process in hydrogels **1** and **2**, concentration-dependent CD studies were performed.[43,57,58] The hydrogel concentrations ranging from 20 to 600 μM were chosen for the concentration dependent CD analysis. These are the concentrations in line with the concentration-dependent UV/vis analysis. The unusual CD spectra for hydrogels are observed because of the presence of aromatic chromophores. The contribution of each aromatic side chain to the amide region of peptides is quite characteristic and causes interference with amide CD in the far-UV region. The observed CD spectrum for hydrogel **1** shows two negative signals around 204 and 220 nm and a positive signal around 226 nm, suggesting the presence of a helical conformation [59] (Figure 2.18e). The CD spectrum for hydrogel **2** shows two positive signals around 196 and 226 nm (20-600 μM). The intensity of Cotton effect is increased steadily with the increase in hydrogel **2** concentrations with nonsignificant shifting of the peak positions during the concentration variations (Figure 2.18f). The aromatic chromophores of the hydrogels **1** and **2** have different π-π* transitions in the region of near- and far-UV. These transitions are classified by different properties of their excited states, for example, $1L_b$, $1L_a$, $1B_b$, and $1B_a$. The aromatic chromophores of hydrogel **1** interact with adjacent peptide groups,[60] which leads to a positive local band (L_a) at the wavelength around 234 nm and L_b band is observed around 269 nm (20-600 μM) (Figure 2.18e). However, hydrogen bonding of phenolic OH in hydrogel **2** gives rise to a further red shift of the L_a band at 240 nm and the L_b band at 287 nm (20-600 μM) (Figure 2.18f). The very strong negative Cotton effect due to π-π* transition of aromatic chromophores is centered at 248 and 270 nm (20-600 μM) for hydrogels **1** and **2**, respectively.[61,62] On the basis of the results from concentration-dependent CD spectra, we conclude that hydrogel **1** favors a helical conformation. Rheological experiments were performed to elucidate the mechanical strength and thixotropic nature of hydrogels.[7,42] The rheological study is very crucial to determine the hydrogel strength and stiffness for biological applications. The oscillatory frequency sweep measurements for hydrogels (20 mM) show a higher storage modulus (G′) compared to the loss modulus (G″) during the experiment, indicating the viscoelastic nature of the hydrogels. An increase in hydrogel **1** ($G' > 10^4$) stiffness compared to hydrogel **2** ($G' > 10^3$) is evidenced from oscillatory frequency sweep measurements (Figure 2.19a,c). Rheological strain sweep experiments were

performed to investigate thixotropic nature of the hydrogels upon external strain at a constant angular frequency of 10 rad/sec (Figure 2.19b,d). In step 1, hydrogels were subjected below the deformation limit (at a low strain, γ = 0.1% for hydrogel **1** and 0.5% for hydrogel **2**). Storage moduli (G′) of hydrogels **1** and **2** are greater than their loss moduli (G″) indicating the cross-linked network in the hydrogels. In step 2, hydrogels were subjected at a higher strain (γ = 40%), where the storage modulus (G′) decreased below the loss modulus (G″). These results indicate that the cross-linked networks of hydrogels ruptured and turned into liquid-like sol state. In step 3, when a low strain (γ = 0.1% for hydrogel **1** and 0.5% for hydrogel **2**) was applied for 100 s, the mechanical properties of the hydrogel quickly recovered because of the reformation of 3D crosslinked networks. The periodic low/high strain was applied with an interval of 100 s up to six cycles to ensure the self-healing nature of the hydrogels.

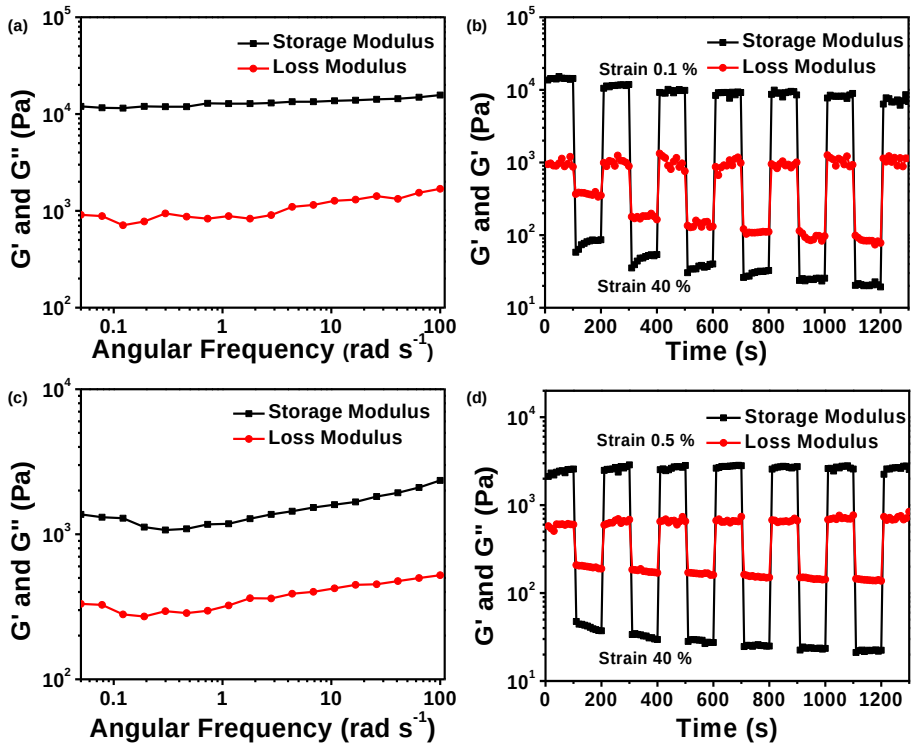

Figure 2.19 (a,c) Dynamic frequency sweep experiments and (b,d) strain sweep experiments for hydrogels **1** and **2**, respectively.

The self-healing nature of hydrogel **2** (almost 100% mechanical strength recovery) is better than hydrogel **1** owing to the dynamic deformation-reconstruction of the 3D fibrillar network (Figure 2.19b,d). The fast recovery of the hydrogel strength was apparently because of the formation of hydrogen bonding, *π*-*π* stacking, and noncovalent interactions within the gelator molecules. The hydrogel strength recovery time was very short and recovered in 100 s interval only. Apart from the thixotropic nature, these hydrogels also show injectable property, and the volume was controlled by injecting hydrogels onto glass slides without gelation and blockage within the needle. The mechanical strength of the hydrogels is also

visually confirmed by forming tough and shape-memory hydrogels at 20 mM concentration (Figure 2.20). This type of injectable, tough, robust, and shape-memory[63] hydrogels would be of great interest in the area of biomaterial implantations and 3D bioprinting.[64,65] Therefore, considering shape-memory, injectable, and self-healing properties of hydrogels, these hydrogels were further used for antibacterial and cell culture experiments.

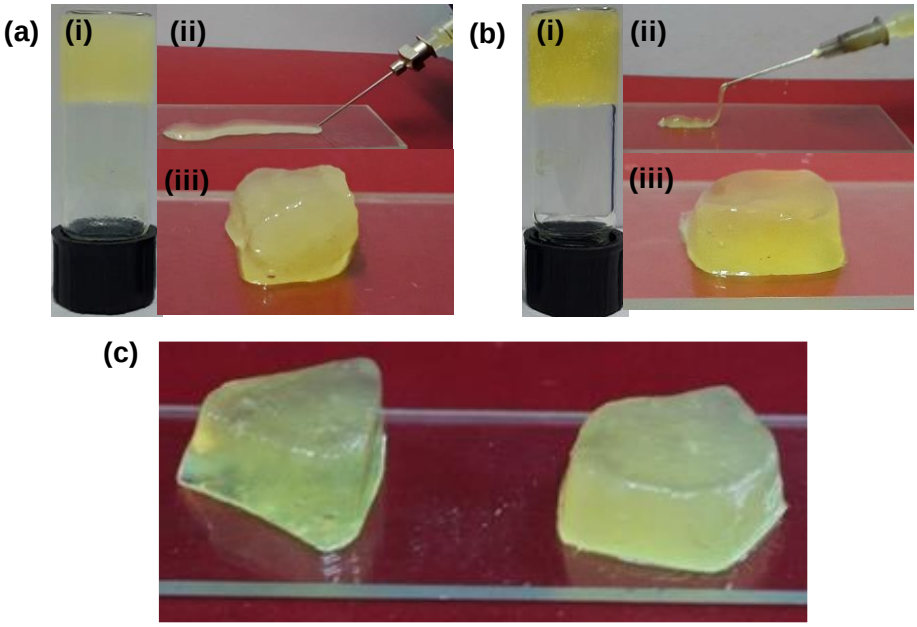

Figure 2.20 Optical photographs (a,b): (i) inverted vial demonstrating hydrogel formation, (ii) syringe injection, and (iii) 3D block of self-supporting hydrogels **1** and **2**, respectively. (c) Optical images of triangular and pentagonal shapes of hydrogel **2**.

Microbial contaminations due to the biomaterial implantations are a major challenging problem that requires designing a material possessing inherent antibacterial properties. Keeping abovementioned points in mind, antibacterial efficacy of hydrogels was evaluated by optical density and agar well-diffusion method.[66] However, when using agar well-diffusion method, diffusion of the hydrogel is very less because of the hydrogel stiffness, and therefore, the observed zone of inhibition is small in diameter. Antibacterial activity of hydrogels was measured by optical density (OD_{625}) method to avoid physical obstacles of the hydrogels. The OD_{625} values for Gram-positive (*S. aureus* and *B. subtilis*) and Gram-negative (*E. coli*, *P. aeruginosa*, and *S. typhi*) bacteria indicate that growth of the Gram-positive bacteria was significantly inhibited by hydrogels **1** and **2** (Figure 2.21a,b). The maximum antibacterial activity of hydrogel **1** is observed at 125 and 250 μM concentrations, whereas the MIC_{50} is found at 12.5 and 125 μM concentrations for *S. aureus* and *B. subtilis* bacteria, respectively. The maximum antibacterial efficacy of hydrogel **2** against *S. aureus* and *B. subtilis* is observed at 1000 and 500 μM concentrations, respectively. However, MIC_{50} values of hydrogel **2** are 250 and 125 μM for *S. aureus* and *B. subtilis*, respectively.

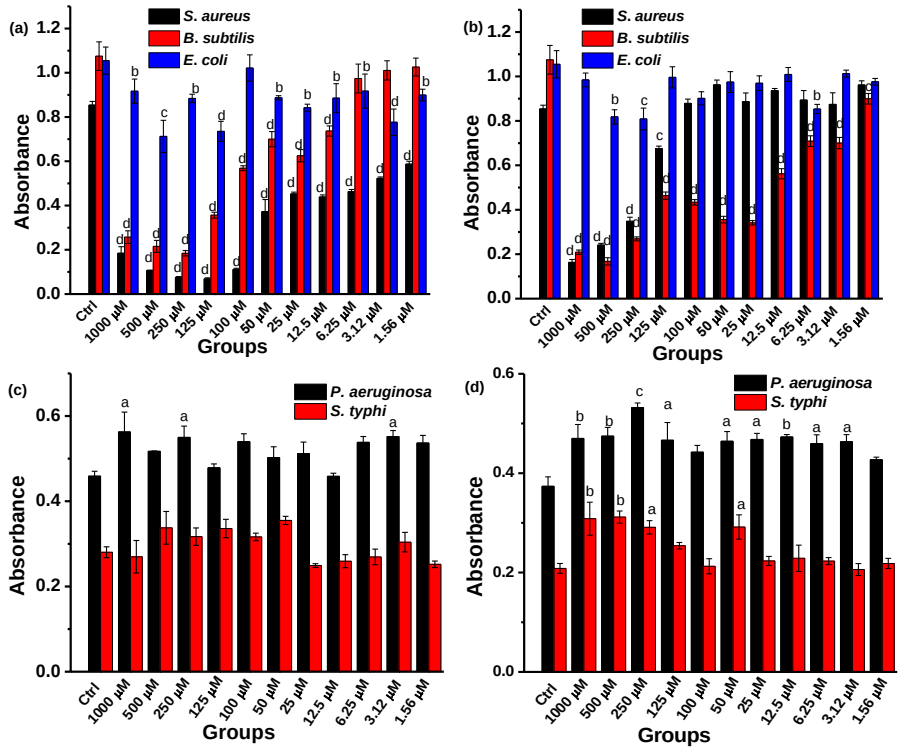

Figure 2.21 Antibacterial study of the effect of 11 various concentrations of (a) hydrogel **1** and (b) hydrogel **2** (ranging from 1000 to 1.56 μM) on two Gram-positive and one Gram-negative bacteria. The effect of 11 various concentrations of (c) hydrogel **1** and (d) hydrogel **2** (ranging from 1000 to 1.56 μM) on two Gram-negative bacteria, as shown by absorbance at 625 nm. Data are shown as mean ± SEM (N = 3). $^{a}p < 0.05$; $^{b}p < 0.01$; $^{c}p < 0.001$ and $^{d}p < 0.0001$, as compared to control group.

The hydrogels **1** and **2** are found to be ineffective against Gram-negative (*E. coli*) bacteria at the concentration range from 1000 to 1.56 μM, where inhibition is not ≥50% (Figure 2.21a,b). Further, the antibacterial efficacy of peptide hydrogels are evaluated using other Gram-negative (*P. aeruginosa* and *S. typhi*) bacteria, and the hydrogels are ineffective against Gram-negative bacteria (Figure 2.21c,d) at the concentration range from 1000 to 1.56 μM. Hydrogel **1** (1000 μM concentration) is more viscous and sparingly soluble in nutrient broth medium, whereas hydrogel **2** (1000 μM concentration) forms a homogenous solution in nutrient broth medium. Hence, the diluted form of hydrogel **1** is homogeneously distributed within the broth media and shows higher antibacterial efficacy as compared to the higher concentrations. In the case of hydrogel **2**, all studied concentrations are homogeneously distributed. Therefore, higher concentrations of hydrogel **2** are more effective and further dilution decreases the antibacterial efficacy of hydrogel **2** against Gram-positive bacteria. The lower CACs and the greater hydrophobicity of peptide **1** (log P = 5.96) in comparison with peptide **2** (log P = 5.63)[67] significantly influence the antibacterial efficacy of their corresponding hydrogels. However, antibacterial efficacies of hydrogels are also evaluated at higher concentrations (5, 7.5, 10, 15, and 20 mM). The higher concentrations of hydrogel

1 show antibacterial activity against Gram-positive bacteria, whereas hydrogel **2** shows potent antibacterial activity against Gram-positive and Gram-negative bacteria (Figure 2.22a,b). The present antibacterial data suggests that different structural complexities between Gram-positive and Gram-negative bacteria are responsible for the differential antibacterial activities of hydrogels.

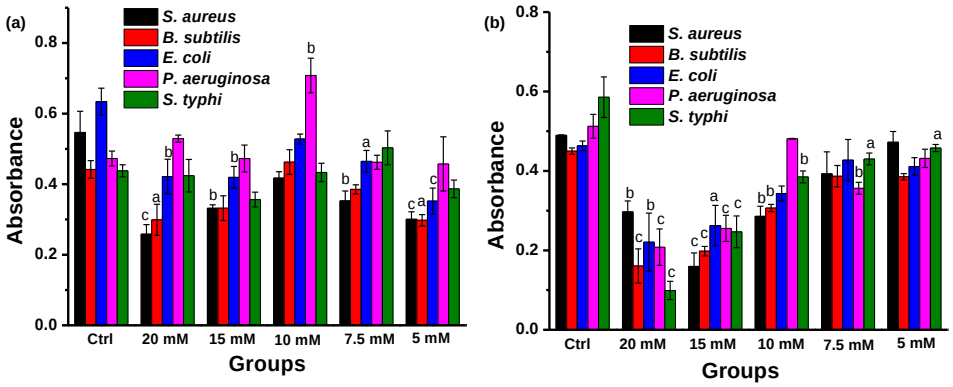

Figure 2.22 Antibacterial study of the effect of 5 higher concentrations of (a) hydrogel **1** and (b) hydrogel **2** (ranging from 20 to 5 mM) on two Gram-positive and three Gram-negative bacteria, as shown by absorbance at 625 nm. Data are shown as mean ± SEM (N=3). $^{a}p < 0.05$; $^{b}p < 0.01$; $^{c}p < 0.001$ and $^{d}p < 0.0001$, as compared to control group.

A single lipid membrane in Gram-positive bacteria is covered by a cell wall composed of thick a peptidoglycan layer, lipoteichoic, and teichoic acid. The cell wall of Gram-negative bacteria is thin and composed of a peptidoglycan layer located between periplasmic space generated due to the inner and outer lipid membranes. The cell wall of Gram-positive bacteria is directly exposed to the hydrogel surface, which could make easier to penetrate the cell wall and disrupt the cell membrane, whereas, the extra lipopolysaccharide cell membrane present in Gram-negative bacteria works as a selective filter and might prevent the antibacterial activity of the hydrogels (except higher concentrations of hydrogel **2**). The higher concentrations (20 and 10 mM) of hydrogel **2** show antibacterial efficacy against Gram-negative bacteria (Figure 2.22a,b). The aqueous channel present in the outer membrane of porin protein provides a selective entrance for the tyrosine-containing less hydrophobic hydrogel **2**, and antibacterial efficacy is observed against Gram-negative bacteria.[68] The entire experiments were performed under a laminar airflow chamber, and aseptic conditions were maintained during the experiments. All experiments were repeated three times for each sample, and average data are shown. Furthermore, cytotoxicity of hydrogels was evaluated by the MTT assay on hWBCs, which represents the cellular viability and/or proliferations.[69] In the present study, MTT data show a nonsignificant decrease in MTT absorbance at higher concentrations (from 200 to 1.25 μM) of hydrogel **1** (Figure 2.23a). However, lower concentrations of hydrogel **1** (0.625 and 0.312 μM) show a significant increase in MTT values. The MTT data from hydrogel **1** suggests that hydrogel **1** exerts slightly toxic results on cellular viability

and/or proliferation at higher concentrations. Interestingly, lower concentrations (0.625 and 0.312 μM) of hydrogel **1** are found to be safe and exert a marginal positive influence on cell viability and proliferation.

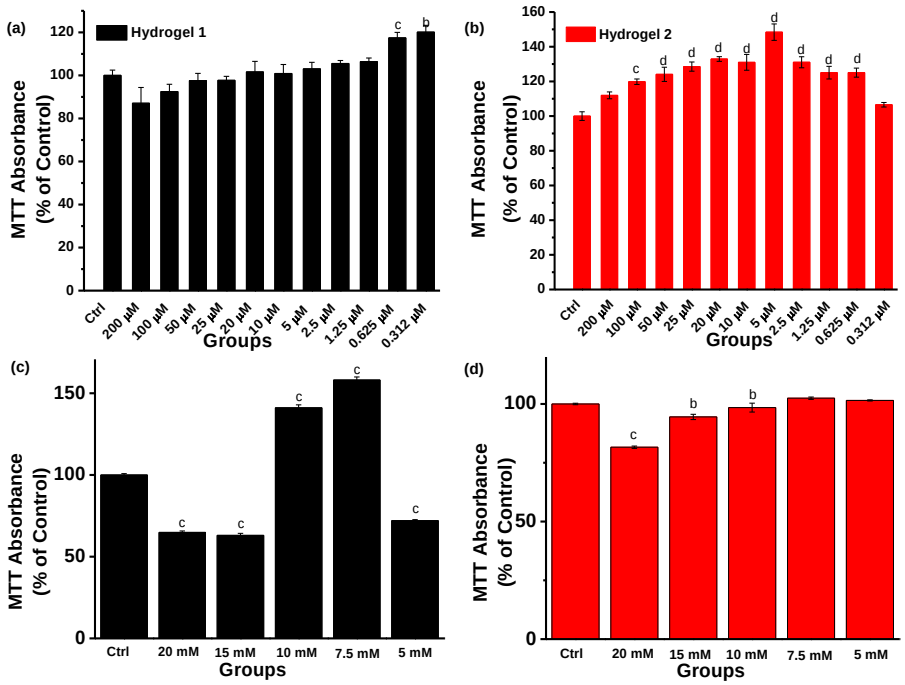

Figure 2.23 Comparative study of the effects of 11 various concentrations of (a) hydrogel **1** and (b) hydrogel **2** (ranging from 200 to 0.312 μM) on cytotoxicity/viability assessment on total WBCs (isolated from human blood). The effects of 5 higher concentrations of (c) hydrogel **1** and (d) hydrogel **2** (ranging from 20 to 5 mM), as shown by the MTT assay. Data are shown as mean ± SEM (N = 5). $^{a}p < 0.05$; $^{b}p < 0.01$; $^{c}p < 0.001$ and $^{d}p < 0.0001$, as compared to control group.

MTT data from hydrogel **2** (Figure 2.23b) consistently show increase in cell viability in a dose-dependent manner. Hydrogel **2** shows significant increase in MTT absorbance at 100 μM concentration, which reaches highest at 5 μM concentration. Studied concentrations lower than 5 μM show decrease in MTT values. The biosafety parameters of hydrogels are evaluated by mixing the cells directly with the various concentrations of the hydrogels (5, 7.5, 10, 15, and 20 mM). Interestingly, it is found that the higher concentrations of hydrogels do not exert considerable toxicity on cell viability (Figure 2.23c,d). Furthermore, biocompatibility of hydrogels was assessed by hemolytic activity experiments using hRBCs. Hydrogel **1** shows an increase in hemolysis at higher concentrations (200-25 μM) (Figure 2.24a), whereas lower concentrations (20 and 10 μM) of hydrogel **1** show a decrease in hemolysis significantly. Lower concentrations (5-0.312 μM) of hydrogel **1** show nonsignificant changes in these values. In line to MTT data, hydrogel **2** (Figure 2.24b) shows a marginal (4-6%) increase in hemolysis at higher concentrations (200-25 μM). However, at lower concentrations (20, 10, 5, and 0.625 μM), hydrogel **2** shows a nonsignificant

decrease in hemolysis, whereas all other studied concentrations (2.5, 1.25, and 0.312 μM) show a nonsignificant increase in hemolysis (~1-2%). Marginal fluctuations in hemolysis data are observed, which might be the outcome of osmotic influence due to the hydrogel consistency or partial sedimentation. Furthermore, top five higher concentrations (5, 7.5, 10, 15, and 20 mM) of hydrogels are employed for the hemolysis study. The higher hydrogel concentrations (15 and 20 mM) show an increase in hemolysis, and the lower concentrations (10, 7.5, and 5 mM) of the hydrogels are hemocompatible (Figure 2.24c,d).

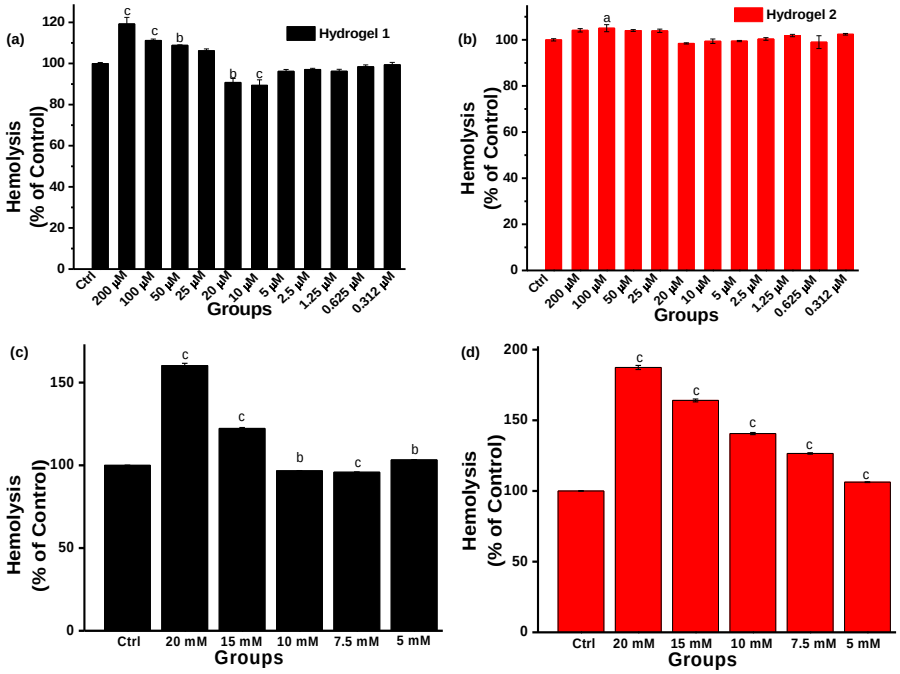

Figure 2.24 Comparative study of the effects of 11 various concentrations of (a) hydrogel **1** and (b) hydrogel **2** (ranging from 200 to 0.312 μM) on hemolysis on RBCs (isolated from human blood). The effects of 5 higher concentrations of (a) hydrogel **1** and (b) hydrogel **2** (ranging from 20 to 5 mM), as shown by absorbance at 540 nm. Data are presented as percentage of control group and shown as mean ± SEM (N = 3). $^{a}p < 0.05$; $^{b}p < 0.01$; $^{c}p < 0.001$ and $^{d}p < 0.0001$, as compared to control group.

Further, to understand the effect of hydrogels on human cell LPO experiment was performed.[70] In response to hydrogel **1** treatment, a nonsignificant increase in LPO values at higher concentrations (200-20 μM) and a nonsignificant decrease in LPO values at lower concentrations (10-0.312 μM) are observed (Figure 2.25a). In response to hydrogel **2** treatment, all studied concentrations show a significant decrease in LPO values (Figure 2.25b), as compared to the control group. These data consistently reveal that hydrogel **2** is safe and does not exert any cytotoxic effect. Further, LPO study indicates that hydrogel **2** decreases the oxidative stress significantly and shows free-radical scavenging activity. The LPO experiments were conducted using higher concentrations (5, 7.5, 10, 15, and 20 mM) of the

hydrogels to evaluate the biosafety and biocompatibility of the hydrogels on human blood cell membranes (Figure 2.25c,d). Both the hydrogels show inhibition of LPO in a dose-dependent manner, and higher concentrations of hydrogels are more effective than the lower concentrations. However, hydrogel **2** is found to be more effective at all high doses as compared to hydrogel **1**.

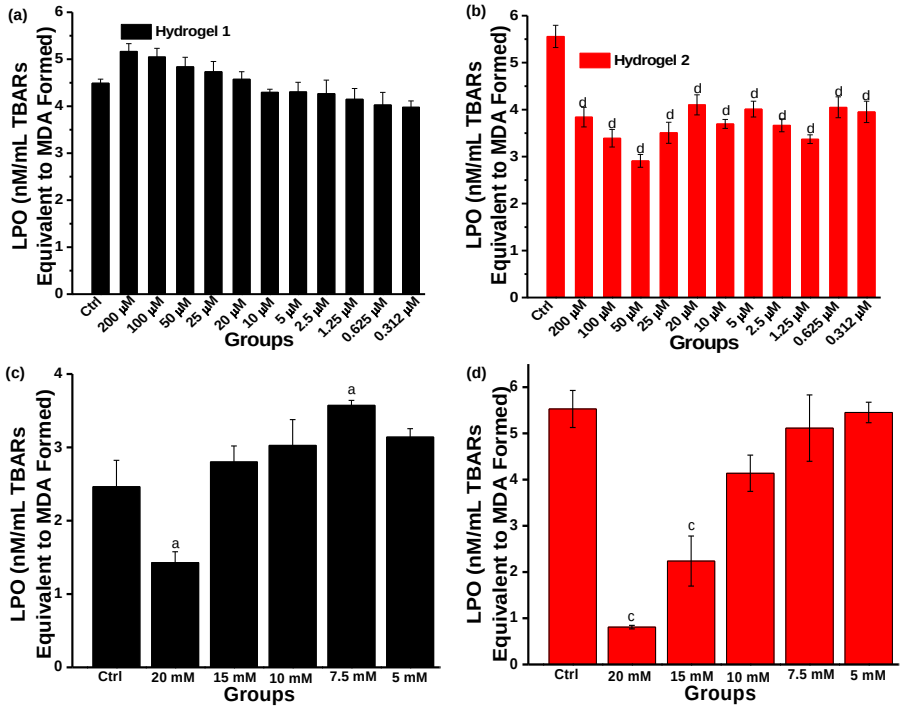

Figure 2.25 Comparative study of the effects of 11 various concentrations of (a) hydrogel **1** and (b) hydrogel **2** (ranging from 200 to 0.312 μM) on LPO in TBARs formed equivalent to nM/mL MDA formed in RBCs (isolated from the human blood). the effects of 5 higher concentrations of (a) hydrogel **1** and (b) hydrogel **2** (ranging from 20 to 5 mM). Data are presented as percentage of control group and shown as mean ± SEM (N = 6). $^{a}p < 0.05$; $^{b}p < 0.01$; $^{c}p < 0.001$ and $^{d}p < 0.0001$, as compared to control group.

Comprehensively, results from the present study suggest that both the studied hydrogels **1** and **2** are biocompatible but hydrogel **2** is better for biological applications. On the basis of the present study, it is observed that the outcomes of the hydrogel treatments with erythrocytes and WBCs are dependent on complex interactions of biophysical parameters such as viscosity and osmosis and biochemical variables including that of free-radical scavenging potential, membrane permeability, intracellular and extracellular accumulation of hydrogels, and changes in molecular trafficking across the cells due to the presence of hydrogels.

2.4 Conclusion

In conclusion, we have successfully developed novel Amoc-capped dipeptide-based injectable, self-healable, and shape-memory hydrogels with inherent

antibacterial properties for biomedical applications. Self-supporting hydrogels were obtained through molecular self-assembly of Amoc-capped dipeptides at physiological conditions (pH 7.4, 37 °C). The noncovalent interactions such as hydrogen bonding and π-π stacking interactions are the driving force for the self-assembly of Amoc-capped dipeptides. TEM and SEM revealed 3D dense nanofibrillar networks of the hydrogels. The rheological experiments revealed that the hydrogels are robust and self-healing up to several cycles with nonsignificant loss of their strength. The self-assembly process was systematically analyzed by fluorescence spectroscopy, and the presence of a secondary structure in peptide hydrogels were confirmed by PXRD, FTIR, and CD spectroscopy experiments. The supramolecular aggregation behavior of peptide gelators were studied by concentration-dependent CD and fluorescence spectroscopy. Furthermore, these self-supporting hydrogel surfaces were used for biological applications. The antibacterial efficacy of the hydrogels was evaluated against two Gram-positive and three Gram-negative bacteria. These hydrogels showed potent antibacterial efficacy against Gram-positive bacteria, whereas the higher concentrations of hydrogel **2** showed antibacterial efficacy against Gram-positive and Gram-negative pathogenic bacteria. The hemolysis study suggests that hydrogels are hemocompatible. Furthermore, cytotoxicity of hydrogels was investigated against hWBCs, and the data from MTT assay revealed that both the hydrogels were biocompatible toward the human cells. The biosafety parameters of hydrogels were also evaluated by direct mixing of cells with the hydrogels. In accordance with MTT data, LPO data also revealed that these hydrogels decrease LPO values and demonstrated that hydrogels are safe toward the human cell membrane. These experiments confirmed that our designed hydrogels satisfy the increasing demand of injectable biomaterials for the localized bacterial infections and biomaterial implantations.

2.5 References

(1) Du X., Zhou J., Shi J., Xu B. (2015), Supramolecular hydrogelators and hydrogels: from soft matter to molecular biomaterials, Chem. Rev., 115, 13165-13307 (DOI: 10.1021/acs.chemrev.5b00299).

(2) Luo Z., Zhang S. (2012), Designer nanomaterials using chiral self-assembling peptide systems and their emerging benefit for society, Chem. Soc. Rev., 41, 4736-4754 (DOI: 10.1039/C2CS15360B).

(3) Zhan J., Cai Y., Ji S., He S., Cao Y., Ding D., Wang L., Yang Z. (2017), Spatiotemporal control of supramolecular self-assembly and function, ACS Appl. Mater. Interfaces, 9, 10012-10018 (DOI: 10.1021/acsami.7b00784).

(4) Amabilino D. B., Smith D. K., Steed J. W. (2017), Supramolecular materials, Chem. Soc. Rev., 46, 2404-2420 (DOI: 10.1039/C7CS00163K).

(5) Das A. K., Maity I., Parmar H. S., McDonald T. O., Konda M. (2015), Lipase-catalyzed dissipative self-assembly of a thixotropic peptide bolaamphiphile hydrogel for human umbilical cord stem-cell proliferation, Biomacromolecules, 16, 1157-1168 (DOI: 10.1021/bm501835v).

(6) Zhao F., Ma M. L., Xu B. (2009), Molecular hydrogels of therapeutic agents, Chem. Soc. Rev., 38, 883-891 (DOI: 10.1039/B806410P).
(7) Li J., Geng L., Wang G., Chu H., Wei H. (2017), Self-healable gels for use in wearable devices., Chem. Mater., 29, 8932-8952 (DOI: 10.1021/acs.chemmater.7b02895).
(8) Deming T. J. (2014), Preparation and development of block copolypeptide vesicles and hydrogels for biological and medical applications., Wiley Interdiscip. Rev.: Nanomed. Nanobiotechnol., 6, 283-297 (DOI: 10.1002/wnan.1262).
(9) Bevilacqua M. P., Huang D. J., Wall B. D., Lane S. J., Edwards III C. K., Hanson J. A., Benitez D., Solomkin J. S., Deming T. J. (2017), Amino acid block copolymers with broad antimicrobial activity and barrier properties, Macromol. Biosci., 17, 1600492 (DOI: 10.1002/mabi.201600492).
(10) Zhang Z., Wang X., Wang Y., Hao J. (2018), Rapid-forming and self-healing agarose-based hydrogels for tissue adhesives and potential wound dressings, Biomacromolecules, 19, 980-988 (DOI: 10.1021/acs.biomac.7b01764).
(11) Wang R., Li Q., Chi B., Wang X., Xu Z., Xu Z., Chen S., Xu H. (2017), Enzyme-induced dual-network ε-poly-l-lysine-based hydrogels with robust self-healing and antibacterial performance, Chem. Commun., 53, 4803-4806 (DOI: 10.1039/C6CC09326D).
(12) Hoque J., Konai M. M., Sequeira S. S., Samaddar S., Haldar J. (2016), Antibacterial and antibiofilm activity of cationic small molecules with spatial positioning of hydrophobicity: an in vitro and in vivo evaluation, J. Med. Chem., 59, 10750-10762 (DOI: 10.1021/acs.jmedchem.6b01435).
(13) Li L., Yan B., Yang J., Huang W., Chen L., Zeng H. (2017), Injectable self-healing hydrogel with antimicrobial and antifouling properties, ACS Appl. Mater. Interfaces, 9, 9221-9225 (DOI: 10.1021/acsami.6b16192).
(14) Roy S., Das P. K. (2008), Antibacterial hydrogels of amino acid-based cationic amphiphiles, Biotechnol. Bioeng., 100, 756-764 (DOI: 10.1002/bit.21803).
(15) Wu J., Hou S., Ren D., Mather P. T. (2009), Antimicrobial properties of nanostructured hydrogel webs containing silver, Biomacromolecules, 10, 2686-2693 (DOI: 10.1021/bm900620w).
(16) Fullenkamp D. E., Rivera J. G., Gong Y. -K., Lau K. H. A., He L., Varshney R., Messersmith P. B. (2012), Mussel-inspired silver-releasing antibacterial hydrogels, Biomaterials, 33, 3783-3791 (DOI: 10.1016/j.biomaterials.2012.02.027).
(17) Lakes A. L., Peyyala R., Ebersole J. L., Puleo D. A., Hilt J. Z., Dziubla T. D. (2014), Synthesis and characterization of an antibacterial hydrogel containing covalently bound vancomycin, Biomacromolecules, 15, 3009-3018 (DOI: 10.1021/bm5006323).
(18) Nandi N., Gayen K., Ghosh S., Bhunia D., Kirkham S., Sen S. K., Ghosh S., Hamley I. W., Banerjee A. (2017), Amphiphilic peptidebased supramolecular, non-cytotoxic stumuli-responsive hydrogels with antibacterial activity, Biomacromolecules, 18, 3621-3629 (DOI: 10.1021/acs.biomac.7b01006).

(19) Hancock R. E. W., Sahl H.-G. (2006), Antimicrobial and host-defense peptides as new anti-infective therapeutic strategies, Nat. Biotechnol., 24, 1551-1557 (DOI: 10.1038/nbt1267).
(20) Wimley W. C., Hristova K. (2011), Antimicrobial peptides: successes, challenges and unanswered questions, J. Membr. Biol., 239, 27-34 (DOI: 10.1007/s00232-011-9343-0).
(21) Irwansyah I., Li Y.-Q., Shi W., Qi D., Leow W. R., Tang M. B. Y., Li S., Chen X. (2015), Gram-positive antimicrobial activity of amino acid-based hydrogels, Adv. Mater., 27, 648-654 (DOI: 10.1002/adma.201403339).
(22) Giano M. C., Ibrahim Z., Medina S. H., Sarhane K. A., Christensen J. M., Yamada Y., Brandacher G., Schneider J. P. (2014), Injectable bioadhesive hydrogels with innate antibacterial properties, Nat. Commun., 5, 4095 (DOI: 10.1038/ncomms5095).
(23) Shirbin S. J., Lam S. J., Chan N. J.-A., Ozmen M. M., Fu Q., O'Brien-Simpson N., Reynolds E. C., Qiao G. G. (2016), Polypeptide-based macroporous cryogels with inherent antimicrobial properties: the importance of a macroporous structure, ACS Macro Lett., 5, 552-557 (DOI: 10.1021/acsmacrolett.6b00174).
(24) Jiang L., Xu D., Sellati T. J., Dong H. (2015), Self-assembly of cationic multidomain peptide hydrogels: supramolecular nanostructure and rheological properties dictate antimicrobial activity, Nanoscale, 7, 19160-19169 (DOI: 10.1039/C5NR05233E).
(25) Watson E., Tatara A. M., Kontoyiannis D. P., Mikos A. G. (2017), Inherently antimicrobial biodegradable polymers in tissue engineering, ACS Biomater. Sci. Eng., 3, 1207-1220 (DOI: 10.1021/acsbiomaterials.6b00501).
(26) O'Connell G., Garcia J., Amir J. (2017), 3D bioprinting: new directions in articular cartilage tissue engineering, ACS Biomater. Sci. Eng., 3, 2657-2668 (DOI: 10.1021/acsbiomaterials.6b00587).
(27) Pang J. H., Farhatnia Y., Godarzi F., Tan A., Rajadas J., Cousins B. G., Seifalian A. M. (2015), In situ endothelialization: bioengineering considerations to translation, Small, 11, 6248-6264 (DOI: 10.1002/smll.201402579).
(28) Lee K. Y., Mooney D. J. (2001), Hydrogels for tissue engineering, Chem. Rev., 101, 1869-1880 (DOI: 10.1021/cr000108x).
(29) Zhang J., Muirhead B., Dodd M., Liu L., Xu F., Mangiacotte N., Hoare T., Sheardown H. (2016), An injectable hydrogel prepared using a PEG/vitamin E copolymer facilitating aqueous-driven gelation, Biomacromolecules, 17, 3648-3658 (DOI: 10.1021/acs.biomac.6b01148).
(30) Yu L., Zhang Z., Zhang H., Ding J. (2009), Mixing a sol and a precipitate of block copolymers with different block ratios leads to an injectable hydrogel, Biomacromolecules, 10, 1547-1553 (DOI: 10.1021/bm900145g).
(31) Unterman S., Charles L. F., Strecker S. E., Kramarenko D., Pivovarchik D., Edelman E. R., Artzi N. (2017), Hydrogel nanocomposites with independently tunable rheology and mechanics, ACS Nano, 11, 2598-2610 (DOI: 10.1021/acsnano.6b06730).

(32) Huang Q., Zou Y., Arno M. C., Chen S., Wang T., Gao J., Dove A. P., Du J. (2017), Hydrogel scaffolds for differentiation of adipose-derived stem cells, Chem. Soc. Rev., 46, 6255-6275 (DOI: 10.1039/C6CS00052E).
(33) Zhou M., Smith A. M., Das A. K., Hodson N. W., Collins R. F., Ulijn R. V., Gough J. E. (2009), Self-assembled peptide-based hydrogels as scaffolds for anchorage-dependent cells, Biomaterials, 30, 2523-2530 (DOI: 10.1016/j.biomaterials.2009.01.010).
(34) Park H., Guo X., Temenoff J. S., Tabata Y., Caplan A. I., Kasper F. K., Mikos A. G. (2009), Effect of swelling ratio of injectable hydrogel composites on chondrogenic differentiation of encapsulated rabbit marrow mesenchymal stem cells in vitro, Biomacromolecules, 10, 541-546 (DOI: 10.1021/bm801197m).
(35) Guvendiren M., Lu H. D., Burdick J. A. (2012), Shear-thinning hydrogels for biomedical applications, Soft Matter, 8, 260-272 (DOI: 10.1039/C1SM06513K).
(36) Raeburn J., Cardoso A. Z., Adams D. J. (2013), The importance of the self-assembly process to control mechanical properties of low molecular weight hydrogels, Chem. Soc. Rev., 42, 5143-5156 (DOI: 10.1039/C3CS60030K).
(37) Salick D. A., Kretsinger J. K., Pochan D. J., Schneider J. P. (2007), Inherent antibacterial activity of a peptide-based beta-hairpin hydrogel, J. Am. Chem. Soc., 129, 14793-14799 (DOI: 10.1021/ja076300z).
(38) Schierholz J. M., Beuth J. Implant infections: a haven for opportunistic bacteria, J. Hosp. Infect., 2001, 49, 87-93 (DOI: 10.1053/jhin.2001.1052).
(39) Song A., Rane A. A., Christman K. L. (2012), Antibacterial and cell-adhesive polypeptide and poly(ethylene glycol) hydrogel as a potential scaffold for wound healing, Acta Biomater., 8, 41-50 (DOI: 10.1016/j.actbio.2011.10.004).
(40) An Y. H., Alvi F. I., Kang Q., Laberge M., Drews M. J., Zhang J., Matthews M. A., Arciola C. R. (2005), Effects of sterilization on implant mechanical property and biocompatibility, Int. J. Artif. Organs, 28, 1126-1137 (DOI: 10.1177/039139880502801110).
(41) Biswas S., Rasale D. B., Das A. K. (2016), Blue light emitting self-healable graphene quantum dot embedded hydrogels, RSC Adv., 6, 54793-54800 (DOI: 10.1039/C6RA06587B).
(42) Datta S., Samanta S. K., Bhattacharya S. (2013), Induction of supramolecular chirality in the self-assemblies of lipophilic pyrimidine derivatives by choice of the amino acid-based chiral spacer, Chem.Eur. J., 19, 11364-11373 (DOI: 10.1002/chem.201300605).
(43) Zhang X., Gao Y., Lin Y., Hu J., Ju Y. (2015), Photo-induced conversion from supramolecular to covalently linked polymers based on anthracene appended amphiphiles, Polym. Chem., 6, 4162-4166 (DOI: 10.1039/C5PY00476D).
(44) Hu J., Wang P., Lin Y., Yang S., Song B., Wang Q. (2014), Dual responsive supramolecular amphiphiles: guest molecules dictate the architecture of pyridinium-tailored anthracene assemblies, Org. Biomol. Chem., 12, 4820-4823 (DOI: 10.1039/C4OB00936C).

(45) Liyanage W., Nilsson B. L. (2016), Substituent effects on the self-assembly/coassembly and hydrogelation of phenylalanine derivatives, Langmuir, 32, 787-799 (DOI: 10.1021/acs.langmuir.5b03227).
(46) Yan X., Zhu P., Li J. (2010), Self-assembly and application of diphenylalanine-based nanostructures, Chem. Soc. Rev., 39, 1877-1890 (DOI: 10.1039/B915765B).
(47) Liu H., Cong D., Li B., Ye L., Ge Y., Tang X., Shen Y., Wen Y., Wang J., Zhou C., Yang B. (2017), Discrete dimeric anthracene stackings in solids with enhanced excimer fluorescence, Cryst. Growth Des., 17, 2945-2949 (DOI: 10.1021/acs.cgd.7b00460).
(48) Kornmueller K., Lehofer B., Leitinger G., Amenitsch H., Prassl R. (2018), Peptide self-assembly into lamellar phases and the formation of lipid-peptide nanostructures, Nano Res., 11, 913-928 (DOI: 10.1007/s12274-017-1702-4).
(49) Barth A., Zscherp C. (2002), What vibrations tell about proteins, Q. Rev. Biophys., 35, 369-430 (DOI: 10.1017/S0033583502003815).
(50) Cheng G., Castelletto V., Moulton C. M., Newby G. E., Hamley I. W. (2010), Hydrogelation and self-assembly of fmoc-tripeptides: unexpected influence of sequence on self-assembled fibril structure, and hydrogel modulus and anisotropy, Langmuir, 26, 4990-4998 (DOI: 10.1021/la903678e).
(51) Kong J., Yu S. (2007), Fourier transform infrared spectroscopic analysis of protein secondary structures, Acta Biochim. Biophys. Sin., 39, 549-559 (DOI: 10.1111/j.1745-7270.2007.00320.x).
(52) Makin O. S., Serpell L. C. (2005), Structures for amyloid fibrils, FEBS J., 272, 5950-5961 (DOI: 10.1111/j.1742-4658.2005.05025.x).
(53) Zouev I., Cao D.-K., Sreevidya T. V., Telzhensky M., Botoshansky M., Kaftory M. (2011), Photodimerization of anthracene derivatives in their neat solid state and in solid molecular peptides, Cryst. Eng. Comm., 13, 4376-4381 (DOI: 10.1039/C0CE00739K).
(54) Hinoue T., Shigenoi Y., Sugino M., Mizobe Y., Hisaki I., Miyata M., Tohnai N. (2012), Regulation of π-stacked anthracene arrangement for fluorescence modulation of organic solid from monomer to excited oligomer emission, Chem. Eur. J., 18, 4634-4643 (DOI: 10.1002/chem.201103518).
(55) Shao H., Parquette J. R. (2010), A π-conjugated hydrogel based on an fmoc-dipeptide naphthalene diimide semiconductor, Chem. Commun., 46, 4285-4287 (DOI: 10.1039/C0CC00701C).
(56) Ikeda M., Tanida T., Yoshii T., Hamachi I. (2011), Rational molecular design of stimulus-responsive supramolecular hydrogels based on dipeptides, Adv. Mater., 23, 2819-2822 (DOI: 10.1002/adma.201004658).
(57) Hifsudheen M., Mishra R. K., Vedhanarayanan B., Praveen V. K., Ajayaghosh A. (2017), The helix to super-helix transition in the self-assembly of π-systems: superseding of molecular chirality at hierarchical level, Angew. Chem. Int. Ed., 56, 12634-12638 (DOI: 10.1002/anie.201707392).
(58) George S. J., Ajayaghosh A., Jonkheijm P., Schenning A. P. H. J., Meijer E. W. (2004), Coiled-coil gel nanostructures of oligo(pphenylenevinylene)s:

gelation-induced helix transition in a higher-order supramolecular self-assembly of a rigid π-conjugated system, Angew. Chem. Int. Ed., 43, 3422-3425 (DOI: 10.1002/anie.200453874).
(59) Lee J., Kang D., Choi J., Huang W., Wadman M., Barron A. E., Seo J. (2018), Effect of side chain hydrophobicity and cationic charge on antimicrobial activity and cytotoxicity of helical peptoids, Bioorg. Med. Chem. Lett., 28, 170-173 (DOI: 10.1016/j.bmcl.2017.11.034).
(60) Liu G., Liu J., Feng C., Zhao Y. (2017), Unexpected right-handed helical nanostructures co-assembled from l-phenylalanine derivatives and achiral bipyridines, Chem. Sci., 8, 1769-1775 (DOI: 10.1039/C6SC04808K).
(61) Woody R. W. (1978), Aromatic side-chain contributions to the far ultraviolet circular dichroism of peptides and proteins, Biopolymers, 17, 1451-1467 (DOI: 10.1002/bip.1978.360170606).
(62) Kelly S. M., Jess T. J., Price N. C. (2005), How to study proteins by circular dichroism, Biochim. Biophys. Acta-Proteins Proteomics, 1751, 119-139 (DOI: 10.1016/j.bbapap.2005.06.005).
(63) Fang Z., Zheng N., Zhao Q., Xie T. (2017), Healable, reconfigurable, reprocessable thermoset shape memory polymer with highly tunable topological rearrangement kinetics, ACS Appl. Mater. Interfaces, 9, 22077-22082 (DOI: 10.1021/acsami.7b05713).
(64) Hart L. R., Li S., Sturgess C., Wildman R., Jones J. R., Hayes W. (2016), 3D printing of biocompatible supramolecular polymers and their composites, ACS Appl. Mater. Interfaces, 8, 3115-3122 (DOI: 10.1021/acsami.5b10471).
(65) Biswas A., Malferrari S., Kalaskar D. M., Das A. K. (2018), Arylboronate esters mediated self-healable and biocompatibledynamic g-quadruplex hydrogels as promising 3d-bioinks, Chem. Commun., 54, 1778-1781 (DOI: 10.1039/C7CC09051J).
(66) Du H., Wang Y., Yao X., Luo Q., Zhu W., Li X., Shen Z. (2016), Injectable cationic hydrogels with high antibacterial activity and low toxicity, Polym. Chem., 7, 5620-5624 (DOI: 10.1039/C6PY01346E).
(67) log P value was calculated by using online prediction program. http://www.molinspiration.com.
(68) Brown L., Wolf J. M., Prados-Rosales R., Casadevall A. (2015), Through the wall: extracellular vesicles in gram-positive bacteria, mycobacteria and fungi, Nat. Rev. Microbiol., 13, 620-630 (DOI: 10.1038/nrmicro3480).
(69) Maity I., Parmar H. S., Rasale D. B., Das A. K. (2014), Self-programmed nanovesicle to nanofibre transformation of a dipeptide appended bolaamphiphile and its dose dependent cytotoxic behavior, J. Mater. Chem. B, 2, 5272-5279 (DOI: 10.1039/C4TB00365A).
(70) Parmar H. S., Kar A. (2008), Medicinal values of fruit peels from citrus sinensis, punica granatum, and musa paradisiaca with respect to alterations in tissue lipid peroxidation and serum concentration of glucose, insulin and thyroid hormones, J. Med. Food, 11, 376381 (DOI: doi.org/10.1089/jmf.2006.010).

Chapter 3

Investigations of Anti-Inflammatory Activity of a Peptide-Based Hydrogel using Rat Air Pouch Model

3.1 Introduction

An increasing demand of functional materials in various interdisciplinary areas of research has emphasized the development of smart functional biomaterials, which feature a variety of applications in the areas of drug delivery, tissue engineering, wound healing, antimicrobial therapy, and 3D printing.[1-13] Molecular self-assembly is adopted to construct a class of biomaterials.[14-16] Molecular self-assembly is a fundamental and ubiquitous process in nature, which plays an imperative role in many areas of chemical biology for the spontaneous construction of supramolecular architectures.[17-21] Self-assembling cationic and surfactant-like peptides form various supramolecular nanostructures, which enhance antimicrobial activity by interacting with lipid membranes.[22-24] Peptide-based low-molecular-weight hydrogels (LMWHs) have drawn significant attention owing to their therapeutic values and potential applications in the areas of biomedicine.[25-27] The high-water content, biocompatibility, hemocompatibility, and non-immunogenicity of peptide-based LMWHs make them attractive candidates for biomedical applications.[28-30] Additionally, peptide-based LMWHs show thixotropic and self-healing behavior.[31,32] The thixotropic properties of hydrogels enable rapid gel-sol-gel transitions that serve as carriers for cell incorporation and transfer to the target site.[33] However, several problems are associated with the implantable biomaterials because of infection and inflammation induced by the implantable biomaterials at the target site.[2,34] Therefore, the development of injectable and implantable biomaterials with innate anti-inflammatory and antimicrobial activity has become a demanding task to minimize the inflammatory response and infections induced by the biomaterials.[35-37] A number of peptide-based LMWHs have been developed, and their in vitro cytotoxicity was evaluated using different cell lines.[32,37] Despite their in vitro biocompatibility, it is noteworthy that their potential biocompatibility must be confirmed after in vivo injection or implantation of peptide-based LMWHs.[38-40] Inflammation is a hallmark of host immune response against foreign invaders, materials, and pathogens which is mediated via cytokine signaling and immune cell infiltration.[41] It is widely accepted that biomaterials having inherent anti-inflammatory activity prevent the undesired immune response by inhibiting cyclooxygenase response. [42,43] Nevertheless, peptide-based nonsteroidal LMWHs with an ability to alleviate foreign body response using an in vivo study with the rat air pouch model would have great attraction in current research. The rat air pouch is one of the most elegant in vivo models to study acute-granulomatous inflammation. In this model, an air pouch is made by the subcutaneous injection of sterile air over several days into the thoracic region of the back of the rat. Injection of the inflammatory agent carrageenan induces an oxidative stress response, increment in the fluid exudate volume, and a histological change in the inner cellular lining of the rat air pouch.[44-46] In the present work, these parameters were quantified and used to determine the extent of the anti-inflammatory activity of a synthesized peptide-based LMWH.

3.2 Experimental Section

3.2.1 Materials and Methods

Materials required for this study were purchased from commercial sources and used without further purification. 9-Anthracenemethanol and 4-nitrophenyl chloroformate were purchased from Sigma-Aldrich, U.S.A. L-leucine (L), L-phenylalanine (F), dicyclohexylcarbodiimide (DCC), 1-hydroxybenzotriazole (HOBt) were purchased from SRL, India. All solvents were purchased from Merck and distilled prior to use. Tetrahydrofuran (THF) and *N,N'*-dimethylformamide (DMF) were dried using the standard procedure. Lambda carrageenan (Type IV) was purchased from Himedia Pvt. Ltd. Mumbai, India. Thin-layer chromatography (TLC) was performed on pre-coated silica gel plates (Kieselgel 60 F_{254}, Merck). Peptide and their intermediates were purified by Flash Chromatography (TELEDYNE ISCO, USA; model: CombiFlash®Rf+) using silica gel (100-200 mesh) with EtOAc/hexane (ratio as required) as eluent. HPLC analysis was carried out using a Dionex HPLC-Ultimate 3000 (High Performance Liquid Chromatography) pump. A Dionex Acclaim^{TM} 120 C18 column of 250 mm length with an internal diameter 4.6 mm and 5 µm fused silica particles at a flow rate of 1 mL min^{-1} coupled with UV-Vis detector. NMR spectroscopy was performed in $CDCl_3$ and DMSO-d_6 on a Bruker AV 400 MHz spectrometer. The chemical shifts (δ) are reported in ppm, downfield of tetramethylsilane (TMS); peak multiplicities are reported as follows: singlet (s), doublet (d), triplet (t), quartet (q) and multiplet (m). FTIR spectroscopy was performed on KBr pellets on a Bruker Tensor 27 FTIR spectrophotometer. Electrospray ionization mass spectrometry (ESI-MS) was acquired on a Bruker micrOTOF-Q II mass spectrometer. The conventional solution phase methodology was used for the synthesis of peptide **3**.

3.2.2 Synthesis of 3

Scheme 3.1 Synthetic pathway of **3**

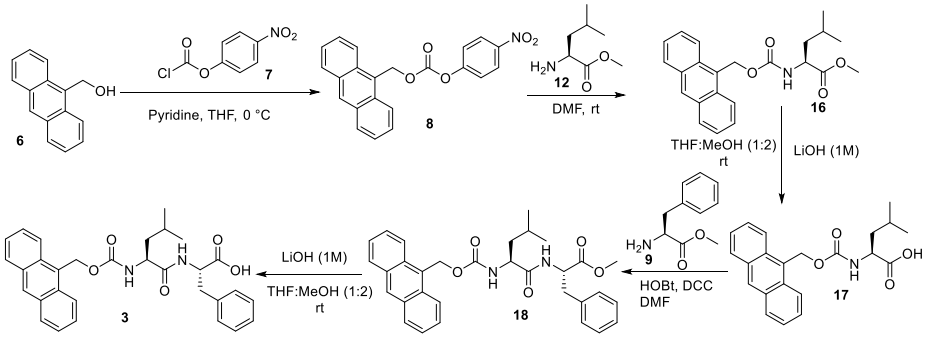

3.2.2.1 Synthesis of 8

7 (1.5 g, 7.44 mmol) was solubilized in dry THF under N_2 atmosphere. The solution was ice-cooled and pyridine (0.648 g, 8.18 mmol) was added into the cold solution. The white slurry was obtained after the addition of pyridine. **6** (1.29 g, 6.2 mmol) was solubilized in dry THF and the solution was added into the reaction mixture by several portions. The reaction mixture was allowed to stir overnight at room temperature. Product conversion was checked by TLC. After completion of the reaction, THF was evaporated by a rotary evaporator. The crude reaction mixture

was diluted with ethyl acetate (50 mL) and the mixture was washed with 1 M HCl (3 × 30 mL) and successively with brine. The yellow-green product was obtained by evaporating the solvent under reduced pressure. The product was recrystallized by using benzene and yellow needle-shaped crystal of **8** was further used for the synthesis of **3**.

Yield: 1.7 g (73%). ^{1}H NMR (400 MHz, $CDCl_3$): δ = 8.58 (s, 1H, Amoc), 8.42-8.40 (d, *J* = 8.88 Hz, 2Hs, Ph), 8.26- 8.24 (d, *J*= 8.44 Hz, 2Hs, Amoc), 8.08-8.06 (d, *J* = 8.40 Hz, 2H, Amoc), 7.65-7.61 (t, *J* = 7 Hz, 2H, Amoc), 7.55-7.51 (t, *J* = 7.48 Hz, 2H, Amoc), 7.37-7.35 (d, *J* = 8.36 Hz, 2H, Ph), 6.39 (s, 2H, Amoc) ppm.

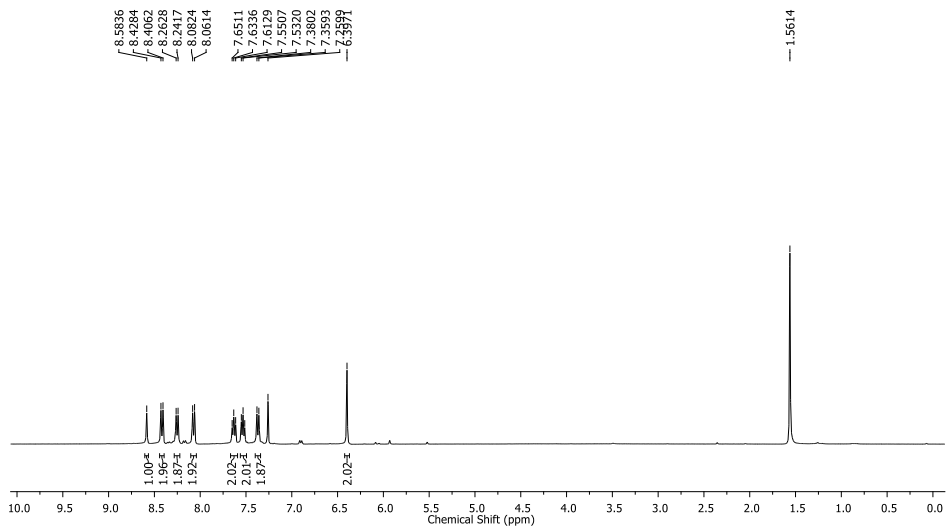

Figure 3.1 ^{1}H NMR spectrum (400 MHz) of **8** in $CDCl_3$.

3.2.2.2 Synthesis of 16

1.5 g (4.02 mmol) of **8** was dissolved in 3 mL dry DMF. The reaction mixture was ice-cooled. The hydrochloride salt of **12** (1.46 g, 8.04 mmol) was neutralized using saturated Na_2CO_3 (10 mL) solution and the product was extracted using ethyl acetate (3 × 30 mL). The neutralized **12** solution was concentrated and added to the reaction mixture and allowed to stir for 12 h. Product conversion was confirmed by TLC. After completion of the reaction, ethyl acetate (25 mL) was added and washed with 1 M HCl (3 × 30 mL), saturated Na_2CO_3 solution (3 × 30 mL) and then with brine. Solid yellow **16** was obtained after evaporating the solvent under reduced pressure.

Yield: 1.32 g (86%); FT-IR (KBr): ῡ = 3313 (s, NH), 1738 (s, COOMe), 1682 (s, amide I band), 1625 (s, amide I band), 1535 (s, amide II band) cm^{-1}; ^{1}H NMR (400 MHz, $CDCl_3$): δ = 8.50 (s, 1H, Amoc), 8.38–8.36(d, *J* = 8.60 Hz, 2H, Amoc), 8.03–8.01 (d, *J* = 8.28 Hz, 2H, Amoc), 7.59–7.47 (m, 4H, Amoc), 6.21–6.10 (q, 2H, Amoc), 5.09–5.07 (d, *J* = 7.56 Hz, 1H, NH), 4.44 (m, 1H, C^{α} H of Leu), 3.72 (s, 3H, OCH_3), 1.64–1.60 (m, 1H, C^{γ} H of Leu), 1.57–1.48 (m, 2H, C^{β} Hs of Leu), 0.97–0.90 (t, 6H, C^{δ} Hs of Leu) ppm; MS (ESI): *m/z* calcd for $C_{23}H_{25}NO_4$: 402.1681 $[M+Na]^+$; found: 402.1680.

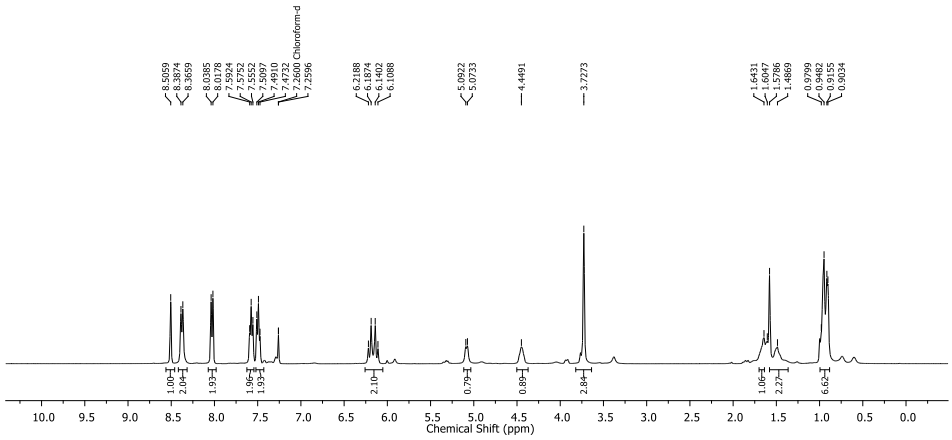

Figure 3.2 ^{1}H NMR spectrum (400 MHz) of **16** in DMSO-d_6.

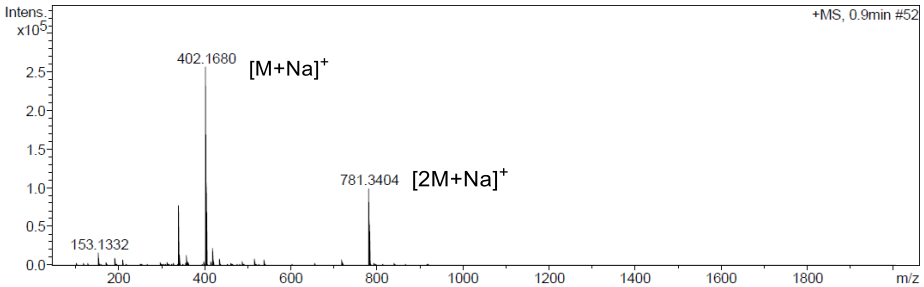

Figure 3.3 ESI-MS spectrum of **16**.

3.2.2.3 Synthesis of 17

1.0 g (2.63 mmol) of **16** was completely solubilized in the mixture of THF:MeOH (1:2, 30 mL). In the reaction mixture, 1 M LiOH (2 mL) solution was added slowly. The progress of hydrolysis was monitored by TLC and reaction mixture was stirred up to 6 h for complete hydrolysis. After the completion of the reaction, excess solvent was evaporated and diluted with 30 mL of distilled water. The aqueous solution of the product was taken into the separating funnel and slowly washed with diethyl ether (20 mL). The aqueous layer was collected and cooled in an ice bath. Then, the solution was acidified with 1 M HCl. The pH of aqueous layer was adjusted to 2 and the product was extracted with ethyl acetate (3 × 30 mL). The ethyl acetate layer was dried over anhydrous Na_2SO_4 and evaporated under reduced pressure to obtain **17** as yellow sticky product.

Yield: 0.850 g (88%); FT-IR (KBr): $\bar{\upsilon}$ = 3337 (s, NH), 1712 (s, COOH), 1682 (s, amide I band), 1623 (s, amide I band), 1523 (s, amide II band) cm^{-1}; ^{1}H NMR (400 MHz, DMSO-d_6): δ = 8.68 (s, 1H, Amoc), 8.40-8.38 (d, *J* = 8.8 Hz, 2H, Amoc), 8.14-8.11 (d, *J* = 8.28 Hz, 2H, Amoc), 7.62-7.53 (m, 4H, Amoc), 7.45-7.43 (d, *J* = 8.04 Hz, 1H, NH), 6.08 (s, 2H, Amoc), 4.01-3.98 (m, 1H, C^{α} H of Leu), 1.58 (m, 1H, C^{γ} H of Leu), 1.47-1.42 (m, 2H, C^{β} Hs of Leu) 0.84-0.81 (m, 6H, C^{δ} Hs of Leu) ppm; MS (ESI): *m/z* calcd for $C_{22}H_{23}NO_4$: 388.1525 $[M+Na]^+$; found: 388.1611.

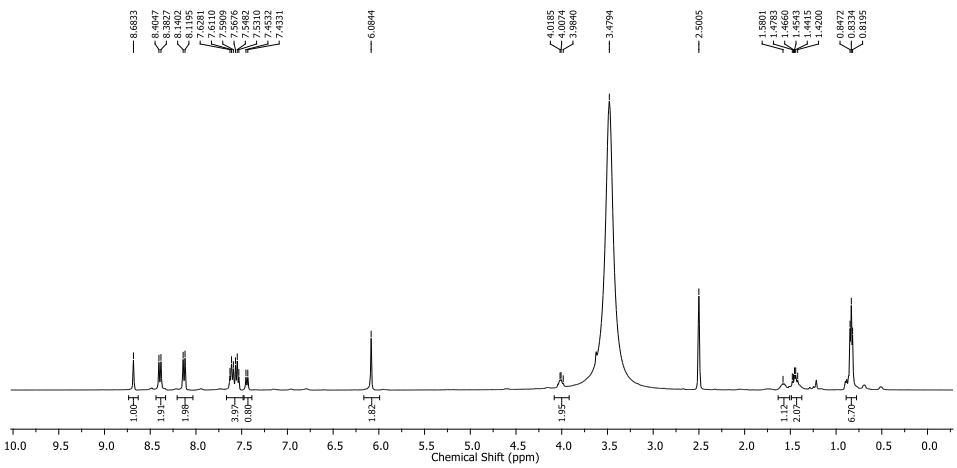

Figure 3.4 ^{1}H NMR spectrum (400 MHz) of **17** in DMSO-d_6.

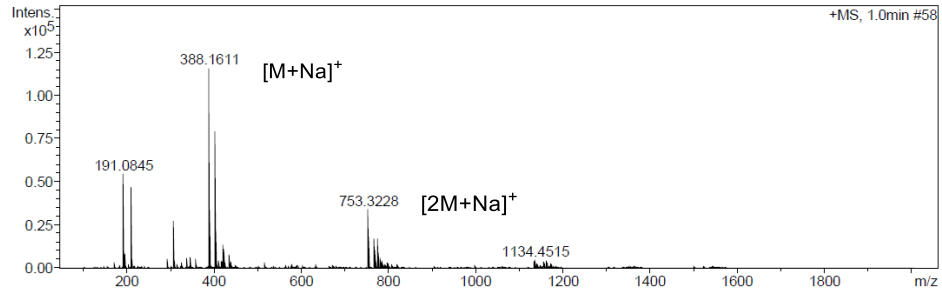

Figure 3.5 ESI-MS spectrum of **17**.

3.2.2.4 Synthesis of 18

0.7 g (1.91 mmol) of **4** and HOBt (0.361 g, 2.67 mmol) were stirred in 3 mL of DMF. A neutralized solution of **9** (0.825 g, 3.82 mmol) was extracted from its corresponding hydrochloride salt. It was concentrated and added to the reaction mixture followed by coupling agent DCC (0.551 g, 2.67 mmol) at 0 °C and allowed to stir at room temperature for 12 h. After the reaction, the reaction mixture was diluted with ethyl acetate and the organic layer was washed with 1 M HCl (3 × 30 mL), saturated Na_2CO_3 (3 × 30 mL) and brine solution. Ethyl acetate layer was dried over anhydrous Na_2SO_4 and evaporated under vacuum to found **18** as yellow-orange solid.

Yield: 0.880 g (87%); FT-IR (KBr): $\bar{\upsilon}$ = 3294 (s, NH), 1741 (s, COOMe), 1688 (s, amide I band), 1650 (s, amide I band), 1537 (s, amide II band) cm^{-1}; ^{1}H NMR (400 MHz, DMSO-d_6): δ = 8.69 (s, 1H, Amoc), 8.40-8.38 (d, *J* = 8.68 Hz, 2H, Amoc), 8.24 (d, *J* = 7.4 Hz, 1H, NH), 8.14-8.12 (d, *J* = 8.16 Hz, 2H, Amoc), 7.60-7.55 (m, 4H, Amoc), 7.24-7.17 (m, 6H, NH and Ph of Phe), 6.07 (s, 2H, Amoc), 4.47-4.42 (m, 1H, C^{α} H of Phe), 4.13-4.07 (m, 1H, C^{α} H of Leu), 3.54 (s, 3H, OCH_3), 3.00-2.93 (m, 2H, C^{β} Hs of Phe), 1.50-1.48 (m,1H, C^{γ} H of Leu), 1.32-1.29 (m, 2H, C^{β} Hs of Leu), 0.84-0.80 (m, 6H, C^{δ} Hs of Leu) ppm; MS (ESI): *m/z* calcd for $C_{32}H_{34}N_2O_5$: 549.2365 $[M+Na]^+$; found: 549.2521.

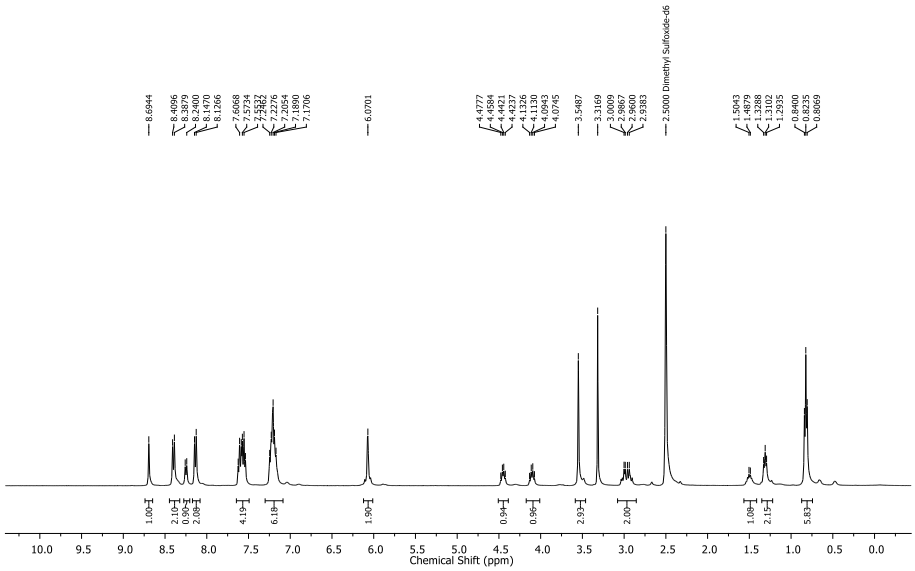

Figure 3.6 ^{1}H NMR spectrum (400 MHz) of **18** in DMSO-d_6.

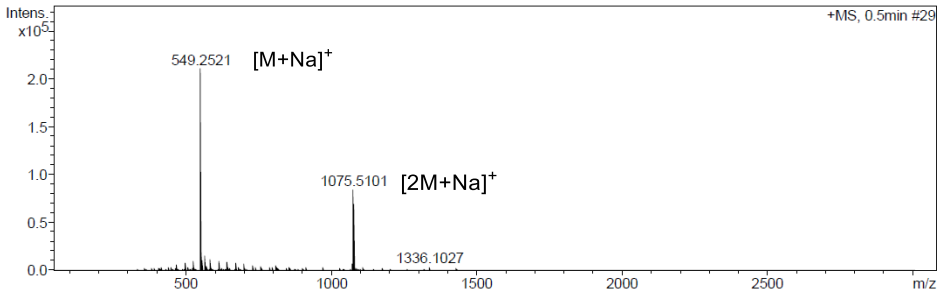

Figure 3.7 ESI-MS spectrum of **18**.

3.2.2.5 Synthesis of 3

0.5 g (0.95 mmol) of **18** was dissolved in 10 mL dry THF and 20 mL MeOH. In the reaction mixture, 1 M LiOH (6 mL) solution was added. The hydrolysis progress was monitored by TLC. The reaction mixture was stirred up to 4 h for complete hydrolysis. After the completion of reaction, excess solvent was evaporated and diluted with 50 mL of distilled water. The water mixture was taken in a separating funnel and slowly washed with diethyl ether (20 mL). The aqueous layer was collected and cooled in an ice bath. Then, the solution was acidified with 1 M HCl. The pH of aqueous layer was adjusted to 2 and the product was extracted with ethyl acetate (3 × 30 mL). The ethyl acetate layer was dried over anhydrous Na_2SO_4 and evaporated under reduced pressure to obtain **3** as white solid.

Yield: 0.391 g (80%); FT-IR (KBr): $\bar{\upsilon}$ = 3288 (s, NH), 1727 (s, COOH), 1687 (s, amide I band), 1647 (s, amide I band), 1531 (s, amide II band) cm^{-1}; ^{1}H NMR (400 MHz, DMSO-d_6): δ = 12.72 (s, 1H, COOH), 8.68 (s, 1H, Amoc), 8.40-8.38 (d, *J* = 8.68 Hz, 2H, Amoc), 8.14-8.12 (d, *J* = 8.16 Hz, 2H, Amoc), 8.03-8.01 (d, *J* = 7.68 Hz, 1H, NH), 7.60-7.55 (m, 4H, Amoc), 7.24-7.15 (m, 6H, NH and Ph of Phe), 6.11-6.02 (m, 2H, Amoc), 4.44-4.39 (m, 1H, C^{α} H of Phe), 4.12-4.07 (m, 1H, C^{α} H of Leu), 3.05-2.89 (m, 2H, C^{β} Hs of Phe), 1.52-1.48 (m, 1H, C^{γ} H of Leu), 1.33-1.30 (m, 2H, C^{β} Hs of Leu), 0.83-0.80 (t, *J* = 14.72 Hz, 6H, C^{δ} Hs of Leu) ppm;

^{13}C NMR (100 MHz, DMSO-d_6): δ = 172.76, 172.10, 155.99, 137.45, 130.92, 130.48, 129.18, 128.90, 128.61, 128.07, 127.29, 126.59, 126.33, 125.25, 124.22, 58.10, 53.29, 53.17, 36.66, 24.07, 22.90, 21.51 ppm; HRMS (ESI): *m/z* calcd for $C_{31}H_{32}N_2O_5$: 535.2209 $[M+Na]^+$; found: 535.2213.

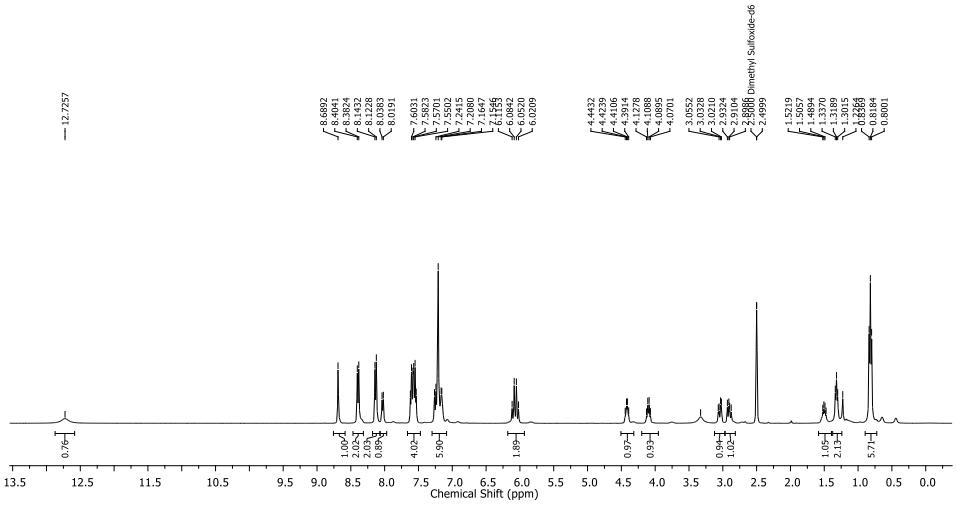

Figure 3.8 ^{1}H NMR spectrum (400 MHz) of **3** in DMSO-d_6.

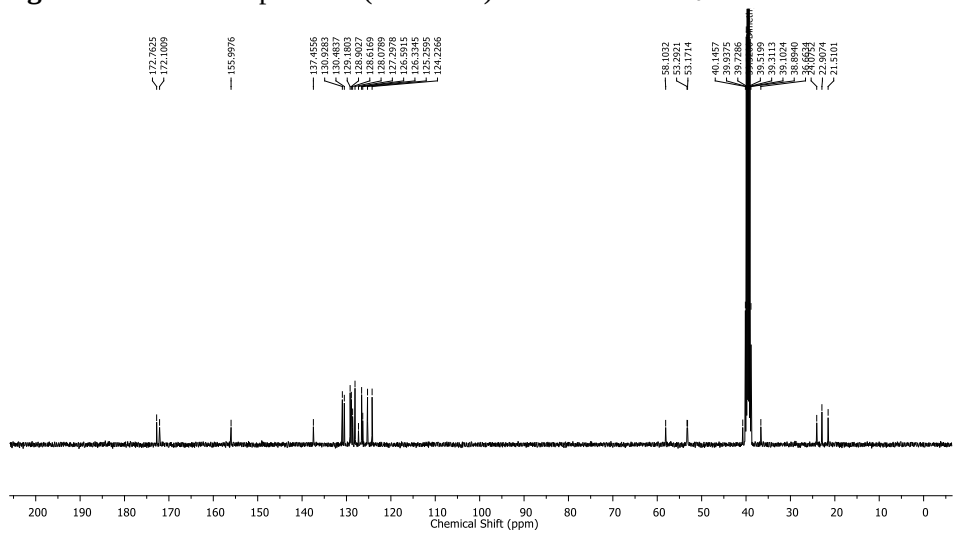

Figure 3.9 ^{13}C NMR spectrum (100 MHz) of **3** in DMSO-d_6.

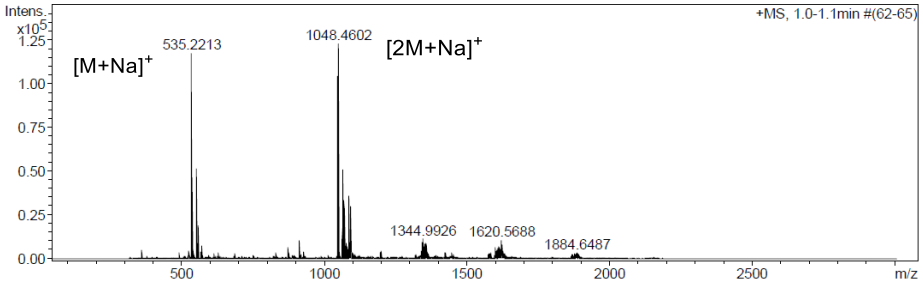

Figure 3.10 HRMS spectrum of **3**.

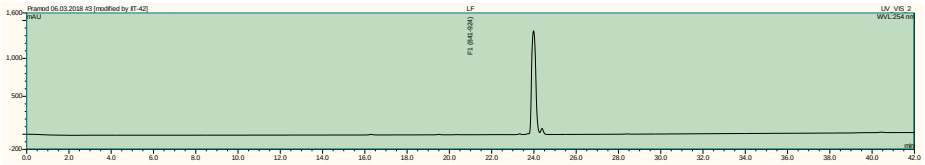

Figure 3.11 HPLC chromatogram of **3** at 254 nm.

3.2.3 Preparation of the Hydrogel

A self-supporting hydrogel of the peptide (molecular weight 512.5962) was prepared by using the pH method. a 10.25 mg portion of the peptide was suspended in 1 mL of ultrapure water (20 mM) in a glass vial. This suspension was partially solubilized by slow addition of aqueous 0.5 M NaOH and stirred for 30 min for complete solubilization of dipeptide. The pH of the solutions (pH 10) was decreased slowly by addition of 0.1 M HCl, and the final pH was maintained at 7.4. The viscous solution of the peptide was kept resting at 37 °C for 15 min to get a strong and self-supporting hydrogel. The formation of a stable and tough hydrogel was confirmed by the test tube inversion method.

3.2.4 Characterizations

The synthesized peptide **3** and the corresponding hydrogel **3** were characterized by various spectroscopic techniques. The absorption spectra of the diluted hydrogel were recorded using a Varian Cary 100 Bio UV/vis spectrophotometer at concentrations ranging from 5 to 400 μM. However, the absorption spectra are shown only in the concentration range from 5 to 100 μM because of saturation of absorption spectra at higher concentrations (200, 300, and 400 μM). Fluorescence emission and excitation spectra of the aqueous peptide (10 μM) and the corresponding hydrogel **3** (20 mM) were recorded on Horiba Scientific Fluoromax-4 spectrophotometer in a quart cuvette (10 × 10 mm^2) at 25 °C. The slit width for the emission and excitation spectra was set at 2 nm, and the data pitch was 1 nm. The emission spectra of the aqueous peptide and hydrogel were recorded at λ_{ex} 365 nm, and the data range was 375-600 nm. The excitation spectra of the aqueous peptide were recorded at λ_{em} 412 nm, and the data range was 402-250 nm. The excitation spectra of the hydrogel were recorded at λ_{em} 477 nm, and the data range was 467-250 nm. The concentration-dependent fluorescence spectra of the aqueous hydrogel (ranging from 0.062 to 15 mM) and hydrogel (20 mM) were recorded to investigate the supramolecular interactions between peptides. The critical aggregation concentration for the peptides was determined by a concentration-dependent fluorescence experiment by using a fluorescence intensity versus peptide concentration plot. A time-correlated single photon counting (TCSPC) instrument was used to measure decay traces of the hydrogels. TCSPC studies were performed on a Horiba Yovin (Model Fluorocube-01-NL) instrument. Samples were excited at λ_{ex} 375 nm using a picosecond diode laser, and emission was recorded at λ_{em} 412 and 477 nm for the peptide and hydrogel, respectively. The signals were collected at magic angle (54.701) polarization using a photomultiplier tube (TBX-07C) as a detector, which had a dark count of less than 20 cps. The instrument response function (IRF, fwhm B 140 ps) was recorded using a very dilute scattering solution. Data analysis was performed using IBH

DAS (version 6, HORIBA Scientific, Edison, NJ) decay analysis software. The excited state average lifetimes of the hydrogel was measured by using the equation

$$<\tau> = \sum_{i=1}^{n} \alpha_i \, \tau_i$$

where τ_i values are the fluorescence lifetimes of various fluorescent species and ai values are the normalized pre-exponential factors. The circular dichroism (CD) spectra were recorded at 25 °C using a JASCO J-815 spectropolarimeter at aqueous hydrogel concentrations ranging from 5 to 400 μM (in line with concentration-dependent UV/vis experiments). The spectra were recorded in a quartz cell (path length 1 mm) within the range 500-190 nm with a data pitch of 0.1 nm. The bandwidth was set at 1 nm, the scanning speed was 20 nm min^{-1}, and the response time was 1 s. Experimental data were recorded in triplicate, and the average data are shown. Fourier transform infrared (FT-IR) spectra of the hydrogel and peptide were recorded on a Bruker (Tensor 27) FT-IR spectrophotometer by using the KBr pellet technique. The FT-IR measurements were recorded within the range 500-4000 cm^{-1} over 64 scans at a resolution of 4 cm^{-1} and interval of 1 cm^{-1}.

3.2.5 Morphological Study of the Hydrogel

The nanostructural morphology present in the self-assembled hydrogel was characterized by microscopic techniques. A field-emission scanning electron microscopy (FE-SEM) experiment was performed on a JEOL scanning electron microscope (Model No: JSM-7600F). In this experiment, 50 μL of the hydrogel (20 mM) was diluted with 150 μL of water and 20 μL of the aqueous solution of the hydrogel was placed on a glass coverslip. The glass coverslip containing the hydrogel sample was dried first in the air and then under vacuum and coated with gold. Transmission electron microscope (TEM) images were captured with a Tecnai-G2-F20 instrument manufactured by FEI, operated at an accelerating voltage of 200 kV. A 50 μL portion of the hydrogel (20 mM) was diluted with 450 μL of water, and the dilute solution of the hydrogel (20 μL) was dried on carbon-coated copper grids (300 mesh) by slow evaporation in the air and then allowed to dry separately under reduced pressure at room temperature. The nano structural morphology of the hydrogel was analyzed by TEM experiments using 2% (w/v) phosphortungstic acid as a negative stain.

3.2.6 Rheological Properties of the Hydrogels

The mechanical strength of the hydrogel was analyzed by rheological experiments. Rheological experiments were performed at 25 °C on an Anton PaarPhysica MCR 301 rheometer. The viscoelastic properties of the hydrogel were measured by measuring the storage modulus (G′) and loss modulus (G″). A 1 mL portion of the hydrogel was transferred to a rheometer plate by using a micro spatula and kept hydrated by using a solvent trap. A stainless-steel parallel plate (diameter 25 mm) was used to sandwich the hydrogel with TruGap (0.5 mm). The amplitude sweep experiment was performed to determine the region of deformation of the hydrogel in which linear viscoelasticity is valid. The exact strain (0.5%) for the hydrogel was determined by a linear viscoelastic (LVE) regime at a constant frequency of 10 rad s^{-1}. The mechanical strengths of the hydrogel were determined by a

frequency sweep experiment using the same strain percent determined by an amplitude sweep experiment. In a frequency sweep measurement, the graph was plotted as a function of frequency in the range 0.05-100 rad s^{-1}. The step strain experiment was performed to evaluate the thixotropic and self-healing nature of the hydrogel by varying low-high-low strain for every 100 s at a constant frequency of 10 rad s^{-1}.

3.2.7 Antibacterial Experiment

3.2.7.1 Inoculum Preparation

The optical density OD_{620} method was employed for antibacterial experiments. Nutrient broth (NB) medium was used for bacterial growth and cultivation. NB media was prepared by mixing peptone (10 g), yeast extracts (3 g), and sodium chloride (5 g, NaCl) in 1000 mL of sterile distilled water. The pH of the NB medium was adjusted to pH 7.0 using 0.1 M NaOH solution. The NB medium was sterilized in an Erlenmeyer flask (25 mL) at a pressure of 15 lb and temperature of 121 °C for 30 min. The microbial cultures of *Staphylococcus aureus* (MTCC 96) and *Escherichia coli* (MTCC 739) bacteria were obtained as lyophilized powders from the Institute of Microbial Technology Chandigarh (CSIR-IMTech), India. Fresh inoculums of *Staphylococcus aureus* and *Escherichia coli* bacteria were prepared. A single colony was harvested and subsequently inoculated in sterilized nutrient broth medium for bacterial growth. The bacterial inoculums were kept shaking in an incubator at 37 °C overnight. The turbidity of fresh overnight cultured bacterial suspensions was diluted as 0.5 McFarland standard to give a working concentration in the range of (1-2) × 10^8 colony-forming units (cfu mL^{-1}).[47] The optical density of all cultures was measured before and after incubation at OD_{620} nm under aseptic conditions.

3.2.7.2 Antibacterial Assay

The hydrogel (40 mM) for the antibacterial test was prepared as described in Preparation of the Hydrogel. A 500 μL portion of the hydrogel (40 mM) was placed in a 2 mL sterile microcentrifuge tube (triplicate). A 400 μL amount of NB media was mixed with the hydrogel, and 100 μL of bacterial inoculum (working inoculums size 1 × 10^6 cfu mL^{-1}) was placed in the tubes (total hydrogel dilution 1:1). For other hydrogel concentrations, the stock gel (40 mM) was used and final working concentrations (15, 10, 5, and 2.5 mM) were maintained after NB and culture addition for the antibacterial test. The bacterial solution devoid of the hydrogel in nutrient broth was used as the control, and only nutrient broth was used as a blank. The gel control was prepared using similar concentrations of the hydrogel without adding the bacterial culture to subtract the gel background. All of the tubes were kept in an incubator at 37 °C for 24 h. After incubation, 500 μL of sterile NB media was added to microcentrifuge tubes and centrifuged at 1500 rpm for 5 min to avoid the hydrogel turbidity in the bacterial absorbance. A 200 μL portion of supernatant having the bacterial culture was taken in the sterile centrifuge tube, and 1.5 mL volume was maintained by adding 1300 μL of sterile water. The absorbance OD_{620} values of control and test gel were recorded manually in the spectrophotometer. The absorbance of gel control was recorded and

subtracted from the absorbance of the test gel. The absorbance of the test sample was compared with the absorbance of control, and data are shown as the percentage of control groups.

3.2.8 In Vitro Biocompatibility Experiments

3.2.8.1 Isolation of Blood

The blood sample was collected from a healthy Wistar albino male rat in a vacuum tube in which sodium citrate solution (3.2% w/v) was added as an anticoagulant.

3.2.8.2 Isolation of RBCs (Red Blood Cells) and WBCs (White Blood Cells)

Erythrocytes (RBCs) were isolated from blood by using centrifugation at 1500 rpm for 5 min at 4 °C. Leukocytes (WBCs) were collected from buffy coat using a sterile syringe, and the rest of the cells were washed three times with 10 mM PBS (0.9% w/v NaCl, pH 7.4).

3.2.8.3 Hemolytic Activity

To study hemolytic activity, a 2% (v/v) suspension of erythrocytes in PBS (10 mM) was used. The aqueous hydrogel concentrations used for hemolytic activity were in line with the cell culture experiment (200 to 12.5 μM). Briefly, 950 μL of cell suspension was incubated with 50 μL of the hydrogel (final concentrations ranging from 200 to 12.5 μM). Only PBS was used as a blank, whereas control samples had erythrocytes in the buffer and were devoid of the hydrogel (considered as zero lysis). Erythrocytes treated with 1% (w/v) Triton X-100 were considered as complete lysis (100% lysis). The mixtures were then incubated at 37 °C for 2 h. After the completion of incubation, mixtures were centrifuged very carefully at 1000 rpm for 10 min at 4 °C. Each experiment was performed in triplicate (n = 3). The percentage of hemolysis was analyzed using absorbance of the supernatant at 540 nm against control (zero lysis and 100% lysis).

3.2.8.4 MTT Viability Assay

The cytotoxic effects of the hydrogel (1000, 800, 600, 400, 200, 100, 50, 25, 12.5, and 6.25 μM peptide concentrations) were evaluated by performing a 3-(4,5-dimethylthiazol-2-yl)-2,5-diphenyltetrazolium bromide (MTT) assay. The human embryonic kidney 293 cell line (HEK293) and HeLa cells were used for the MTT assay. The cells were trypsinized and seeded (8.0×10^3 and 5.0×10^3 cells/well for HEK293 and HeLa cells, respectively) in a 96-well culture plate (number of wells for each peptide concentration n = 8) and allowed to grow for 24 h in 100 μL of DMEM (Dulbecco's Modified Eagle Medium contains 4 mM L glutamine, 1000 mg/L glucose, and 110 mg/L sodium pyruvate) with 10% FBS (fetal bovine serum) and 1% antibiotic (penicillin-streptomycin) solution. After 80% confluency, DMEM media was slowly removed from the wells and a fresh 190 μL of the medium was placed in the wells. Cells were treated with 10 μL of the hydrogel (final peptide concentrations after media dilution ranged from 1000 to 6.25 μM) for 48 h at 37 °C and 5% CO_2. The control groups were treated with 10 μL of PBS (10 mM, pH 7.4) in place of the hydrogel. After incubation, the medium was carefully removed by pipet and 20 μL of MTT (5 mg/mL stock) was placed in each well and incubated for additional 4 h at 37 °C to allow intracellular reduction of the soluble yellow MTT to insoluble purple formazan crystals. These crystals were

dissolved by adding 100 μL of DMSO, and absorbance was taken at 570 nm using a microplate reader (Synergy H1 multimode microplate reader).

3.2.9 In Vivo Anti-Inflammatory Experiments

3.2.9.1 Animals

In vivo experiments were performed according to the Institutional Animal Ethical Committee (IAEC) guidelines, and approval was received prior to in vivo experiments. Wistar albino male rats (weight 180 ± 10 g) were housed in polypropylene cages in a standard photoperiod (14 h light/10 h dark)- and temperature-controlled (27 ± 1 °C) room with the provision of laboratory feed (Gold Mohur feed, Hindustan Lever Limited, Mumbai, India) and water ad libitum. Animals were maintained in accordance with the guidelines of the Committee for the Purpose of Control and Supervision of Experiments on Animals (CPCSEA), Ministry of Environment, Forest and Climate Change, New Delhi, Government of India (Reg. No. 779/Po/Ere/S/03/CPCSEA).

3.2.9.2 Carrageenan-Induced Inflammation

The animals were divided into six groups (n = 5) and labeled as control (normal control, disease control, and drug control) and test groups (1, 0.5, and 0.25% hydrogel groups; 19.51, 9.75, and 4.87 mM peptide). The air pouch was made on the back of the Wistar rat (for five groups) except for the normal control group. To create an air pouch, 20 mL of sterile air was injected subcutaneously into the intrascapular area of the back of the rat. The air pouch cavity was maintained by reinjecting 10 mL of sterile air on the third and sixth days, respectively. After formation of a stable air pouch (on the seventh day), 1 mL of carrageenan (2% w/v) dissolved in normal saline (0.9%) was directly injected into the air pouch of rats (total five groups except normal control) to induce the inflammatory response. To evaluate the biological activity of Amoc-capped hydrogel, 0.2 mL of various doses of the hydrogel (1, 0.5, and 0.25% hydrogel groups) was injected into the air pouch after 4 h carrageenan treatment. In the drug control group, 0.2 mL of the standard anti-inflammatory drug indomethacin (10 mg/kg) was injected after 4 h carrageenan treatment. In the disease control group, only carrageenan was given to induce acute inflammation. After 48 h incubation (on the ninth day), the overnight fasted animals were sacrificed under mild anesthesia. Various parameters were analyzed as described below.[48]

3.2.9.3 Total and Differential WBCs Count

A small incision was made in the thoracic region of the pouch wall, and 10 mL of ice-cold PBS was injected through the incision. The fluid content mixed with PBS inside the pouch was carefully removed using a sterile Pasteur pipet. These fluid contents were centrifuged at 5000 rpm for 10 min. Exudate cells were separated, and the total/differential WBCs were counted microscopically after staining air-dried smears with Wright stain. The larger exudate volume in the disease control group in comparison to the test group signifies the maximum inflammation induced by carrageenan.

3.2.9.4 Histology

The histological experiment was performed after carrageenan, indomethacin, and hydrogel treatment on the endothelial tissue of the inner lining of the air pouch. A small portion of the tissue specimen was fixed in buffered formalin (10% v/v) and embedded in paraffin wax. The sections were cut to 4 μm thickness, stained with hematoxylin and eosin, and viewed under a light microscope for the histological examinations of the control and experimental rats.

3.2.9.5 Lipid Peroxidation Assay (LPO)

The endothelial tissue of the inner lining of the air pouch was carefully homogenized in 10% (w/v) ice-cold PBS (1 mM, pH 7.4). After complete tissue homogenization, the homogenate was centrifuged at 10000 rpm for 10 min and the supernatant was separated with the help of a micropipet. The experiment was performed using 0.2 mL of tissue homogenate in 0.2 mL of SDS (8.1% w/v), and 1.5 mL of acetic acid (20% v/v) was added to provide the acidic medium for the peroxidation reaction. Finally, 1.5 mL of TBA (1% w/v) was added to the reaction mixture and an additional 0.6 mL of water was added to make up the reaction volume to 4 mL. The control experiment was performed as mentioned above using another 1.5 mL of water in place of 1% TBA (total amount of water 2.1 mL). These experimental setups were kept in a boiling water (95 °C) bath for 1 h to give a pink solution. Finally, 4 mL of freshly prepared TCA (10% w/v) was added to stop the reaction. The amount of thiobarbituric acid reactive substances (TBARs) formed was measured by taking the absorbance at 532 nm. A standard curve was made to calculate the amount of TBARs formed equivalent to malondialdehyde formed in nM/mL.

3.2.10 Statistical Analyses

Data are presented as the percentage of the control group and shown as mean ± SEM ($^{a}p < 0.05$; $^{b}p < 0.01$; $^{c}p < 0.001$, and $^{d}p < 0.0001$) in comparison to the control group. Data were analyzed by nonparametric analysis of variance (ANOVA) followed by post hoc Dunnett's multiple comparison tests, using a trial version of Graph Pad Prism version 7.03 for Windows (GraphPad, San Diego, CA).

3.3 Results and Discussion

We have designed and synthesized an Amoc-capped dipeptide (Amoc-LF-OH; L = L-leucine, F = L-phenylalanine). The synthesized peptide is insoluble in water. Hence, the peptide was solubilized in ultrapure water by increasing the pH by addition of 0.5 M NaOH. The pH of the system was slowly decreased by addition of 0.1 M HCl solution. The peptide entraps a large amount of water and forms a self-supporting hydrogel under physiological conditions (pH 7.4, 37 °C) (**Scheme 3.2**). Introducing Amoc moiety in low-molecular-weight-based peptides provides optimal hydrophobicity, which enhances their self-assembling propensity for biological applications. In a previous report, a bulky amino acid leucine attached adjacent to an Fmoc (9-fluorenylmethoxycarbonyl) group showed higher anti-inflammatory activity (NPC 15199 (9-(fluorenylmethoxycarbonyl)leucine)). However, reduction of the size of the side chains of amino acids such as alanine (NPC 14688) and glycine (NPC 14692) attached adjacent to the Fmoc group

significantly decreased anti-inflammatory activity.[49] The structural similarity of the designed peptide with a previously reported Fmoc-capped anti-inflammatory peptide (NPC 15199) motivated us to investigate the inherent anti-inflammatory and antibacterial efficacies.[35,49,50]

Scheme 3.2 Chemical Structures of Amoc-Capped Dipeptide[a]

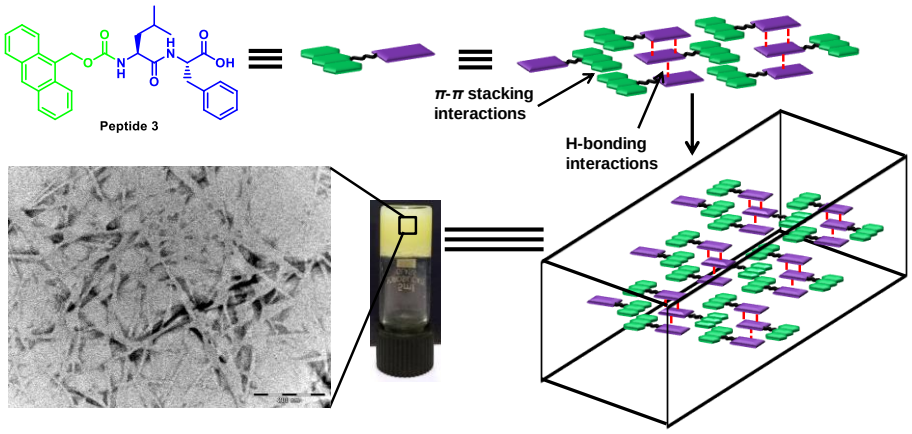

[a]Graphical Representation of the Self-Assembly of Amoc-Capped Dipeptide Leading to the Formation of Self-Supporting Hydrogel

The self-assembling nature of the Amoc-capped peptide leads to the formation of a nano-structural morphology which was analyzed by electron microscopy (SEM and TEM) (Figure 3.12a, b). The SEM image of the hydrogel demonstrates porous and highly dense cross-linked nanofibrillar networks (Figure 3.12a). TEM images further demonstrate the presence of entangled nanofibrillar networks with an average diameter of 15 nm and length of several micrometers (Figure 3.12b). Concentration dependent UV/vis spectra were collected to understand the intermolecular interactions in supramolecular aggregates (Figure 3.12c).[28] The absorption maxima centered at 254 nm (π-π* transitions) are observed due to the presence of phenylalanine. Multiple absorption bands from 346 to 385 nm are observed, which are associated with the anthracene moiety present in the peptide. The concentration-dependent UV/vis spectra showed a nonsignificant shift of absorption maxima at all studied concentrations (5 to 100 μM). The intensity of absorption maxima increases gradually with an increase in peptide concentration, which could be attributed to the involvement of intermolecular interactions among peptide molecules. Further, the fluorescence spectroscopic technique was used to characterize the self-assembly process. The emission spectra of the hydrogel (20 mM) and the aqueous peptide solution (10 μM) were recorded to investigate the change in the emission maxima (Figure 3.12d).[6] The emission spectrum of the aqueous peptide shows three sharp emission bands between 393 and 435 nm with a emission maximum at 412 nm (λ_{ex} 365 nm). The emission spectrum of the hydrogel showed a broad emission maximum at 477 nm (λ_{ex} 365 nm) due to the head to tail interaction of the peptide in the *J* aggregate state.[4,6] The red-shifted (65 nm) emission spectrum of the hydrogel in the self-assembled state evidences the involvement of π-π stacking and intermolecular hydrogen bonding

interactions.[31] The excitation spectra of the peptide (λ_{em} 412 nm) and corresponding hydrogel (λ_{em} 477 nm) were recorded. The excitation spectra of the peptide and hydrogel show excitation peaks at 365 and 370 nm, respectively (Figure 3.12e). Furthermore, the critical aggregation concentration (CAC) and self-assembling behavior of the peptide were studied with the help of a concentration-dependent fluorescence experiment (Figure 3.12f, g).[31]

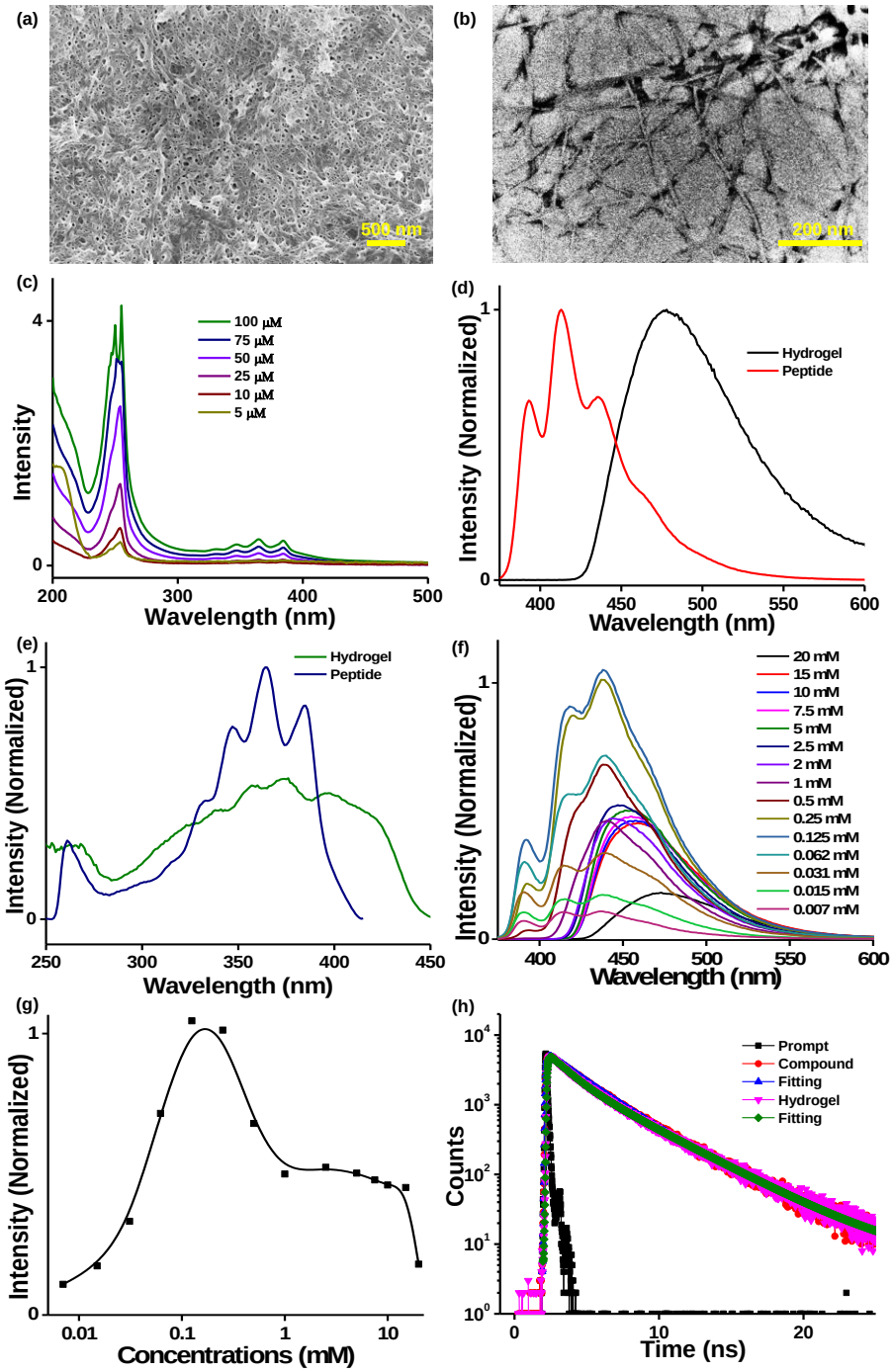

Figure 3.12 (a, b) SEM and TEM images of the hydrogel, respectively. (c) Concentration-dependent UV/vis spectra of aqueous hydrogel solutions. (d)

Fluorescence spectra (λ_{ex} 365 nm) of the hydrogel (20 mM) and aqueous peptide solution (10 μM). (e) Excitation spectra of the hydrogel (20 mM, λ_{em} 477 nm) and aqueous peptide (10 μM, λ_{em} 412 nm). (f) Concentration-dependent fluorescence spectra (λ_{ex} = 365 nm) using various concentrations of hydrogel (20-0.007 mM). (g) Concentration-dependent fluorescence (λ_{ex} 365 nm) maxima showing the critical aggregation concentration of peptides. (h) Decay traces of hydrogel (20 mM) and peptide (10 μM) solutions.

A decrease in the hydrogel concentrations (20 to 0.062 mM) results in a blue shift and change in the pattern of emission spectra. The highest concentration of peptide in the hydrogel (20 mM) leads to aggregation-caused quenching (ACQ) in the fluorescence spectra. The intensity of the emission spectra becomes constant (15 to 1 mM) due to strong supramolecular interactions among peptides. Further, hydrogel dilutions (1 to 0.125 mM) lead to the loss of supramolecular interactions among peptides and the highest fluorescence intensity is observed at 0.125 mM peptide. The fluorescence intensity decreases again with the hydrogel dilutions (0.125 to 0.007 mM) because of the lesser number of available fluorophore moieties. The results from the concentration-dependent fluorescence study indicate that the CAC value of the peptide is 1 mM, approximately. A time-correlated single photon counting (TCSPC) was employed to measure the fluorescence lifetime and the decay profiles of the excited state species of the aqueous peptide (10 μM) and hydrogel (20 mM) by excitation-emission wavelength at 375-475 nm, respectively (Figure 3.12h).[31] The decay traces for the aqueous peptide and corresponding hydrogel are fitted with a biexponential function. The average lifetime for the aqueous peptide is calculated as 3 ns with lifetime components of 2.2371 ns (62%) and 4.2462 ns (38%), whereas the average lifetime for the hydrogel is calculated as 2.64 ns with lifetime components of 1.3013 ns (50%) and 3.9607 ns (50%).

Table 3.1 Decay parameters of the peptide (10 μM) and corresponding hydrogel (20 mM)

Name	α_1	α_2	τ_1 **(ns)**	τ_2 **(ns)**	τ_a **(ns)**	χ^2
Peptide	0.62	0.38	2.2371	4.2462	3.0	1.06
Hydrogel	0.50	0.50	1.3013	3.9607	2.63	1.14

τ_a = Average lifetime
α = Normalized amplitude of each component

In line with fluorescence experiments, the shorter excited state lifetime for the hydrogel in comparison to the aqueous peptide reveals the effect of ACQ. In order to investigate the secondary structure and hydrogen-bonding interactions present in the peptide and the corresponding hydrogel, an FT-IR experiment was performed (Figure 3.13a). The enhancement of the IR signal in the amide I region

(1600-1700 cm^{-1}) is mainly associated with the involvement of hydrogen bonds among amide groups.[31] The peptide shows a peak at 1647 cm^{-1}, whereas the hydrogel shows an intense peak at 1635 cm^{-1} indicating a more ordered β-sheet-like arrangement in the hydrogel state.[51] Concentration-dependent CD spectroscopy was employed to study the self-assembling behavior of the aqueous hydrogel (Figure 3.13b).[31]

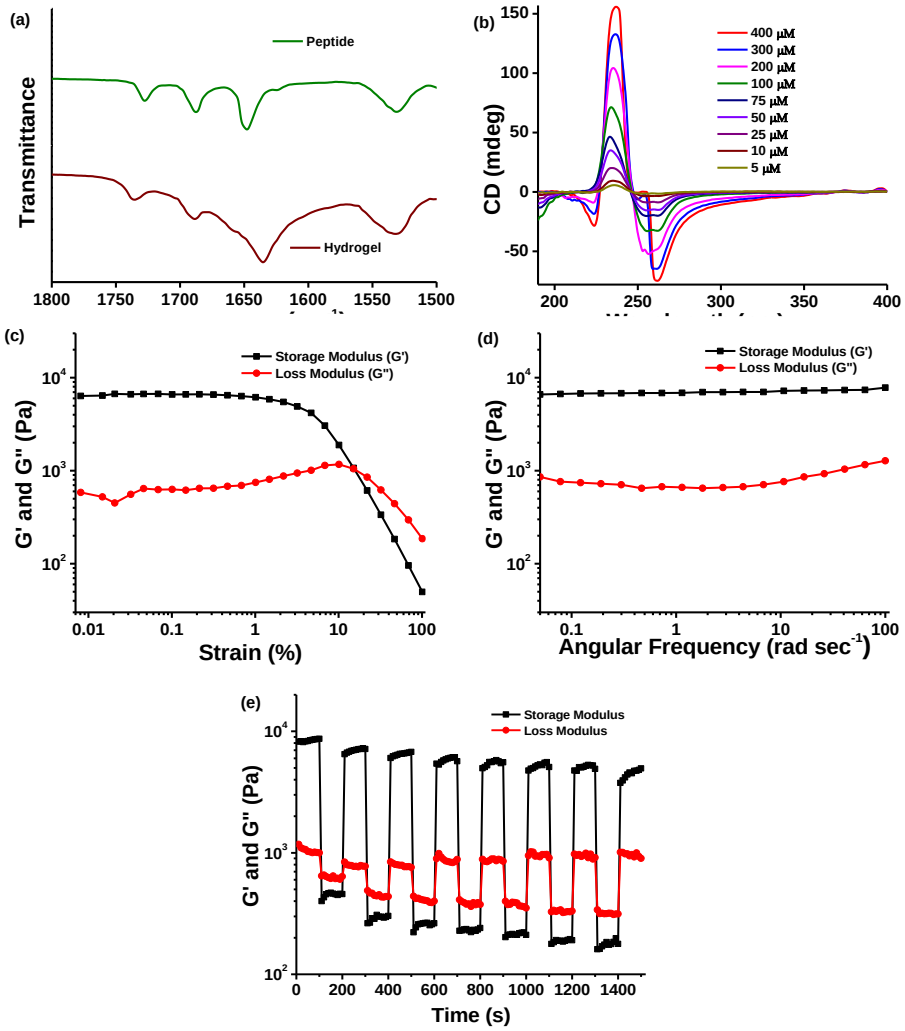

Figure 3.13 (a) FTIR spectra of peptide and hydrogel. (b) Concentration-dependent CD spectra of diluted hydrogel solutions. (c, d, e) Amplitude, frequency and step strain sweep experiments, respectively.

The aqueous hydrogel (5 to 400 μM) was used for the concentration dependent CD experiment. The observed CD spectra of self-assembled peptide show strong bisignated CD absorption in the range of 235-265 nm which is associated with the aromatic chromophores present in the peptides. The self-assembling behavior of the peptides from lower to higher concentrations (5 to 400 μM) results in a red shift in CD absorption in the aromatic region. These results reveal the involvement of π-π stacking and hydrogen-bonding interactions for the formation of chiral

supramolecular aggregates. The aqueous hydrogel (200 to 400 μM) shows a negative CD absorption at 223 nm due to an n-π* transition of the amide groups. The amide CD is not seen at lower concentrations (5 to 100 μM) of the aqueous hydrogel, which might be attributed to the strong intervention of aromatic side chains. From the concentration-dependent CD and fluorescence experiments, we conclude that noncovalent interactions are prominent at higher concentrations (≥200 μM) of peptides. Furthermore, the stiffness and viscoelastic nature of the hydrogel were elucidated with the help of rheological experiments.[30,52] The amplitude sweep experiment was performed at a constant angular frequency of 10 rad/s to determine the linear viscoelastic region (LVR) of the hydrogel (Figure 3.13c). The amplitude sweep experiment suggests that 0.5% strain is within the LVR for the hydrogel and is valid for the oscillatory frequency sweep experiment. The oscillatory frequency sweep experiment reveals that the storage modulus (G′) is greater than the loss modulus (G″) over the entire frequency range, indicating the formation of a tough and rigid hydrogel (Figure 3.13d). Further, the thixotropic nature of the hydrogel was evaluated by a strain sweep experiment at a constant angular frequency of 10 rad/s (Figure 3.13e). In the strain sweep experiment, the reversibility of gel-sol-gel transitions was evaluated by periodically changing the low-high strain. Initially, the hydrogel was kept below the deformation limit at lower strain (γ = 0.5%) for 100 s. At lower strain, the storage modulus (G′) of the hydrogel is greater than the loss modulus (G″) of the hydrogel for 100 s, indicating the formation of a tough and highly cross linked self-assembled network. At higher strain (γ = 40%), the storage modulus of the hydrogel decreases below the loss modulus of the hydrogel, indicating the formation of a sol-like state due to the deformation of the self-assembled network. Again, at lower strain (γ = 0.5%), the storage modulus (G′) exceeds the loss modulus (G″) of the hydrogel, which further indicates very fast recovery (100 s) of its mechanical strength due to the reconstruction of the self-assembled network. The results from step strain and frequency sweep experiments evidence that the hydrogel stiffness is suitable for the biological applications. However, the hydrated environment of the hydrogel and other biomaterials generates a favorable microenvironment for bacterial adhesion, growth, and biofilm formation. Most of the Gram-positive bacteria contain teichoic acid in their cell envelopes, which is responsible for bacterial adhesion and biofilm formation on the surface of biomaterials.[34] Hence, to overcome these challenges, the antibacterial efficacy of the hydrogel was evaluated at the gelation concentration (20 mM) and various other dilutions (2.5, 5, 10, 15 mM) of the hydrogel against Gram-positive (*S. aureus*) and Gram-negative (*E. coli*) pathogenic bacteria (Figure 3.14a, b). The growth of Gram-positive and Gram-negative bacteria is significantly inhibited by the hydrogel. The maximum antibacterial efficacy against Gram-positive and Gram-negative bacteria is observed at a gelation concentration of 20 mM. Further, dilution of the hydrogel (20-2.5 mM) decreases the antibacterial efficacy against Gram-positive and Gram-negative bacteria. The antibacterial efficacy of the hydrogel against Gram-negative bacteria is less than that against Gram-positive bacteria.

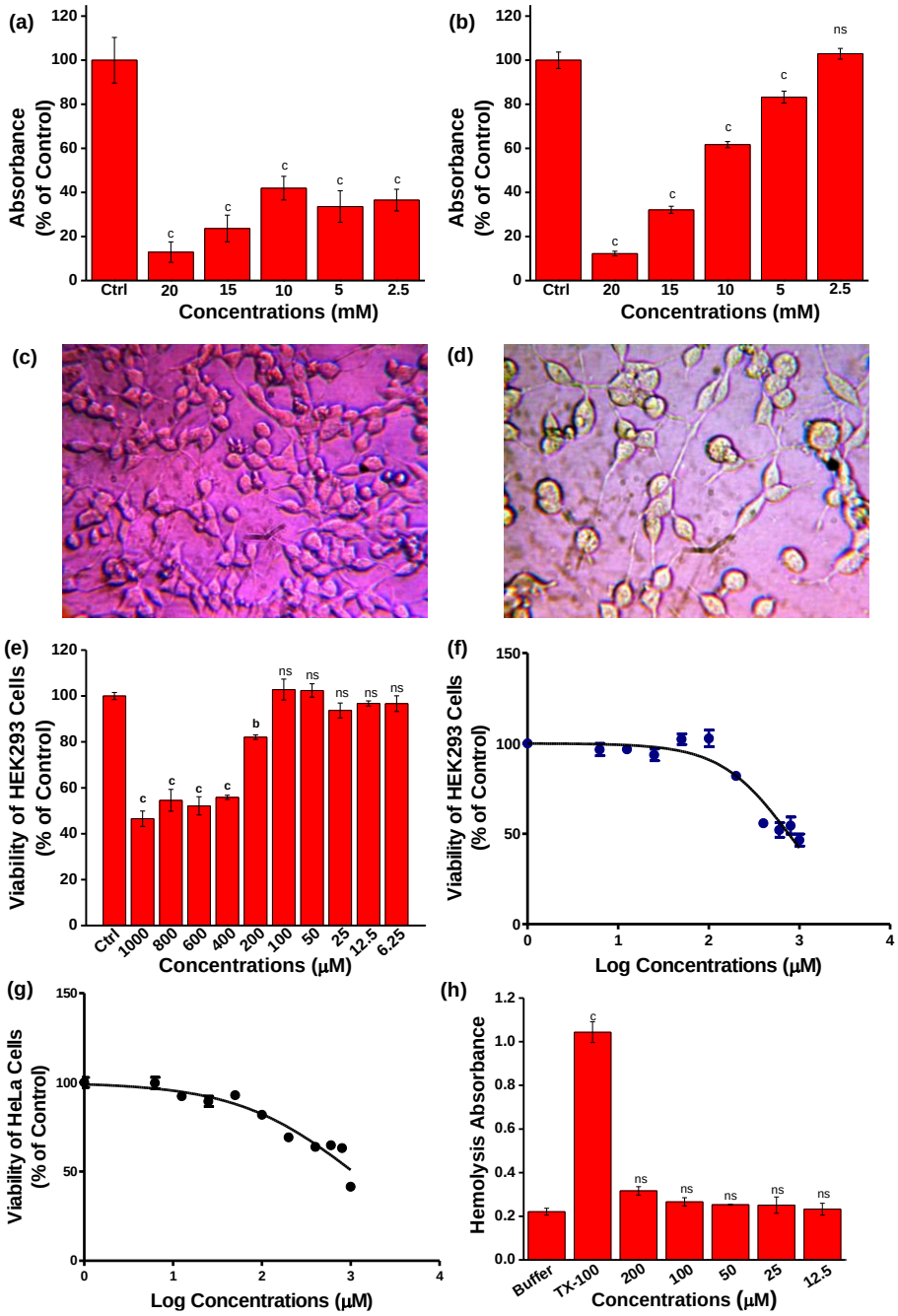

Figure 3.14 The antibacterial experiments against (a) *S. aureus*. (b) *E. coli* bacteria, respectively. Optical microscope (original magnification 100X) photograph of HEK293 cells during cell culture experiment taken from 96 well plate: (c) before hydrogel treatment. (d) 48 h after hydrogel (200 μM) treatment shows intact cellular morphology. Cell culture experiment using HEK293 and HeLa cells: (e, f) HEK293 cell viability and IC_{50} plot. (g) IC_{50} plot for HeLa cells. (h) Hemolysis data. Data are presented as the percentage of the control group and shown as mean ± SEM. $^{a}p < 0.05$; $^{b}p < 0.01$; $^{c}p < 0.001$, and $^{d}p < 0.0001$, as compared to the control group (n = 5). The non-significant data are shows as "ns".

Lower concentrations of the hydrogel (2.5, 5, and 10 mM) are ineffective against Gram-negative bacteria because inhibition is ≤50%. However, the hydrogel shows potent antibacterial efficacy against Gram-positive bacteria. The self-assembling peptide interacts with the lipid membrane present in Gram-negative and Gram-positive bacteria. The amphipathic nature of the self-assembling peptide could be the driving force behind the antibacterial efficacy of the hydrogel.[22-24] The amphiphilic nature of the peptide leads to aggregation with the bacterial lipid membrane, which results in the membrane permeation and disruption through various noncovalent interactions.[53,54] The extra lipopolysaccharide membrane present in Gram-negative bacteria might retard the antibacterial efficacy of peptides against Gram-negative bacteria in comparison to Gram-positive bacteria.[34] The biocompatibility of the biomaterials must cover various biological aspects such as non-cytotoxicity, non-immunogenicity, and biodegradability.[38] Prior to in vivo experiments, the in vitro cytotoxicity of the prepared hydrogel was evaluated using cell culture experiments (Figure 3.14c, d).[39] In vitro cytotoxicity of the hydrogel (1000 to 6.25 μM) to cellular viability and proliferation of normal cells were evaluated using HEK293 cells (Figure 3.14e). The data from the cytotoxicity study represents that the hydrogel is noncytotoxic for the growth and viability of HEK293 cells up to 200 μM hydrogel concentration (82% cell viability). Further, dilutions of the hydrogel (200 to 6.25 μM) show a significant increase in growth and viability of HEK293 cells in a dose-dependent manner (cell viability ≥95%). Higher concentrations (1000 to 400 μM) of hydrogel show significant inhibition to cell viability. The IC_{50} value (759 μM) for the hydrogel is calculated by a nonlinear fitting of the cell viability of HEK293 cells against various hydrogel concentrations (Figure 3.14f). However, another cell culture experiment was performed using HeLa cells. The IC_{50} values (1063 μM) for HeLa cells corroborate the non-cytotoxicity of the hydrogel (Figure 3.14g). In order to investigate the compatibility of the hydrogel toward mammalian blood cells, a hemolysis study was performed with red blood cells using various concentrations of hydrogel (200 to 12.5 μM) (Figure 3.14h).[55] The highest hemolysis (5% only) is observed at a 200 μM hydrogel concentration. Further, dilution of the hydrogel (200 to 12.5 μM) decreases the hemolysis (~5 to 1%) in a dose-dependent manner. These cytotoxicity data further authenticate the biocompatibility of the peptide for in vivo applications. Biomaterial-mediated acute inflammation remains a huge challenge for researchers. In this regard, the in vivo compatibility and therapeutic potential of the Amoc-capped peptide hydrogel were investigated using the rat air pouch model of inflammation (Figure 3.15a, b). Hematoxylin-eosin (H&E) staining is an excellent technique for the observation of gross tissue morphology, infiltration of inflammatory cells, tissue edema, and injury due to the injection or implantation of the biomaterials into the target site.[56] The histological examinations of endothelial tissue reveal normal tissue architecture in the control group (Figure 3.15c).

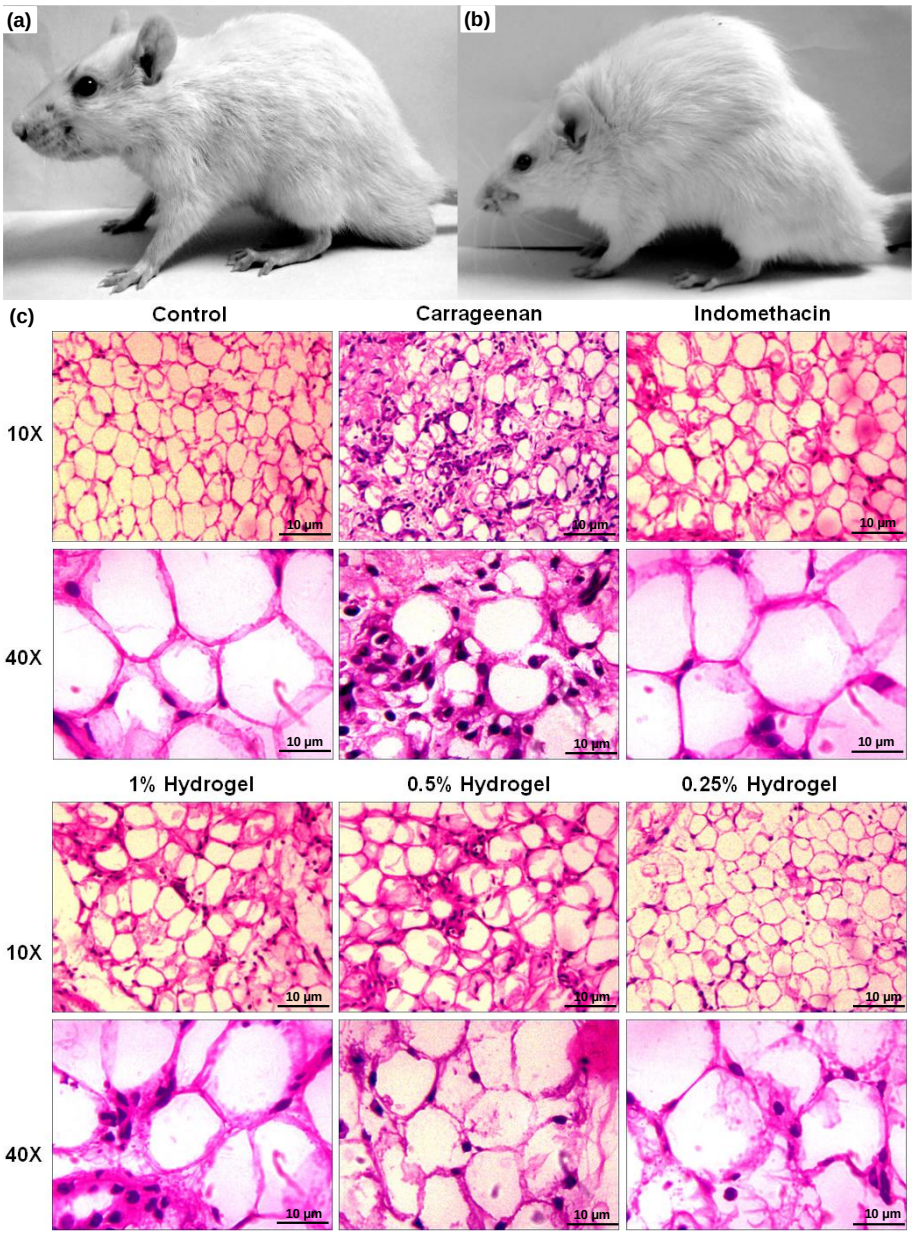

Figure 3.15 Optical photographs of (a) a normal rat and (b) a rat having an air pouch. (c) Endothelial tissue histology images of the rat air pouch wall after termination of the experiments at 10X and 40X, respectively.

The carrageenan-treated group shows edema in endothelial tissue, which is marked by the increased widths of endothelial cells with a concomitant decrease in interstitial spaces and masking of adipocyte size and the highest infiltration of inflammatory cells such as neutrophils and macrophages (Figure 3.16a, b). In the indomethacin-treated group, reduction of inflammatory cells was observed similar to the normal tissue architecture. The hydrogel-treated groups show dose-dependent behavior in inflammation (1 to 0.25% hydrogel).

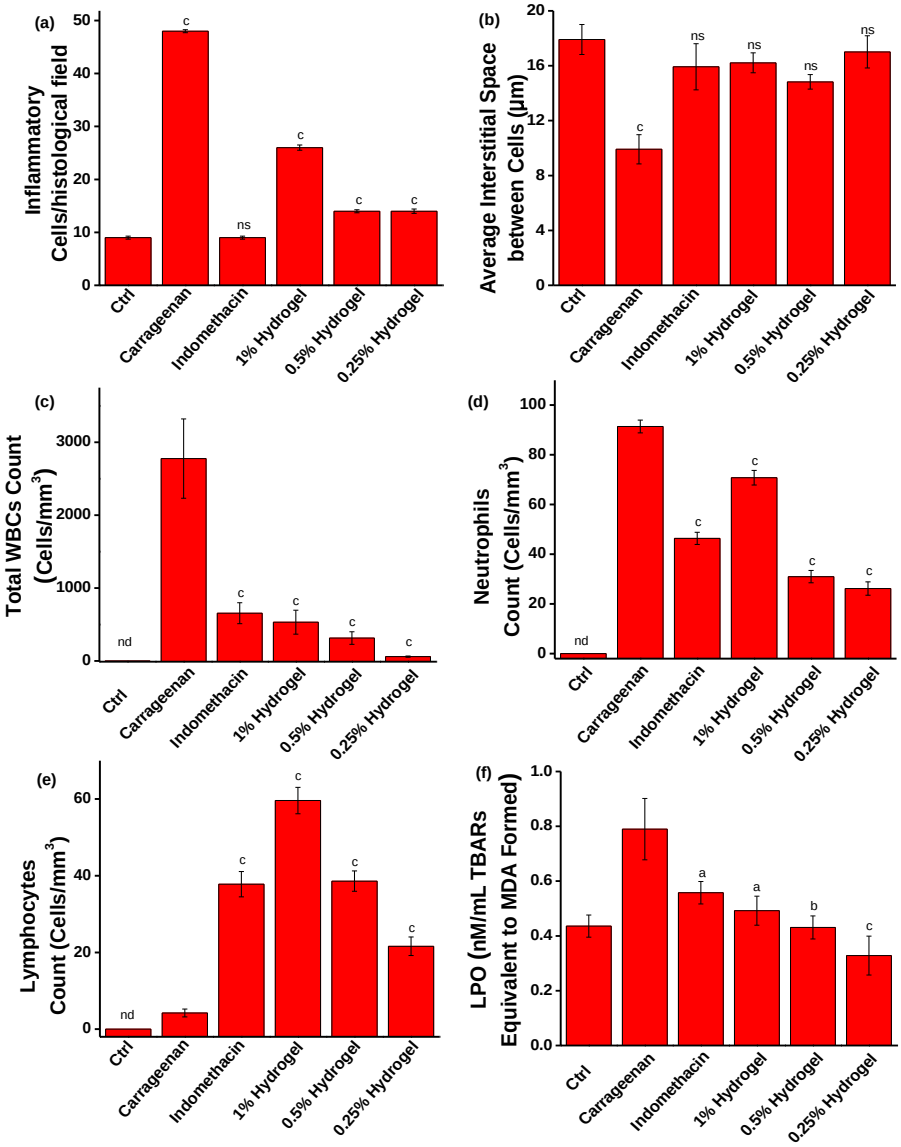

Figure 3.16 (a) Average inflammatory cell number per histological field (400X magnification). (b) Average interstitial space between adipocytes per histological field (400X magnification). Differential WBCs counts in air pouch fluid exudates collected after termination of the experiments (a) Neutrophile, (b) Lymphocyte, respectively. (e) Total WBC count in air pouch exudates. (f) LPO assay on endothelial tissue extracted from the air pouch wall.

The maximum numbers of inflammatory cells are seen in the 1% hydrogel treated group which are less than those for the carrageenan-treated group. However, further lower doses of hydrogel (0.5 and 0.25%) lead to a significant decrease in inflammatory cells and tissue architectures, which revert back toward normalcy. The best anti-inflammatory activity is observed with 0.25% hydrogel. Furthermore, total and differential white blood cell (WBC) counts of air pouch exudate corroborate the histology data (Figure 3.16c, d, e). The maximum WBCs are seen in the carrageenan-treated group, whereas in the control group no WBCs

are detected. The total WBC count is significantly decreased by indomethacin. However, the hydrogel treatment further decreases WBC count in a dose-dependent manner and the lowest WBC number is observed with the 0.25% hydrogel treated group. In line with histology, this experiment also reveals that 0.25% hydrogel is best for anti-inflammatory activity. A differential WBC count suggests that the hydrogel significantly reduces the inflammatory cell neutrophils and macrophages. Our data consistently reveal that the hydrogel works as an anti-inflammatory agent (Figure 3.16d, e). A lipid peroxidation (LPO) assay was performed to further evaluate the oxidative damage by hydrogel treatment on the endothelial tissue of the rat air pouch (Figure 3.16f).[57] A significant increase in LPO value is observed in the carrageenan-injected group, in comparison to the control. Treatment with the anti-inflammatory drug indomethacin reduces the LPO value. Interestingly, hydrogel treatment further reduces LPO values in a dose-dependent manner (1 to 0.25% hydrogel), which confirms the nontoxic and anti-inflammatory nature of the hydrogel.

3.4 Conclusion

In summary, we have designed and developed an Amoc-capped peptide-based LMWH and the therapeutic potential of the hydrogel in inflammation was evaluated by a rat air pouch model of acute inflammation. The inherent antibacterial efficacy of the hydrogel against pathogenic bacteria also opens a new avenue for LMWHs as a biological containment free implantable biomaterial. In vitro biocompatibility of the peptide offers a significant promise for therapeutic applications. Furthermore, an in vivo study of acute inflammation gives insight into the biocompatibility as well as anti-inflammatory potential of the hydrogel in a dose-dependent manner. We believe that our designed material may work as an implantable biomaterial for wound healing and targeted drug and cell delivery applications.

3.5 References

(1) Green J. J., Elisseeff J. H. (2016), Mimicking biological functionality with polymers for biomedical applications, Nature, 540, 386-394 (DOI: 10.1038/nature21005).

(2) Hu B., Owh C., Chee P. L., Leow W. R., Liu X., Wu Y. L., Guo P., Loh X. J.Chen X. (2018), Supramolecular Hydrogels for Antimicrobial Therapy, Chem. Soc. Rev. 47, 6917-6929 (DOI: 10.1039/C8CS00128F).

(3) Du X. W., Zh J., Shi J. F., Xu B. (2015), Supramolecular Hydrogelators and Hydrogels: From Soft Matter to Molecular Biomaterials. Chem. Rev. 115, 13165-13307 (DOI: 10.1021/acs.chemrev.5b00299) .

(4) Babu S. S., Praveen V. K., Ajayaghosh A. (2014), Functional π-Gelators and their Applications, Chem. Rev. 114, 1973-2129 (DOI: 10.1021/cr400195e).

(5) O'Banion C. P., Nguyen L. T., Wang Q., Priestman M. A., Holly S. P., Parise L. V., Lawrence D. S. (2016), The Plasma Membrane as a Reservoir, Protective

Shield, and Light Triggered Launch Pad for Peptide Therapeutics, Angew. Chem., Int. Ed. 55, 950-954 (DOI: 10.1002/anie.201508767).
(6) Zhou M., Smith A. M., Das A. K., Hodson N. W., Collins R. F., Ulijn R. V., Gough J. E. (2009), Self-Assembled Peptide-Based Hydrogels as Scaffolds for Anchorage-Dependent Cells, Biomaterials, 30, 2523-2530 (DOI: 10.1016/j.biomaterials.2009.01.010).
(7) Heek T., Kuehne C., Depner H., Achazi K., Dernedde J., Haag R. (2016), Synthesis, Photophysical, and Biological Evaluation of Sulfated Polyglycerol Dendronized Perylenebisimides (PBIs)-A Promising Platform for Anti-Inflammatory Theranostic Agents?, Bioconjugate Chem., 27, 727-736 (DOI: 10.1021/acs.bioconjchem.5b00683).
(8) Biswas A., Malferrari S., Kalaskar D. M., Das A. K. (2018), Arylboronate Esters Mediated Self-Healable and Biocompatible Dynamic G-Quadruplex Hydrogels as Promising 3D-Bioinks, Chem. Commun., 54, 1778-1781 (DOI: 10.1039/C7CC09051J).
(9) Webber M. J., Kessler J. A., Stupp S. I. (2010), Emerging Peptide Nanomedicine to Regenerate Tissues and Organs, J. Intern. Med, 267, 71-88 (DOI: 10.1111/j.1365-2796.2009.02184. x.).
(10) Broderick A. H., Stacy D. M., Tal-Gan Y., Kratochvil M. J., Blackwell H. E., Lynn D. M. (2014), Surface Coatings that Promote Rapid Release of Peptide-Based AgrC Inhibitors for Attenuation of Quorum Sensing in Staphylococcus Aureus, Adv. Healthcare Mater, 3, 97-105 (DOI: 10.1002/adhm.201300119).
(11) Savyasachi A. J., Kotova O., Shanmugaraju S., Bradberry S. J., Ó'Máille G. M., Gunnlaugsson T. (2017), Supramolecular Chemistry: A Toolkit for Soft Functional Materials and Organic Particles, Chem, 3, 764-811 (DOI: 10.1016/j.chempr.2017.10.006).
(12) Pashuck E. T., Stevens M. M. (2012), Designing Regenerative Biomaterial Therapies for the Clinic, Sci. Transl. Med, 4, 160sr4 (DOI: 10.1126/scitranslmed.3002717).
(13) Xu W., Song Q., Xu J.-F., Serpe M. J., Zhang, Xi. (2017), Supramolecular Hydrogels Fabricated from Supramonomers: A Novel Wound Dressing Material, ACS Appl. Mater. Interfaces, 9, 11368-11372 (DOI: 10.1021/acsami.7b02850).
(14) Wang H., Feng Z., Xu B. (2017), Bioinspired Assembly of Small Molecules in Cell Milieu, Chem. Soc. Rev, 46, 2421-2436 (DOI: 10.1039/C6CS00656F).
(15) Lampel A., Ulijn R. V., Tuttle T. (2018), Guiding Principles for Peptide Nanotechnology Through Directed Discovery, Chem. Soc. Rev, 47, 3737-3758 (DOI: 10.1039/C8CS00177D).
(16) Kubota R., Liu S., Shigemitsu H., Nakamura K., Tanaka W., Ikeda M., Hamach I. (2018), Imaging-Based Study on Control Factors over Self-Sorting of Supramolecular Nanofibers Formed from Peptide- and Lipid-Type Hydrogelators, Bioconjugate Chem., 29, 2058-2067 (DOI: 10.1021/acs.bioconjchem.8b00260).
(17) Makam P., Gazit E. (2018), Minimalistic Peptide Supramolecular Co-Assembly: Expanding the Conformational Space for Nanotechnology, Chem. Soc. Rev, 47, 3406-3420 (DOI: 10.1039/C7CS00827A).

(18) Amabilino D. B., Smith D. K., Steed J. W. (2017), Supramolecular Materials, Chem. Soc. Rev., 46, 2404-2420 (DOI: 10.1039/C7CS00163K).
(19) Okesola B. O., Smith D. K., (2016), Applying Low-Molecular Weight Supramolecular Gelators in an Environmental Setting-Self-Assembled Gels as Smart Materials for Pollutant Removal, Chem. Soc. Rev, 45, 4226-4251 (DOI: 10.1039/C6CS00124F).
(20) Mali K. S., Pearce N., Feyter S. D., Champness N. R. (2017), Frontiers of Supramolecular Chemistry at Solid Surfaces, Chem. Soc. Rev, 46, 2520-2542 (DOI: 10.1039/C7CS00113D).
(21) Sevim S., Sorrenti A., Franco C., Furukaw S., Pané, S., deMello A. J., Puigmartí-Luis J. (2018), Self-Assembled Materials and Supramolecular Chemistry within Microfluidic Environments: From Common Thermodynamic States to Non-Equilibrium Structures, Chem. Soc. Rev, 47, 3788-3803 (DOI: 10.1039/C8CS00025E).
(22) Beter M., Kara H. K., Topal A. E., Dana, A., Tekinay A. B., Guler M. O. (2017), Multivalent Presentation of Cationic Peptides on Supramolecular Nanofibers for Antimicrobial Activity, Mol. Pharmaceutics, 14, 3660-3668 (DOI: 10.1021/acs.molpharmaceut.7b00434).
(23) Dehsorkhi A., Castelletto V., Hamley I. W. (2013), Interaction between a Cationic Surfactant-like Peptide and Lipid Vesicles and Its Relationship to Antimicrobial Activity, Langmuir, 29, 14246-14253 (DOI: 10.1021/la403447u.).
(24) Castelletto V., Barnes R. H., Karatzas,K. A., Edwards-Gayle C. J. C., Greco F., Hamley I. W., Rambo R., Seitsonen J., Ruokolainen J. (2018), Arginine-Containing Surfactant-Like Peptides: Interaction with Lipid Membranes and Antimicrobial Activity, Biomacromolecules, 19, 2782-2794 (DOI: 10.1021/acs.biomac.8b00391).
(25) Draper E. R., Adams D. J. (2017), Low-Molecular-Weight Gels: The State of the Art, Chem., 3, 390-410 (DOI: 10.1016/j.chempr.2017.07.012).
(26) Zhao F., Ma M. L., Xu B. (2009), Molecular Hydrogels of Therapeutic Agents, Chem. Soc. Rev, 38, 883-891 (DOI: 10.1039/B806410P).
(27) Versluis F., van Esch J. H., Eelkema R. (2016), Synthetic Self-Assembled Materials in Biological Environments, Adv. Mater, 28, 4576-4592 (DOI: 10.1002/adma.201505025).
(28) Arslan E., Garip I. C., Gulseren G., Tekinay A. B., Guler M. O. (2014), Bioactive Supramolecular Peptide Nanofibers for Regenerative Medicine. Adv. Healthcare Mater, 2014, 3, 1357-1376 (DOI: 10.1002/adhm.201300491).
(29) Li Y., Rodrigues J., Tomas H. (2012), Injectable and Biodegradable Hydrogels: Gelation, Biodegradation and Biomedical Applications, Chem. Soc. Rev. 2012, 41, 2193-2221 (DOI: 10.1039/c1cs15203c).
(30) Restu W. K., Nishida Y., Yamamoto S., Ishii J., Maruyama T. (2018), Short Oligopeptides for Biocompatible and Biodegradable Supramolecular Hydrogels, Langmuir, 34, 8065-8074 (DOI: 10.1021/acs.langmuir.8b00362).
(31) Gavel P. K., Dev D., Parmar H. S., Bhasin S., Das A. K. (2018), Investigations of Peptide-Based Biocompatible Injectable Shape-Memory Hydrogels:

Differential Biological Effects on Bacterial and Human Blood Cells, ACS Appl. Mater. Interfaces, 10, 10729-10740 (DOI: 10.1021/acsami.8b00501).
(32) Nandi N., Gayen K., Ghosh S., Bhunia D., Kirkham S., Sen S. K., Ghosh S., Hamley I. W., Banerjee A. (2017), Amphiphilic Peptide-Based Supramolecular, Noncytotoxic, Stimuli-Responsive Hydrogels with Antibacterial Activity, Biomacromolecules, 18, 3621-3629 (DOI: 10.1021/acs.biomac.7b01006.).
(33) Lee K. Y., Mooney D. J. (2001), Hydrogels for Tissue Engineering, Chem. Rev, 101, 1869-1880 (DOI: 10.1021/cr000108x).
(34) Arciola C. R., Campoccia D., Montanaro L. (2018), Implant Infections: Adhesion, Biofilm Formation and Immune Evasion, Nat. Rev. Microbiol, 16, 397-409.
(35) Irwansyah I., Li Y. Q., Shi W., Qi D., Leow W. R., Tang M. B. Y., Li S., Chen X. (2015), Gram Positive Antimicrobial Activity of Amino Acid Based Hydrogels, Adv. Mater., 27, 648-654 (DOI: 10.1002/adma.201403339).
(36) Wang H., Zhu H., Fu W., Zhang Y., Xu B., Gao F., Cao Z., Liu W. (2017), A High Strength Self-Healable Antibacterial and Anti-Inflammatory Supramolecular Polymer Hydrogel, Macromol. Rapid Commun, 38, 1600695 (DOI: 10.1002/marc.201600695).
(37) Markey A., Workman V., L., Bruce I. A., Woolford T. J., Derby B., Miller A. F., Cartmella S. H., Saiani A. (2017), Peptide Hydrogel in vitro Non-Inflammatory Potential, J. Pept. Sci, 23, 148-154 (DOI: 10.1002/psc.2940).
(38) Kohane D. S., Langer R. (2010), Biocompatibility and Drug Delivery Systems, Chem. Sci, 1, 441-446 (DOI: 10.1039/C0SC00203H).
(39) Hoque J., Bhattacharjee B., Prakash R. G., Paramanandham K., Haldar J. (2018), Dual Function Injectable Hydrogel for Controlled Release of Antibiotic and Local Antibacterial Therapy. Biomacromolecules, 19, 267-278 (DOI: 10.1021/acs.biomac.7b00979).
(40) Li J., Kuang Y., Shi J., Gao Y., Zhou J., Xu B. (2013), The Conjugation of Nonsteroidal Anti-inflammatory Drugs (NSAID) to Small peptides for Generating Multifunctional Supramolecular Nanofibers/Hydrogels. Beilstein, J. Org. Chem, 9, 908-917 (DOI: 10.3762/bjoc.9.104).
(41) Su J., Hu B. H., Lowe W. L., Kaufman D. B., Messersmith P. B. (2010), Anti-Inflammatory Peptide-Functionalized Hydrogels for Insulin-Secreting Cell Encapsulation, Biomaterials, 31, 308-314 (DOI: 10.1016/j.biomaterials.2009.09.045).
(42) Smith C. E., Soti S., Jones T. A., Nakagawa A., Xue D., Yin H. (2017), Non-Steroidal Anti-Inflammatory Drugs are Caspase Inhibitors, Cell Chem. Biol, 24, 281-292 (DOI: 10.1016/j.chembiol.2017.02.003).
(43) Li J., Kuang Y., Gao Y., Du X., Shi J., Xu B. (2013), D-Amino Acids Boost the Selectivity and Confer Supramolecular Hydrogels of a Nonsteroidal Anti-Inflammatory Drug (NSAID), J. Am. Chem. Soc. 2013, 135, 542-545 (DOI: 10.1021/ja310019x).
(44) Kim J. E., Park K. M., Lee S. Y., Seo J. H., Yoon I. S., Bae C. S., Yoo J. C., Bang M. A., Cho S. S., Park D. H. (2017), Anti-Inflammatory Effect of Allium

Hookeri on Carrageenan-Induced Air Pouch Mouse Model, PLoS One, 12 (12), No. e0190305 (DOI: 10.1371/journal.pone.0190305).
(45) Masferrer J. L., Zweifel B. S., Manning P. T., Hauser S. D., Leahy K. M., Smith W. G., Isakson P. C., Seibert K. (1994), Selective Inhibition of Inducible Cyclooxygenase 2 in vivo is Antiinflammatory and Nonulcerogenic, Proc. Natl. Acad. Sci. U. S. A., 91, 3228-3232 (DOI: 10.1073/pnas.91.8.3228).
(46) Jain M., Parmar H. S. (2011), Evaluation of Antioxidative and Anti-Inflammatory Potential of Hesperidin and Naringin on the Rat Air Pouch Model of Inflammation, Inflammation Res., 60, 483-491 (DOI: 1,0.1007/s00011-010-0295-0).
(47) Wiegand I., Hilpert K., Hancock R. E. W. (2008), Agar and Broth Dilution Methods to Determine the Minimal Inhibitory Concentration (MIC) of Antimicrobial Substances, Nat. Protoc., 3, 163-175 (DOI: 10.1038/nprot.2007.521).
(48) Duarte D. B., Vasko M. R., Fehrenbacher J. C. (2016), Models of Inflammation: Carrageenan Air Pouch, Curr. Protoc. Pharmacol, 72, 5.6.1-5.6.9 (DOI: 10.1002/0471141755.ph0506s56.).
(49) Burch R. M., Weitzberg M., Blok N., Muhlhauser R., Martin D., Farmer S. G., Bator J. M., Connor J. R., Ko C., Kuhn W., Mcmillan B. A., Raynor M., Shearer B. G., Tiffany C., Wilkins D. E. (1991), N-(fluorenyl-9-methoxycarbonyl) Amino Acids, a Class of Antiinflammatory Agents with a Different Mechanism of Action, Proc. Natl. Acad. Sci. U. S. A., 88, 355-359 (DOI: 10.1072/pnas.88.2.355).
(50) Yang Z., Gu H., Zhang Y., Wanga L., Xu B. (2004), Small Molecule Hydrogels Based on a Class of Antiinflammatory Agents, Chem. Commun., 2, 208-209 (DOI: 10.1039/B310574A).
(51) Clarke D. E., Parmenter C. D. J., Scherman O. A. (2018), Tunable Pentapeptide Self Assembled β Sheet Hydrogels, Angew. Chem., Int. Ed., 57, 7709-7713 (DOI: 10.1002/anie.201801001).
(52) Li C., Chen P., Shao Y., Zhou X., Wu Y., Yang Z., Li Z., Weil T., Liu D. (2015), A Writable Polypeptide-DNA Hydrogel with Rationally Designed Multi Modification Sites, Small, 11, 1138-1143 (DOI: 10.1002/smll.201401906).
(53) Zhao X., Pan F., Xu H., Yaseen M., Shan H., Hauser C. A. E., Zhang S., Lu J. R. (2010), Molecular Self-Assembly and Applications of Designer Peptide Amphiphiles, Chem. Soc. Rev, 39, 3480-3498 (DOI: 10.1039/B915923C).
(54) Hamley I. W. (2011), Self-assembly of amphiphilic peptides, Soft Matter, 7, 4122-4138 (DOI: 10.1039/C0SM01218A).
(55) Fischer M., Vahdatzadeh M., Konradi R., Friedrichs J., Maitz M. F., Freudenberg U., Werner C. (2015), Multilayer Hydrogel Coatings to Combine Hemocompatibility and Antimicrobial Activity, Biomaterials, 56, 198-205 (DOI: 10.1016/j.biomaterials.2015.03.056).
(56) op'tVeld R. C., van den Boomen O. I., Lundvig D. M. S., Bronkhorst E. M., Kouwer P. H. J., Jansen J. A., Middelkoop E., Von den Hoff J. W., Rowan A. E., Wagener D. T. G. (2018), Thermosensitive Biomimetic Polyisocyanopeptide

Hydrogels May Facilitate Wound Repair, Biomaterials, 181, 392-401 (DOI: 10.1016/j.biomaterials.2018.07.038).
(57) Qu J., Zhao X., Liang Y., Zhang T., Ma P. X., Guo B. (2018), Antibacterial Adhesive Injectable Hydrogels with Rapid Self-Healing, Extensibility and Compressibility as Wound Dressing for Joints Skin Wound Healing, Biomaterials, 183, 185-199 (DOI: 10.1016/j.biomaterials.2018.08.044).

Chapter 4

Evaluation of a Peptide-Based Coassembled Nanofibrous and Thixotropic Hydrogel for Dermal Wound Healing

4.1 Introduction

In recent years, self-assembling systems have attracted great attention for the construction of functional materials with the rationalized properties and functions.[1−5] The well-defined nanostructured materials could be achieved by participation of various noncovalent interactions such as hydrogen bonding and electrostatic, hydrophobic, and π−π stacking interactions among molecular building blocks.[6−11] One of the most important soft biomaterials, which exhibits self-healing and stimuli-responsive behavior, is obtained using the involvement of reversible noncovalent interactions of self-assembling systems.[12−14] In the light of recent biomaterial science advancement, the self-healing biomaterials, which recover the mechanical strength in a very short time, have been used in various interdisciplinary areas including drug delivery, wound healing, 3D bioprinting, tissue engineering, and antimicrobial therapy.[15−23] Among the various biomaterials, amino acids and peptide-based hydrogels have been extensively investigated owing to their high water content, chemical simplicity, biocompatibility, biodegradability, and tunable mechanical properties.[24−27] The Amoc (9-anthracenemethoxycarbonyl)-protected peptide-based hydrogelators possess excellent self-assembling behaviors owing to their inherent hydrophobicity and aromaticity.[11,14] The incorporation of aromatic moieties at the side chains of Amoc-capped peptides could enhance the π−π interactions. Among the various side chains, FF-based (F = phenylalanine) building blocks self-assemble into the various nanostructures such as nanotubes, nanospheres, nanowires, and nanofibrils.[28] Therefore, FF-based nanofibrous materials are highly demanding because of their functional similarity with natural extracellular matrices.[6,28] Additionally, their complex nanostructures and biological activity can be easily controlled and tuned using a simple precursor.[29−32] To achieve this, several supramolecular coassembled systems have been developed using cyclodextrins with self-assembling peptides and other organic molecules which support cell viability, promote cell attachments and migration, and provide mechanical strength.[33−36] In the area of supramolecular chemistry, cyclodextrins are an important class of cyclic oligosaccharides having six to eight interlinked D-glucose units with hydrophilic exterior and hydrophobic interior, which can increase noncovalent interactions between cyclodextrins and self-assembling peptides.[37,38] The outer hydrophilic surfaces of cyclodextrins increase the hydrogen bonding interactions between guest molecules, whereas the interior hydrophobic cavities accommodate bulky nonpolar groups.[39] The supramolecular complexes between cyclodextrins and peptides have progressively attracted researchers to design and synthesize biological active biomaterials.[40,41] The coassembled hydrogels driven by coassembly of cyclodextrins and peptides would have great promise in the area of wound healing owing to their hydrated environment, nanofibrillar morphology, excellent biocompatibility, self-healable activity, and sustained release of bioactive component for antibacterial therapy.[39−42] Wound healing is one of the universal and important issues in health care which restores the normal functions of tissues and cellular architectures to

protect against the foreign invaders, mechanical and chemical injury, and regulate the body temperature.[43–45] However, in vivo wound healing possesses several challenges such as bacterial infection, inflammatory and immune mechanism for the restoration of normal tissues, and cellular function.[46,47] The skin is considered as the largest and fastest growing organ in the animal body which serves as a self-renewing and self-repairing interface between the body and the external environment.[48–50] An ideal hydrogel for wound healing must prevent bacterial infection, allows gaseous exchange, and provides a hydrated environment for epithelial cell migration and proliferations.[47,50] The wound healing is a multistage process which consists the following events: (1) coagulation, (2) inflammation, (3) mesenchymal cell differentiation, proliferation and migration, (4) angiogenesis, (5) re-epithelization, and (6) collagen synthesis.[51,52] Coagulation or hemostasis is the first and early stage of wound healing which starts with vascular constriction, platelet aggregation, and fibrin formation to stop the bleeding.[53] The hemostatic clot and wound tissues release proinflammatory cytokines, proadhesive molecules, and growth factor such as fibroblast, epidermal, and platelet-derived growth factor.[53] The proinflammatory cytokines actuate the acute inflammation by the sequential recruitment of the inflammatory cells such as neutrophils, macrophages, and lymphocytes into the wound site.[51–53] These inflammatory cells are responsible for clearance of invading microbes, apoptotic cells, and other cellular debris near the wound site.[51–53] In this healing process, the inflammatory cells promote the cell proliferation and regeneration stage of wound healing.[51,52] It is well accepted that the moist environment has an important role in the rapid wound healing process, and dry environments cause tissue death which further delay in the healing process.[53,54] However, excessive moist environment nearby the wound site causes microbial infection and wound may enter into the nonhealing chronic inflammatory state.[49] The development of modern inherent antibacterial hydrogels provides alternative biomaterials for wound healing process by eliminating the biocontaminants and maintains the hydrated environment.[55] Second, the ideal wound healing biomaterials must not evoke the undesired inflammatory or allergic response.[56,57] Therefore, the design and fabrication of peptide-based bioactive biomaterials using cyclodextrins, which show in vivo wound healing activity, have paid great attention in the current research.[33,35,40,58] The objectives of the present work are as follows: (1) design and synthesis of bioactive dipeptide, (2) development of self-healable coassembled biomaterial with β-cyclodextrin (β-CD), (3) in vitro assessment of cytotoxicity of coassembled hydrogel, (4) antibacterial activity, and (5) in vivo wound healing activity.

4.2 Experimental Section

4.2.1 Materials and Methods

All the materials used for this project were procured from commercial sources and used as received. The 9-anthracenemethanol, 4-nitrophenyl chloroformate and pyridine were purchased from Sigma-Aldrich (Merck KGaA), India. L-phenylalanine (F), dicyclohexylcarbodiimide (DCC) and 1-hydroxybenzotriazole

(HOBt) were purchased from SRL, India. The β-cyclodextrin (β-CD) hydrated was procured from Alfa Aesar, India. The chemicals for biological experiments *i.e.* peptone powder, yeast extract, agar agar powder, Dulbecco's Modified Eagle Medium (DMEM), Minimum Essential Medium Eagle (MEM), Trypsin-EDTA solution 1X, Penicillin-Streptomycin antibiotic solution 100X and 3-(4,5-dimethythiazol-2-yl)2,5-diphenyl tetrazolium bromide (MTT) powder were purchased from HiMedia Laboratories Pvt. Ltd., India. The silverex gel (silver nitrate 0.2% w/w, Sun Pharma, India), povidone-iodine (Win Medicare Pvt. Ltd., India), Dynapar AQ (Diclofenac 75 mg/mL injection) Tegaderm (3M bandage), hair removal cream Anne French (Pfizer, India), and the disposable biopsy punch (8 mm, amazon, India) were purchased commercially for the research purposes. All solvents were analytical grade and purchased from Rankem, India; and Merck, India. The HPLC grade acetonitrile (ACN) and methanol (MeOH) were used for the analysis of the synthesized molecules. Solvents were distilled prior to use and kept in 4Å molecular sieves. Tetrahydrofuran (THF), *N,N'*-dimethylformamide (DMF), ethyl acetate (EtOAc), MeOH, hexane were dried using the standard procedure. Thin-layer chromatography was performed on pre-coated silica gel plates (Kieselgel 60 F_{254}, Merck). Synergy H1 multimode microplate reader was used for 96-well microplates reading at 25 °C.

4.2.2 Synthesis of 4

Scheme 4.1 Synthetic pathway of **4**

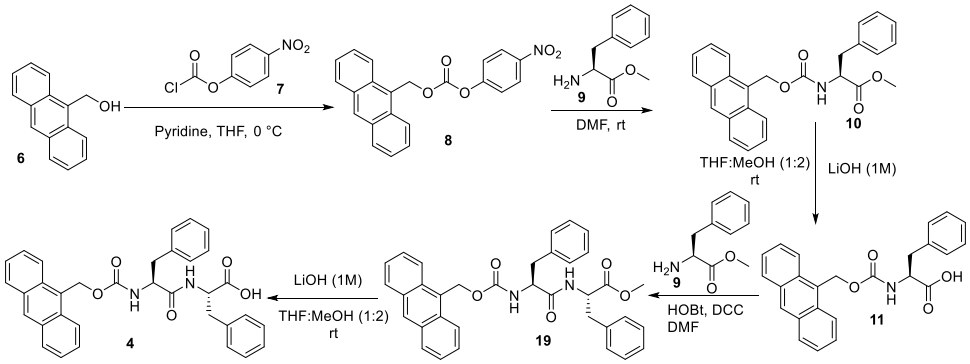

4.2.2.1 Synthesis of 8

7 (1.5 g, 7.44 mmol) was solubilized in dry THF under N_2 atmosphere. The solution was ice-cooled and pyridine (0.648 g, 8.18 mmol) was added into the cold solution. The white slurry was obtained after the addition of pyridine. **6** (1.29 g, 6.2 mmol) was solubilized in dry THF and the solution was added into the reaction mixture by several portions. The reaction mixture was allowed to stir overnight at room temperature. Product conversion was checked by TLC. After completion of the reaction, THF was evaporated by a rotary evaporator. The crude reaction mixture was diluted with ethyl acetate (50 mL) and the mixture was washed with 1 M HCl (3 × 30 mL) and successively with brine. The yellow-green product was obtained by evaporating the solvent under reduced pressure. The product was recrystallized by using benzene and yellow needle-shaped crystal of **8** was further used for the synthesis of **4**.

Yield: 1.7 g (73%). ^{1}H NMR (400 MHz, $CDCl_3$): δ = 8.58 (s, 1H, Amoc), 8.42-8.40 (d, *J* = 8.88 Hz, 2Hs, Ph), 8.26- 8.24 (d, *J*= 8.44 Hz, 2Hs, Amoc), 8.08-8.06 (d, *J* = 8.40 Hz, 2H, Amoc), 7.65-7.61 (t, *J* = 7 Hz, 2H, Amoc), 7.55-7.51 (t, *J* = 7.48 Hz, 2H, Amoc), 7.37-7.35 (d, *J* = 8.36 Hz, 2H, Ph), 6.39 (s, 2H, Amoc) ppm.

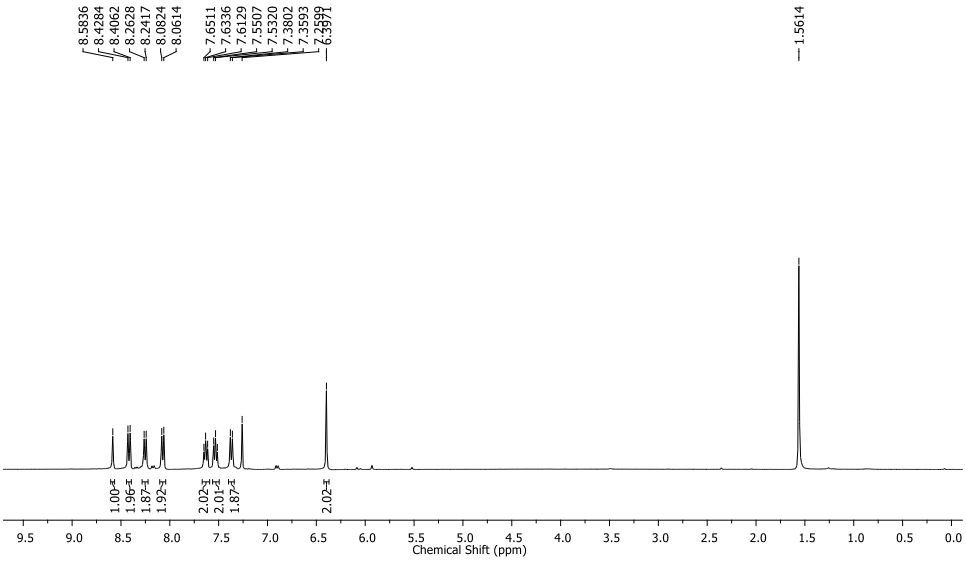

Figure 4.1 ^{1}H NMR spectrum (400 MHz) of **8** in $CDCl_3$.

4.2.2.2 Synthesis of 10

8 (1.2 g, 3.48 mmol) was dissolved in 3 mL dry DMF. The hydrochloride salt of **9** (1.25 g, 6.96 mmol) was neutralized using saturated Na_2CO_3 (10 mL) solution and the product was extracted using EtOAc (3 × 30 mL). The neutralized **9** was drop-wise added to ice-cooled reaction mixture and allowed to stir for 12 h. The product conversion was confirmed by TLC. After completion of the reaction, EtOAc (25 mL) was added and washed with 1 M HCl (3 × 30 mL), saturated Na_2CO_3 solution (6 × 30 mL) and then with brine. Solid yellow **10** was obtained after evaporating the solvent under reduced pressure. The product **10** was recrystallized in cold methanol.

Yield: 1.32 g (86%); FT-IR (KBr): $\bar{\upsilon}$ = 3302 (s, NH), 1743 (s, COOMe), 1687 (s, amide I band), 1658 (s, amide I band), 1543 (s, amide II band) cm^{-1}; ^{1}H NMR (400 MHz, DMSO-d_6): δ = 8.68 (s, 1H, Amoc), 8.34–8.31 (d, *J* = 8.72 Hz, 2H, Amoc), 8.13–8.11 (d, *J* = 8.24 Hz, 2H, Amoc), 7.72–7.70 (d, *J* = 7.92, 1H, NH), 7.62–7.53 (m, 4H, Amoc), 7.20–7.19 (br, m, 5H, Phe), 6.07–5.97 (q, 2H, Amoc), 4.29–4.28 (br, m, 1H, C^{α} H of Phe), 3.61 (s, 3H, OCH_3), 3.02–2.79 (m, 2H, C^{β} H of Phe) ppm; MS (ESI): *m/z* calcd for $C_{26}H_{23}NO_4$: 436.1525 $[M+Na]^+$; found: 436.1654.

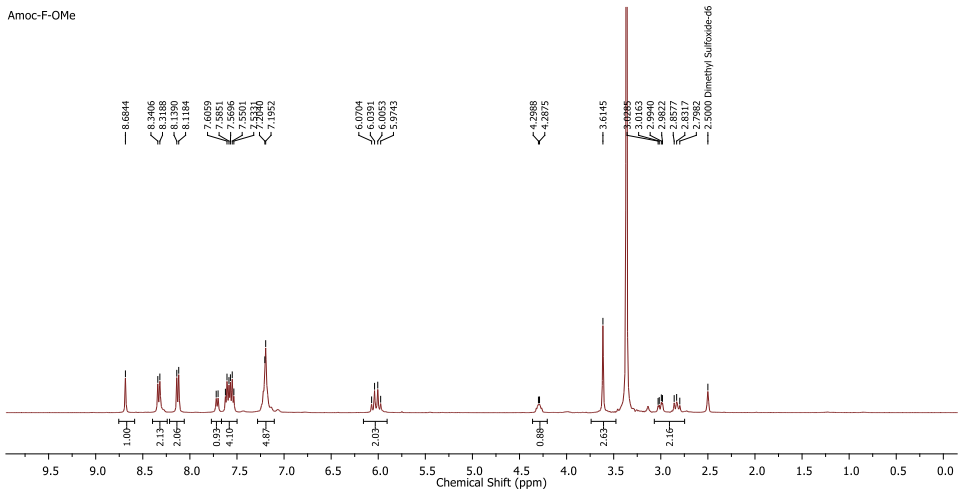

Figure 4.2 ^{1}H NMR spectrum (400 MHz) of **10** in DMSO-d_6.

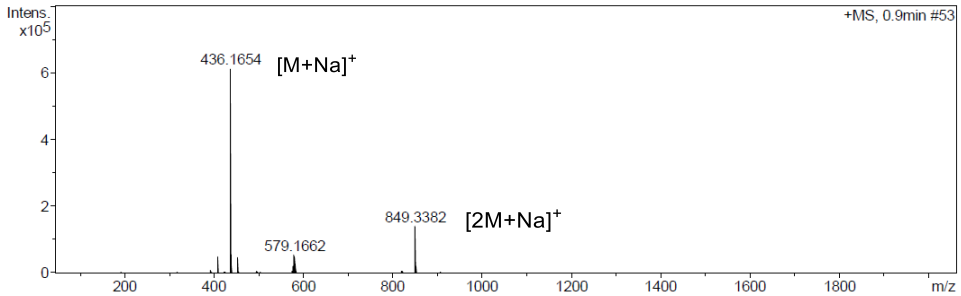

Figure 4.3 ESI-MS spectrum of **10**.

4.2.2.3 Synthesis of 11

10 (1.2 g, 2.90 mmol) was dissolved in 15 mL THF and 30 mL MeOH. In the reaction mixture, 1 M LiOH solution was slowly added for hydrolysis. The reaction mixture was stirred for 6 h and progress of the hydrolysis was monitored by TLC. Then 1 M LiOH solution was added in every 30 min interval according to the progress of the hydrolysis. The excess solvent was evaporated and remaining mixture was taken in the separating funnel. The mixture was very carefully washed with diethyl ether (2 × 20 mL). The hydrolyzed solution was taken in the conical flask and acidified with 1 M HCl (pH 2). The acidified solution was extracted three times with EtOAc (3 × 30 mL) and dried over anhydrous Na_2SO_4. The solution was evaporated and solid yellow **11** was obtained. The solid yellow mass was recrystallized in dry THF.

Yield: 0.860 g (74%); FT-IR (KBr): $\tilde{\upsilon}$ = 3294 (s, NH), 1690 (s, amide I band), 1624 (s, amide I band), 1537 (s, amide II band) cm^{-1}; ^{1}H NMR (400 MHz, DMSO-d_6): δ = 8.67 (s, 1H, Amoc), 8.35–8.31 (d, *J* = 8.64 Hz, 2H, Amoc), 8.13–8.11 (d, *J* = 8.16 Hz, 2H, Amoc), 7.61–7.52 (m, 4H, Amoc), 7.50–7.48 (br m, 1H, NH), 7.19 (s, 5H, Phe), 6.05–5.95 (q, 2H, Amoc), 4.20 (br s, 1H, C^{α} H of Phe), 3.05–2.76 (m, 1H, C^{β} H of Phe), 2.82–2.76 (m, 1H, C^{β} H of Phe) ppm. MS (ESI): *m/z* calcd for $C_{25}H_{21}NO_4$: 422.1368 $[M+Na]^+$; found: 422.1330.

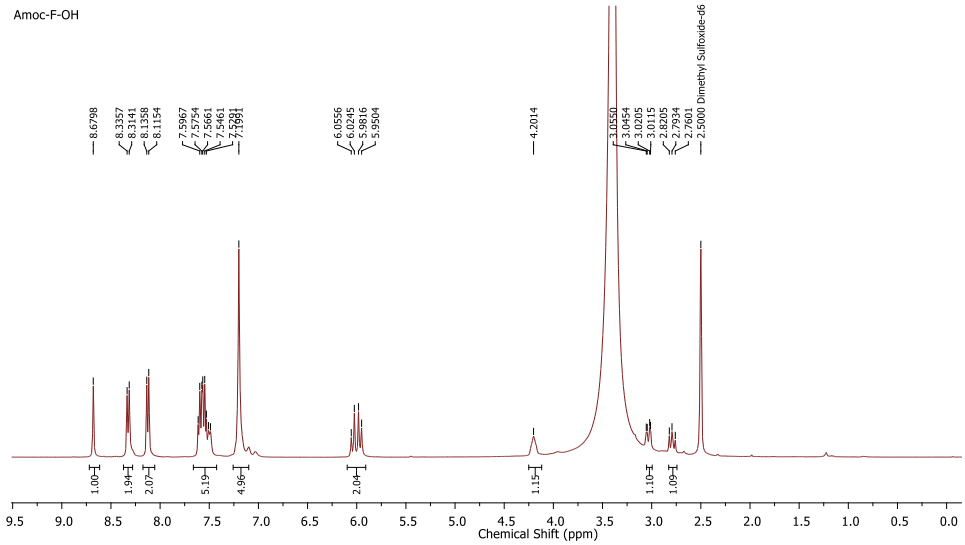

Figure 4.4 ^{1}H NMR spectrum (400 MHz) of **11** in DMSO-d_6.

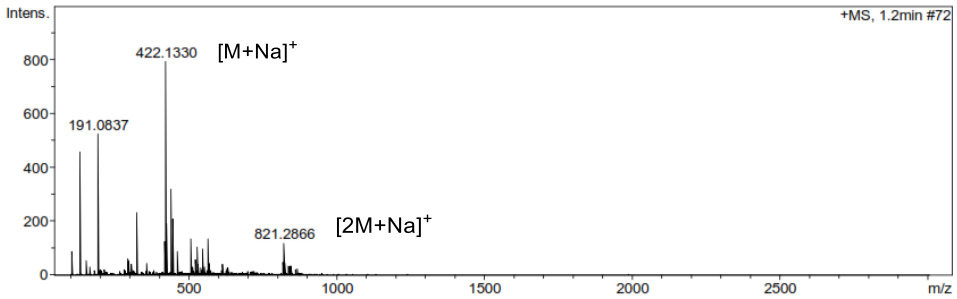

Figure 4.5 ESI-MS spectrum of **11**.

4.2.2.4 Synthesis of 19

11 (1.0 g, 2.50 mmol) and HOBt (0.406 g, 3.0 mmol) was dissolved in 3 mL dry DMF. The coupling reagent DCC (0.619 g, 3.0 mmol) was added to the reaction mixture. The reaction mixture was ice-cooled. The hydrochloride salt of **9** (0.896 g, 5.0 mmol) was neutralized using saturated Na_2CO_3 (10 mL) solution and the product was extracted using ethyl acetate (3 × 30 mL). The neutralized solution of **9** was added to the reaction mixture and allowed to stir for 12 h. The product conversion was confirmed by TLC. The reaction mixture was filtered by sintered glass funnel (Borosil, G4) to remove urea by product. Ethyl acetate (25 mL) was added to the reaction mixture and washed with 1 M HCl (3 × 30 mL), saturated Na_2CO_3 solution (3 × 30 mL). Solid yellow **19** was obtained after evaporating the solvent under reduced pressure. The solid product was dissolved in ACN and insoluble urea was removed by vacuum filtration. The ACN was evaporated at reduced pressure and solid mass of **19** was purified by flash chromatography using EtOAc: hexane (1:4) as eluent.

Yield: 1.2 g (85%); FT-IR (KBr): $\bar{\upsilon}$ = 3296 (s, NH), 1731 (s, COOMe), 1694 (s, amide I band), 1690 (s, amide I band), 1655 (s, amide I band), 1647 (s, amide I band), 1536 (s, amide II band) cm^{-1}; ^{1}H NMR (400 MHz, DMSO-d_6): δ = 8.67 (s, 1H, Amoc), 8.45–8.43 (d, *J* = 7.44 Hz, 1H, NH), 8.30–8.28 (d, *J* = 8.4 Hz, 2H,

Amoc), 8.13–8.11 (d, J = 8.08 Hz, 2H, Amoc), 7.59–7.26 (m, 4H, Amoc), 7.33–7.31 (d, J = 8.72 Hz, 1H, NH), 7.28–7.19 (br, m, 10H, ph of Phe), 5.99–5.89 (m, 2H, Amoc), 4.51–4.46 (m, 1H, C^{α} H of Phe), 4.34–4.30 (m, 1H, C^{α} H of Phe), 3.56 (s, 3H, OCH_3), 3.06–2.87 (m, 3H, C^{β} Hs of Phe), 2.66–2.60 (m, 1H, C^{β} Hs of Phe) ppm; MS (ESI): *m/z* calcd for $C_{35}H_{32}N_2O_5$: 583.2209 $[M+Na]^+$; found: 583.2279.

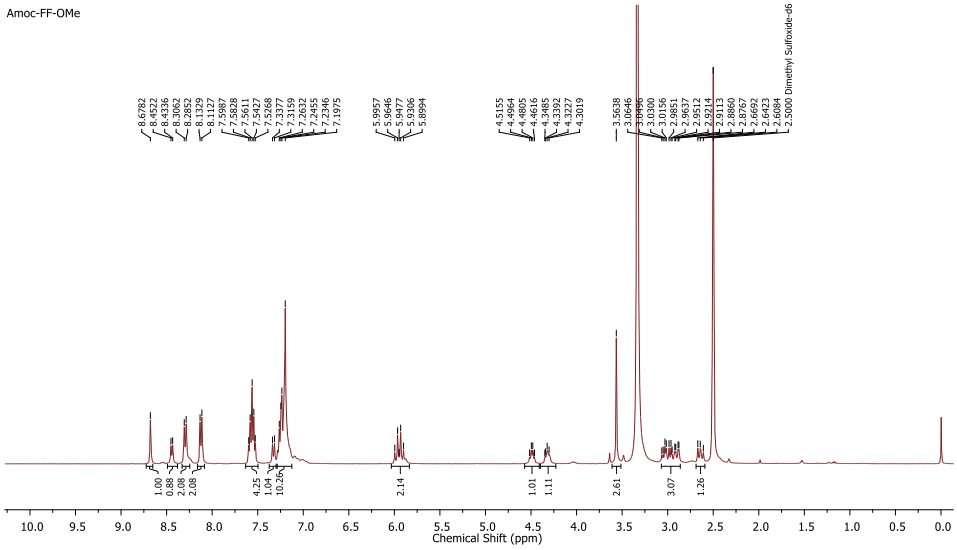

Figure 4.6 ^{1}H NMR spectrum (400 MHz) of **19** in DMSO-d_6.

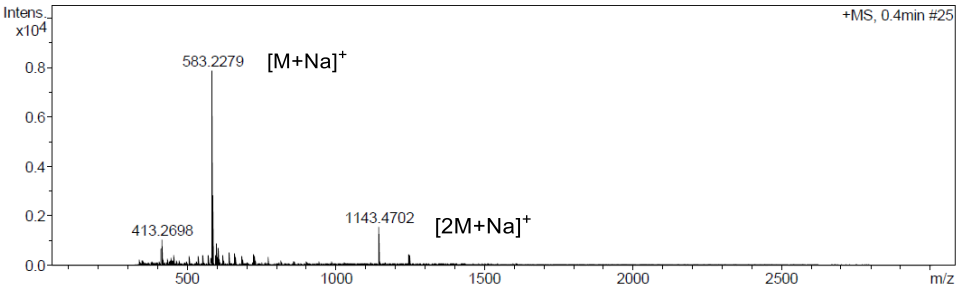

Figure 4.7 ESI-MS spectrum of **19**.

4.2.2.5 Synthesis of 4

19 (0.600 g, 1.07 mmol) was completely solubilized in the mixture of THF:MeOH (1:2, 30 mL). In the reaction mixture, 2 mL of 1 M LiOH solution was added slowly. The progress of the hydrolysis was monitored by TLC and reaction mixture was stirred up to 6 h for complete hydrolysis. After the completion of the reaction, excess solvent was evaporated and diluted with 30 mL of distilled water. The aqueous solution of the product was taken into the separating funnel and slowly washed with diethyl ether (20 mL). The aqueous layer was collected and cooled in an ice bath. Then, the solution was acidified with 1 M HCl (pH 2). The product was extracted with ethyl acetate (3 × 30 mL). The ethyl acetate layer was dried over anhydrous Na_2SO_4 and evaporated under reduced pressure to obtain **4** as yellow product. The yellow product was recrystallized in dry THF.

Yield: 0.489 g (83 %); FT-IR (KBr): $\bar{\upsilon}$ = 3289 (s, NH), 1710 (s, COOH), 1690 (s, amide I band), 1657 (s, amide I band), 1650 (s, amide I band), 1533 (s, amide II band) cm^{-1}; ^{1}H NMR (400 MHz, DMSO-d_6): δ = 8.67 (s, 1H, Amoc), 8.29–8.23

(m, 3H, 2H of Amoc and NH), 8.13–8.11 (d, J = 7.84 Hz, 2H, Amoc), 7.59–7.52 (m, 4H, Amoc), 7.31–7.29 (d, J = 8.8 Hz, 1H, NH), 7.24–7.13 (m, 11H, 10H of ph of Phe and NH), 5.97–5.89 (m, 2H, Amoc), 4.47–4.30 (m, 2H, C^{α} H of Phe), 3.09–3.05 (m, 2H, C^{β} H of Phe), 2.95–2.88 (m, 2H, C^{β} H of Phe) ppm; ^{13}C NMR (100 MHz, DMSO-d_6): δ = 173.30, 172..05, 156.48, 138.48, 137.88, 131.40, 130.95, 129.72, 129.64, 129.38, 129.13, 128.70, 128.48, 127.53, 127.11, 126.71, 125.74, 124.64, 58.67, 56.57, 54.00, 37.88, 37.23 ppm; HRMS (ESI): *m/z* calcd for $C_{34}H_{30}N_2O_5$: 569.2052 $[M+Na]^+$; found: 569.2059.

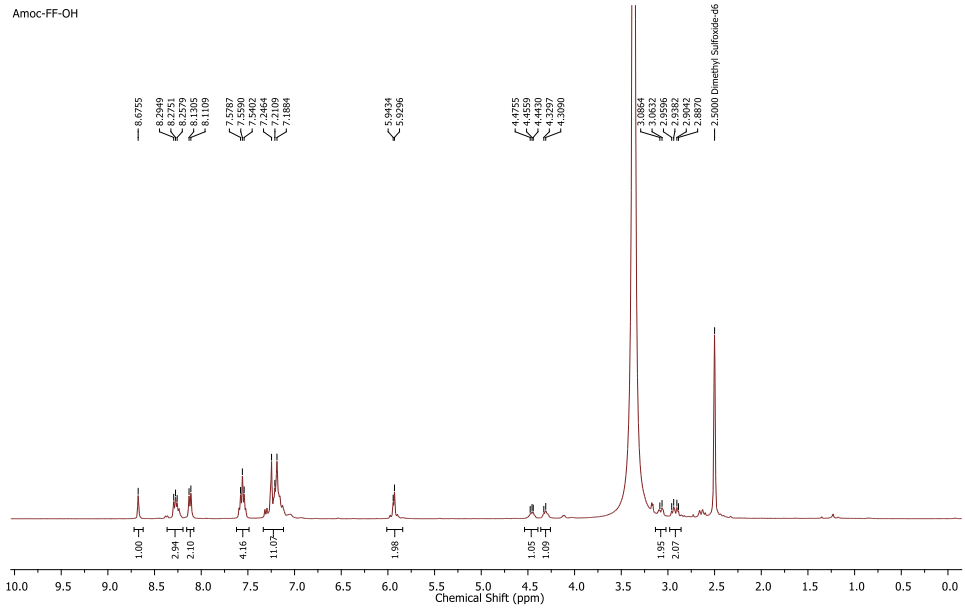

Figure 4.8 ^{1}H NMR spectrum (400 MHz) of **4** in DMSO-d_6.

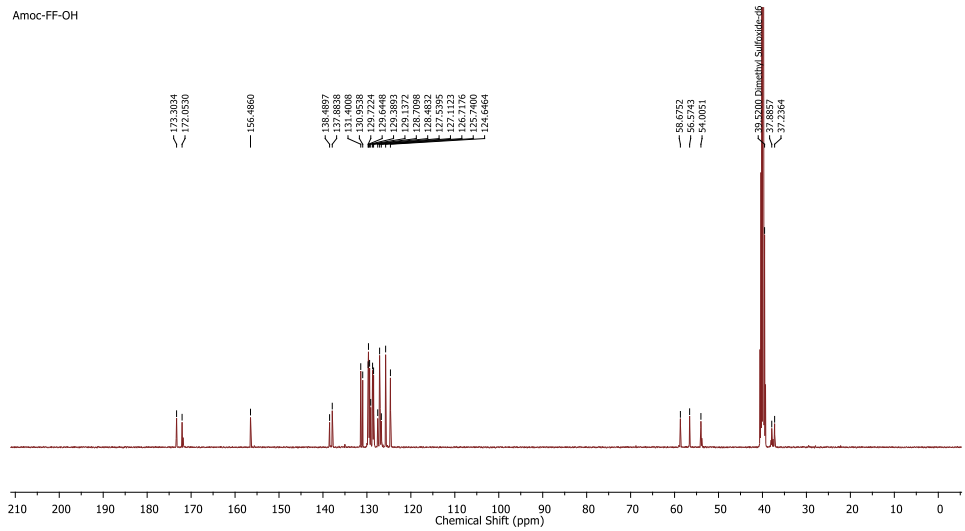

Figure 4.9 ^{13}C NMR spectrum (100 MHz) of **4** in DMSO-d_6.

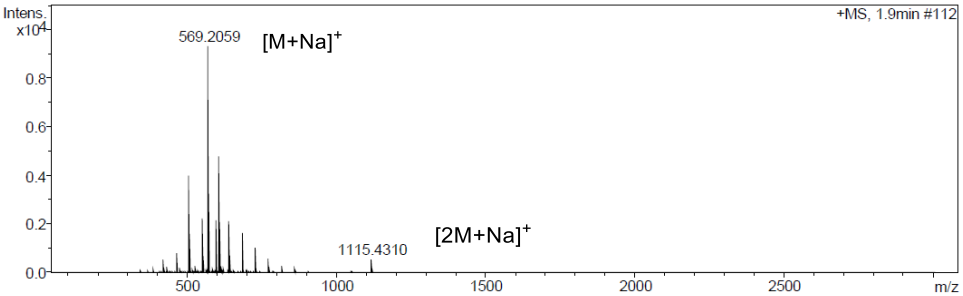

Figure 4.10 HRMS spectrum of **4**.

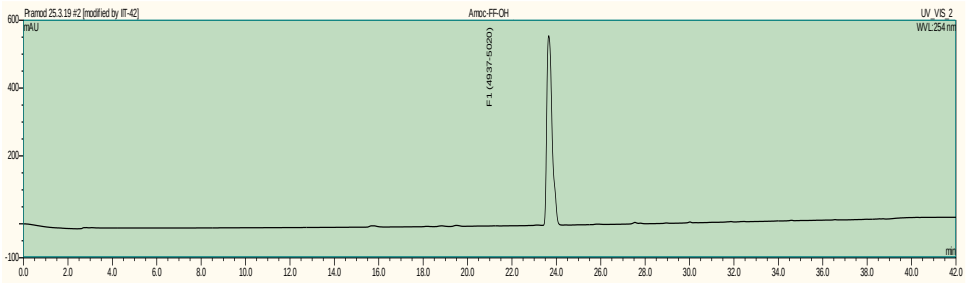

Figure 4.11 HPLC chromatogram of **4** at 254 nm.

4.2.3 Purification of the Peptide

Peptide and their intermediates were purified by Flash Chromatography (TELEDYNE ISCO, USA; model: CombiFlash®Rf+) using silica gel (200 mesh size) with EtOAc/hexane (ratio as required) as eluent. The purified peptides were recrystallized in THF by slow evaporation methods to get crystalline peptides and used for further experiments.

4.2.4 Preparation of Hydrogels

4.2.4.1 Hydrogel 4

In a glass vial, peptide **4** (20 mmol L^{-1}) was added in 2 mL of ultrapure water. Peptide **4** was added by dropwise addition of 0.5 M NaOH for dissolution and the solution was stirred for 30 min. For complete dissolution, the peptide solution was ultrasonicated at room temperature. The physiological pH of the solutions was maintained by 0.1 M HCl, and the turbid solutions of the peptide **4** turns into hydrogel **4** at 37 °C. After 30 min of incubation, the formation of hydrogel **1** was examined by inverted vial method.

4.2.4.2 Hydrogels 5−8

Peptide **4** (20 mmol L^{-1}) was taken in four different glass vials containing 2 mL of Milli-Q water. The *β*-CD (5, 10, 20, 40 mmol L^{-1}) was added to these peptide solutions and the peptide/*β*-CD molar ratio was maintained as 1:0.25, 1:0.5, 1:1, and 1:2, respectively. The pH of the mixture was elevated by slow addition of 0.5 M NaOH, and these solutions were stirred for 30 min to obtain the clear peptide/*β*-CD solution. The pH of the solution was slowly decreased to pH 7.4 by slow addition of 0.1 M HCl solution. These solutions were kept in rest for 30 min at 37 °C, which form hydrogels **5**, **6**, **7**, and **8** (peptide/*β*-CD; 1:0.25, 1:0.5, 1:1, and 1:2), respectively.

4.2.5 Characterizations

4.2.5.1 Spectroscopic and High-Performance Liquid Chromatography (HPLC) Experiments

The nuclear magnetic resonance spectroscopy (NMR) experiments were performed in $CDCl_3$ and DMSO-d_6 on a Bruker AV 400 MHz spectrometer. The peptide concentrations used for the ^1H and ^{13}C NMR were 2-5 and 120-130 mmol L^{-1}, respectively. The chemical shifts (δ) are reported in ppm, downfield of tetramethyl silane (TMS). Peak multiplicities are reported as follows: singlet (s), doublet (d), triplet (t), quartet (q) and multiplet (m) and broad (b). The electrospray ionization mass spectrometry (ESI-MS) was acquired on a Bruker micrOTOF-Q II mass spectrometer by a positive-mode electrospray ionization process. HPLC analysis was carried out using a Dionex HPLC-Ultimate 3000 pump. A Dionex Acclaim™ 120 C18 column of 250 mm length with an internal diameter 4.6 mm and 5 µm fused silica particles at a flow rate of 1 mL min^{-1} coupled with UV-Vis detector. UV-vis spectroscopy was performed on JASCO V-750 spectrometer. The concentration-dependent UV-vis experiments were performed using diluted hydrogels (500, 250, 125, 62.5, 31.25, 15.62, 7.81, 3.90 µmol L^{-1}). The circular dichroism spectra were recorded at 25 °C using a JASCO J-815 spectropolarimeter. The concentration-dependent circular dichroism experiments were performed using diluted hydrogels (20, 8, 4, 2, 1, 0.5, 0.25 mmol L^{-1}). The FTIR spectroscopy was performed on KBr pellets on a Bruker Tensor 27 FTIR spectrophotometer. The hydrogel was placed between crystal Zn−Se windows for FTIR analysis and scanned between 600-4000 cm^{-1}. The powder X-ray diffraction spectroscopy (PXRD) was performed in the 2θ range of 6° ~ 60° using a Bruker D2 Phaser X-ray diffractometer with a Cu-Kα radiation source (λ = 1.5414 Å). Confocal laser scanning microscope (CLSM) was performed using an inverted microscope (Olympus, model no. FV1200MPE, IX-83).

4.2.5.2 Electron Microscopy Experiments

The high-resolution transmission electron microscopy (HRTEM) images were captured using a FEI electron microscope (model: Tecnai G2, F30), operated at an accelerating potential of 300 kV (Magnification, 58X to 1×10^6X). The images were captured using 2% (w/v) phosphotungstic acid as a negative stain. The dilute solution (2 mmol L^{-1}) of the hydrogel was used for the HRTEM experiment.

4.2.5.3 Rheological Experiments

Rheological experiments were performed at 25 °C on an Anton Paar Physica MCR 301 rheometer. The amplitude sweep experiment was performed at constant frequency of 10 rad s^{-1} and region of deformation was evaluated. The hydrogels **4-8** were placed in between of a stainless steel parallel-plate (diameter: 25 mm) with TruGap (0.5 mm). The frequency sweep experiment was performed in the range of 0.05-100 rad s^{-1} with the same strain percent found by amplitude sweep experiment. The step strain experiment was performed by varying low-high-low strain at constant frequency of 10 rad s^{-1}.

4.2.6 Antibacterial Test

4.2.6.1 Inoculum Growth

The nutrient agar (NA) plate method was used to evaluate the antibacterial activity of the hydrogels. The bacterial culture *Staphylococcus aureus* (*S. aureus*, MTCC 87), *Bacillus subtilis* (*B. subtilis*, MTCC 441) and *Escherichia coli* (*E. coli*, MTCC 484) bacteria were procured from the Institute of Microbial Technology Chandigarh (CSIR-IMTech), India. Fresh inoculum was grown in nutrient broth (NB) and used for the experiments. The NA was prepared by dissolving peptone (10 gm), yeast extract (3 gm), NaCl (5 gm), agar-agar powder (20 gm) in 1000 mL water. The NB was prepared similarly as NA by eliminating agar-agar powder and autoclaved before use.

4.2.6.2 Hydrogel Treatment

The hydrogel was prepared by maintaining the aseptic conditions. The sterile Milli-Q water, 0.5 M NaOH and 0.1 M HCl were used for the hydrogel preparation under the laminar air flow. The hydrogel **7** (20 mmol L^{-1}) was treated with *S. aureus* and *B. subtilis* and *E. coli* bacteria. The bacterial culture was grown for 12 h at 37 °C and used for the experiment. The absorbance (OD_{600} = 0.1) of bacterial culture was set according to McFarland standard (2×10^8 cfu/mL). A 100 µL of hydrogel **7** was transferred in a sterile centrifuge tube and 400 µL of NB was added slowly on the top of hydrogel. A 10 µL of bacterial culture (2×10^6 cfu/mL) was added to the NB containing hydrogel **7**. The microcentrifuge tubes were incubated at 37 °C for 12 h for the bacterial growth. After treatment, 10 µL of bacterial suspension containing hydrogel **7** was 10-fold diluted and whole plate streaked in a sterile nutrient agar plate. The reduction in the bacterial colonies was visually observed in the nutrient agar plate.

4.2.7 Cell Culture Experiments

The cell culture experiments were performed in DMEM (Dulbecco's Modified Eagle Medium contains 4 mM L-glutamine, 1000 mg/L glucose, and 110 mg/L sodium pyruvate) with 10% FBS (fetal bovine serum) and 1% antibiotic (penicillin-streptomycin) solution. The hydrogels **4** and **7** were diluted in cell culture media and used for the experiments. The resulting hydrogels concentrations for the cell culture experiments were in the range of 200 to 12.5 µmol L^{-1}. The MCF-7 and HEK293 cells were used for the biocompatibility test. The hydrogels were treated with MCF-7 and HEK293 (8×10^3 cells/well) cells for 24 h at 37 °C. After treatment, the cell culture media was removed very carefully and cells were washed with PBS (10 mmol L^{-1}, pH 7.4) to remove the excess hydrogel. After washing, the fresh DMEM (Dulbecco's Modified Eagle Medium) was added into the 96 well plate. The cytotoxic effect was evaluated by 3-(4,5-dimethylthiazol-2-yl)-2,5-diphenyltetrazolium bromide (MTT) assay. The absorbance was taken at 570 nm using a microplate reader.

4.2.8 Confocal Experiments

The A431 cells were grown in sterile cover slip in DMEM for 24 h. The different hydrogel concentrations (50 and 100 µM) were treated with the cells for the uptake of peptides (6 h at 37 °C). The cells were washed twice with PBS to remove the excess hydrogel. The cells were treated with thiazole orange (50 and 100 µM) for 30 min. The excess dye was slowly removed by PBS washing. The cells were fixed

in paraformaldehyde (4% w/v) and mounted in fresh glass slide for the confocal laser scanning microscopy (CLSM). The hydrogel **7** and thiazole orange were excited at λ_{ex} = 405 and 488 nm, respectively.

4.2.9 Wound Healing Experiments

In vivo wound healing experiments were performed according to the Institutional Animal Ethical Committee (IAEC) guidelines. The experimental approval was taken prior to the wound healing experiments. Wistar albino male rats (weight 180 ± 10 gm) were housed in polypropylene cages in a standard photoperiod (14 h, light:10 h, dark, 27 ± 2 °C) with the provision of laboratory feed (Gold Mohur feed, Hindustan Lever Limited, Mumbai, India) and water *ad libitum*. Animals were maintained in accordance with the guidelines of the Committee for the Purpose of Control and Supervision of Experiments on Animals (CPCSEA), Ministry of Environment, Forest and Climate Change, New Delhi, Government of India (Reg. No. 779/Po/Ere/S/03/CPCSEA).

4.2.9.1. Wound Creation and Hydrogel Injection

For the wound creation (1 day), each rat was anesthetized by subcutaneous injection of a cocktail of ketamine (50−60 mg/kg) and xylazine (10 mg/kg). The dorsal hairs were removed by using hair removal cream (Anne French; Pfizer, India). The wounding area was marked and then sterilized with povidone-iodine solution prior to incision. A disposable biopsy punch (8 mm) was used to induce wound on each side (two wounds) of the dorsal midline of the rat. Then, the rats were divided into different experimental groups such as disease control, drug control, hydrogel **7**, and *β*-CD group, and each group contains five rats (n = 5). For the wound healing assay, the standard drug (silverex gel 0.2% w/w), hydrogel **7**, and *β*-CD were applied on the wound site with the help of a micropipette (100 μL/wound). The disease control group was given phosphate-buffered saline (PBS) on the wound site. After 1 h, the wound site was covered and fixed by placing Tegaderm-3M dressing bandage over the wound. The wet environment of the hydrogel sometimes creates troubleshoot for the Tegaderm-3M bandage; hence, the interval was maintained for proper hydrogel drying on the wound site. Diclofenac injection was subcutaneously given after a 4 h interval of the wounding. Hydrogel **7**, standard drug, *β*-CD, and PBS were given on every alternate day. On day 7, the rats were anesthetized and wound size was photographed. The wound tissues were carefully collected in the PBS for the histology analysis and fixed in buffered formaldehyde (10% v/v). On day 12, the experiment was terminated and reduction in the wound area was photographed by a digital camera. The rats were anesthetized and the wound tissues were collected in the PBS for histology and biochemical analysis. The wound tissues were fixed for the histological analysis.

4.2.9.2 Histology Experiments

The wound tissue histology was performed on days 1 and 12. The small tissue specimen was collected by biopsy punch, and the tissue fixation was performed in formalin solution (10% v/v). The fixed tissues were properly dehydrated and embedded in paraffin wax and small sections were cut into 4 μm thickness. The sections were stained with hematoxylin and eosin (H&E staining), and images

were captured in an inverted optical microscope for the histology analysis of the wound healing process.

4.2.9.3 Hydroxyproline Assay

The wound tissues were dried on the blotting paper and properly chopped into small pieces. The chopped tissues (10% w/v) were slowly homogenized in ice-cold PBS (10 mM, pH 7.4). The homogenized solution was centrifuged at 10,000 rpm (4 °C) for 15 min. The supernatant was slowly separated for the hydroxyproline assay and performed as previously reported.[74] The stock L-hydroxyproline solution (1 mg/mL) was prepared in Mill-Q water. The Ehrlich's reagent (1 M) was prepared by dissolving 1.5 g of p-dimethylaminobenzaldehyde in n-propanol/perchloric acid (2:1 v/v, 3 mL) and volume was maintained 10 mL by addition of Mill-Q water. The chloramine-T (0.056 M) reagent was prepared by addition of 1.26 g of chloramine-T in 20 mL of n-propanol/water (1:1), and final volume was maintained as 100 mL by addition of acetate-citrate buffer (pH 6.5, 100 mmol L−1). The tissue homogenate (200 μL) was taken in a 2 mL microcentrifuge tube and 50 μL of 10 M NaOH solution was added to the vial. The tissue homogenate sample was hydrolyzed by autoclaving at 121 °C for 30 min. Chloramine-T (750 μL) was added to this sample and kept for 25 min at room temperature. Ehrlich's reagent (500 μL) was added to the sample and kept at 70 °C for 30 min for the chromophore development. The water (500 μL) was added and absorbance was recorded at 550 nm using a spectrophotometer.

4.2.9.4 Nitrite Assay

The standard nitrite solution (1.44 mmol L^{-1}) was prepared by dissolving 1 mg of sodium nitrite in 10 mL of Milli-Q water. The tissue homogenate was mixed properly, and 400 μL of homogenate was taken in a microcentrifuge tube. Griess reagent (100 μL) was added to this tube at room temperature and mixed thoroughly with a micropipette. Milli-Q water (1.5 mL) was added to this tube and incubated for 20 min at room temperature. The solution turns into pink color and the absorbance was recorded at 548 nm.

4.2.9.5 Protein Estimation

The NanoDrop 2000 spectrophotometer was used for the protein estimation. The tissue homogenate was diluted 5-fold, and 1 μL of sample was placed on the measurement probe and absorbance was recorded at 280 nm. The BSA protein (1 mg/mL) was used as the standard known protein sample, and absorbance was compared with the absorbance of the tissue homogenate.

4.2.10 Statistical Analyses

The biological data are shown as mean ± standard error of the mean. $*p < 0.05$; $**p < 0.01$; $***p < 0.001$, and $****p < 0.0001$ as compared to the control group. The data were analyzed by one-way ANOVA (nonparametric), followed by Neuman-Keuls multiple comparison tests, using a Graph Pad Prism (GraphPad, San Diego, CA).

4.3 Results and Discussion

In this work, an Amoc-capped peptide **4** (Amoc-FF-OH; F = L-phenylalanine) was synthesized by conventional solution-phase methodology and well characterized by Fourier transform infrared (FTIR) spectroscopy, mass spectrometry, and ^{1}H and ^{13}C NMR spectroscopic techniques (Figure 4.01-4.10). The purity of the synthesized peptide was analyzed by high-performance liquid chromatography (HPLC) technique, and purified peptide was used for the biological assays (Figure 4.11). The synthesized peptide was used for the preparation of hydrogels **4–8** (Table 4.1). The peptide **4** (20 mmol L^{-1}) forms self-assembled hydrogel **4** at physiological conditions (pH 7.4, 37 °C) by a simple pH switch method. However, the coassembled hydrogels **5–8** were prepared by the incorporation of peptide **4** (20 mmol L^{-1}, 1 equivalent) with various molar ratios of *β*-cyclodextrin (*β*-CD) (5, 10, 20, and 40 mmol L^{-1}; 1:0.25, 1:0.5, 1:1, and 1:2) (Table 4.1).

Table 4.1 Preparation of the hydrogels **4-8** with different concentrations of *β*-CD and their physical nature

S. No.	Peptide (mmol L^{-1})	*β*-CD (mmol L^{-1})	Peptide/*β*-CD (molar ratio)	Temp., pH	Hydrogel	Nature of Hydrogel
1	20	-	-	37 °C, 7.4	**4**	Strong, nonhomogeneous
2	20	5	1:0.25	37 °C, 7.4	**5**	Weak homogeneous
3	20	10	1:0.50	37 °C, 7.4	**6**	Homogeneous, self-recoverable
4	20	20	1:1	37 °C, 7.4	**7**	Homogeneous, self-recoverable, injectable
5	20	40	1:2	37 °C, 7.4	**8**	Very weak, unstable

The peptide **4** was mixed with various molar ratios of *β*-CD and partially solubilized by dropwise addition of 0.5 M NaOH, and the pH was maintained as 10. The solution was kept under stirring at room temperature for 30 min. The solubility of the peptide **4** increases with the increase of *β*-CD concentrations, and maximum solubility was observed at an equimolar ratio of peptide/*β*-CD (1:1). After complete dissolution, the pH of the solution was slowly reduced by dropwise addition of 0.1 M HCl. The final pH of the solution was maintained to 7.4. The viscous solutions slowly encapsulate the large amount of water and turns into well-defined hydrogels **5–8** after keeping at rest at 37 °C for 30 min (Scheme 4.1). The self-assembled hydrogel **4** is strong and does not show the syringe injectability (Table 4.1). To overcome this limitation, hydrogels have been engineered by incorporation of *β*-CD. The hydrogel stability and mechanical strength are greatly

affected by β-CD concentrations (Table 4.1). The greater β-CD concentration (40 mmol L^{-1}) in hydrogel **8** significantly reduces the hydrogel stability and shows precipitation after 48 h at 37 °C (Table 4.1). However, the lower β-CD concentration (5 mmol L^{-1}) in hydrogel **5** results in the weaker hydrogel (Table 4.1). The most striking results were achieved at 10 and 20 mmol L^{-1} concentrations of β-CD in hydrogels **6** and **7**, respectively. These hydrogels are stable, homogeneous in nature, and show simple syringe injection without any blockage (Table 4.1).

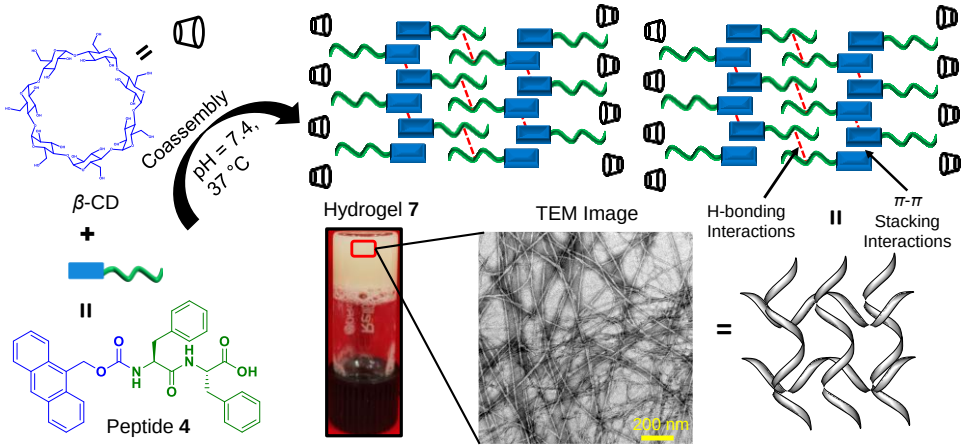

Scheme 4.2 Graphical representation of coassembly between peptide 1 and β-CD leading to the formation of ordered structures which results into hydrogel **7** (Peptide 1:β-CD = 1:1).

Furthermore, these physical observations of hydrogels **4–8** are corroborated by rheological experiments (Figures 4.12a-j). The rheological experiments were performed to evaluate the mechanical strength of hydrogels **4–8**.[4,14,59] The viscoelastic nature of the hydrogels are confirmed by amplitude sweep experiments (Figures 4.12a,c,e,g,i). The amplitude sweep experiments were performed to evaluate the exact strain percent where the linear viscoelastic (LVE) region is valid for hydrogels **4–8**. The amplitude sweep data show variation in the storage modulus (G′) and loss modulus (G″) with the crossover point (G′ = G″) at a constant angular frequency 10 rad/s. The amplitude sweep experiments show elastic-like character (G′ > G″) of the hydrogels at low strain and liquid-like character (G′ < G″) at high strain. The self-assembled hydrogel **4** shows high storage (>10^4) and loss moduli (>10^3) (Figure 4.12a,b). Noteworthy, the values of G′ and G″ decrease owing to the presence of β-CD in hydrogels **5–8** (Figures 4.12c-j). The higher crossover values for hydrogels **5–7** suggest the elastic behavior of hydrogels which dominate over viscous behavior (Figure 4.12c,e,g). Hydrogel **8** does not show the plateau region with a linear decrease in storage and loss moduli which could be the outcome of a weaker three-dimensional network present in hydrogel **5** (Figure 4.12i).[35,36] Further, the dynamic frequency sweep

experiments were performed within the LVE region to ensure the solid-like character of hydrogels **4–8** (Figures 4.12b,d,f,h,j).[20]

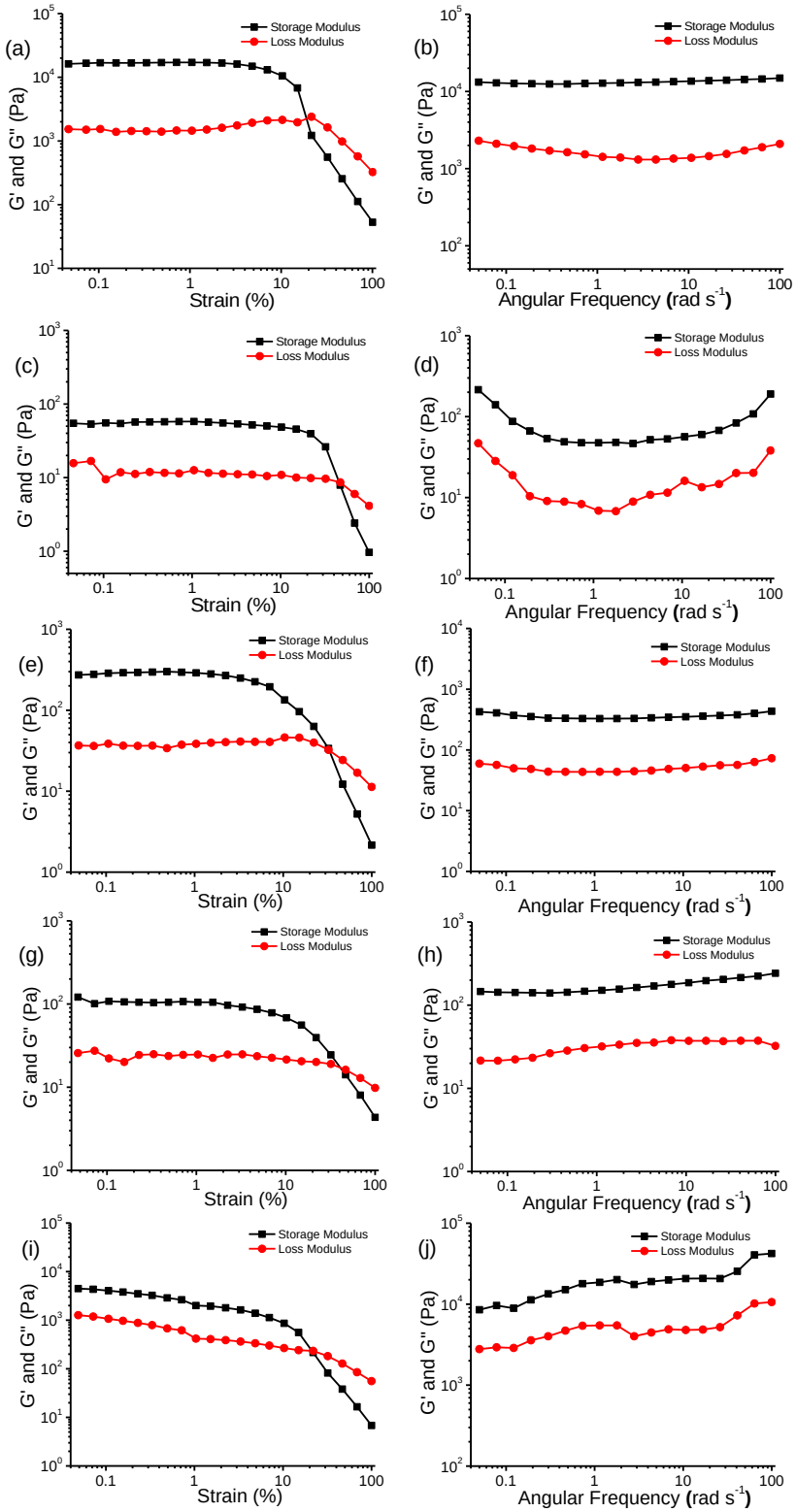

Figure 4.12 (a,c,e,g,i) Amplitude sweep experiments; (b,d,f,h,j) Frequency sweep experiments of hydrogels **4-8**, respectively.

The frequency sweep data of hydrogels **4**, **6**, and **7** suggest that G′ and G″ are independent of applied frequency and show solid-like behavior in the entire oscillating frequency (100−0.05 rad/s) region (Figures 4.12b,f,h).[34] As expected, hydrogels **5** and **8** show frequency-dependent G′ and G″, which suggest the formation of a weaker three-dimensional network (Figure 4.12d,j). The rheological data from amplitude and frequency sweep suggest that hydrogels **4**, **6**, and **7** show better mechanical strength compared to hydrogels **5** and **8**. Noteworthy, as compared to hydrogel **4**, the values of G′ and G″ decrease dramatically in the case of hydrogels **6** and **7**. Interestingly, biomaterials with lower viscosity and lower G′ and G″ are easier to inject to the target site compared to biomaterials with high viscosity and high G′ and G″.[20,36,37] The other advantages of biomaterials with low G′ and G″ show better self-recovery properties after injection to the target site.[35] Importantly, the hydrogels for better wound healing applications must retain the three-dimensional network after gel-sol-gel conversion.[20,39] To ensure the in vivo applicability, the step strain experiments were performed to evaluate the thixotropic and self-healing properties of hydrogels **4** and **7** (Figure 4.13a,b).[26,39]

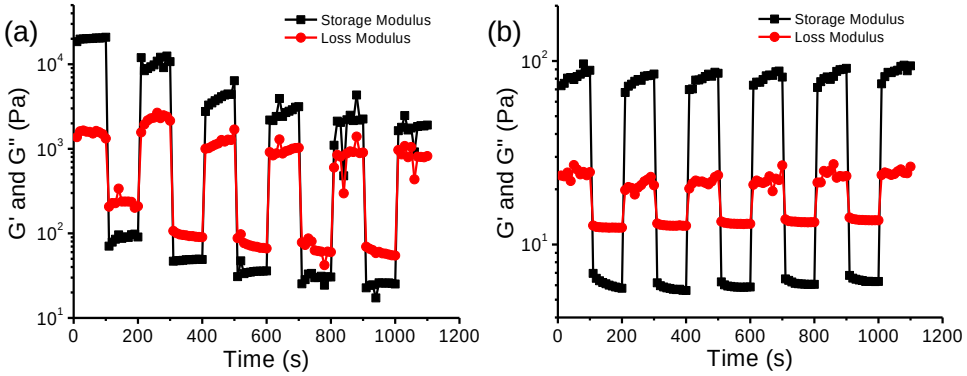

Figure 4.13 (a,b) Step strain experiments of hydrogels **4** and **7**, respectively.

Hydrogels **4** and **7** were subjected to the periodically low-high-low (1, 40, and 1%) strain at a constant angular frequency (10 rad s^{-1}). The low strain (1%) shows solid-like (G′ > G″) character, but the high strain (40%) shows liquid-like (G′ < G″) character, which is recovered (G′ > G″) again when low strain (1%) was applied. Hydrogel **7** shows better self-recovery (almost 95%) compared to hydrogel **4** (Figure 4.13b). The equimolar ratio of the peptide and *β*-CD could provide substantial noncovalent interactions including hydrogen bonding; thus, hydrogel **7** exhibits better thixotropic and self-recovery properties.[25,60] The thixotropic nature of the hydrogel depends on the dynamic cross-linking ability of gelator molecules.[25] The higher applied strain breaks the entangled nanofibrillar network and the hydrogel converts into sol-like state owing to the disruption of noncovalent interactions. However, the noncovalent interactions including hydrogen bonding between gelators recovered very rapidly at the low strain, and sol-state turns into the gel state because of the reconstruction of fibrillar networks. The other stoichiometric ratio of peptide/*β*-CD results in a change in the mechanical strength

of the hydrogel probably because of the imbalanced orientations and interactions between the peptide and β-CD. The thixotropic behavior of hydrogel **7** potentially indicates the biological importance of the recoverable three-dimensional network (Figure 4.13b). Ultimately, hydrogel **7** has been chosen for the biological applications because of the better injectability and quick self-recovery ability (Figure 4.14a,b).[25]

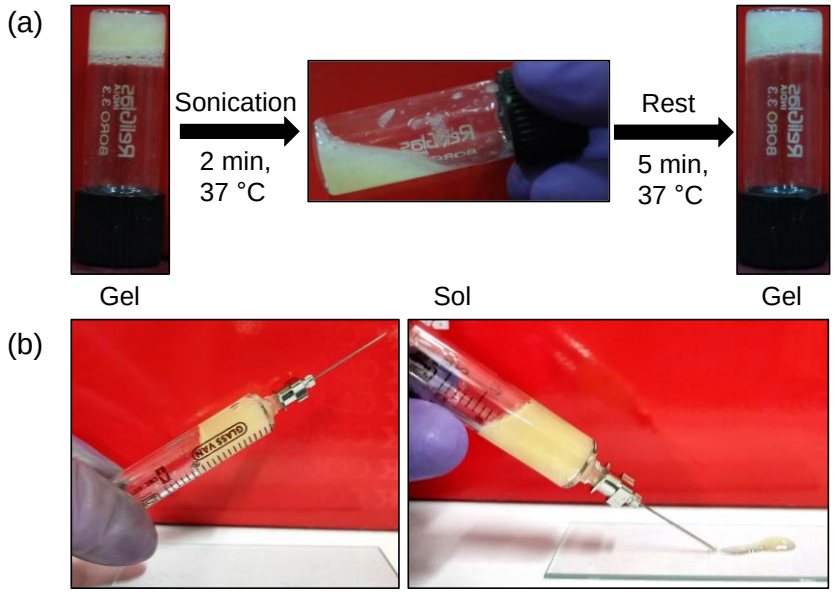

Figure 4.14 The optical photographs of hydrogel **7** showing: (a) reversible gel-sol-gel conversion; (b) syringe injectability.

The nanostructural morphology of hydrogel **7** was analyzed by high resolution transmission electron microscopy (HRTEM) (Figure 4.15a,b).[29]

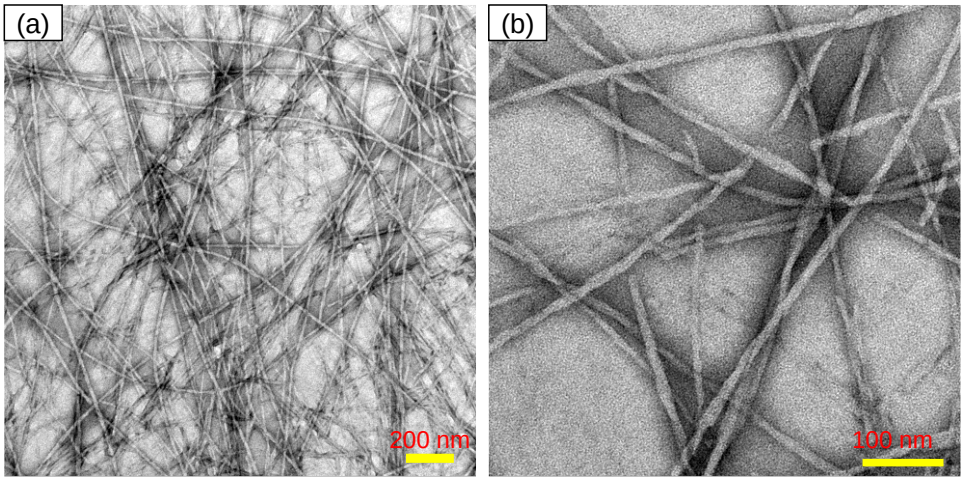

Figure 4.15 HRTEM images of hydrogel **7**. (a) Entangled nanofibers and (b) twisted nanofibers.

The HRTEM data suggests the highly entangled fibrous networks present in hydrogel **7** (Figure 4.15a). The TEM images show that the entangled fibrillar networks are highly twisted (Figure 4.15b). The twisted fibers could be the result of lateral association of multiple one-dimensional nanofibers which adhered by hydrogen bonding interactions.[61] The observed average width of the nanofibers is 10−15 nm with several micrometers in length. The driving force behind the hydrogelation of peptide and *β*-CD was investigated by various techniques such as ^{1}H NMR, FTIR, and powder X-ray diffraction (PXRD) spectroscopy.[30,31,62] Hydrogel **7** was freeze-dried and used for ^{1}H NMR and PXRD spectroscopic analysis, which is represented as xerogel **7**. ^{1}H NMR spectroscopy was employed to investigate the noncovalent interactions present between *β*-CD and peptide **4** (Figure 4.16).[63]

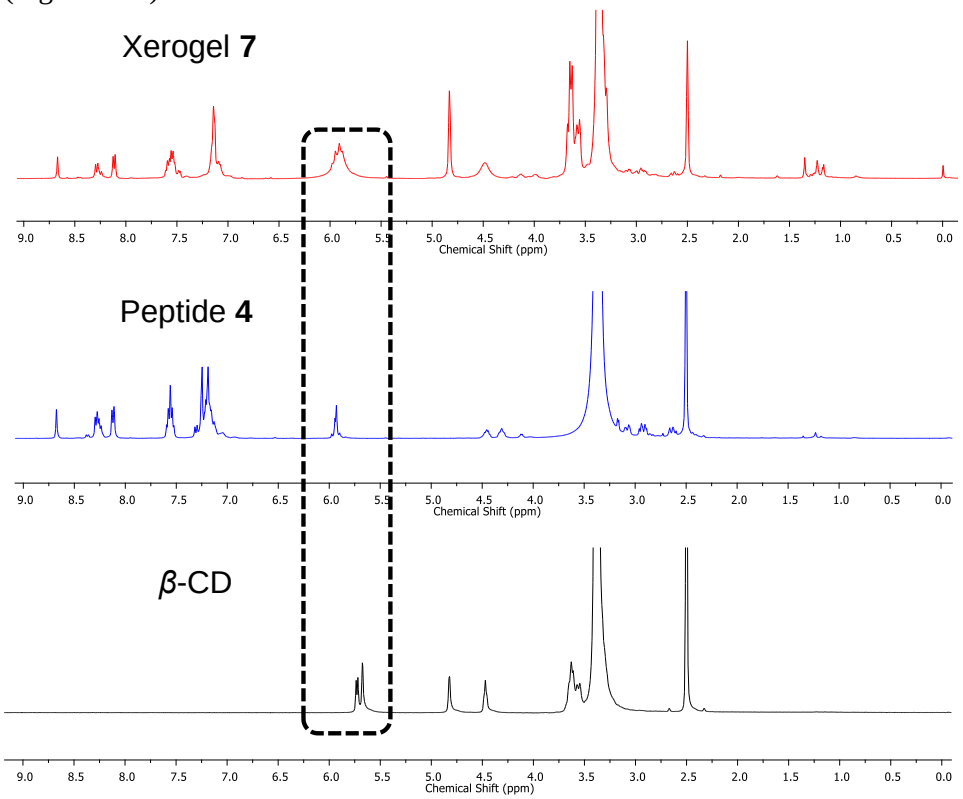

Figure 4.16 ^{1}H NMR (400 MHz, 25 °C) data of *β*-CD, peptide **4** and xerogel **7** in DMSO-d_6.

^{1}H NMR spectroscopy was employed for free *β*-CD, peptide **4**, and xerogel **7**. The ^{1}H NMR data of xerogel **7** show the significant change in the chemical shift value (deshielding) of the secondary hydroxyl group (2-OH and 3-OH) located in the wider rim of the *β*-CD, which could be attributed from noncovalent interactions between peptide **4** and *β*-CD (Figure 4.16).[63] The ^{1}H NMR data of xerogel **7** show a change in the chemical shift value of amide proton owing to the noncovalent interactions between the peptide and *β*-CD. Moreover, the chemical shift values of the internal protons (H3 and H5) of the *β*-CD are nonsignificantly affected, which

suggest exclusion of the peptide from the β-CD cavity.[63] Furthermore, the FTIR spectroscopic experiments were employed to investigate the noncovalent interactions present between peptide and β-CD (Figures 4.17a).[64,65]

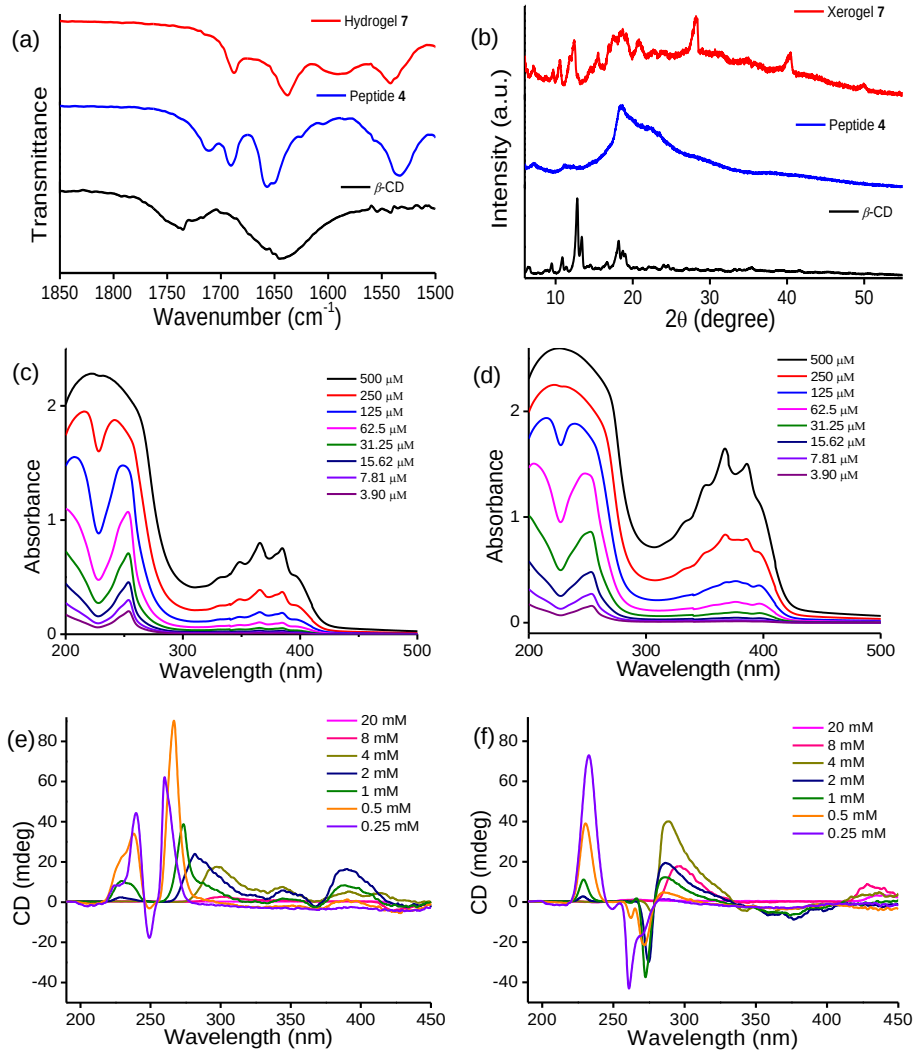

Figure 4.17 (a) FTIR and (b) PXRD spectra of β-CD, peptide **4**, and hydrogel **7**. (c,d) Concentration-dependent circular dichroism spectra of hydrogels **4** and **7**, respectively.

The FTIR spectrum of peptide **4** exhibits C=O stretching vibrations for carboxylic acid group at 1713 cm^{-1}. The amide I peaks are observed at 1691, 1658, and 1650 cm^{-1}, respectively, which show randomness present in peptide **4**. However, the FTIR spectrum of hydrogel **7** shows shifting in amide I peaks toward the lower wavenumber at 1687 and 1638 cm^{-1}, respectively. The shifting of amide I toward the lower wavenumber suggests a more ordered structure present in hydrogel **7** owing to the involvement of noncovalent interactions between peptide **4** and β-CD molecules (Figure 4.17a).[64] The FTIR spectrum of hydrogel **7** reveals a β-sheet

like structure of peptides with an antiparallel arrangement.[31,66,67] The coassembly of peptide **4** and *β*-CD was further investigated by PXRD spectroscopy (Figure 4.17b).[40,59,64] The PXRD spectrum of *β*-CD shows characteristic sharp peaks at 2Θ = 9.47, 10.80, 12.72, and 13.40°, respectively, which suggest a high-degree of crystallinity of *β*-CD with cage-like structure (Figure 4.17b).[40] These characteristic peaks of *β*-CD may associate with the cavity diameter (6-6.5 Å) and height of the *β*-CD ring (7.9 Å).[40] The PXRD spectrum of peptide shows a broad peak at 18.42°, giving a d-spacing value of 4.8 Å, which suggests an inter strand-type hydrogen bonding distance (Figure 4.17b).[8,22] However, the PXRD spectrum of xerogel **7** shows crystalline nature, which is evident by a series of sharp peaks at 10.50, 12.38, 18.65, 20.74, 28.26, and 40.50°.[40] There is a small shift in d-spacing value from 4.8 to 4.75 Å owing to the coassembly of peptide **4** and *β*-CD. The PXRD investigation of xerogel **7** showed a peak at 8.70° with a d-spacing value 10.15 Å because of the β-sheet-like antiparallel arrangement of peptides.[14,67] The PXRD peaks at 28.26 and 40.50° correspond to d-spacings of 3.15 Å and 2.22 Å, which could be attributed from hydrogen bonding interactions between peptide **4** and *β*-CD units.[62] In comparison with the PXRD data of *β*-CD and peptide, xerogel **7** shows ordered structural arrangement in the coassembled state (Figure 4.17b).[40] In addition, the UV/vis spectroscopy was performed to investigate the absorption maxima of hydrogels **4** and **7** for circular dichroism spectroscopy (Figure 4.17c,d). The supramolecular interactions and secondary structure present in hydrogels **4** and **7** were analyzed by concentration-dependent circular dichroism spectroscopy (Figure 4.17e,f).[8,26,29,31] The circular dichroism spectra of hydrogel **4** show positive cotton at 340−390 nm owing to the π−π* transition of the anthracene ring (Figure 4.17e).[8,68] However, the circular dichroism spectra of hydrogel **7** show a very weak negative cotton effect at 350−385 nm, which suggest different orientations of noncovalent interactions between peptide **4** and *β*-CD (Figure 4.17f).[8,68] Additionally, the prominent π−π* transitions due to the aromatic moieties are observed between 230 and 270 nm for hydrogels **4** and **7** (Figure 4.17e,f).[31,69] The circular dichroism spectra of hydrogels **4** and **7** show significant variations in positive signals as lowering the concentrations.[26] Importantly, the aromatic peak positions in hydrogel **4** continuously shift toward the lower wavelength with the decrease in concentration, which suggest loss of supramolecular interactions between assembling entities(Figure 4.17e).[26] Moreover, hydrogel **7** shows the decrease in the intensity of positive signal as lowering of the concentrations (Figure 4.17f). These experimental results indicate that *β*-CD could be present between two β-sheet type of structure forming units, and further dilution leads to the decrease in the intensity of positive signal (Figure 4.17e,f).[26] Microbial infection and biofilm formation on the surface of biomaterials are serious global challenge and health issue.[70,71] Inherent antibacterial hydrogels prevent bacterial contaminations and serve as an alternative weapon against drug resistant bacteria.[55,72] The bacterial infections occurred in acute wounds lead toward the chronicity and delay in the healing process. The ideal biomaterials for wound

healing and drug delivery applications must eliminate the biological contaminations without evoking the unwanted allergic reactions.[55−57]

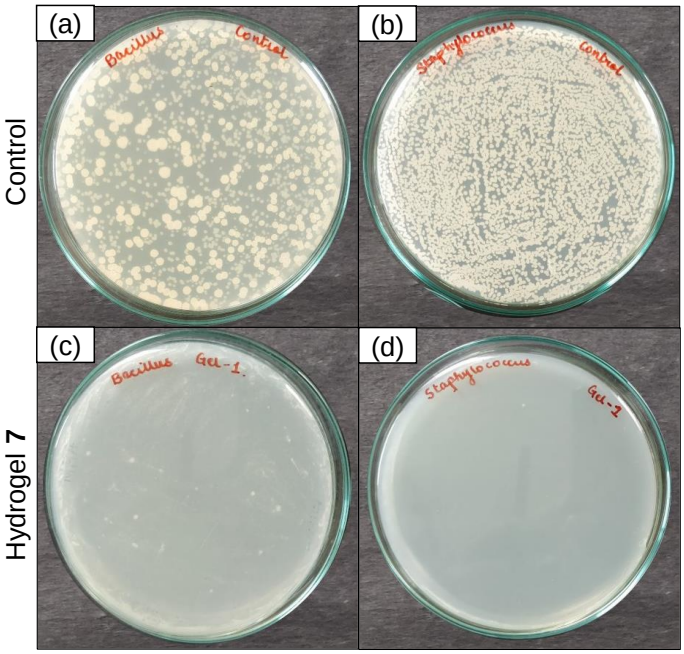

Figure 4.18 Optical photographs of antibacterial activity of hydrogel **7** against: (a,b) *B. subtilis*; (c,d) *S. aureus* bacteria.

The self-assembling tendency of peptide-based materials has great advantage in the area of bacterial infection therapy.[16,72] The peptides aggregate in the solution and form various nanostructures, which interact with the lipid bilayer of cell membranes.[16,73] On the basis of these hypotheses, the inherent antibacterial activity of hydrogel **7** was investigated by the nutrient agar plate method against Gram-positive (*S. aureus* and *B. subtilis*) and Gram-negative (*E. coli*) pathogenic bacteria (Figure 4.18).[22] The antibacterial test data show that hydrogel **7** inhibits the growth of Gram-positive bacteria (Figure 4.18). The twisted nanofibrillar structure of the peptide is characterized by HRTEM, and the β-sheet-like arrangement of peptide in hydrogel **7** is evaluated by FTIR and PXRD spectroscopies. Hence, the supramolecular aggregation of peptides leads to the formation of a well-defined structure, which could be the driving force for antibacterial activity against the Gram-positive bacteria.[74] The stable secondary structural features of peptides allow them to interact with bacterial lipid membranes. These interactions depolarize the lipid membranes and eventually disrupt the bacterial cell membranes by the formation of micropores.[74] However, hydrogel **7** was ineffective against Gram-negative bacteria owing to extra lipopolysaccharide membrane present in Gram-negative bacteria, which acts as a barrier between aggregating peptides and the lipid cell membranes (Figure 4.18).[16] Prior to in vivo experiments, in vitro cell viability experiment was performed to evaluate the biocompatibility of hydrogels **4** and **7** using MCF-7 and HEK293 cell lines (Figure 4.19a-d).[22,23]

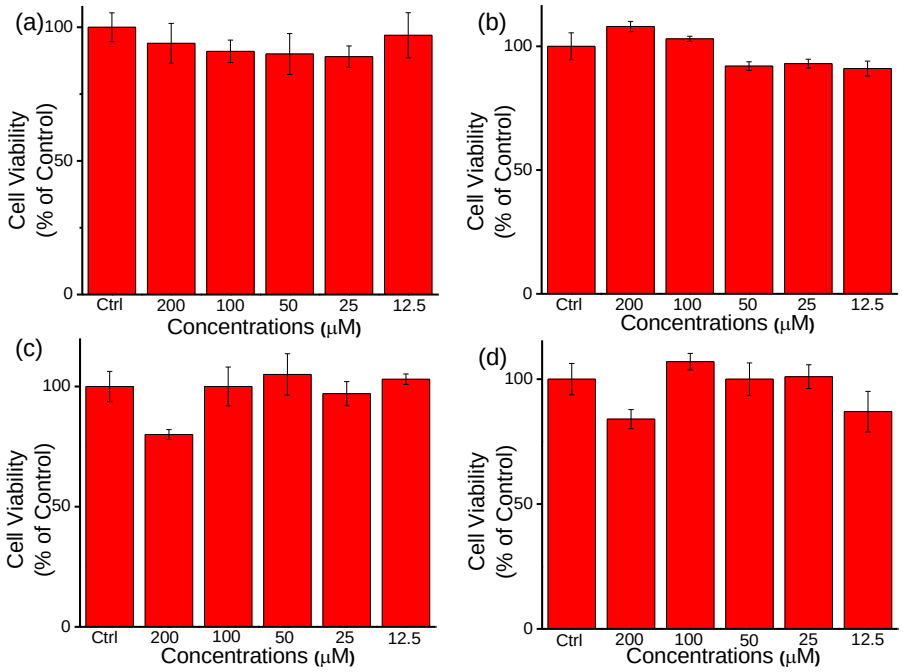

Figure 4.19 In vitro biocompatibility experiment by MTT test: (a,c) Hydrogel **4** and (b,d) hydrogel **7** using MCF-7 and HEK293 cell lines, respectively. The data are shown as mean ± standard error of the mean (n = 5).

The cell viability of MCF-7 is greater than the HEK293 cells for hydrogels **4** and **7** (Figure 4.19a,b). The HEK293 cell line was used as normal cell line for biocompatibility assessment of hydrogels **4** and **7** (Figure 4.19c,d). The MTT experiments data suggest that hydrogels **4** and **7** are biocompatible and noncytotoxic till 200 μmol L^{-1} (Figure 4.19a-d).

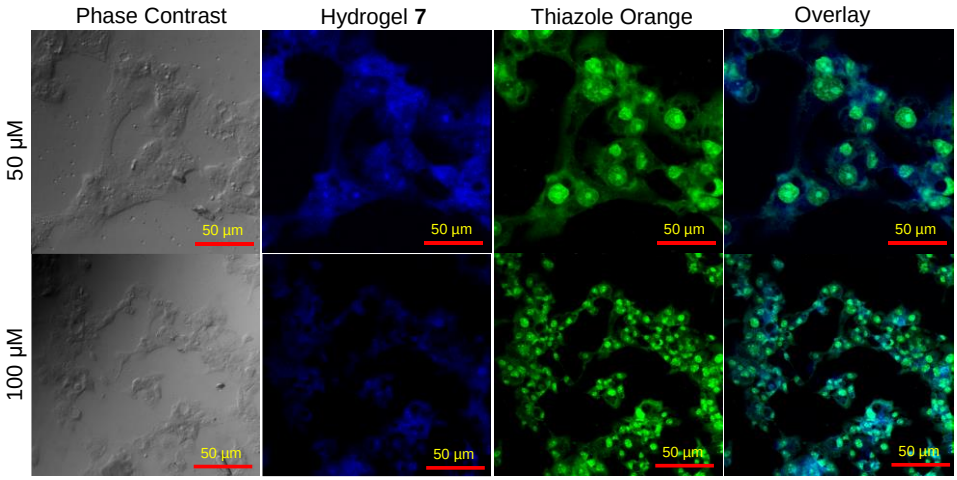

Figure 4.20 Confocal microscopy images of A431 cells treated with hydrogel **7** (50 and 100 μM) and thiazole orange (100 μM) for 4 h at excitation wavelength λ_{ex} = 405 and 488 nm, respectively.

To gain insight into the cell penetrations, hydrogel **7** treated cells were analyzed by a confocal laser scanning microscope using an excitation wavelength of λ_{ex} = 405 nm for the fluorescence signals (Figure 4.20). The confocal laser scanning microscopy (CLSM) images of A431 cells show the blue signal, which indicates the intracellular uptake of hydrogel **7**. The green channel was used for the thiazole orange dye at an excitation wavelength of λ_{ex} = 488 nm (Figure 4.20). To investigate the in vivo wound healing efficacy of hydrogel **7**, the cutaneous wound healing assay was performed (Figure 4.21). The present work was hypothesized that the nanofibrillar morphology of inherent antibacterial and biocompatible hydrogel **7** could significantly improve the in vivo wound healing.[44,49,50,54,58] The nanofibrous morphology of the biocompatible hydrogel can work as a substrate for fibroblast cell attachment and migration.[16,34] The antibacterial activity of nanofibrous hydrogel can maintain the moist condition and combats with bacteria for longer time period.[20] The nanofibrous structure of the hydrogel serves as a sealant, which enhances the wound closure activity.[20] The in vivo wounds (8 mm diameter size) were created using punch biopsy method in Wistar albino male rats, and the wound healing was monitored by taking photographs of the wound site (Figure 4.21).[49,58]

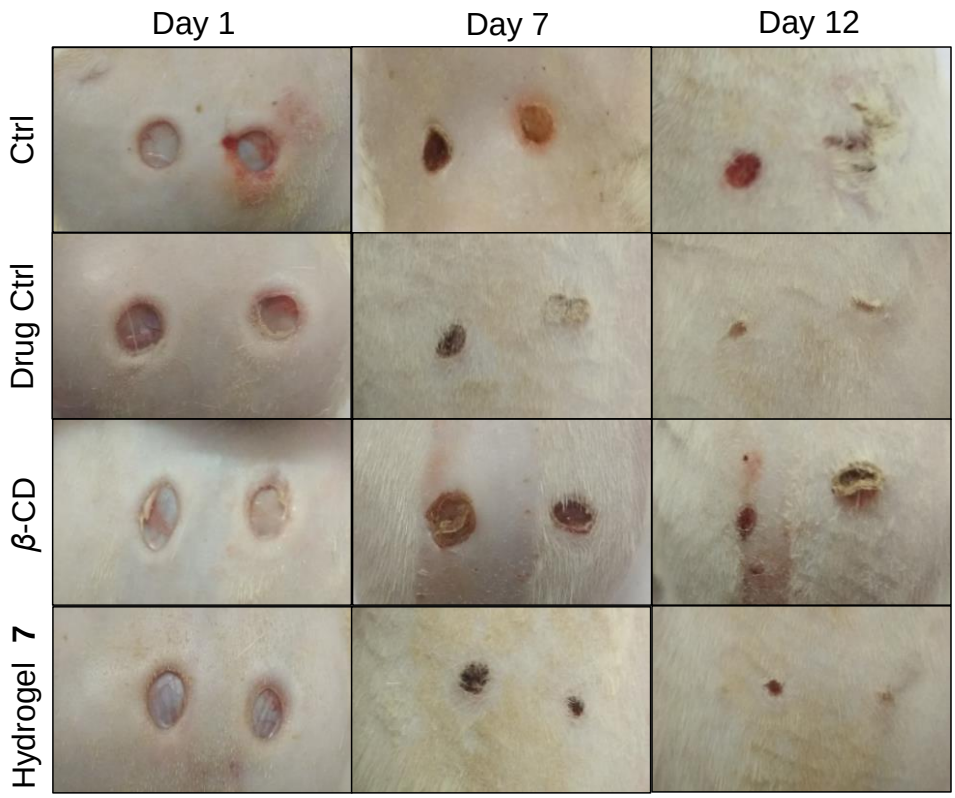

Figure 4.21 Optical photographs of in vivo wound healing activity of different groups showing the increase in healing activity using hydrogel **7**.

The experiment was divided into four different groups and labeled control (negative control), drug control (positive control), *β*-CD, and hydrogel **7**. The silverex cream (silver nitrate gel 0.2% w/w) was used as the standard drug for wound healing experiments. In the test groups, hydrogel **7** was applied on the wound site on every alternate day. In the negative control group, phosphate buffer was applied in place of hydrogel **7**. Hydrogel **7** contains equimolar ratio of *β*-CD; hence, the effect of *β*-CD in the wound healing process was evaluated by applying the same amount of aqueous *β*-CD instead of hydrogel **7** on the wound site. The positive control group (0.2% silverex cream) shows maximum wound healing activity after 12 days of incubation. After 12 days of incubation, hydrogel **7** shows a positive result in wound healing as compared to negative control and *β*-CD groups. The nanofibrillar morphology and inherent antibacterial efficacy of hydrogel **7** could be the driving force for better wound healing activity (Figure 4.21). The histopathological evaluation of the wound site demonstrates the more insights about the in vivo wound healing activity of different control groups and the test hydrogel **7** (Figure 4.22).[20,43,44,50,58] The histological analysis of wound site demonstrates the degree of re-epithelization in different experimental groups such as negative control, drug control, *β*-CD, and hydrogel **7** (Figure 4.22).[43] The tissue section was collected immediately after wounding of the rats and histology images are shown as day 1 for all groups. The histology images (wounding day 1) of different groups are considered as normal tissue architecture and compared with histology images (day 12) of respective groups after the termination of the experiments. The control group shows thick epidermis layer on day 1, but the fragmented and irregular epidermis layer is observed after 12 days of incubation, which suggest incomplete healing process in the control group.[44]

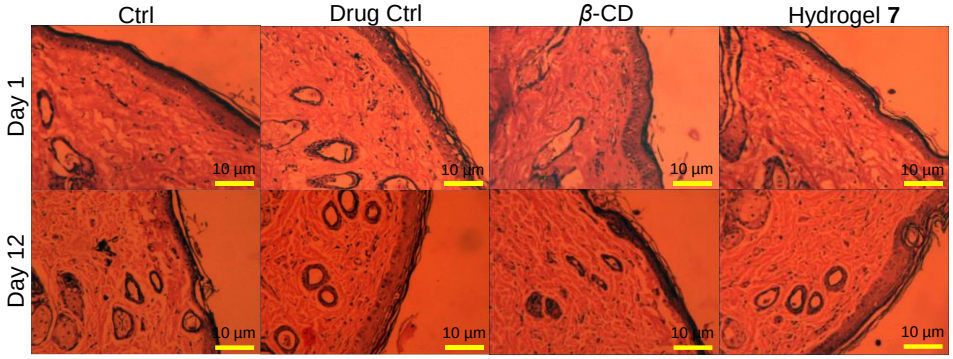

Figure 4.22 Epithelial tissue histology images of different groups showing wound healing by H&E staining technique. Tissue histology images are labeled a = epidermis layer; b = dermis layer; c = sweat gland; and d = sebaceous gland.

The epidermis thickness is the same as on day 1 in the drug control group after 12 days of incubation, which suggests maximum wound healing activity of silverex cream.[43,44] The histology images of *β*-CD-treated group show that a thin epidermis layer shows delayed wound healing. However, the histology images of hydrogel **7** treated group show distinct wound healing activity, which is evident from full

thickness of the epidermis layer after 12 days of incubation.[50] The architecture of the epidermis layer is recovered after the treatment of hydrogel **7** (Figure 4.22).[50]

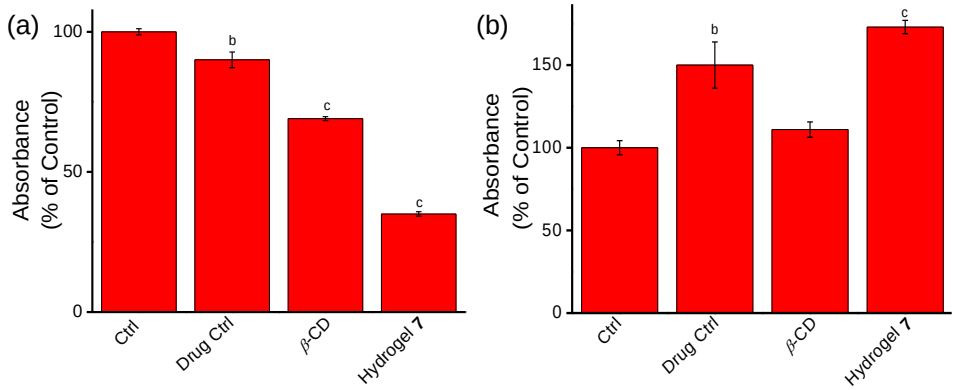

Figure 4.23 Biochemical analysis data of wound tissue after termination of the experiments: (a) nitrite estimation by Griess reagent and (b) collagen protein estimation by hydroxyproline assay, respectively. The data are shown as mean ± standard error of the mean (n = 5). $^{a}p < 0.05$; $^{b}p < 0.01$; $^{c}p < 0.001$, and $^{d}p < 0.0001$ as compared to the control group.

The nitrite is the metabolite of nitric oxide (NO), which is the common and important biochemical parameter for the evaluation of the extent of inflammation.[45,46,52] The shorter half-life of NO could lead to the generation of oxidized products nitrate and nitrite, which are considered as the indicators of NO production.[45,52] However, the promising role of NO on early wound healing is well accepted owing to the biochemical impact of NO on cell proliferation, angiogenesis, clotting, and inflammation.[45,46,75] After a certain period of the time, the elevated level or overproduction of nitrite shows prolonged inflammation near the wound site, which may retard the wound healing process.[45,46,52] Therefore, the Griess assay was performed to evaluate the level of nitrite present near the wound site after the termination of the wound healing experiments (Figure 4.23a).[52] The negative and positive control group show higher nitrite level after termination of the experiment. The experimental data reveals that hydrogel **7** significantly reduces the nitrite level among the other groups. The reduction in the nitrite level further corroborates the better wound healing potential of hydrogel **7** in comparison to the *β*-CD (Figure 4.23a).[45,46,52] Collagen is a structural protein and essential for tissue remolding and hardening during the wound healing process, which is quantified by hydroxyproline estimation assay (Figure 4.23b).[76] Hydroxyproline is an important structural amino acid of collagen protein and provides crucial information of collagen metabolism.[48] The collagen content significantly increases in a standard drug control group compared to negative control. However, hydrogel **7** shows highest collagen content compared to other groups, which signifies the maximum wound healing activity by hydrogel **7** (Figure 4.23b).[48] The *β*-CD-treated group shows a slight increase in collagen content compared to the negative control. The hydroxyproline assay was cross-examined by measuring the total

protein content present in the wound tissue homogenate by spectrophotometers (Figure 4.24).[48] These experimental data suggest highest protein content present in hydrogel **7** treated group compared to all other groups, which could be the reason behind better wound healing efficacy of hydrogel **7**.[48,76] Overall, these experimental data showed the in vivo wound healing activity of coassembled hydrogel **7** and corroborate the previous hypothesis regarding the in vitro and in vivo wound healing efficacy of nanofibrillar inherent antibacterial thixotropic hydrogels.

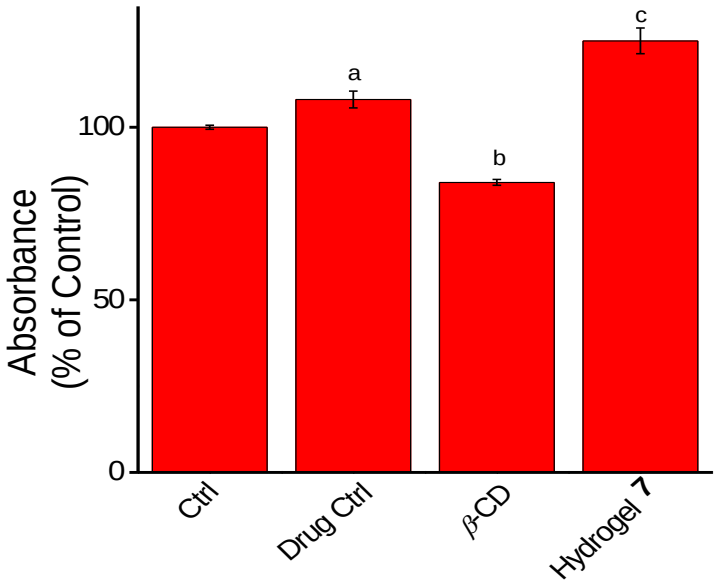

Figure 4.24 The total protein estimation in the wound tissue homogenate by Nanodrop spectrophotometer at 280 nm. The data are shown as mean ± standard error of the mean (n = 5). $^{a}p < 0.05$; $^{b}p < 0.01$; $^{c}p < 0.001$, and $^{d}p < 0.0001$ as compared to the control group.

4.4 Conclusion

In conclusion, we have designed and synthesized an Amoc-capped dipeptide by using conventional solution-phase methodology. The Amoc-capped dipeptide self-assembled into water and formed hydrogel **4** by a simple pH switch method at physiological conditions (pH 7.4, 37 °C). Similarly, the coassembled hydrogel **7** was prepared by addition of equimolar *β*-CD in the peptide solution. The rheological investigations suggested that hydrogel **4** was tough, robust, and nonthixotropic in nature. However, the simple syringe injectability and better thixotropy were achieved by incorporation of *β*-CD with self-assembling peptide **4** (hydrogel **4**). HRTEM images of hydrogel **7** revealed the nanofibrillar network because of the involvement of noncovalent interactions between the peptide and *β*-CD. The supramolecular interactions between *β*-CD and peptides in hydrogel **7** were analyzed by ^{1}H NMR and FTIR experiments. The hydroxyl groups located in the wider rim of *β*-CD interacted with the amide groups of peptides via hydrogen bonding interactions. Furthermore, the PXRD data showed noncovalent

interactions between peptide **4** and *β*-CD, leading to the formation of ordered structures. Additionally, the concentration-dependent circular dichroism experiment of hydrogel **7** showed different dichroic signals after incorporation of *β*-CD with peptide. Hydrogel **7** inhibited the growth of Gram-positive bacteria, which showed the importance of inherent antibacterial properties of hydrogel **7** as wound healing biomaterials. The cell culture experiments showed biocompatibility of the hydrogel **7** and CLSM revealed the cell penetration ability of hydrogel **7**. Hydrogel **7** exhibited potent in vivo wound healing activity. The histology data showed thick and intact epidermis layer after the treatment with hydrogel **7**. Hydrogel **7** reduced NO level and increased the hydroxyproline content, which could be the reason behind the better wound healing activity. The in vivo wound healing efficacy shown by hydrogel **7** could be mediated through pleiotropic biological effects including the maintenance of moisture around the wound area because of the hydration property of the hydrogel. The antibacterial effects of the hydrogel protected from the infection and triggering of inflammatory pathway.

4.5 References

(1) Du X., Zhou J., Shi J., Xu B. (2015), Supramolecular hydrogelators and hydrogels: from soft matter to molecular biomaterials. Chem. Rev., 115, 13165−13307 (DOI: 10.1021/acs.chemrev.5b00299).

(2) Reches M., Gazit E. (2003), Casting metal nanowires within discrete self-assembled peptide nanotubes. Science, 300, 625−627 (DOI: 10.1126/science.1082387).

(3) Harada A., Takashima Y., Nakahata M. (2014), Supramolecular polymeric materials via cyclodextrin-guest interactions. Acc. Chem. Res., 47, 2128−2140 (DOI: 10.1021/ar500109h).

(4) Mann J. L., Yu A. C., Agmon G., Appel E. A. (2018), Supramolecular polymeric biomaterials. Biomater. Sci., 6, 10−37 (DOI: 10.1039/C7BM00780A).

(5) Zhou M., Qian Y., Zhu Y., Matson J. (2020), Elastase-triggered h_2s delivery from polymer hydrogels. Chem. Commun., 56, 1085−1088 (DOI: 10.1039/C9CC08752D).

(6) Tao K., Levin A., Adler-Abramovich L., Gazit E. (2016), Fmoc-modified amino acids and short peptides: simple bio-inspired building blocks for the fabrication of functional materials. Chem. Soc. Rev., 45, 3935−3953 (DOI: 10.1039/C5CS00889A).

(7) Bhattacharya S., Samanta S. K. (2016), Soft-nanocomposites of nanoparticles and nanocarbons with supramolecular and polymer gels and their applications. Chem. Rev., 116, 11967−12028 (DOI: 10.1021/acs.chemrev.6b00221).

(8) Das A. K., Collins R., Ulijn R. V. (2008), Exploiting enzymatic (reversed) hydrolysis in directed self-assembly of peptide nanostructures. Small, 4, 279−287 (DOI : 10.1002/smll.200700889).

(9) Falcone N., Kraatz H.-B. (2018), Supramolecular assembly of peptide and metallo-peptide gelators and their stimuli-responsive properties in biomedical applications. Chem.- Eur. J., 24, 14316−14328 (DOI: 10.1002/chem.201801247).

(10) Maiti B., Abramov A., Pérez-Ruiz R., Díaz Díaz D. (2019), The prospect of photochemical reactions in confined gel media. Acc. Chem. Res., 52, 1865−1876 (DOI: 10.1021/acs.accounts.9b00097).
(11) Gavel P. K., Parmar H. S., Tripathi V., Kumar N., Biswas A., Das A. K. (2019), Investigations of anti-inflammatory activity of a peptide-based hydrogel using rat air pouch model. ACS Appl. Mater. Interfaces, 11, 2849−2859 (DOI: 10.1021/acsami.8b19228).
(12) Takashima Y., Otani K., Kobayashi Y., Aramoto H., Nakahata M., Yamaguchi H., Harada A. (2018), Mechanical properties of supramolecular polymeric materials formed by cyclodextrins as host molecules and cationic alkyl guest molecules on the polymer side chain. Macromolecules, 51, 6318−6326 (DOI: 10.1021/acs.macromol.8b01410).
(13) Shigemitsu H., Hamachi I. (2017), Design strategies of stimuli-responsive supramolecular hydrogels relying on structural analyses and cell-mimicking approaches. Acc. Chem. Res., 2017, 50, 740−750 (DOI: 10.1021/acs.accounts.7b00070).
(14) Gavel P. K., Dev D., Parmar H. S., Bhasin S., Das A. K. (2018), Investigations of peptide-based biocompatible injectable shape-memory hydrogels: differential biological effects on bacterial and human blood cells. ACS Appl. Mater. Interfaces, 10, 10729−10740 (DOI: 10.1021/acsami.8b00501).
(15) Hu B., Owh C., Chee P. L., Leow W. R., Liu X., Wu Y.-L., Guo P., Loh X. J., Chen X. (2018), Supramolecular hydrogels for antimicrobial therapy. Chem. Soc. Rev., 47, 6917−6929 (DOI: 10.1039/C8CS00128F).
(16) Hamley I. W. (2017), Small bioactive peptides for biomaterials design and therapeutics. Chem. Rev., 117, 14015−14041 (DOI: 10.1021/acs.chemrev.7b00522).
(17) Cheetham A. G., Chakroun R. W., Ma W., Cui H. (2017), Self-assembling prodrugs. Chem. Soc. Rev., 46, 6638−6663 (DOI: 10.1039/C7CS00521K).
(18) Li S., Dong S., Xu, W., Tu S., Yan L., Zhao C., Ding J., Chen X. (2018), Antibacterial hydrogels. Adv. Sci., 5, 1700527 (DOI: 10.1002/advs.201700527).
(19) Liu Y., He W., Zhang Z., Lee B. (2018), Recent developments in tough hydrogels for biomedical applications. Gels, 4, 46 (DOI: 10.3390/gels4020046).
(20) Zhao X., Wu H., Guo B., Dong R., Qiu Y., Ma P. X. (2017), Antibacterial anti-oxidant electroactive injectable hydrogel as self-healing wound dressing with hemostasis and adhesiveness for cutaneous wound healing. Biomaterials, 122, 34−47 (DOI: 10.1016/j.biomaterials.2017.01.011).
(21) Wu H., Liu S., Xiao L., Dong X., Lu Q., Kaplan D. L. (2016), Injectable and pH-responsive silk nanofiber hydrogels for sustained anticancer drug delivery. ACS Appl. Mater. Interfaces, 8, 17118−17126 (DOI: 10.1021/acsami.6b04424).
(22) Nandi N., Gayen K., Ghosh S., Bhunia D., Kirkham S., Sen S. K., Ghosh S., Hamley I. W., Banerjee A. (2017), Amphiphilic peptide-based supramolecular, noncytotoxic, stimuli-responsive hydrogels with antibacterial activity. Biomacromolecules, 18, 3621−3629 (DOI: 10.1021/acs.biomac.7b01006).

(23) Jian H., Wang M., Dong Q., Li J., Wang A., Li X., Ren P., Bai S. (2019), Dipeptide self-assembled hydrogels with tunable mechanical properties and degradability for 3d bioprinting. ACS Appl. Mater. Interfaces, 11, 46419−46426 (DOI: 10.1021/acsami.9b13905).
(24) Irwansyah I., Li Y.-Q., Shi W., Qi D., Leow W. R., Tang M. B. Y., Li S., Chen X. (2015), Gram-positive antimicrobial activity of amino acid-based hydrogels. Adv. Mater., 27, 648−654 (DOI: 10.1002/adma.201403339).
(25) Raymond D. M., Abraham B. L., Fujita T., Watrous M. J., Toriki E. S., Takano T., Nilsson B. L. (2019), Low-molecular-weight supramolecular hydrogels for sustained and localized in vivo drug delivery. ACS Appl. Bio Mater., 2, 2116−2124 (DOI: 10.1021/acsabm.9b00125).
(26) Sun Z., Li Z.; He Y., Shen R., Deng L., Yang M., Liang Y., Zhang Y. (2013), Ferrocenoyl phenylalanine: a new strategy toward supramolecular hydrogels with multistimuli responsive properties. J. Am. Chem. Soc., 135, 13379−13386 (DOI : 10.1021/ja403345p).
(27) Qi Y., Min H., Mujeeb A., Zhang Y., Han X., Zhao X., Anderson G. J., Zhao Y., Nie G. (2018), Injectable hexapeptide hydrogel for localized chemotherapy prevents breast cancer recurrence. ACS Appl. Mater. Interfaces, 10, 6972−6981 (DOI: 10.1021/acsami.7b19258).
(28) Yan X., Zhu P., Li J. (2010), Self-assembly and application of diphenylalanine-based nanostructures. Chem. Soc. Rev., 39, 1877−1890 (DOI: 10.1039/B915765B).
(29) Li Q., Jia Y., Dai L., Yang Y., Li J. (2015), Controlled rod nanostructured assembly of diphenylalanine and their optical waveguide properties. ACS Nano, 9, 32689−32695 (DOI: 10.1021/acsnano.5b00623).
(30) Manchineella S., Murugan N. A., Govindaraju T. (2017), Cyclic dipeptide-based ambidextrous supergelators: minimalistic rational design, structure-gelation studies, and in situ hydrogelation. Biomacromolecules, 18, 3581−3590 (DOI: 10.1021/acs.biomac.7b00924).
(31) Vargiu A. V., Iglesias D., Styan K. E., Waddington L. J., Easton C. D., Marchesan S. (2016), Design of a hydrophobic tripeptide that self-assembles into amphiphilic superstructures forming a hydrogel biomaterial. Chem. Commun., 52, 5912−5915 (DOI: 10.1039/C5CC10531E).
(32) Sahoo J. K., Vandenberg M. A., Ruiz Bello E. E., Nazareth C. D., Webber M. J. (2019), Electrostatic-driven self-sorting and nanostructure speciation in self-assembling tetrapeptides. Nanoscale, 11, 16534−16543 (DOI: 10.1039/C9NR03440D).
(33) Chen Y., Liu Y. (2010), Cyclodextrin-based bioactive supramolecular assemblies. Chem. Soc. Rev., 39, 495−505 (DOI: 10.1039/B816354P).
(34) Redondo-Gómez C., Abdouni Y., Becer C. R., Mata A. (2019), Self-assembling hydrogels based on a complementary host-guest peptide amphiphile pair. Biomacromolecules, 20, 2276−2285 (DOI: 10.1021/acs.biomac.9b00224).
(35) Chen M. H., Wang L. L., Chung J. J., Kim Y.-H., Atluri P., Burdick J. A. (2017), Methods to assess shear-thinning hydrogels for application as injectable

biomaterials. ACS Biomater. Sci. Eng., 3, 3146−3160 (DOI: 10.1021/acsbiomaterials.7b00734).
(36) Rodell C. B., MacArthur J. W., Dorsey S. M., Wade R. J., Wang L. L., Woo Y. J., Burdick J. A. (2015), Shear-thinning supramolecular hydrogels with secondary autonomous covalent crosslinking to modulate viscoelastic properties in vivo. Adv. Funct. Mater., 25, 636−644 (DOI: 10.1002/adfm.201403550).
(37) Chen G., Jiang M. (2011), Cyclodextrin-based inclusion complexation bridging supramolecular chemistry and macromolecular self-assembly. Chem. Soc. Rev., 40, 2254−2266 (DOI: 10.1039/C0CS00153H).
(38) Radu C.-D., Parteni O., Ochiuz L. (2016), Applications of cyclodextrins in medical textiles-review. J. Controlled Release, 224, 146−157 (DOI: 10.1016/j.jconrel.2015.12.046).
(39) Mantooth S. M., Munoz-Robles B. G., Webber M. J. (2019), Dynamic hydrogels from host−guest supramolecular interactions. Macromol. Biosci., 19, 1800281 (DOI: 10.1002/mabi.201800281).
(40) Hou S.-S., Hsu Y.-Y., Lin J.-H., Jan J.-S. (2016), Alkyl-poly(l-threonine)/cyclodextrin supramolecular hydrogels with different molecular assemblies and gel properties. ACS Macro Lett., 5, 1201−1205 (DOI: 10.1021/acsmacrolett.6b00716).
(41) Schneider H.-J., Agrawal P., Yatsimirsky A. K. (2013), Supramolecular complexations of natural products. Chem. Soc. Rev., 42, 6777−6800 (DOI: 10.1039/C3CS60069F).
(42) Liu K., Jiang X., Hunziker P. (2016), Carbohydrate-based amphiphilic nano delivery systems for cancer therapy. Nanoscale, 8, 16091−16156 (DOI: 10.1039/c6nr04489a).
(43) Basu A., Celma G., Strømme M., Ferraz N. (2018), In vitro and in vivo evaluation of the wound healing properties of nano-fibrillated cellulose hydrogels. ACS Appl. Bio Mater., 1, 1853−1863 (DOI: 10.1021/acsabm.8b00370).
(44) Rao B. R., Kotcherlakota R., Nethi S. K., Puvvada N., Sreedhar B., Chaudhuri A., Patra C. R. (2018), $Ag_2[Fe(CN)_5NO]$ Nanoparticles exhibit antibacterial activity and wound healing properties. ACS Biomater. Sci. Eng., 4, 3434−3449 (DOI: 10.1021/acsbiomaterials.8b00759).
(45) Malone-Povolny M. J., Maloney S. E., Schoenfisch M. H. (2019), Nitric oxide therapy for diabetic wound healing. Adv. Healthcare Mater., 8, 1801210 (DOI: 10.1002/adhm.201801210).
(46) Luo J.-d., Chen A. F. (2005), Nitric oxide: a newly discovered function on wound healing. Acta Pharmacol. Sin., 26, 259−264 (DOI: 10.1111/j.1745-7254.2005.00058.x).
(47) Hoque J., Prakash R. G., Paramanandham K., Shome B. R., Haldar J. (2017), Biocompatible injectable hydrogel with potent wound healing and antibacterial properties. Mol. Pharm., 14, 1218−1230 (DOI: 10.1021/acs.molpharmaceut.6b01104).
(48) Udhayakumar S., Shankar K. G., Sowndarya S., Rose C. (2017), Novel fibrous collagen-based cream accelerates fibroblast growth for wound healing

applications: in vitro and in vivo evaluation. Biomater. Sci., 5, 1868−1883 (DOI: 10.1039/C7BM00331E).
(49) Zhang Y., Lu L., Chen Y., Wang J., Chen Y., Mao C., Yang M. (2019), Polydopamine modification of silk fibroin membranes significantly promotes their wound healing effect. Biomater. Sci., 7, 5232−5237 (DOI : 10.1039/C9BM00974D).
(50) Xiao Y., Reis L. A., Feric N., Knee E. J., Gu J., Cao S., Laschinger C., Londono C., Antolovich J., McGuigan A. P., Radisic M. (2016), Diabetic wound regeneration using peptide-modified hydrogels to target re-epithelialization. Proc. Natl. Acad. Sci. U.S.A., 113, E5792−E5801 (DOI: 10.1073/pnas.1612277113).
(51) Gurtner G. C., Werner S., Barrandon Y., Longaker M. T. (2008), Wound repair and regeneration. Nature, 453, 314−321 (DOI: 10.1038/nature07039).
(52) Maia L. B., Moura J. J. G. (2014), How biology handles nitrite. Chem. Rev., 114, 5273−5357 (DOI: 10.1021/cr400518y).
(53) Naik S., Larsen S. B., Gomez N. C., Alaverdyan K., Sendoel A., Yuan S., Polak L., Kulukian A., Chai S., Fuchs E. (2017), Inflammatory memory sensitizes skin epithelial stem cells to tissue damage. Nature, 550, 475−480 (DOI: 10.1038/nature24271).
(54) He H., Xiao Z., Zhou Y., Chen A., Xuan X., Li Y., Guo X., Zheng J., Xiao J., Wu J. (2019), Zwitterionic poly(sulfobetaine methacrylate) hydrogels with optimal mechanical properties for improving wound healing in vivo. J. Mater. Chem. B, 7, 1697−1707 (DOI: 10.1039/C8TB02590H).
(55) Giano M. C., Ibrahim Z., Medina S. H., Sarhane K. A., Christensen J. M., Yamada Y., Brandacher G., Schneider J. P. (2014), Injectable bioadhesive hydrogels with innate antibacterial properties. Nat. Commun., 5, 4095 (DOI: 10.1038/ncomms5095).
(56) Zhang L., Cao Z., Bai T., Carr L., Ella-Menye J.-R., Irvin C., Ratner B. D., Jiang S. (2013), Zwitterionic hydrogels implanted in mice resist the foreign-body reaction. Nat. Biotechnol., 31, 553−556 (DOI: 10.1038/nbt.2580).
(57) Su J., Hu B.-H., Lowe W. L., Kaufman D. B., Messersmith P. B. (2010), Anti-inflammatory peptide-functionalized hydrogels for insulin secreting cell encapsulation. Biomaterials, 31, 308−314 (DOI: 10.1016/j.biomaterials.2009.09.045).
(58) Sangabathuni S., Murthy R. V., Gade M., Bavireddi H., Toraskar S., Sonar M. V., Ganesh K. N., Kikkeri R. (2017), Modeling glyco-collagen conjugates using a host-guest strategy to alter phenotypic cell migration and in vivo wound healing. ACS Nano, 11, 11969−11977 (DOI: 10.1021/acsnano.7b01789).
(59) Hawes C. S., Lynes A. D., Byrne K., Schmitt W., Ryan G., Möbius M. E., Gunnlaugsson T. (2017), A resilient and luminescent stimuli-responsive hydrogel from a heterotopic 1,8-naphthalimidederived ligand. Chem. Commun., 53, 5989−5992 (DOI: 10.1039/C7CC03482B).
(60) Wang J., Liu K., Xing R., Yan X. (2016), Peptide self-assembly: thermodynamics and kinetics. Chem. Soc. Rev., 45, 5589−5604 (DOI: 10.1039/C6CS00176A).

(61) Yuan C., Ji W., Xing R., Li J., Gazit E., Yan X. (2019), Hierarchically oriented organization in supramolecular peptide crystals. Nat. Rev. Chem., 3, 567−588.
(62) Draper E. R., Morris K. L., Little M. A., Raeburn J., Colquhoun C., Cross E. R., McDonald T. O., Serpell L. C., Adams D. J. (2015), Hydrogels formed from Fmoc amino acids. CrystEngComm, 17, 8047−8057 (DOI: 10.1039/C5CE00801H).
(63) Schneider H.-J., Hacket F., Rüdiger V., Ikeda H. (1998), NMR studies of cyclodextrins and cyclodextrin complexes. Chem. Rev., 98, 1755−1786 (DOI: 10.1021/cr970019t).
(64) Zhang Y., Yang D., Han J., Zhou J., Jin Q., Liu M., Duan P. (2018), Circularly polarized luminescence from a pyrene-cyclodextrin supra-dendron. Langmuir, 34, 5821−5830 (DOI: 10.1021/acs.langmuir.8b01035).
(65) Yuan C., Levin A., Chen W., Xing R., Zou Q., Herling T. W., Challa P. K., Knowles T. P. J., Yan X. (2019), Nucleation and growth of amino acid and peptide supramolecular polymers through liquid−liquid phase separation. Angew. Chem., Int. Ed., 58, 18116−18123 (DOI: 10.1002/ange.201911782).
(66) Xing R., Yuan C., Li S., Song J., Li J., Yan X. (2018), Charge-induced secondary structure transformation of amyloid-derived dipeptide assemblies from β-sheet to α-helix. Angew. Chem., Int. Ed., 57, 1537−1542 (DOI: 10.1002/anie.201710642).
(67) Mehta A. K., Lu K., Childers W. S., Liang Y., Dublin S. N., Dong J., Snyder J. P., Pingali S. V., Thiyagarajan P., Lynn D. G. (2008), Facial symmetry in protein self-assembly. J. Am. Chem. Soc., 130, 9829−9835 (DOI: 10.1021/ja801511n).
(68) Hu J., Gao L., Zhu Y., Wang P., Lin Y., Sun Z., Yang S., Wang Q. (2017), Chiral assemblies from an achiral pyridinium-tailored anthracene. Chem.-Eur. J., 23, 1422−1426 (DOI: 10.1002/chem.201604730).
(69) Woody R. W. (1978), Aromatic side-chain contributions to the far ultraviolet circular dichroism of peptides and proteins. Biopolymers, 17, 1451−1467 (DOI: 10.1002/bip.1978.360170606).
(70) Franco A. R., Fernandes E. M., Rodrigues M. T., Rodrigues F. J., Gomes M. E., Leonor I. B., Kaplan D. L., Reis R. L. (2019), Antimicrobial coating of spider silk to prevent bacterial attachment on silk surgical sutures. Acta Biomater., 99, 236−246 (DOI: 10.1016/j.actbio.2019.09.004).
(71) Pappas H. C., Phan S., Yoon S., Edens L. E., Meng X., Schanze K. S., Whitten D. G., Keller D. J. (2015), Self-Sterilizing, self-cleaning mixed polymeric multifunctional antimicrobial surfaces. ACS Appl. Mater. Interfaces, 7, 27632−27638 (DOI: 10.1021/acsami.5b06852).
(72) Pranantyo D., Liu P., Zhong W., Kang E.-T., Chan-Park M. B. (2019), Antimicrobial peptide-reduced gold nanoclusters with charge-reversal moieties for bacterial targeting and imaging. Biomacromolecules, 20, 2922−2933 (DOI: 10.1021/acs.biomac.9b00392).
(73) Li Y., Fukushima K., Coady D. J., Engler A. C., Liu S., Huang Y., Cho J. S., Guo Y., Miller L. S., Tan J. P. K., Ee P. L. R., Fan W., Yang Y. Y., Hedrick J. L. (2013), Broad-spectrum antimicrobial and biofilm-disrupting hydrogels:

stereocomplex-driven supramolecular assemblies. Angew. Chem., Int. Ed., 52, 674−678 (DOI: 10.1002/anie.201206053).
(74) Brogden K. A. (2005), Antimicrobial peptides: pore formers or metabolic inhibitors in bacteria? Nat. Rev. Microbiol., 3, 238−250 (DOI: 10.1038/nrmicro1098).
(75) Naghavi N., De Mel A., Alavijeh O. S., Cousin B. G., Seifalian A. M. (2013), Nitric oxide donors for cardiovascular implant applications. Small, 9, 22−35 (DOI: 10.1002/smll.201200458).
(76) Reddy G. K., Enwemeka C. S. (1996), A simplified method for the analysis of hydroxyproline in biological tissues. Clin. Biochem., 29, 225−9 (DOI: 10.1016/0009-9120(96)00003-6).

Chapter 5

Investigations of a Coassembled Hydrogel as a Wound Dressing System

5.1 Introduction

Molecular self-assembly plays vital role for the design and fabrication of functional materials.[1-3] In search of regenerative medicines, extensive research efforts have been given for the development of soft materials.[4] Particularly, self-assembly of biomolecules offers a promising approach for the development of soft materials.[5,6] Self-assembly is a spontaneous and fundamental process in nature where molecules adopt specific and well-defined structures with the help of various non-covalent interactions including hydrogen bonding, ionic, hydrophobic and van der Waals interactions.[7] However, non-covalent interactions are considered as weak interactions but their collective interactions produce ordered nanostructures.[8] Molecular self-assembly plays very crucial role in many biological systems for the construction of various hierarchical structures using the 'bottom up' approach.[9,10] The self-assembly of molecules forms thermodynamically stable structures such as spheres, rods, fibers, tubes vesicles.[11] Self-assembly of biomolecules can be induced by various external stimuli such as pH, temperature, ultrasonication and enzymatic reactions.[12,13] The stimuli responsive molecules change their conformations owing to the noncovalent interactions upon changing the physical and chemical environment.[14] The stimuli responsive self-assembly undergoes changes in physiochemical properties of materials which is used for the regenerative medicine development.[15] However, the challenge in self-assembly is to design and develop a stimuli responsive building block which can exhibit the ordered structures.[16]

Recently, peptide-based hydrogelators have paid a great attention in the various areas ranging from biomedical science to biochemical engineering for the construction of highly thixotropic, biocompatible, biodegradable, and non-immunogenic soft biomaterials.[17-20] Among the various self-assembling peptides, dipeptide-based hydrogelators are easy to design, synthesize and functionalize with biological active molecules, thus low molecular weight peptides are interesting class of building blocks for the preparation of self-assembled materials.[21] Several self-assembling peptide-based soft biomaterials were used for various in vitro and in vivo biological applications including cell culture, drug delivery, antimicrobial, anticancer, tissue repair therapy and wound healing purposes.[22-26] The cross-linked network of hydrogels encapsulates drug molecules via noncovalent interactions and deliver to the target site upon administration.[27] The difference in physicochemical environment of target site actuates the sustained release of drug from hydrogels.[28] The self-assembling peptides have been employed for the development of anticancer and antimicrobial therapeutics.[29] These peptides selectively interact with cell membrane and cell organelle of tumorigenic and nontumorigenic cells.[30] The inherent hydrophobicity, charge and conformation of self-assembling peptides have been utilized for the development of antibacterial hydrogels.[31] During past decades, the peptide-based inherent antimicrobial hydrogels have been utilized for acute and chronic wound healing applications.[32] The self-assembled hydrogels possess fibrillar and pores morphology which allows gaseous exchange and maintain the moist

environment.[33] The fibrillar structures of hydrogel stop the bleeding, guide the fibroblast cell migration and accelerate the quality of wound healing.[33] Additionally, the anti-inflammatory peptide-based hydrogels reduce the acute inflammation which promote the wound healing activity.[32,33] Therefore, peptide-based self-assembled antimicrobial hydrogels possess all the merits required for an ideal wound dressing material.

The 9-anthracenemethoxycarbonyl (Amoc)-capped peptides exhibit stimuli-responsive hydrogelations under mild conditions.[34] The stiffness and viscoelastic properties of Amoc-capped hydrogels can be tuned through incorporation of cyclodextrin with self-assembling peptides by coassembly approach.[32] Other advantages of the Amoc-capped coassembled hydrogel demonstrate better shear thinning and syringe injectability which can be used to fill the tissue defects and cavities. Additionally, the Amoc-capped hydrogels have been used for antibacterial and anti-inflammatory applications owing to the optimum hydrophobicity and higher aggregation propensity via aromatic interactions.[21,22] In the current report, we have designed an Amoc-capped dipeptide-based noncytotoxic hydrogelator for the preparation of soft biomaterials which can exhibit the inherent antibacterial and in vivo wound dressing activity.

5.2 Experimental Section

5.2.1 Materials and Methods

All the materials used for this project were procured from commercial sources and used as received. The 9-anthracenemethanol, 4-nitrophenyl chloroformate and pyridine were purchased from Sigma-Aldrich (Merck KGaA), India. L-phenylalaninne (F), dicyclohexylcarbodiimide (DCC) and 1-hydroxybenzotriazole (HOBt) were purchased from SRL, India. The *β*-cyclodextrin (CD) hydrated was procured from Alfa Aesar, India. The chemicals for biological experiments *i.e.* peptone powder, yeast extract, agar agar powder, Dulbecco's Modified Eagle Medium (DMEM), Minimum Essential Medium Eagle (MEM), Trypsin-EDTA solution 1X, Penicillin-Streptomycin antibiotic solution 100X and 3-(4,5-dimethythiazol-2-yl)2,5-diphenyl tetrazolium bromide (MTT) powder were purchased from HiMedia Laboratories Pvt. Ltd., India. The silverex gel (silver nitrate 0.2% w/w, Sun Pharma, India), povidone-iodine (Win Medicare Pvt. Ltd., India), Dynapar AQ (Diclofenac 75 mg/mL injection) Tegaderm (3M bandage), hair removal cream Anne French (Pfizer, India), and the disposable biopsy punch (8 mm, amazon, India) were purchased commercially for the research purposes. All solvents were analytical grade and purchased from Rankem, India; and Merck, India. HPLC grade acetonitrile (ACN) and methanol (MeOH) were used for the analysis of the synthesized molecules. Solvents were distilled prior to use and kept in 4Å molecular sieves. Tetrahydrofuran (THF), *N,N'*-dimethylformamide (DMF), ethyl acetate (EtOAc), MeOH, hexane were dried using the standard procedure. Thin-layer chromatography was performed on pre-coated silica gel plates (Kieselgel 60 F_{254}, Merck). Synergy H1 multimode microplate reader was used for 96-well microplates reading at 25 °C.

5.2.2 Synthesis of 5

Scheme 5.1 Synthetic pathway of **5**

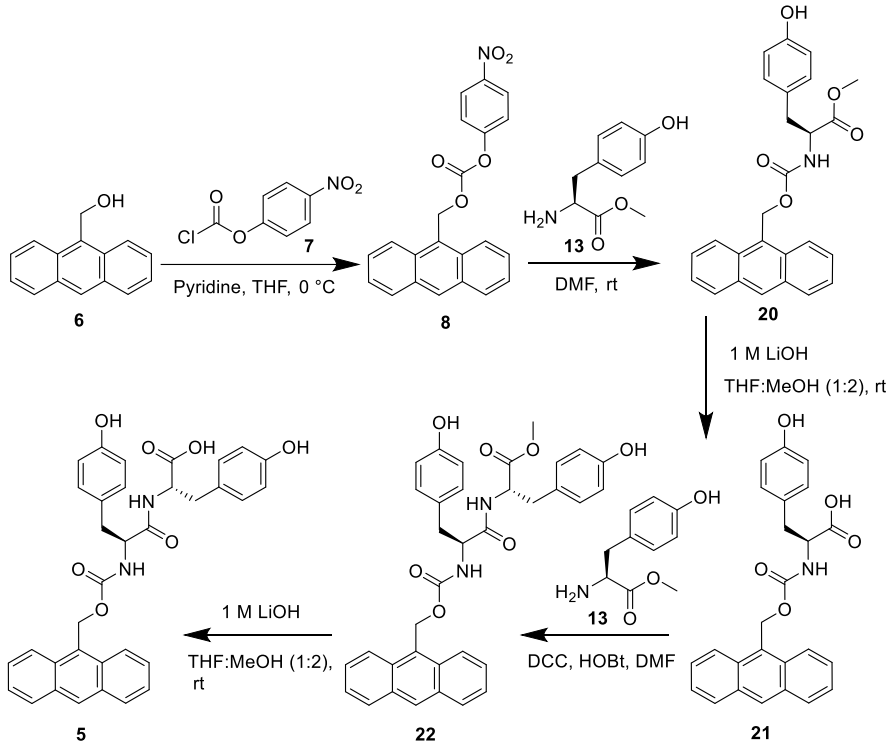

5.2.2.1 Synthesis of 8

7 (1.16 g, 5.76 mmol) was solubilized in 15 mL dry THF under N_2 atmosphere. The solution was ice-cooled and pyridine (0.456 g, 5.76 mmol) was added into the cold solution. The white slurry was obtained after the addition of pyridine. **6** (1.0 g, 4.80 mmol) was solubilized in 15 mL dry THF and the solution was added into the reaction mixture by several portions. The reaction mixture was allowed to stir overnight at room temperature. Product conversion was checked by TLC. After completion of the reaction, THF was evaporated by a rotary evaporator. The crude reaction mixture was diluted with ethyl acetate (50 mL) and the mixture was washed with 1 M HCl (3 × 30 mL) and successively with brine. The yellow-green product was obtained by evaporating the solvent under reduced pressure. The product was recrystallized using benzene and yellow needle-shaped crystal of **8** was further used for the synthesis of **5**.

Yield: 1.36 g (76%). ^{1}H NMR (400 MHz, $CDCl_3$): δ = 8.58 (s, 1H, Amoc), 8.42-8.40 (d, *J* = 8.88 Hz, 2Hs, Ph), 8.26- 8.24 (d, *J*= 8.44 Hz, 2Hs, Amoc), 8.08-8.06 (d, *J* = 8.40 Hz, 2H, Amoc), 7.65-7.61 (t, *J* = 7 Hz, 2H, Amoc), 7.55-7.51 (t, *J* = 7.48 Hz, 2H, Amoc), 7.37-7.35 (d, *J* = 8.36 Hz, 2H, Ph), 6.39 (s, 2H, Amoc) ppm.

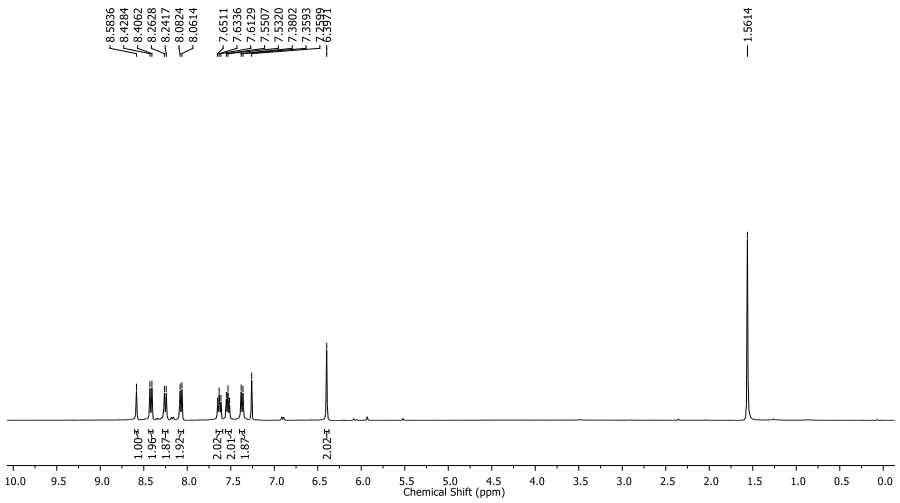

Figure 5.1 ^{1}H NMR spectrum (400 MHz) of **8** in $CDCl_3$.

5.2.2.2 Synthesis of 20

1.2 g (3.21 mmol) of **8** was dissolved in 3 mL dry DMF. The reaction mixture was ice-cooled. The hydrochloride salt of **13** (1.49 g, 6.42 mmol) was neutralized using saturated Na_2CO_3 (20 mL) solution and the product was extracted using ethyl acetate (3 × 30 mL). The neutralized solution of **13** was added to the reaction mixture and allowed to stir for 12 h. Product conversion was confirmed by thin layer chromatography (TLC). After completion of the reaction, ethyl acetate (25 mL) was added and washed with 1 M HCl (3 × 30 mL), saturated Na_2CO_3 solution (6 × 30 mL) and then with brine. Yellow colour solid **20** was obtained after evaporating the solvent under reduced pressure. The product **20** was crystalized in cold methanol.

Yield: 1.12 g (81%); FT-IR (KBr): $\bar{\upsilon}$ = 3302 (s, NH), 1747 (s, COOMe), 1691 (s, amide I band), 1613 (s, amide I band), 1591 (s, amide II band), 1507 (s, amide II band) cm^{-1}; ^{1}H NMR (400 MHz, DMSO-d$_6$): δ = 9.23 (s, 1H, OH, Tyr), 8.68 (s, 1H, Amoc), 8.34–8.32 (d, *J* = 8.76 Hz, 2H, Amoc), 8.14–8.12 (d, *J* = 8.24 Hz, 2H, Amoc), 7.65–7.53 (m, 5H, NH, Amoc), 6.98–6.96 (d, *J* = 8.2 Hz, 2H, Tyr), 6.62–6.60 (d, *J* = 8.24 Hz, 2H, Tyr), 6.07–5.96 (q, 2H, Amoc), 4.22–4.16 (dd, *J* = 9.28 Hz, 8.96 Hz, 1H, C$^\alpha$H of Tyr), 3.60 (s, 3H, OCH_3), 2.89–2.84 (dd, *J* = 5.2 Hz, 5.08 Hz, 1H, C$^\beta$ H of Tyr), 2.73–2.67 (m, 1H, C$^\beta$ H of Tyr) ppm; MS (ESI): *m/z* calcd for $C_{26}H_{23}NO_5$: 452.1474 [M+Na]$^+$; found: 452.1575.

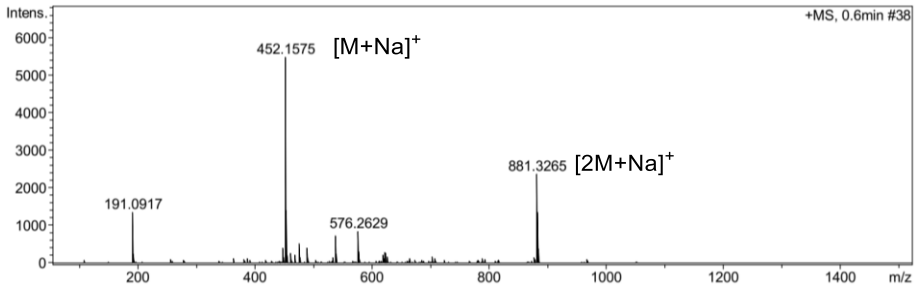

Figure 5.2 ESI-MS spectrum of **20**.

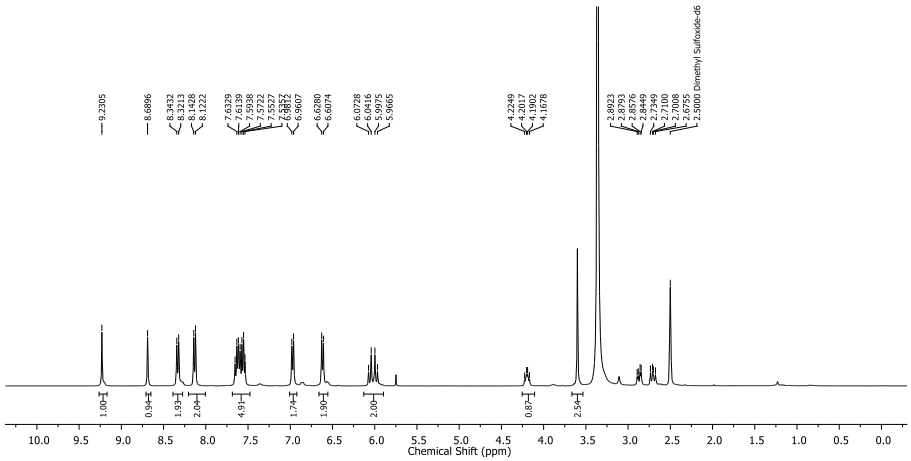

Figure 5.3 ^{1}H NMR (400 MHz, DMSO-d_6) spectrum of **20**.

5.2.2.3 Synthesis of 21

20 (1.0 g, 2.32 mmol) was solubilized in 10 mL THF and 20 mL MeOH. In the reaction mixture, 1 M LiOH solution was slowly added for hydrolysis. The reaction mixture was stirred for 6 h and progress of the hydrolysis was monitored by TLC. Then 1 M LiOH solution was added in every 30 min interval according to the progress of the hydrolysis. The excess solvent was evaporated and remaining mixture was taken in the separating funnel. The mixture was very carefully washed with diethyl ether (2 × 20 mL). The hydrolyzed solution was taken in the conical flask and acidified with 1 M HCl (pH 2). The acidified solution was extracted three times with EtOAc (3 × 30 mL) and dried over anhydrous Na_2SO_4. The solution was evaporated and solid yellow **7** was obtained. The solid yellow mass was recrystallized in dry THF.

Yield: 0.790 g (82%); FT-IR (KBr): $\bar{\upsilon}$ = 3305 (s, NH), 1690 (s, amide I band), 1611 (s, amide I band), 1596 (s, amide II band), 1540 (s, amide II band), 1514 cm^{-1}; ^{1}H NMR (400 MHz, DMSO-d_6): δ = 9.22 (br s, 1H, OH, Tyr), 8.68 (s, 1H, Amoc), 8.34–8.31 (d, J = 8.64 Hz, 2H, Amoc), 8.13–8.11 (d, J = 8.20 Hz, 2H, Amoc), 7.62–7.53 (m, 4H, Amoc), 7.42–7.40 (d, J = 7.96 Hz, 1H, NH), 6.99–6.97 (d, J = 7.92 Hz, 2H, Tyr), 6.62–6.60 (d, J = 7.92 Hz, 2H, Tyr), 6.06–5.94 (q, 2H, Amoc), 4.11 (br s, 1H, C^{α}H of Tyr), 2.93–2.88 (dd, J = 3.84 Hz, 3.64 Hz, 1H, C^{β} H of Tyr), 2.70–2.64 (m, 1H, C^{β} H of Tyr) ppm; MS (ESI): *m/z* calcd for $C_{25}H_{21}NO_5$: 438.1317 $[M+Na]^+$; found: 438.1331.

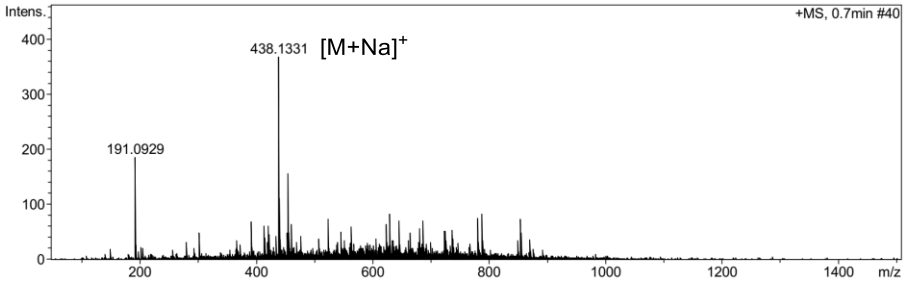

Figure 5.4 ESI-MS spectrum of **21**.

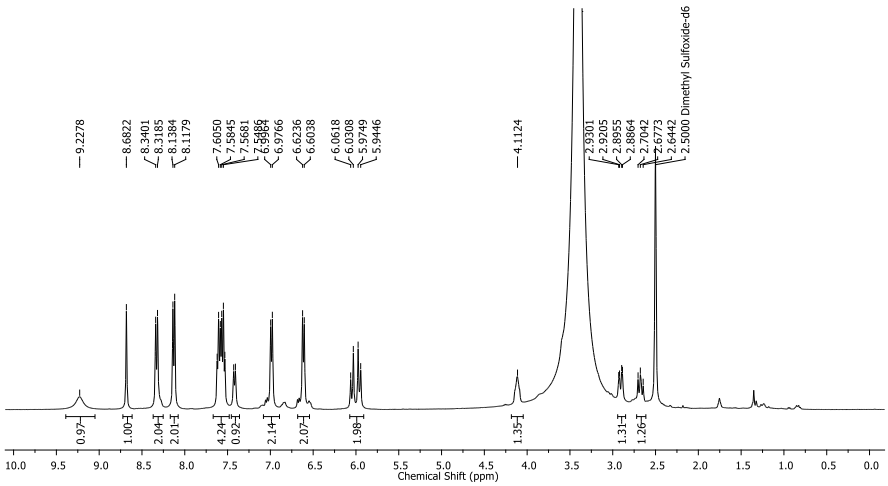

Figure 5.5 ^{1}H NMR (400 MHz, DMSO-d$_6$) spectrum of **21**.

5.2.2.4 Synthesis of 22

21 (1.0 g, 2.40 mmol) and HOBt (0.441 g, 2.88 mmol) was dissolved in 3 mL dry DMF. The coupling reagent DCC (0.595 g, 2.88 mmol) was added to the reaction mixture. The reaction mixture was ice-cooled. The hydrochloride salt of **13** (1.11 g, 4.80 mmol) was neutralized using saturated Na_2CO_3 (15 mL) solution and the product was extracted using ethyl acetate (3 × 30 mL). The neutralized solution of **13** was added to the reaction mixture and allowed to stir for 12 h. The product conversion was confirmed by TLC. The reaction mixture was filtered by sintered glass funnel (Borosil, G4) to remove urea by product. Ethyl acetate (25 mL) was added to the reaction mixture and washed with 1 M HCl (3 × 30 mL), saturated Na_2CO_3 solution (3 × 30 mL). Solid yellow **22** was obtained after evaporating the solvent under reduced pressure. The solid product was dissolved in ACN and insoluble urea was removed by vacuum filtration. The ACN was evaporated at reduced pressure and solid mass of **22** was purified by flash chromatography using EtOAc:hexane as eluent.

Yield: 0.996 g (70%); FT-IR (KBr): $\bar{\upsilon}$ = 3437 (br, OH), 3298 (NH), 1734 (s, COOMe), 1690 (s, amide I band), 1652 (s, amide I band), 1569 (s, amide II band), 1516 (s, amide II band) cm^{-1}; ^{1}H NMR (400 MHz, DMSO-d$_6$): δ = 9.25 (s, 1H, OH, Tyr), 9.17 (s, 1H, OH, Tyr), 8.68 (s, 1H, Amoc), 8.30–8.28 (d, *J* = 8.64, 3H, NH, Amoc), 8.13–8.11 (d, *J* = 8.12 Hz, 2H, Amoc), 7.61–7.52 (m, 4H, Amoc), 7.25–7.23 (d, *J* = 8.6 Hz, 1H, NH), 7.02–6.97 (m, 4H, Tyr), 6.68–6.67 (d, *J* = 7.92 Hz, 2H, Tyr), 6.61–6.59 (d, *J* = 7.84 Hz, 2H, Tyr), 5.98–5.91 (m, 2H, Amoc), 4.41–4.36 (m, 1H, C$^\alpha$ H of Tyr), 4.25–4.20 (m, 1H, C$^\alpha$ H of Tyr), 3.55 (s, 3H, OCH_3), 2.91–2.77 (m, 4H, C$^\beta$ H of Tyr) ppm; MS (ESI): *m/z* calcd for $C_{35}H_{32}N_2O_7$: 615.2107 $[M+Na]^+$; found: 615.2036.

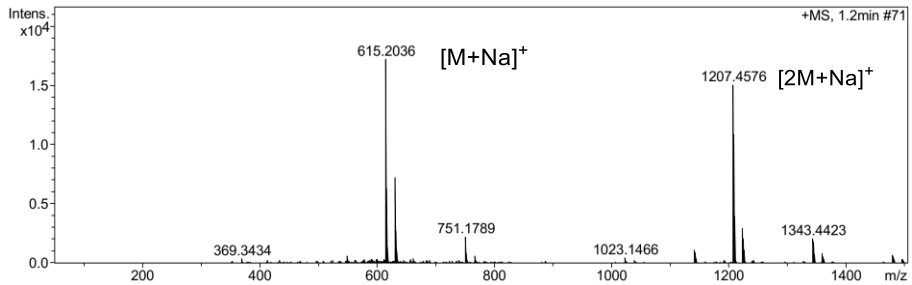

Figure 5.6 ESI-MS spectrum of **22**.

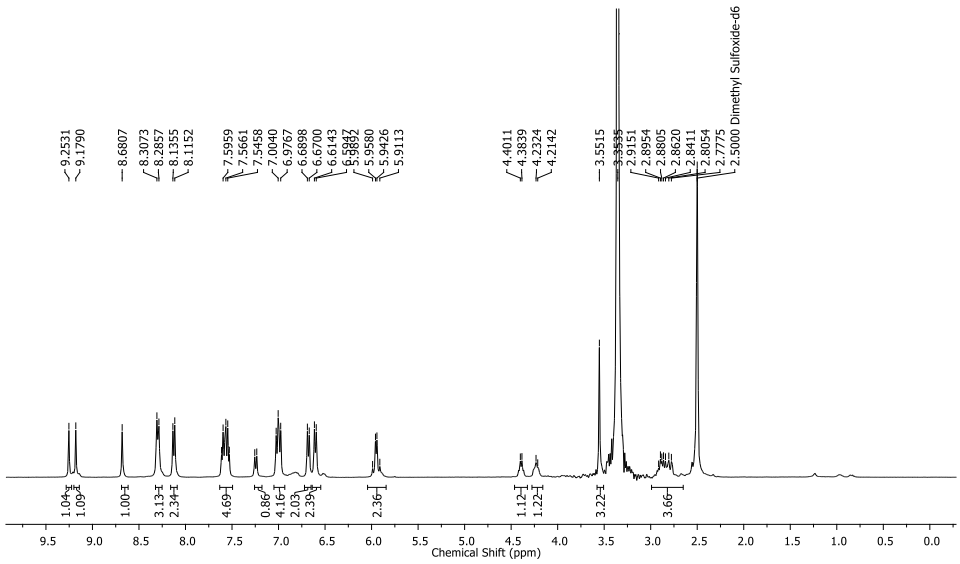

Figure 5.7 ^{1}H NMR (400 MHz, DMSO-d_6) spectrum of **22**.

5.2.2.5 Synthesis of 5

22 (0.800 g, 1.07 mmol) was completely solubilized in the mixture of THF:MeOH (1:2, 30 mL). A 3 mL of 1 M LiOH solution was added slowly. The progress of the hydrolysis was monitored by TLC and reaction mixture was stirred up to 6 h for complete hydrolysis. After the completion of the reaction, excess solvent was evaporated and diluted with 30 mL of distilled water. The aqueous solution of the product was taken into the separating funnel and slowly washed with diethyl ether (20 mL). The aqueous layer was collected and cooled in an ice bath. The solution was acidified with 1 M HCl (pH 2) and product was extracted with EtOAc (3 × 30 mL). The EtOAc layer was dried over anhydrous Na_2SO_4 and evaporated under reduced pressure to obtain **5** as yellow product. The yellow product was recrystallized in dry THF and hexane.

Yield: 0.617 g (79%); FT-IR (KBr): $\bar{\upsilon}$ = 3418 (br, OH), 3298 (s, NH), 1703 (s, COOH), 1689 (s, amide I band), 1652 (amide I band), 1632 (amide I band) 1571 (amide II band), 1513 (s, amide II band) cm^{-1}; ^{1}H NMR (400 MHz, DMSO-d_6): δ = 9.22 (s, 1H, OH, Tyr), 9.17 (s, 1H, OH, Tyr), 8.67 (s, 1H, Amoc), 8.29–8.27 (d, *J* = 8.60, 2H, Amoc), 8.13–8.09 (m, 3H, NH, Amoc), 7.60–7.52 (m, 4H, Amoc), 7.25–7.22 (d, *J* = 8.64 Hz, 1H, NH), 7.04–6.97 (dd, *J* = 8.08 Hz, 7.96 Hz, 4H, Tyr),

6.68–6.58 (dd, J = 8.04 Hz, 7.96 Hz, 4H, Tyr), 5.94 (s, 2H, Amoc), 4.38–4.34 (m, 1H, C^{α}H of Tyr), 4.23–4.20 (m, 1H, C^{α}H of Tyr), 2.97–2.66 (m, 4H, C^{β}H of Tyr) ppm; ^{13}C NMR (100 MHz, DMSO-d_6): δ = 173.47, 172.12, 156.50, 156.24, 131.42, 130.99, 130.69, 130.60, 129.42, 129.16, 127.52, 127.19, 125.79, 124.65, 115.54, 115.33, 58.71, 56.98, 54.39, 37.14, 36.53 ppm; HRMS (ESI): *m/z* calcd for $C_{34}H_{30}N_2O_7$: 601.1951 $[M+Na]^+$; found: 601.1943.

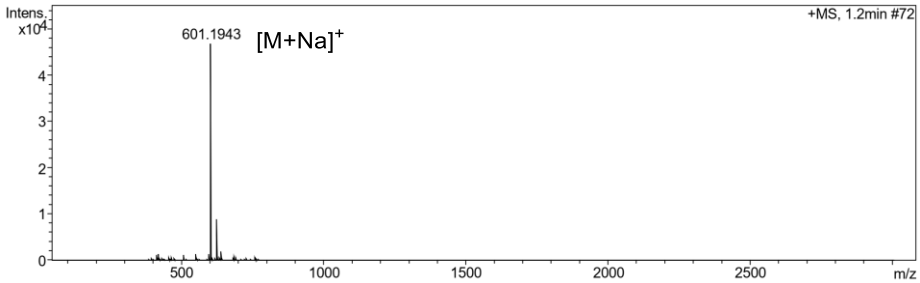

Figure 5.8 HRMS spectrum of **5**.

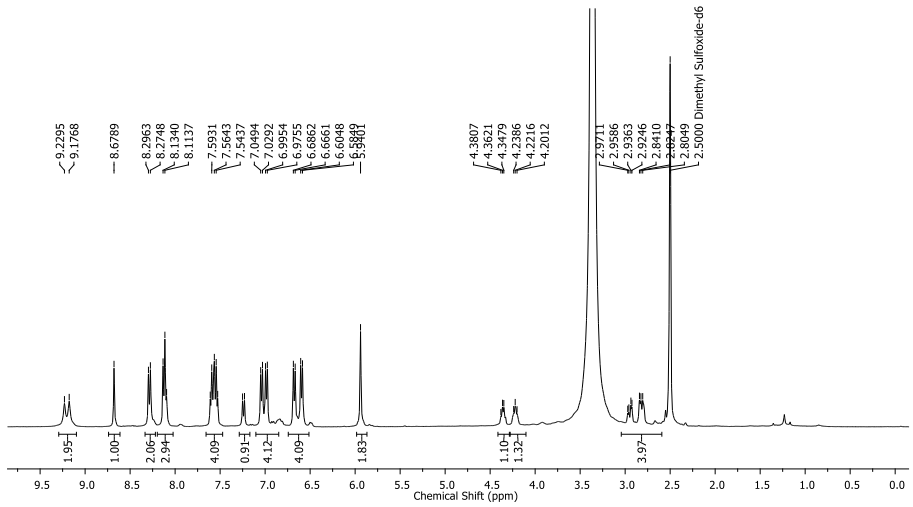

Figure 5.9 ^{1}H NMR (400 MHz, DMSO-d_6) spectrum of **5**.

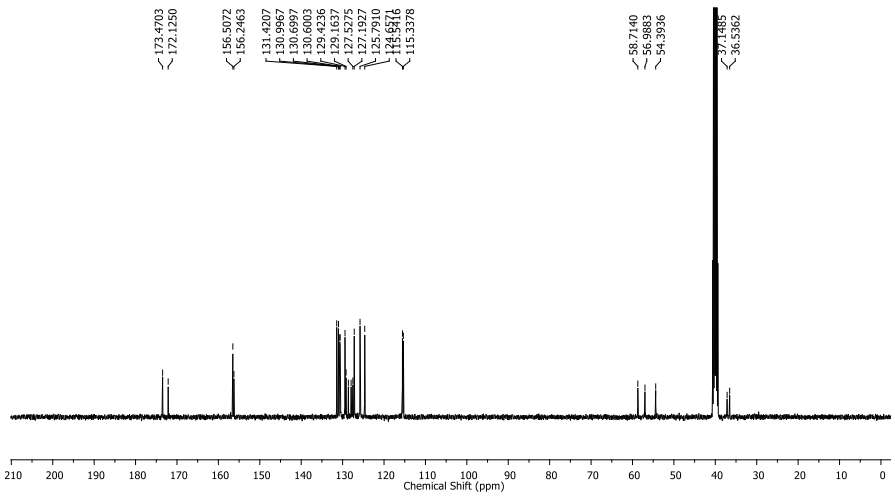

Figure 5.10 ^{13}C NMR (100 MHz, DMSO-d_6) spectrum of **5**.

5.2.3 Purification of the Peptide

Peptide **5** and their intermediates were purified by Flash Chromatography (TELEDYNE ISCO, USA; model: CombiFlash®Rf+) using silica gel (200 mesh size) with EtOAc/hexane (ratio as required) as eluent. The purified peptides were recrystallized in THF by slow evaporation methods to get crystalline peptides and used for further experiments.

5.2.4 Preparation of Hydrogels

5.2.4.1 Hydrogel 9

In a glass vial, peptide **5** (20 mmol L^{-1}) was added in 2 mL of ultra-pure water and solubilized by dropwise addition of 0.5 M NaOH. The pH of the solutions was slowly reduced by 0.1 M HCl and the turbid solutions of the peptide **5** turns into the hydrogel **9** at pH 7.4 and 37 °C. The self-supporting hydrogel **9** was formed which was examined by vial inversion method.

5.2.4.2 Hydrogels 10

The peptide **5** (20 mmol L^{-1}) was taken in glass vials containing 2 mL of Milli-Q water. The *β*-CD (20 mmol L^{-1}) was added to the peptide solutions. The pH of the mixture was elevated by slow addition of 0.5 M NaOH and these solutions were stirred for 30 min to get the clear peptide/*β*-CD solution. The pH of the solution was slowly decreased to pH 7.4 by slow addition of 0.1 M HCl solution. The solutions were kept in rest for 30 min at 37 °C which form self-supporting hydrogel **10**.

5.2.5 Characterizations

5.2.5.1 Spectroscopic Experiments

The nuclear magnetic resonance spectroscopy (NMR) experiments were performed in $CDCl_3$ and DMSO-d_6 on a Bruker AV 400 MHz spectrometer. The peptide concentrations used for the ^1H and ^{13}C NMR were 2-5 and 120-130 mmol L^{-1} respectively. The chemical shifts (δ) are reported in ppm, downfield of tetramethylsilane (TMS). Peak multiplicities are reported as follows: singlet (s), doublet (d), triplet (t), quartet (q) and multiplet (m) and broad (b). The electrospray ionization mass spectrometry (ESI-MS) was acquired on a Bruker micrOTOF-Q II mass spectrometer by a positive-mode electrospray ionization process. The circular dichroism spectra were recorded at 25 °C using a JASCO J-815 spectropolarimeter. The concentration-dependent circular dichroism experiments were performed using diluted hydrogel **10** (20, 8, 4, 2, 1, 0.5, 0.25, 0.125, 0.062 mmol L^{-1}). The FTIR spectroscopy was performed on KBr pellets on a Bruker Tensor 27 FTIR spectrophotometer. The hydrogel was placed between crystal Zn−Se windows for FTIR analysis and scanned between 600-4000 cm^{-1}.

5.2.5.2 Electron Microscopy Experiments

The high-resolution transmission electron microscopy (HRTEM) images were captured using a FEI electron microscope (model: Tecnai G2, F30), operated at an accelerating potential of 300 kV (Magnification, 58X to 1×10^6X). The images were captured using 2% (w/v) phosphotungstic acid as a negative stain. The dilute solution (1-2 mmol L^{-1}) of the hydrogels **9** and **10** were used for the HRTEM experiment.

5.2.5.3 Rheological Experiments

Rheological experiments were performed at 25 °C on an Anton Paar Physica MCR 301 rheometer. The amplitude sweep experiment was performed at constant frequency of 10 rad s^{-1} and region of deformation was evaluated. The hydrogels **9** and **10** were placed in between of a stainless steel parallel-plate (diameter: 25 mm) with TruGap (0.5 mm). The frequency sweep experiment was performed in the range of 0.05-100 rad s^{-1} with the same strain percent found by amplitude sweep experiment. The step strain experiment was performed by varying low-high-low strain at constant frequency of 10 rad s^{-1}.

5.2.6 Antibacterial Test

5.2.6.1 Inoculum Growth

The nutrient agar (NA) plate method was used to evaluate the antibacterial activity of the hydrogels. The bacterial culture *Staphylococcus aureus* (*S. aureus*, MTCC 87) and *Bacillus subtilis* (*B. subtilis*, MTCC 441) bacteria were procured from the Institute of Microbial Technology Chandigarh (CSIR-IMTech), India. Fresh inoculum was grown in nutrient broth (NB) and used for the experiments. The NA was prepared by dissolving peptone (10 gm), yeast extract (3 gm), NaCl (5 gm), agar-agar powder (20 gm) in 1000 mL water. The NB was prepared similarly as NA by eliminating agar-agar powder and autoclaved before use.

5.2.6.2 Hydrogel Treatment

The hydrogel **10** was prepared by maintaining the aseptic conditions. The sterile Milli-Q water, 0.5 M NaOH and 0.1 M HCl were used for the hydrogel preparation under the laminar air flow. The hydrogel **10** (20 mmol L^{-1}) was treated with Gram-positive (*S. aureus* and *B. subtilis*) and Gram-negative (*E. coli*) bacteria. The bacterial culture was grown for 12 h at 37 °C and used for the experiment. The absorbance (OD_{600} = 0.1) of bacterial culture was set according to McFarland standard (2×10^8 cfu/mL). A 100 µL of hydrogel **10** was transferred in a sterile centrifuge tube and 400 µL of NB was added slowly on the top of the hydrogel. A 10 µL of bacterial culture (2×10^6 cfu/mL) was added to the NB containing hydrogel **10**. The microcentrifuge tubes were incubated at 37 °C for 12 h for the bacterial growth. After treatment, 10 µL of bacterial suspension containing hydrogel was 10-fold diluted and whole plate streaked in a sterile nutrient agar plate. The reduction in the bacterial colonies was visually observed in the nutrient agar plate.

5.2.7 Cell Culture Experiments

The cell culture experiments were performed in DMEM (Dulbecco's Modified Eagle Medium contains 4 mM L-glutamine, 1000 mg/L glucose, and 110 mg/L sodium pyruvate) with 10% FBS (fetal bovine serum) and 1% antibiotic (penicillin-streptomycin) solution. The hydrogels **9** and **10** were diluted in cell culture media and used for the experiments. The resulting hydrogels concentrations for the cell culture experiments were in the range of 200 to 12.5 µmol L^{-1}. The HEK293 cells were used for the biocompatibility test. The hydrogels were treated with HEK293 (8×10^3 cells/well) cells for 24 h at 37 °C. After treatment, the cell culture media was removed very carefully and cells were washed with PBS (10

mmol L^{-1}, pH 7.4) to remove the excess hydrogel. After washing, the fresh DMEM (Dulbecco's Modified Eagle Medium) was added into the 96 well plate. The cytotoxic effect was evaluated by 3-(4,5-dimethylthiazol-2-yl)-2,5-diphenyltetrazolium bromide (MTT) assay. The absorbance was taken at 570 nm using a microplate reader (Synergy H1 multimode microplate reader).[11]

5.2.8 In vivo Wound Healing Experiments

In vivo wound healing experiments were performed according to the Institutional Animal Ethical Committee (IAEC) guidelines. The experimental approval was taken prior to the wound healing experiments. Wistar albino male rats (weight 180 ± 10 gm) were housed in polypropylene cages in a standard photoperiod (14 h, light:10 h, dark, 27 ± 2 °C) with the provision of laboratory feed (Gold Mohur feed, Hindustan Lever Limited, Mumbai, India) and water *ad libitum*. Animals were maintained in accordance with the guidelines of the Committee for the Purpose of Control and Supervision of Experiments on Animals (CPCSEA), Ministry of Environment, Forest and Climate Change, New Delhi, Government of India (Reg. No. 779/Po/Ere/S/03/CPCSEA).

5.2.8.1 Wound Creation and Hydrogel Injection

For the wound creation (1 day), each rat was anesthetized by subcutaneously injection of cocktail of the ketamine (50−60 mg/kg) and xylazine (10 mg/kg). The dorsal hairs were removed by using hair removal cream (Anne French; Pfizer, India). The wounding area was marked and then sterilized with povidone-iodine solution prior to incision. A disposable biopsy punch (8 mm) was used to induce wound on each side (two wounds) of the dorsal midline of the rat. Then, the rats were divided in different experimental groups such as disease control, drug control, hydrogel **10**, and each group contains five rats (n = 5). For the wound healing assay, the standard drug (silverex gel 0.2% w/w) and hydrogel **10** were applied on the wound site with the help of micropipette (100 µL/wound). The disease control group was given PBS on the wound site. After 1h, the wound site was covered and fixed by placing Tegaderm-3M dressing bandage over the wound. The wet environment of hydrogel sometime creates troubleshoot for the Tegaderm-3M bandage; hence, the interval was maintained for proper hydrogel drying on the wound site. The diclofenac injection was subcutaneously given after 4 h interval of the wounding. The hydrogel **10**, standard drug, and PBS were given in every alternate day. On day 12, the experiment was terminated and reduction in the wound area was photographed by digital camera. The rats were anaesthetized and the wound tissues were collected in the PBS for histology and biochemical analysis. The wound tissues were fixed for the histological analysis.

5.2.8.2 Histology Experiments

The wound tissue histology was performed on day 1 and 12. The small tissue specimen was collected by biopsy punch and the tissue fixation was performed in formalin solution (10% v/v). The fixed tissues were properly dehydrated and embedded in paraffin wax and small sections were cut into 4 µm thickness. The sections were stained with hematoxylin and eosin (H&E staining) and images were

captured in an inverted optical microscope for the histology analysis of the wound healing process.

5.2.8.3 Hydroxyproline Assay

The wound tissues were dried on the blotting paper and properly chopped into the small pieces. The chopped tissues (10% w/v) were slowly homogenized in ice-cold PBS (10 mM, pH 7.4). The homogenized solution was centrifuged at 10000 rpm (4 °C) for 15 min. The supernatant was slowly separated for the hydroxyproline assay and performed as previously reported. The stock L-hydroxyproline solution (1 mg/mL) was prepared in Mill-Q water. The Ehrlich's reagent (1 M) was prepared by dissolving 1.5 g of *p*-dimethylaminobenzaldehyde in *n*-propanol/perchloric acid (2:1 v/v, 3 mL) and volume was maintained 10 mL by addition of Mill-Q water. The chloramine-T (0.056 M) reagent was prepared by addition of 1.26 g of chloramine-T in 20 mL *n*-propanol/water (1:1) and final volume was maintained as 100 mL by addition of acetate-citrate buffer (pH 6.5, 100 mmol L^{-1}). The 200 µL of tissue homogenate was taken in a 2 mL microcentrifuge tube and 50 µL of 10 M NaOH solution was added to the vial. The tissue homogenate sample was hydrolyzed by autoclaving at 121 °C for 30 min. A 750 µL of chloramine-T was added to this sample and this sample was kept for 25 min at room temperature. A 500 µL of Ehrlich's reagent was added to the sample and kept at 70 °C for 30 min for the chromophore development. A 500 µL of water was added and absorbance was recorded at 550 nm using a spectrophotometer.

5.2.8.4 Nitrite Assay

The standard nitrite solution (1.44 mmol L^{-1}) was prepared by dissolving 1 mg of sodium nitrite in 10 mL of Milli-Q water. The tissue homogenate was mixed properly and 400 µL of homogenate was taken in a microcentrifuge tube. A 100 µL of Griess reagent was added to this tube at room temperature and mixed thoroughly with a micropipette. A 1.5 mL of Milli-Q water was added to this tube and incubated for 20 min at room temperature. The solution turns into pink color and the absorbance was recorded at 548 nm.

5.2.9 Statistical Analyses

The biological data are shown as mean ± SEM. $^{*}p< 0.05$; $^{**}p< 0.01$; $^{***}p < 0.001$, and $^{****}p< 0.0001$, as compared to the control group. The data were analyzed by one-way ANOVA (nonparametric) followed by Neuman-Keuls multiple comparison tests, using a Graph Pad Prism (GraphPad, San Diego, CA).

5.3 Results and Discussion

Self-assembly of peptide-based soft materials offers an appealing approach for the fabrication of functional biomaterials. In current work, the self-assembling dipeptide was synthesized using robust and rigid 9-anthracenemethoxycarbonyl (Amoc) group for N-terminal aromatic protection. The overall hydrophobicity of the synthesized dipeptide **5** (log P = 5.16) is calculated using online prediction program.[35] The additional hydrophobicity and planarity of Amoc group enable the hydrogelation of tyrosine containing dipeptide **5** (Amoc-YY-OH: Y = L-tyrosine). The dipeptide (20 mmol L^{-1}) self-assembles at physiological conditions

(pH 7.4, 37 °C) which encapsulates the water molecules and results into self-supporting hydrogel **9**. The dipeptide was solubilized at higher pH 10 and subsequently the pH of the system was reduced to 7.4 which entrapped water molecules owing to involvement of noncovalent interactions such as hydrogen bonding, π-π stacking and hydrophobic interactions.

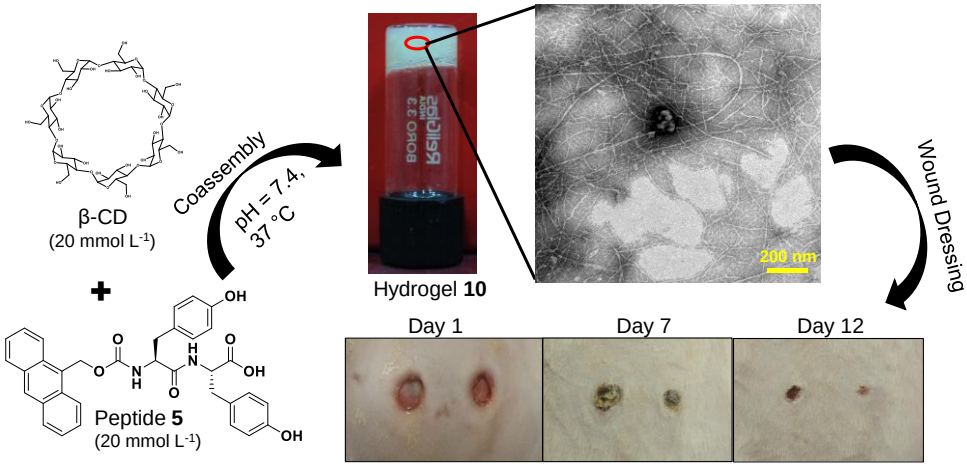

Scheme 5.2 The schematic representation of coassembly of peptide **5** (20 mmol L^{-1}) and *β*-CD (1:1 equivalent) at physiological conditions results into self-supporting hydrogel **10**. The coassembled nanofibrillar hydrogel **10** has been utilized as wound dressing system.

However, the dipeptide tailored with Amoc group has lower water solubility which was tuned by simple incorporation of equimolar ratio of *β*-cyclodextrin (*β*-CD) with self-assembling peptide (1:1 equivalent, peptide:*β*-CD). The dipeptide with *β*-CD (20 mmol L^{-1}; 1:1 equivalent) coassembled at physiological conditions (pH 7.4, 37 °C) and formed self-supporting hydrogel **10** (Scheme 5.2). The greater water solubility of dipeptide due to presence of equimolar *β*-CD could results of noncovalent interactions between *β*-CD and peptides.[36] The rheological experiments were carried out to ensure the formation of self-assembled materials (Figure 5.11). The strain sweep experiment was performed at constant angular frequency (10 rad s^{-1}) to ensure the viscoelastic nature of the hydrogels **9** and **10** (Figure 5.11a,d). The hydrogels **9** and **10** exhibit elastic behavior at low strain and viscous behavior at high strain. The exact strain percent for hydrogels are obtained where linear viscoelastic (LVE) region is valid. Below the critical strain percent (0.5 and 0.1 for hydrogels **9** and **10**, respectively), the rheological properties of hydrogels are independent of oscillatory strain. The values of storage (G') and loss modulus (G") for hydrogel **9** are always greater than the hydrogel **10**. This phenomenon suggests that the mechanical strength of the hydrogel **10** decreases after the incorporation of *β*-CD with self-assembling peptides. The lower mechanical strength of hydrogel **10** compared to hydrogel **9** could be the outcome of coassembly of *β*-CD and peptides.[37] The oscillatory frequency sweep experiments were performed below the LVE region to evaluate the solid-like character of hydrogels **9** and **10** at constant strain percent (Figure 5.11b,e).

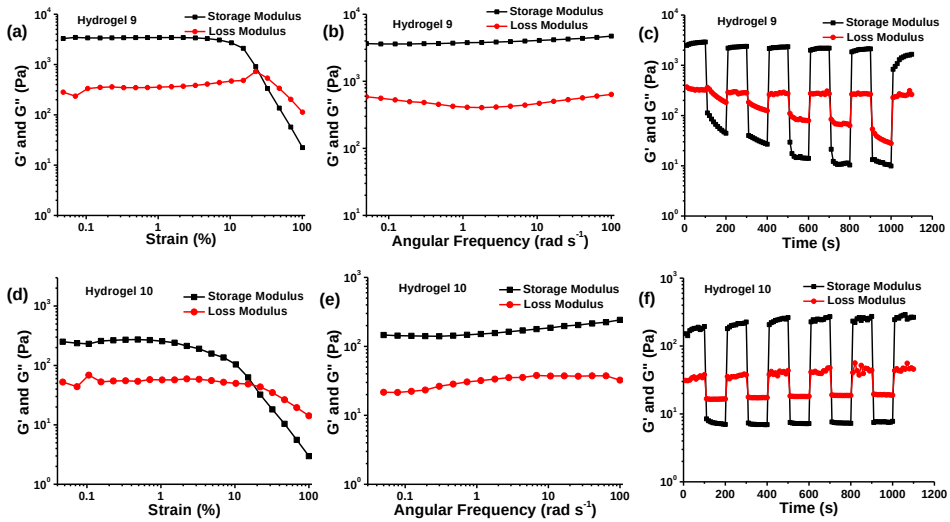

Figure 5.11 (a,d) amplitude sweep, (b,e) frequency sweep, (c,f) step strain experiments data of hydrogels **9** and **10**, respectively.

The frequency sweep data reveals the formation of self-supporting hydrogels because of greater G' values compared to G" values in entire oscillatory frequency region. The rheological properties are independent of oscillatory frequency which suggests solid-like character of hydrogels **9** and **10**. The dynamic step strain experiment was performed at constant angular frequency (10 rad s^{-1}) to study the self-recovery in mechanical strength of the hydrogels **9** and **10** (Figure 5.11c,f). The dynamic high-low-high strain was applied to deform and reform the gel networks because of reversible participation of noncovalent interactions. The step strain experiments exhibit better self-recovery of hydrogel **10** compared to hydrogel **9** which could be the reason of noncovalent interactions between β-CD and peptides. The data from step strain experiments suggests that the hydrogel **10** could be used as an injectable biomaterial owing to the rapid gel-sol-gel conversion.[38]

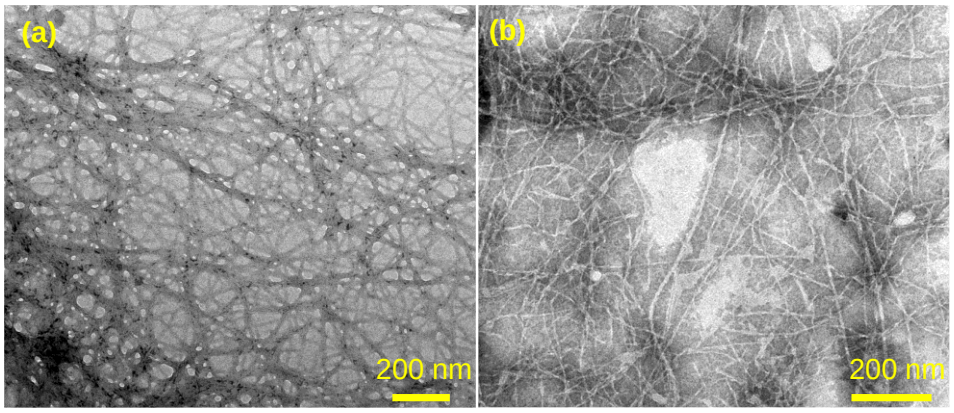

Figure 5.12 (a,b) HRTEM data of hydrogels **9** and **10**, respectively.

Further, the morphology of hydrogels **9** and **10** were analyzed by high-resolution transmission electron microscopy (HRTEM). The HRTEM data demonstrates the presence of dense nanofibrillar network which could entrap a large amount of water through the capillary action and surface tension leading to the formation of self-supporting hydrogels **9** and **10** (Figure 5.12a,b). The fibers are thin in hydrogel **10** with 10-15 nm average diameter, whereas the fibers are entangled in hydrogel **9** with 18-24 nm average diameter. The dense entangled fibrillar networks in HRTEM image corroborate the rheological data which suggests the greater mechanical strength of hydrogel **9** compared to the hydrogel **10**. The FTIR spectroscopy was employed to elucidate the type of secondary structure present in peptide and coassembled xerogel **10** (Figure 5.13a). The FTIR spectrum of *β*-CD shows characteristic peak at 1644 cm^{-1}.

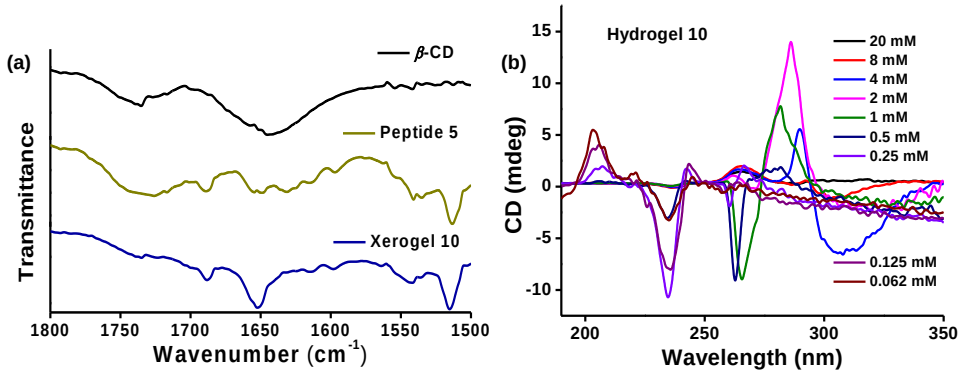

Figure 5.13 (a) FTIR spectra of *β*-CD, peptide **5** and xerogel **10**, respectively; (b) concentration-dependent CD of hydrogel **10**.

The FTIR spectrum of peptide **5** shows amide I peaks at 1688, 1656 and 1648 cm^{-1} which suggest the random structure of peptide. However, the xerogel **10** shows amide I peaks at 1688 and 1650 cm^{-1}.[22] The small shifting in amide band I could be the outcome of hydrogen bonding interactions between peptide and *β*-CD.[32] Furthermore, the concentration-dependent circular dichroism (CD) spectroscopy was employed to investigate the secondary structure and supramolecular aggregation of the peptide in coassembled hydrogel **10** (Figure 5.13b). The CD pattern of hydrogel changes with variation in concentrations which suggests the different orientation of molecules in their aggregated state.[32] Generally, CD spectra of proteins and peptides are studied in two regions such as the far UV (190-240 nm) and near UV (240-320 nm) region. The coassembled hydrogel **10** shows intense CD signals in the near UV region (250-320 nm) owing to presence of aromatic chromophores side chains in the peptides.[39] The dilution of hydrogel **10** (20-0.25 mmol L^{-1}) leads to the blue shift in CD signal suggesting the decrease of supramolecular aggregation of peptides at lower concentrations. The aromatic chromophore present in peptide significantly interferes with the amide CD in the far UV region (20 to 1 mmol L^{-1}). However, the aqueous hydrogel **10** (0.5 mM) shows negative CD signal at 234 and 264 nm owing to n-π* and π-π* transition of

amide and aromatic chromophore groups, respectively. Interestingly, the lower hydrogel **10** concentrations (0.125 and 0.062 mmol L^{-1}) shows additional positive signal at 203 nm owing to π-π* transition of amide group. However, the aromatic CD signal disappears at lower hydrogel **10** concentrations (0.125 and 0.062 mmol L^{-1}) which indicates the loss of extended aromatic stacking interactions.[39] The data from concentration-dependent CD spectra shows the π-π stacking interactions of aromatic groups interfere with the amide CD signal at far UV region. Noteworthy, the hydrogels for desired biomedical applications do not show unwanted immunogenicity and cytotoxicity. Hence, the cell culture experiments were performed to investigate the cytotoxicity of hydrogels **9** and **10** on the viability and growth of HEK293 cell line (Figure 5.14a,b). The HEK293 cell line was used as normal cell line for biocompatibility assessment of the hydrogels **9** and **10**. The hydrogels **9** and **10** show 80% cell viability at 200 μmol L^{-1} concentrations which illustrate the noncytotoxic nature of hydrogels.

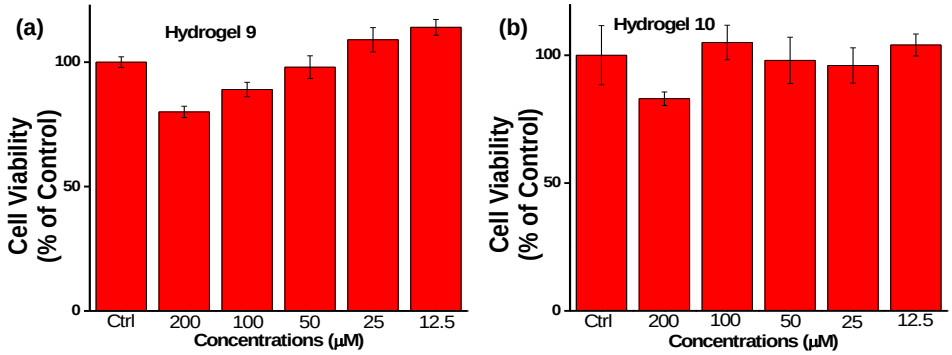

Figure 5.14 The cell culture experiments data using HEK293 cells and hydrogel **9** and **10**. The data are shown as mean ± standard error of the mean (n = 3).

The cytotoxicity data reveals that the hydrogel **10** is better biocompatible compared to hydrogel **9**. Furthermore, the better thixotropy and biocompatibility of hydrogel **10** motivated for the further assessment in biological applications. The innate antibacterial activity of hydrogel **10** was investigated using *S. aureus* and *B. subtilis* Gram positive bacteria (Figure 5.15a-d). On the basis of inherent hydrophobicity and better aggregation propensity, the Amoc-capped dipeptide-based coassembled hydrogel was used for the antibacterial study. The hydrogel **10** shows antibacterial activity against *S. aureus* and *B. subtilis* bacteria. The chronic wounds are mostly infected by *S. aureus* (93%) bacteria and cause slow wound healing.[40] The acute wounds become chronic wounds due to the bacterial infections which significantly increase the morbidity and financial burden. Hence, the biomaterials with innate antibacterial activity against the *S. aureus* bacterial could minimize the bacterial infections, therefore positively contribute in wound dressing process. The self-assembling peptide could lead to the cell membrane permeabilization and depolarization owing to the aggregation of peptides which results antibacterial activity.[41]

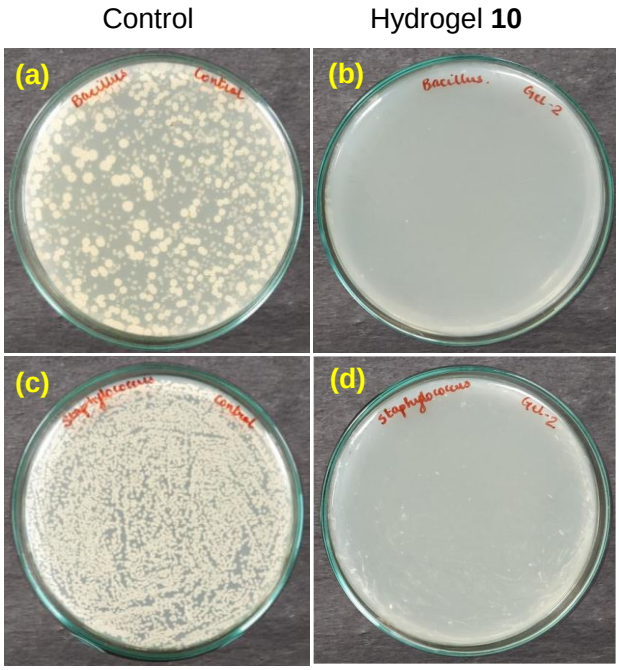

Figure 5.15 Antibacterial activity of hydrogel **10**: (a,b) *B. subtilis*; (c,d) *S. aureus*, respectively (control images are taken from Figure 4.18).

The in vivo cutaneous wound dressing activity of coassembled hydrogel was performed (Figure 5.16).[32] One pair of cutaneous wounds (8 mm) was created on the back of the rat using sterile Biopsy punch. The coassembled hydrogel was applied on the wound for 12 days. The reduction in wound size was photographed by digital camera which showed the distinct wound dressing activity of the hydrogel.

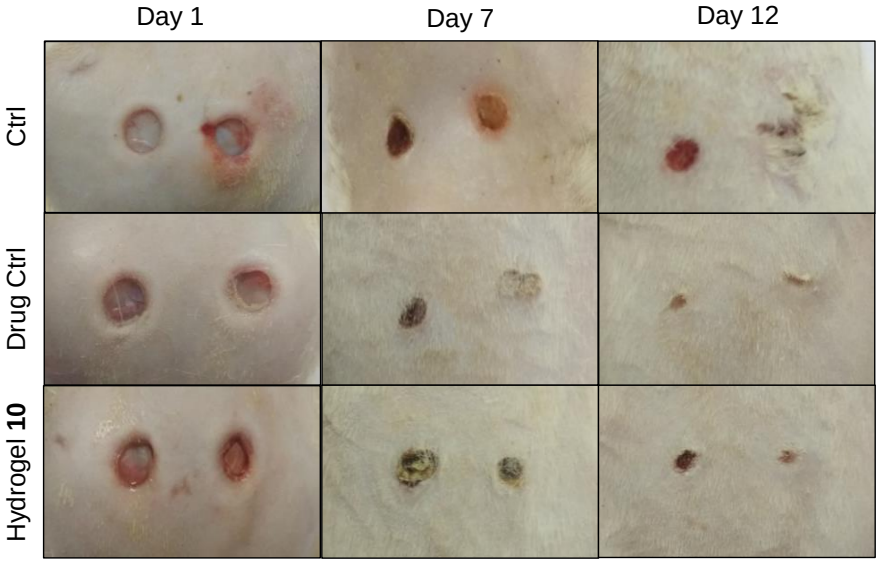

Figure 5.16 The in vivo wound dressing activity of hydrogel **10**. The progress of wound closure was photographed by digital camera at day 1, 7 and 12 and compared with control group (control images are taken from Figure 4.21).

The hydrated microenvironment near the wound site, antibacterial nature, fibrillar structure of coassembled hydrogel could be the reason for wound dressing activity of coassembled hydrogel **10**.[42] Moreover, the wound dressing activity of hydrogel **10** was studied by wound tissue histology experiments (Figure 5.17). The histology data exhibits the formation of regular epidermis layer which ensures the wound dressing activity.[43] The wound healing is complex and multistep process which contains coagulation, inflammation, fibroblast cell proliferation/differentiation, angiogenesis, re-epithelization and collagen synthesis.[44] Inflammation is essential phenomenon to activate the inflammatory cells such as neutrophils, macrophages and lymphocytes which scavenge the microbes and dead cells near the wound site.[44]

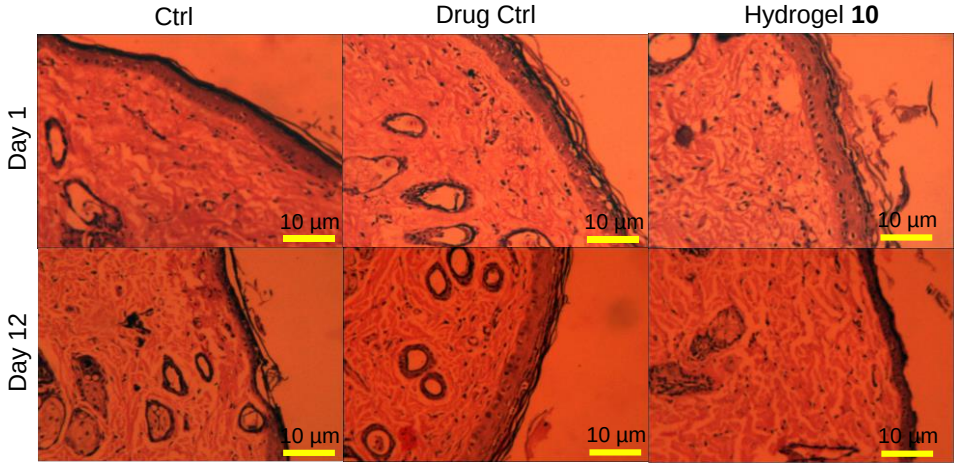

Figure 5.17 The tissue histology images of wound healing experiments (control images are taken from Figure 4.22).

The controlled inflammation promotes the fibroblast cell proliferation and migration for the healing process. However, the inflammation for longer time period causes delayed and impaired wound healing. The production of nitric oxide (NO) is directly associated with inflammatory cells such as macrophages in early phage of wound healing.[45] Hence, the level of inflammation is predicted by nitrite estimation which is the stable metabolite of NO. The Griess reagent was used to estimate the inflammation near the wound site after termination of the experiments (Figure 5.18a). The hydrogel **10** dramatically reduced the inflammation compared to control groups owing to better healing process. However, the drug control group shows greater nitrite level which suggests different mode of action of the silverex cream compared to hydrogel **10**. The hardening and maturation of wound are the last stage which depends upon the collagen fibers content near the wound site.[46] The content of collagen deposition near the wound site is investigated by hydroxyproline assay (Figure 5.18b). Hydroxyproline is structural amino acid of collagen protein which directly correlates the content of collagen protein in a tissue sample. The wound tissue homogenate of control group shows lowest level of collagen protein. However, the drug control and hydrogel group show greater

collagen content compared to control group which suggests the better wound healing process. Overall, the hydrogel **10** reduces inflammation and increases collagen deposition near the wound site, which suggests the wound dressing potential of a coassembled hydrogel. The nanofibrillar structure and inherent antibacterial nature of hydrogel **10** could be the second reason for better cutaneous wound healing process.

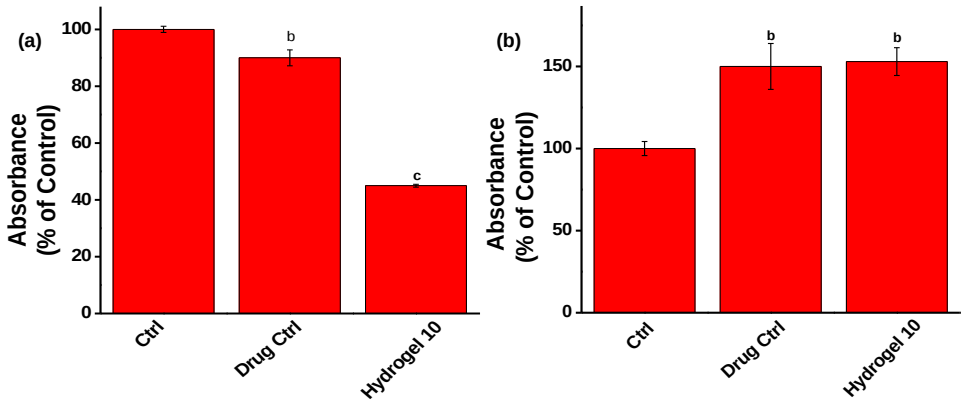

Figure 5.18 Biochemical analysis of wound tissue: (a) nitrite estimation by Griess reagent and (b) collagen protein estimation by hydroxyproline assay, respectively (control data are taken from Figure 4.23). The data are shown as mean ± standard error of the mean (n = 5). $^{a}p < 0.05$; $^{b}p < 0.01$; $^{c}p < 0.001$, and $^{d}p < 0.0001$ as compared to the control group.

5.4 Conclusion

In conclusion, the Amoc-capped dipeptide was synthesized using liquid-phase synthesis by racemization free peptide coupling reactions. The synthesized peptide (20 mmol L^{-1}) encapsulated water molecules through the surface tension and capillary action and formed self-supporting hydrogel **9** at physiological conditions (pH 7.4, 37 °C). The coassembled hydrogel **10** was prepared by simple physical integration of *β*-CD into dipeptide at equimolar concentration. The electron microscopic images of hydrogels **9** and **10** revealed entangled nanofibrillar networks, which were responsible for the self-supporting hydrogels. The mechanical strength of hydrogels was investigated by rheological studies which showed the viscoelastic and robust nature of self-supporting hydrogels. However, the rheological data suggested the thixotropic nature of coassembled hydrogel **10** that was good compared to hydrogel **9**. The cell culture data showed that hydrogel **10** was better cytocompatibile compared to hydrogel **9**. Furthermore, the hydrogel **10** was employed for antibacterial and wound healing applications due to better self-recovery and noncytotoxic nature. The antibacterial data exhibited that the hydrogel **10** was bactericidal for the growth of *B. subtilis* and *S. aureus* bacteria. The hydrogel **10** was employed for in vivo wound dressing applications and found that hydrogel **10** improved the healing process probably due to the antibacterial and nanofibrillar structures. The hydrogel **10** reduced the inflammation near the wound site and significantly increased the collagen deposition. All the

experimental data corroborated that the hydrogel **10** would be promising biomaterials for in vivo wound dressing activity.

5.5 References

(1) J. M. Lehn (2017), Supramolecular chemistry: where from? where to? Chem. Soc. Rev., 46, 2378–2379 (DOI: 10.1039/C7CS00115K).

(2) Amabilino D. B., Smith D. K., Steed J. W. (2017), Supramolecular materials, Chem. Soc. Rev., 46, 2404-2420 (DOI: 10.1039/C7CS00163K).

(3) Babu S. S., Praveen V. K., Ajayaghosh A. (2014), Functional π-gelators and their applications, Chem. Rev. 114, 1973-2129 (DOI: 10.1021/cr400195e).

(4) Du X., Zhou J., Shi J., Xu B. (2015), Supramolecular hydrogelators and hydrogels: from soft matter to molecular biomaterials. Chem. Rev., 115, 13165−13307 (DOI: 10.1021/acs.chemrev.5b00299).

(5) Hamley I. W. (2017), Small bioactive peptides for biomaterials design and therapeutics, Chem. Rev., 117, 14015−14041 (DOI: 10.1021/acs.chemrev.7b00522).

(6) Cheetham A. G., Chakroun R. W., Ma W., Cui H. (2017), Self-assembling prodrugs, Chem. Soc. Rev., 46, 6638−6663 (DOI: 10.1039/C7CS00521K).

(7) Reches M., Gazit E. (2003), Casting metal nanowires within discrete self-assembled peptide nanotubes, Science, 300, 625−627 (DOI: 10.1126/science.1082387).

(8) Grimme S. (2008), Tunable pentapeptide self-assembled β-sheet hydrogels, Angew. Chem., Int. Ed., 47, 3430–3434 (DOI: 10.1002/anie.200705157).

(9) Webber M. J., Kessler J. A., Stupp S. I. (2010), Emerging peptide nanomedicine to regenerate tissues and organs, J. Intern. Med, 267, 71-88 (DOI: 10.1111/j.1365-2796.2009.02184. x.).

(10) Clarke D. E., Parmenter C. D. J., Scherman O. A. (2018), Tunable pentapeptide self-assembled β-sheet hydrogels, Angew. Chem., Int. Ed., 57, 7709–7713 (DOI: 10.1002/anie.201801001).

(11) Uhlenheuer D. A., Petkau K., Brunsveld L. (2010), Combining supramolecular chemistry with biology, Chem. Soc. Rev., 39, 2817–2826 (DOI: 10.1039/B820283B).

(12) Li M., Ning Y., Chen J., Duan X., Song N., Ding D., Su X., Yu Z. (2019), Proline isomerization-regulated tumor microenvironment-adaptable self-assembly of peptides for enhanced therapeutic efficacy, Nano Lett., 19, 7965–7976 (DOI: 10.1021/acs.nanolett.9b03136).

(13) Wang Y., Matson J. B. (2019), Supramolecular nanostructures with tunable donor loading for controlled H_2S release, ACS Appl. Bio Mater., 2, 5093–5098 (DOI: 10.1021/acsabm.9b00768).

(14) Tang J. D., Roloson E. B., Amelung C. D., Lampe K. J. (2019), Rapidly assembling pentapeptides for injectable delivery (RAPID) hydrogels as cytoprotective cell carriers, ACS Biomater. Sci. Eng., 5, 2117–2121 (DOI: 10.1021/acsbiomaterials.9b00389).

(15) Hu B., Lian Z., Zhou Z., Shi L., Yu Z. (2020), Reactive oxygen species-responsive adaptable self-assembly of peptides toward advanced biomaterials, ACS Appl. Bio Mater., (DOI: 10.1021/acsabm.0c00758).
(16) Tang J. D., Mura C., Lampe K. J. (2019), Stimuli-responsive, pentapeptide, nanofiber hydrogel for tissue engineering. J. Am. Chem. Soc., 141, 4886–4899 (DOI: 10.1021/jacs.8b13363).
(17) Qi Y., Min H., Mujeeb A., Zhang Y., Han X., Zhao X., Anderson G. J., Zhao Y., Nie G. (2018), Injectable hexapeptide hydrogel for localized chemotherapy prevents breast cancer recurrence, ACS Appl. Mater. Interfaces, 10, 6972–6981 (DOI: 10.1021/acsami.7b19258).
(18) Ren P., Li J., Zhao L., Wang A., Wang M., Li J., Jian H., Li X., Yan X., Bai S. (2020), Dipeptide self-assembled hydrogels with shear-thinning and instantaneous self-healing properties determined by peptide sequences, ACS Appl. Mater. Interfaces, 12, 21433–21440 (DOI: 10.1021/acsami.0c03038).
(19) Raymond D. M., Abraham B. L., Fujita T., Watrous M. J., Toriki E. S., Takano T., Nilsson B. L. (2019), Low-molecular-weight supramolecular hydrogels for sustained and localized in vivo drug delivery, ACS Appl. Bio Mater., 2, 2116−2124 (DOI: 10.1021/acsabm.9b00125).
(20) Vargiu A. V., Iglesias D., Styan K. E., Waddington L. J., Easton C. D., Marchesan S. (2016), Design of a hydrophobic tripeptide that self-assembles into amphiphilic superstructures forming a hydrogel biomaterial, Chem. Commun., 52, 5912−5915 (DOI: 10.1039/C5CC10531E).
(21) Gavel P. K., Parmar H. S., Tripathi V., Kumar N., Biswas A., Das A. K. (2019), Investigations of anti-inflammatory activity of a peptide-based hydrogel using rat air pouch model, ACS Appl. Mater. Interfaces, 11, 2849−2859 (DOI: 10.1021/acsami.8b19228).
(22) Gavel P. K., Dev D., Parmar H. S., Bhasin S., Das A. K. (2018), Investigations of peptide-based biocompatible injectable shape-memory hydrogels: differential biological effects on bacterial and human blood cells. ACS Appl. Mater. Interfaces, 10, 10729−10740 (DOI: 10.1021/acsami.8b00501).
(23) Baral A., Roy S., Ghosh S., Hermida-Merino D., Hamley I. W., Banerjee A. (2016), A peptide-based mechano-sensitive, proteolytically stable hydrogel with remarkable antibacterial properties, Langmuir, 32, 1836–1845 (DOI: 10.1021/acs.langmuir.5b03789).
(24) Irwansyah I., Li Y. Q., Shi W., Qi D., Leow W. R., Tang M. B. Y., Li S., Chen X. (2015), Gram-positive antimicrobial activity of amino acid-based hydrogels, Adv. Mater., 27, 648–654 (DOI: 10.1002/adma.201403339).
(25) Zhao Y., Wang Z., Mei C., Jiang Z., Feng Y., Gao R., Wang Q., Huang J. (2018), Protein enables conformation transition of a hydrogel based on pentapeptide and boosts immune response in vivo, Bioconjugate Chem., 29, 1519–1524 (DOI: 10.1021/acs.bioconjchem.8b00044).
(26) Das S., Kumar R., Jha N. N., Maji S. K. (2017), Controlled exposure of bioactive growth factor in 3D amyloid hydrogel for stem cells differentiation, Adv. Healthcare Mater., 6, 1700368 (DOI: 10.1002/adhm.201700368).

(27) Shi Y., Wang Z., Zhang X., Xu T., Ji S., Ding D., Yang Z., Wang L. (2015), Multi-responsive supramolecular hydrogels for drug delivery, Chem. Commun., 51, 15265–15267 (DOI: 10.1039/C5CC05792B).
(28) Kalafatovic D., Nobis M., Javid N., Frederix P. W. J. M., Anderson K. I., Saunders B. R., Ulijn R. V. (2015), MMP-9 triggered micelle-to-fibre transitions for slow release of doxorubicin, Biomater. Sci., 3, 246–249 (DOI: 10.1039/C4BM00297K).
(29) He H., Lin X., Guo J., Wang J., Xu B. (2020), Perimitochondrial enzymatic self-assembly for selective targeting the mitochondria of cancer cells, ACS Nano, 14, 6947–6955 (DOI:10.1021/acsnano.0c01388).
(30) Jeena M. T., Jeong K., Go E. M., Cho Y., Lee S., Jin S., Hwang S. W., Jang J. H., Kang C. S., Bang W. Y., Lee E., Kwak S. K., Kim S., Ryu J. H. (2019), Heterochiral assembly of amphiphilic peptides inside the mitochondria for supramolecular cancer therapeutics, ACS Nano, 13, 11022–11033 (DOI: 10.1021/acsnano.9b02522).
(31) Malhotra K., Shankar S., Rai R., Singh Y. (2018), Broad-spectrum antibacterial activity of proteolytically stable self-assembled αγ-hybrid peptide gels, Biomacromolecules, 19, 782–792 (DOI: 10.1021/acs.biomac.7b01582).
(32) Gavel P. K., Kumar N., Parmar H. S., Das A. K. (2020), Evaluation of a peptide-based coassembled nanofibrous and thixotropic hydrogel for dermal wound healing, ACS Appl. Bio Mater., 3, 3326–3336 (DOI: 10.1021/acsabm.0c00252).
(33) Qu J., Zhao X., Liang Y., Zhang T., Ma P. X., Guo B. (2018), Antibacterial adhesive injectable hydrogels with rapid self-healing, extensibility and compressibility as wound dressing for joints skin wound healing, Biomaterials, 183, 185–199 (DOI: 10.1016/j.biomaterials.2018.08.044).
(34) Biswas S., Rasale D. B., Das A. K. (2016), Blue light emitting self-healable graphene quantum dot embedded hydrogels, RSC Adv., 6, 54793–54800 (DOI: 10.1039/C6RA06587B).
(35) https://www.molinspiration.com.
(36) Chen G., Jiang M. (2011), Cyclodextrin-based inclusion complexation bridging supramolecular chemistry and macromolecular self-assembly, Chem. Soc. Rev., 40, 2254−2266 (DOI: 10.1039/C0CS00153H).
(37) Chen M. H., Wang L. L., Chung J. J., Kim Y.-H., Atluri P., Burdick J. A. (2017), Methods to assess shear-thinning hydrogels for application as injectable biomaterials, ACS Biomater. Sci. Eng., 3, 3146−3160 (DOI: 10.1021/acsbiomaterials.7b00734).
(38) Rodell C. B., MacArthur J. W., Dorsey S. M., Wade R. J., Wang L. L., Woo Y. J., Burdick J. A. (2015), Shear-thinning supramolecular hydrogels with secondary autonomous covalent crosslinking to modulate viscoelastic properties in vivo, Adv. Funct. Mater., 25, 636−644 (DOI: 10.1002/adfm.201403550).
(39) Sun Z., Li Z.; He Y., Shen R., Deng L., Yang M., Liang Y., Zhang Y. (2013), Ferrocenoyl phenylalanine: a new strategy toward supramolecular hydrogels with

multistimuli responsive properties, J. Am. Chem. Soc., 135, 13379−13386 (DOI : 10.1021/ja403345p).
(40) Brogden K. A. (2005), Antimicrobial peptides: pore formers or metabolic inhibitors in bacteria? Nat. Rev. Microbiol., 3, 238−250 (DOI: 10.1038/nrmicro1098).
(41) Song J., Yuan C., Jiao T., Xing R., Yang M., Adams D. J., Yan X. (2020), Multifunctional antimicrobial biometallohydrogels based on amino acid coordinated self-assembly, Small, 2020, 16, 1907309 (DOI: 10.1002/smll.201907309).
(42) Xiao Y., Reis L. A., Feric N., Knee E. J., Gu J., Cao S., Laschinger C., Londono C., Antolovich J., McGuigan A. P., Radisic M. (2016), Diabetic wound regeneration using peptide-modified hydrogels to target re-epithelialization, Proc. Natl. Acad. Sci. U.S.A., 113, E5792−E5801 (DOI: 10.1073/pnas.1612277113).
(43) Basu A., Celma G., Strømme M., Ferraz N. (2018), In vitro and in vivo evaluation of the wound healing properties of nano-fibrillated cellulose hydrogels, ACS Appl. Bio Mater., 1, 1853−1863 (DOI: 10.1021/acsabm.8b00370).
(44) Sharifi S., Hajipour M. J., Gould L., Mahmoudi M. (2020), Nanomedicine in healing chronic wounds: opportunities and challenges, Mol. Pharmaceutics, (DOI: 10.1021/acs.molpharmaceut.0c00346).
(45) Naghavi N., De Mel A., Alavijeh O. S., Cousin B. G., Seifalian A. M. (2013), Nitric oxide donors for cardiovascular implant applications, Small, 9, 22−35 (DOI: 10.1002/smll.201200458).
(46) Reddy G. K., Enwemeka C. S. (1996), A simplified method for the analysis of hydroxyproline in biological tissues, Clin. Biochem., 29, 225−9 (DOI: 10.1016/0009-9120(96)00003-6).

Chapter 6

General Conclusions and Scope for Future Work

6.1 General Conclusions

The development of dipeptide-based functional materials for biological applications are gaining immense attention during past decades owing to their simple chemical functionalization, low concentration aggregation propensity, inherent antibacterial activity, biocompatibility and biodegradability.[1-5] However, the design and fabrication of peptide-based functional materials require a good biochemical engineering approach.[6-8] This thesis work is focused on the design and development of N-terminal Amoc-capped self-assembling dipeptide-based biomaterials for various biomedical applications including antibacterial, anti-inflammatory and wound healing. The N-terminal Amoc group has been utilized for aromatic protection of the dipeptides which facilitate the additional hydrophobicity for formation of self-assembled nanostructures. Electron microscopic techniques have been used for the characterization of well-defined nanostructures which showed the noncovalent interactions were driving force for the formation of self-assembled structures. Several spectroscopic techniques have been employed for the investigation of secondary structure present in the dipeptides during the self-assembly process. The spectroscopic and microscopic techniques revealed the noncovalent interactions such hydrogen bonding, π-π stacking and hydrophobic interactions participated in supramolecular arrangement of dipeptides. The photophysical studies showed the extended aromatic interactions between Amoc-capped dipeptides resulted into the self-supporting hydrogels. Rheological investigations exhibited viscoelastic and thixotropic character of self-assembled materials. The biocompatibility of dipeptide-based hydrogels were evaluated by cell culture experiments and found that the hydrogels were noncytotoxic in nature. Furthermore, the dipeptide-based self-assembled materials were employed for various biological studies such as antibacterial, anti-inflammatory and wound healing applications.

Chapter 1 summarizes the basic understanding of supramolecular chemistry which is used as a tool for the programming of the chemical systems for the development well organized micro to nanostructures. This chapter presents brief account about various N-terminus protecting groups and their role in self-assembly. This chapter presents the brief account of the self-assembling peptides and their applications in various interdisciplinary areas of research.

Chapter 2 describe the self-assembly of Amoc-capped dipeptides which entrap the water molecules and formed injectable, thixotropic and self-supporting hydrogels for broad spectrum antibacterial applications against the Gram-positive and Gram-negative bacteria. This chapter describe the link between hydrophobicity, aggregation propensity, secondary structure of the dipeptides and their antibacterial activity. The higher hydrophobicity and better secondary structure propensity of dipeptides were responsible for antibacterial applications. However, the Amoc-capped self-assembling dipeptides showed noncytotoxicity for human blood cells.

Chapter 3 describe the self-assembly of Amoc-capped dipeptide-based injectable and thixotropic hydrogel. The dipeptide self-assembled into hydrogel owing to involvement of aromatic and hydrogen bonding interactions which was established by spectroscopic and microscopic techniques. This chapter illustrate the potential therapeutic application of dipeptide-based hydrogel in acute inflammation. The rat air pouch model of inflammation was utilized for the study of anti-inflammatory activity of self-assembled hydrogel. Furthermore, an in vivo study of acute inflammation gives insight into the biocompatibility as well as anti-inflammatory potential of the hydrogel in a dose-dependent manner.

Chapter 4 describe the coassembly of Amoc-capped dipeptide and β-cyclodextrin for preparation of self-supporting, thixotropic and injectable hydrogel. The mechanical strength of hydrogel was controlled and tuned by physical incorporation of β-cyclodextrin with self-assembling peptides at physiological conditions. The coassembled hydrogel exhibited nanofibrillar structures which are highly twisted and entangled owing to participation of noncovalent interactions. The coassembled hydrogel was antibacterial against the growth of Gram-positive bacteria. Furthermore, the coassembled hydrogel demonstrated in vivo dermal wound healing activity because of inherent antibacterial nature and highly nanofibrillar structure of hydrogel.

Chapter 5 describe the development of Amoc-capped dipeptide-based coassembled hydrogel as wound dressing systems. The coassembled hydrogel was demonstrated nanofibrillar network which encapsulate large amount of water and turns into the thixotropic hydrogel. The hydrogel was biocompatible and inherent antibacterial against Gram-positive bacteria. The hydrogel employed for cutaneous wound dressing activity and observed that the healing process was significantly improved by introduction of the hydrogel. The hydrogel reduced acute inflammation and increased the collagen deposition near the wound site which are the key and important component for the better wound healing activity.

6.2 Scope for Future Work

Self-assembly of peptides and peptide-based materials are expected to enter into the regenerative medicine in near future. The peptide-based materials are inherent biocompatible and biodegradable, hence small structural manipulation *i.e.* nitric oxide functionalization could result into the functional biomaterials for diabetic wound healing. To fulfil the long-standing demand of biomedicine, the self-assembling peptides can be programmed by covalent linkage or coassembly approach with the biological active molecules. The self-assembling peptide-based materials would be promising candidate for hemorrhage control and hemostatic applications. The self-assembling peptides can be functionalized to show the heparin-like activity for anticoagulating applications. Additionally, the peptide-based self-assembled materials would be great candidate as COX inhibitor for acute and chronic inflammations related to rheumatoid arthritis and cancer. The stimuli-responsive self-assembly would be great interest for the development of

anticancer therapeutics. The scope of peptides and peptide-based self-assembled biomaterials are very broad in the area of cell culture, antimicrobial, anti-inflammatory, anticancer, wound healing, drug delivery, bioimaging and 3D bioprinting applications.

6.3 References

(1) Frenkel-Pinter M., Samanta M., Ashkenasy G., Leman L. J. (2020), Prebiotic peptides: molecular hubs in the origin of life, Chem. Rev., 120, 11, 4707–4765 (DOI: 10.1021/acs.chemrev.9b00664).

(2) Wychowaniec J. K., Smith A. M., Ligorio C., Mykhaylyk O. O., Miller A. F., Saiani A. (2020), Role of sheet-edge interactions in β-sheet self-assembling peptide hydrogels, Biomacromolecules, 21, 2285−2297 (DOI: 10.1021/acs.biomac.0c00229).

(3) Pengfei Zou, Wen-Ting Chen, Tongyi Sund, Yuanyuan Gaob, L. Li-Li, Wang H. (2020), Recent advances: peptides and self-assembled peptide-nanosystems for antimicrobial therapy and diagnosis, Biomater. Sci., (DOI: 10.1039/D0BM00789G).

(4) Raza F., Zafar H., You X., Khan A., Wu J., Ge L. (2019), Cancer nanomedicine: focus on recent developments and self-assembled peptide nanocarriers, J. Mater. Chem. B, 7, 7639−7655 (DOI: 10.1039/c9tb01842e).

(5) Mondal S., Das S., Nandi A. K. (2020), A review on recent advances in polymer and peptide hydrogels, Soft Matter, 16, 1404−1454 (DOI: 10.1039/C9SM02127B)

(6) Wang Y., Zhang W., Gongc C., Liua B., Lib Y., Wangd L., Su Z., Wei G. (2020), Recent advances in the fabrication, functionalization, and bioapplications of peptide hydrogels, Soft Matter, (DOI: 10.1039/D0SM00966K).

(7) Gupta S., Singh I., Sharma A. K., Kumar P. (2020), Ultrashort peptide self-assembly: front-runners to transport drug and gene cargos, Front. Bioeng. Biotechnol., 8, 504. (DOI: 10.3389/fbioe.2020.00504).

(8) Jain R., Roy S. (2020) Tuning the gelation behavior of short laminin derived peptides via solvent mediated self-assembly, Mater. Sci. Eng. C, 108, 110483 (DOI: 10.1016/j.msec.2019.110483).